# Properties of piezoresistive silicon nano-scale cantilevers with applications to BioNEMS

Thesis by

Jessica Arlett

In Partial Fulfillment of the Requirements

For the Degree of

Doctor of Philosophy

California Institute of Technology

Pasadena, California

2006

(Defended March 3, 2006)

Acknowledgement

I would like to thank Ben Gudlewski for the enormous effort he has put into the fabrication of BioNEMS devices, especially for being willing to try when I asked for devices of extreme dimensions for sensing Brownian fluctuations. Blake Axelrod, James Maloney, Darron Young, and Hong Tang have all been involved in many of the measurements presented throughout this thesis. In particular, I couldn't have completed the measurements in fluid without Blake Axelrod's adaptation of PDMS-based soft microfluidics (pioneered by Professor Steve Quake's research group) to compatibility with silicon based BioNEMS. The low temperature and vacuum measurements were performed jointly with James Maloney. James and I worked together regularly throughout our time here. His input on all aspects of the project and the discussions we have had are greatly appreciated. The fabrication performed by Melaku Muluneh is also very much appreciated. Many of the microfluidics devices were fabricated by Christina Morales of the microfluidics foundry at Caltech; her willingness to adapt her standard procedures to the requirements of our devices are appreciated. This project has greatly benefited from collaborations with Tronics Microsystems, S.A. This collaboration was made possible by Peter Pfluger and Christian Pisella. A special thanks goes to Natacha Raphoz of Tronics Microsystems, S.A. for her efforts in performing the microscale processing of much of the material used in this thesis. Our requests required many special considerations due to the thinness of the material, the aspect ratios and dimensions we were looking for, and the fragility of our membrane devices. This project wouldn't have been possible without her willingness to depart from standard protocols. The success of our collaboration with Tronics Microsystems, S.A. would not have been

possible without the efforts of Ariel Cao, who established the initial dialog between Caltech and Tronics, S.A. and has followed through throughout the collaboration to ensure smooth communication and a successful partnership. Finally, the magnetic measurements would not have been possible without the magnetic coils, initially fabricated in our lab by Darron Young. This work has benefited from a fruitful collaboration with the research group of Professor Scott Fraser, (Division of Biology, Caltech). Especially significant has been contributions of Professor Scott Fraser, Christie Canaria, and Rusty Lansford to the development of biofunctionalization protocols. I would like to thank Professor Mike Cross (Department of Physics, Caltech) and Professor Mark Paul (Department of Mechanical Engineering, Virginia Polytechnic Institute and State University) for their calculations, simulations, and assistance with the theoretical side of this project. Finally, I'd like to thank Professor Michael Roukes for his guidance and suggestions throughout this project.

Most of all I'd like to thank Evan and Ryan who made the last few years, which might otherwise have been stressful, fun instead.

Over the last decade a great deal of interest has been raised in applications of Microelectromechanical Sensors [MEMS] for the detection of biological molecules and to the study of their forces of interaction. Experiments in these areas have included Force Spectroscopy (Chemical Force Microscopy), MEMS patch clamp technology, and surface stress sensors. All of these technologies suffer from limitations on temporal response and involve devices with active surface areas that are large compared to molecular dimensions. Biofunctionalized nanoelectromechanical systems (BioNEMS) have the potential to overcome both of these hurdles, offering important new prospects for single-molecule force assays that are amenable to large scale integration. Results are presented here on the characterization of piezoresistive silicon cantilevers with applications to BioNEMS devices. The cantilevers were characterized by studying their response in gaseous ambients under a number of drive conditions including magnetic, piezoelectric, and thermal actuation, in addition to passive detection of the thermomechanical response. The measurements were performed at liquid helium temperature, at room temperature, and over a range of pressures (atmospheric pressure to 30mT). Theoretical studies have been performed on the response of these devices to Brownian fluctuations in fluid, on the feasibility of these devices as surface stress sensors, and on improvements in device design as compared to piezoresistive surface stress sensors currently discussed in the literature. The devices were encapsulated in microfluidics and measurements were performed to show the noise floor in fluid. The piezoresistive response of the device in fluid was shown through the use of pulsatory fluidic drive. As a proof of concept, biodetection experiments are presented for biotin labeled beads. The biofunctionalization for the latter experiment was performed entirely

within the microfluidics. A discussion of how these experiments can be extended to other cells, spores, and molecules is presented.

# Table of Contents

*1 Introduction* ____ *1*

**1.1 Motivation** ____ **1**

1.1.1 Overview: Mechanical Sensors for Biology ____ 1

1.1.2 Motion Transduction via Piezoresistive Sensing ____ 5

**1.2 Nanoscale Mechanical Devices: BioNEMS** ____ **6**

1.2.1 BioNEMS Detection Based on a Change in Device Compliance. ____ 8

1.2.2 BioNEMS Detection Based on a Change in Device Damping. ____ 8

1.2.3 Coupled, Multiple-Cantilever Devices ____ 11

1.2.4 Practical Considerations. ____ 13

1.2.5 Specificity and the Stochastic Nature of Single-Analyte Binding Events ____ 13

**1.3 Overview of Thesis** ____ **14**

**1.4 References** ____ **18**

*2 Theoretical Foundation of Piezoresistive NEMS Detection and Realizable Force Sensitivity* ____ *21*

**2.1 Overview** ____ **21**

**2.2 Fluid-Coupled Nanomechanical Devices: Analysis** ____ **21**

2.2.1 Introduction ____ 21

2.2.2 Analytical Calculations for Experimentally Relevant Conditions ____ 23

2.2.3 BioNEMS Displacement Response Function ____ 27

**2.3 Transducer Performance: Calculation of Parameters for Piezoresistive Transduction in p-type NEMS** ____ **36**

2.3.1 Calculation of the Spring Constant and comparison with simulations ____ 36

2.3.2 Calculation of the Cantilever's Effective Mass in Vacuum ____ 40

2.3.3 Piezoresistivity: an Overview ____ 42

2.3.4 Calculation of the Piezoresistive Tranduction Factor 43

**2.4 Force Sensitivity of Piezoresistive BioNEMS Devices: Noise Analysis 45**

**2.5 BioNEMS: Practical Considerations Determining Realizable Sensitivity. 46**

2.5.1 Maximal Transducer Current Bias 46

2.5.2 Low Frequency Transducer Noise 56

**2.6 Conclusions 57**

**2.7 References 58**

***3 Methods of Fabrication and Considerations 60***

**3.1 Fabrication Details 60**

3.1.1 Fabrication Overview 60

3.1.2 Complete Fabrication Procedure for Early Foundry Runs (PHSMEMS, SA) 70

3.1.3 Improved Fabrication Procedure for Foundry Runs (Tronics, SA) 72

3.1.4 Nanofabrication Processes Performed at Caltech 79

3.1.5 Fabrication of the Microfluidics 82

**3.2 Temperature Constraints During Fabrication Due to Diffusion in Silicon 82**

**3.3 Scaling of Piezoresistive Sensors 82**

3.3.1 Summary of the Calculation of the Doping Profile in Doped Silicon with Two Different Doping Levels 83

3.3.2 Summary of Conclusions 84

**3.4 Use of Crystalline Silicon vs Polysilicon 87**

**3.5 References 88**

***4 Device Characterization 89***

**4.1 Measurement of the Gauge Factor 89**

**4.2 Characterization of the Experimental Setup 99**

4.2.1 Characterization of the readout amplifier 100

**4.3 Measurement of 1/f Noise 105**

4.3.1 Measurement of 1/f Noise in Air 105

4.3.2 Measurement of Noise Floor in Fluid 107

**4.4 References 109**

***5 Self-sensing Nanocantilever Force Sensors Yielding Attonewton-scale Resolution 110***

**5.1 Introduction 110**

**5.2 Fabrication 112**

**5.3 Device Characterization 114**

**5.4 Noise Performance and Responsivity 115**

5.4.1 Theoretical Model for Bias-Current-Induced Self Heating of Piezoresistive Devices 118

5.4.2 Experimental Configuration for Temperature Control 119

5.4.3 Experimental Validation of Heating Model 120

5.4.4 Experimental Results: Temperature Dependence of the Quality Factor, Gauge Factor and Thermomechanical Noise 123

**5.5 Ultimate Limits of Semiconductor-Based Piezoresistive Sensing for NEMS 126**

5.5.2 A Comparison of Thermal Conduction Pathways 132

5.5.3 Thermal Conduction via Hole Diffusion under Experimental Conditions 134

**5.6 Conclusion 136**

**5.7 References 137**

***6 Measured response in Gaseous Ambients 139***

**6.1 Introduction 139**

**6.2 Actuation by Heating 140**

**6.3 Magnetic Actuation 145**

6.3.1 Estimation of Coil – Magnetic Cantilever Tip Force 145

6.3.2 First Estimate of Coil-Cantilever Magnetic Force 149

6.3.3 Estimation of Magnetic Force, Taking into Account the Tip Geometry 151

6.3.4 Experimental Results for Magnetic Drive in Vacuum and Ensuing Force Estimation 157

6.3.5 Magnetic Driven Response in Air 159

**6.4 Actuation by Piezoelectric Drive 167**

6.4.1 Introduction 167

6.4.2 Piezoelectric Driven Response in Vacuum 167

6.4.3 Piezoelectric driven Response In Air 169

**6.5 Directions for future experiments 171**

**6.6 References 175**

***7 Measurements in Liquid Ambients 176***

**7.1 Overview 176**

**7.2 Piezoresistive Cantilevers as Flow Meters 179**

7.2.1 Cantilevers with Silicon Piezoresistive Elements 179

7.2.2 Metallic Piezoresistive Cantilevers 186

**7.3 BioNEMS detection of Biotin-labeled beads 189**

**7.4 Direction for Future Experiments 192**

**7.5 References 194**

***8 Brownian Motion in Fluid 195***

**8.1 Introduction 195**

**8.2 Optimization of Dimensions for the Detection of Brownian Fluctuations 197**

8.2.1 Expectations 197

8.2.2 Details of the Calculations 198

**8.3 Doped Silicon vs Metallic Piezoresistors for the Detection of Brownian Fluctuations 200**

**8.4 Optimization of Device Dimensions for Enhancement of the Brownian Noise Spectrum Relative to Johnson Noise 206**

**8.5 Experimental Protocols for the Detection of Brownian Fluctuations 214**

8.5.1 Study of Brownian motion in Cantilevers of Differing Length 214

8.5.2 Viscosity Dependence of Brownian Fluctuations 214

**8.6 References 220**

***9 Conclusion 221***

**9.1 Engineering Challenges to the Development of Useful BioNEMS Sensors 222**

**9.2 Direction for Future Experiments 224**

9.2.1 Detectable damping for a γ to γ' type experiment 225

9.2.2 Future Experiments: BioNEMS Detection Based on Changes in Device Compliance and Correlated 2-Cantilever Experiments 228

**9.3 References 230**

# List of Figures

Fig. 1.2.A BioNEMS device employing single-analyte detection via change in device compliance. 9

Fig. 1.2.B Schematic of analyte detection based on single-cantilever devices. ..... 10

Fig. 1.2.C Schematic of two-cantilever, analyte-coupled devices. ..... 12

Fig. 2.2.A Prototype silicon nanocantilevers. ..... 31

Fig. 2.2.B Amplitude response functions for three prototypical fluid-loaded nanocantilevers. 34

Fig. 2.3.A Geometrical considerations for spring constant calculation ..... 39

Fig. 2.5.A Total, coupled force spectral density for cantilever 1. ..... 50

Fig. 2.5.B Total, coupled force spectral density for cantilever 2. ..... 53

Fig. 2.5.C Total coupled force spectral density for cantilever 3. ..... 54

Fig. 2.5.D Total, low frequency, transducer-coupled force spectral density for cantilever 3. 55

Fig. 3.1.A Device assembly ..... 61

Fig. 3.1.B Sample device showing residue remaining after DRIE ..... 69

Fig. 3.1.C Prototype devices fabricated at caltech ..... 71

These devices fabricated at Caltech using the process described in section 3.1.1. ..... 71

Fig. 3.1.D Typical wafer after processing by PHSMEMS. ..... 75

Fig. 3.1.E Electrode patterning for gold piezoresistive devices ..... 78

Fig. 3.1.F Typical devices fabricated by the procedure outlined in section 3.1.5 ..... 81

Fig. 3.3.A Carrier distribution for a sample of 130 nm thickness ..... 85

Fig. 3.3.B Carrier distribution for a sample of 30 nm thickness ..... 86

Fig. 4.1.A SEM image of device used for probing the gauge factor ..... 92

Fig. 4.1.B Characterization of device displacement-resistance change transduction ..... 93

Fig. 4.1.C Measurement of the gauge factor – DRIE etched membrane ..... 96

Fig. 4.1.D Measurement of the gauge factor – KOH etched membrane ..... 98

Fig. 4.2.A Sample holder assembly ..... 101

Fig. 4.2.B Schematic for custom preamplifier. ..... 102

Fig. 4.2.C Gain curve for the custom preamplifier ..... 103

Fig. 4.2.D Preamplifier noise floor ..... 104

Fig. 4.3.A Measurement and characterization of 1/f noise ..... 106

Fig. 4.3.B Measured noise floor in fluid. ..... 108

Fig. 5.2.A Piezoresistive nanocantilever force sensor. ..... 113

Fig. 5.4.A Temperature dependent performance of nanocantilever force sensor. ..... 124

Fig. 5.4.B Force noise spectral density for the nanocantilever force sensor. ..... 125

Fig. 5.5.A Model for low low temperature thermal transport in semiconducting piezocantilevers. ..... 128

Fig. 5.5.B Optimization of transduced force sensitivity. ..... 131

Fig. 5.5.C Relative heat conduction via phonon- and hole-mediated pathways. ..... 133

Fig. 5.5.D Relative conduction via phonon mediated pathway and hole diffusion under optimum bias conditions ..... 135

Fig. 6.2.A Thermal excitation – schematic depiction ..... 141

Fig. 6.2.B Thermal actuation of a piezoresistive cantilever ..... 144

Fig. 6.3.A Magnetic actuation ..... 146

Fig. 6.3.B Typical devices with magnetic tips ..... 147

Fig. 6.3.C Optical image of a typical magnetic tip ..... 148

Fig. 6.3.D Approximation for initial estimation of coil-tip force ..... 150

Fig. 6.3.E Parameters for calculation of field from magnetic tip ..... 154

Fig. 6.3.F Dependence of magnetic field gradient at the cantilever tip on tip-coil separation 156

Fig. 6.3.G Experimental data for magnetic drive at 40mT ..... 158

Fig. 6.3.H Dependence of detected signal on current applied to magnetic coil ..... 160

Fig. 6.3.I Bridge used to balance the device ..... 162

Fig. 6.3.J Schematic depiction of Source of Residual Background ..... 163

Fig. 6.3.K Raw Data Showing Residual Background Consistent with Carrier Induced Changing Capacitance ..... 164

Fig. 6.3.L Raw data for device with electrodeposited pad ..... 166

Fig. 6.4.A Resonance Curve at 30mTorr with Piezoelectric Actuation ..... 168

Fig. 6.4.B Piezoelectrically driven resonance in Air ....170

Fig. 6.5.A Conceptual schematic of device with piezoelectric actuation ....174

Fig. 7.1.A Metallic piezoresistive cantilever ....178

Fig. 7.2.A Piezoresistive device embedded in microfluidics ....180

Fig. 7.2.B Cantilever response under pulsatory fluidic drive ....184

Fig. 7.2.C Piezoresistive cantilevers as a flow meter ....185

Fig. 7.2.D Device response to fluidic drive for gold piezoresistive cantilevers ....188

Fig. 7.3.A Detection of 0.2μm biotin labeled beads using BioNEMS....191

Fig. 8.3.A 1/f noise and brownian detection for silicon piezoresistors....203

Fig. 8.4.A Dependence of Brownian noise on cantilever thickness ....207

Fig. 8.4.B Dependence of Brownian response on cantilever length ....209

Fig. 8.4.C Dependence of Brownian response on cantilever width ....210

Fig. 8.4.D Dependence of Brownian noise spectrum on width of cantilever legs ....212

Fig. 8.4.E Dependence of Brownian noise spectrum on length of cantilever legs....213

Fig. 8.5.A Devices fabricated to enhance sensitivity to Brownian fluctuations ....215

Fig. 8.5.B Expected response from Brownian fluctions for experimentally realizable metallic piezoresistive devices ....216

Fig. 8.5.C Expected Brownian fluctuations in several alcohol solutions....217

Fig. 8.5.D Expected Brownian fluctuations for a metallic piezoresistive device in several solutions 219

Fig. 9.2.A Response Function for the Cantilever Used for γ to γ' Analysis ....227

# List of Tables

Table 2.2.A Physical parameters for three prototype Si nanocantilevers. .....35

Table 3.1.A Properties of SOI material .....64

Table 3.1.A Early BioNEMS Process Flow for Foundry Runs (PHSMEMS, SA).....73

Table 3.1.A Final BioNEMS foundry process flow.....77

Table 5.4.A Summary of control experiments performed to assess the validity of the heating correction .....122

Table 6.2.A Expected harmonics excited through thermal actuation.....143

Table 6.3.A Initial estimate of force for several different possible pad thicknesses.....152

Table 6.3.A Force estimate for several different possible pad thicknesses.....155

# List of Nonmenclature

$E$ Young's modulus.

G Dimensionless gauge factor for piezoresistive response (section 4.1).

$H(\omega)$ Displacement response function.

$I_b$ Bias current applied to the piezoresistive device to sense the resistance change.

K Spring constant of the device for point loading at the distal end (see section 2.3.1).

$\ell$ Cantilever length.

L Fluidic mass loading.

$\ell_{leg}$ Length of Cantilever legs.

$M_{eff}$ Effective mass of the device (see equation 8, section 2.2.3).

$\mathcal{R}_T$ Electrical transduction factor from displacement domain to voltage domain.

$R_d$ Device Resistance.

$\Re$ Frequency based Reynold's number (see section 2.2.1, $\Re = w^2\omega/4\nu$).

$S_F^{(tot)}$ Force spectral density.

$S_F^J$ Contribution to the force spectral density from Johnson noise.

$S_F^\gamma$ Contribution to the force spectral density from thermomechanical noise.

$S_R^{1/f}$ Contribution to the resistance spectral density from low-frequency "flicker" noise.

$S_V^{(tot)}$ Total (coupled) voltage spectral density.

$S_V^A$ Contribution to the voltage spectral density from the preamplifier.

$S_V^J$ Contribution to the voltage spectral density from Johnson noise.

$S_V^{1/f}$ Contribution to the voltage spectral density from low-frequency "flicker" noise.

$S_V^{\gamma}$ Contribution to the voltage spectral density from thermomechanical noise.

$S_x^{(tot)}$ Total (coupled) displacement spectral density.

$S_x^{\gamma}$ Contribution to the displacement spectral density from thermomechanical noise.

$t$ Cantilever Thickness.

$x$ Displacement of the cantilever tip.

$w$ Cantilever Width .

$w_{leg}$ Width of cantilever legs.

$y$ Used to parametrize the position along the length of the cantilever.

$\alpha$ Effective mass ratio in vacuum (relating the mean square displacement along the cantilever to the displacement at its end) (see section 2.3.2).

$\beta$ Parameter used to correct for the finite thickness of the conducting region of the piezoresistive beams (see section 2.3.4).

$\gamma_{eff}$ Effective damping coefficient (see Eq. 7, section 2.2.3).

$\eta$ Dynamic (shear) viscosity.

$\pi_\ell$ Longitudinal Piezoresistive coefficient.

$\nu$ Kinematic viscosity.

$\xi$ Used to paramaeterize the position within the thickness of the cantilever relative to the neutral axis.

# 1 Introduction

Techniques from nanoscience now enable the creation of ultrasmall electronic devices. Among these, nanoelectromechanical systems (NEMS) in particular offer unprecedented opportunities for sensitive chemical, biological, and physical measurements.[1] For vacuum-based applications NEMS provide extremely high force and mass sensitivity, ultimately below the attonewton and single-Dalton level respectively. In fluidic media, even though the high quality factors attainable in vacuum become precipitously damped due to fluid coupling, extremely small device size and high compliance still yield force sensitivity at the piconewton level – *i.e.,* smaller than that, on average, required to break individual hydrogen bonds that are the fundamental structural elements underlying molecular recognition processes. A profound and unique new feature of nanoscale fluid-based mechanical sensors is that they offer the advantage of unprecedented signal bandwidth (>>1MHz), even at piconewton force levels. Their combined sensitivity and temporal resolution is destined to enable real-time observations of stochastic single-molecular biochemical processes down to the sub-microsecond regime.[2]

## 1.1 Motivation

### 1.1.1 Overview: Mechanical Sensors for Biology

In 1992, Hoh *et al.*[3] pioneered the application of micron scale mechanical sensors to the study of biological molecules and their interaction forces. These UCSB researchers noted discrete steps in the adhesive interaction between a silicon nitride atomic force microscope [AFM] tip and a glass surface, steps that were interpreted as corresponding to an interaction force of 10pN – apparently the average strength of individual hydrogen bonds. Since this pioneering experiment, a growing literature of force spectroscopy, also

known as chemical force microscopy, has shown that a chemically-modified AFM can indeed be tailored to measure the binding force of interactions for a wide range of affinity-based processes, such as single receptor-ligand interactions. In such experiments, the tip of an AFM cantilever is typically functionalized with a receptor of interest, a molecular complex with the analyte is formed and then pulled, and the interaction force applied is read out as proportional to the measured tip deflection. Early studies included probing the biotin-streptavidin interaction force by Lee *et al.*[4] and the study of biotin-avitin, desthiobiotin-avidin, and iminobiotin-avidin by Florin *et al.*[5] Force spectroscopy experiments were extended to cells by Dammer *et al.,*[6] who studied intercellular adhesion forces (of proteoglycan from a marine sponge), and Evans *et al.,*[7] who also observed adhesion forces at the cell surface. A large body of literature has ensued. Force spectroscopy is not limited to studies of interaction forces but has also been applied to the study of conformational changes, *e.g.,* of the enzyme lysozyme[8] and of the unfolding of the protein titin.[9] Force spectroscopy has also been used to study DNA hybridization processes.[10]

Clearly, force spectroscopy has proven to be an extremely fruitful approach for studying biomolecular interactions. However, cantilevers employed for this work are primarily research-oriented probes and not, *per se*, directly applicable for biosensing in the conventional sense (at least not for large scale, real-time applications). However, a related cantilever-based biosensor technology has developed within the field of microelectromechanical systems (MEMS) and has been successfully applied to biological detection in liquids. These *surface-stress sensors* are based upon a direct measurement of

the stress induced by the binding of a *layer* of ligands to an appropriately-prepared ("biofunctionalized") device surface.[11,12,13,14,15,16] Despite the impressive advances in this field, these MEMS-based surface-stress sensing devices have critical limitations. In order to achieve a notable change in surface stress, these sensors require the binding of many ligands (a significant fraction of a monolayer); consequently, surface-stress sensors, in general, suffer from the inability to respond to forces that vary rapidly in time. Especially important are variations on the few μs timescale, characteristic of both important classes of conformational changes in large biomolecules and of low-affinity or non-specific binding processes. As regards the latter, high frequency response may ultimately prove critical to following the stochastic nature of affinity-based interactions, such as the receptor-ligand interaction, especially in the presence of an overabundance of weakly-binding entities. Receptor-ligand pairs interact dynamically: binding, remaining engaged for times ranging from microseconds to seconds (depending on the exact binding affinities and concentrations), and then releasing. Temporal resolution would provide an additional new "dimension" for discrimination between processes.

Ostensibly, the utilization of MEMS or NEMS as sensor devices is simpler than the setup required for force spectroscopy – with sensor devices one waits for the molecule of interest to bind, whereas with force spectroscopy one actively searches for it. Hence, at first glance, biosensor systems may appear simpler in that they do not apparently require a scanning system, feedback, or even a sharp tip, which are essential elements of a force spectroscopy apparatus. However, advanced MEMS and NEMS sensors do indeed require additional system components: microfluidic delivery systems, differential

biofunctionalization (to allow multiplex assays), and complex readout systems, which, in fact, may be feedback-based for optimal performance.

The current state-of-the art of mechanical biosensors and force spectroscopy devices labor with an addition limitation: the majority of force spectroscopy and surface-stress sensor devices employ optical displacement detection of the probe. This detection scheme has proven extremely fruitful for scientific studies of cantilevers with feature sizes of order 1 μm and greater. However, in this thesis we show that greatly increased sensitivity can be attained if the cantilever dimensions are further reduced into the nanometer size regime. Here, however, diffraction limits one's ability to focus optical "interrogation" upon the nanocantilever tips (as required for optical detection); hence alternative detection schemes become essential. Moreover, a totally integrated approach to sensing, such as is provided by electrical schemes, is crucial for the large-scale integration required for multiplex sensing applications. In situ, that is *on chip*, electrical displacement transduction eliminates the need for external equipment typically employed for optical detection. This greatly increases the potential applications of electrically-transduced devices beyond those of the research laboratory setting.

In what follows we describe a new class of nanomechanical biosensors: BioNEMS. These sensors are distinctly different from the aforementioned surface stress sensors. The central point we emphasize in this thesis is that BioNEMS, as we define them, do not sense quasistatic surface-layer induced stress. Instead, BioNEMS sense analyte-induced changes that measurably alter *dynamical* device properties. Moreover, the mechanisms

that underlie BioNEMS sensing scale to the realm of single molecules (a fact that is confirmed by force spectroscopy itself), whereas stress sensing devices do not. We shall describe in what follows the changes that arise from analyte binding to BioNEMS sensors. Among these are: alteration of the nanomechanical device compliance (force constant), changes to device damping, or direct imposition of additional forces or motional correlations to the device. The latter are effective in multiple-cantilever assays, which are described below. At the outset, we stress that for fluid-coupled nanomechanical devices the inertial mass is *not* among the parameters most strongly affected by target capture (analyte binding); hence BioNEMS as described herein are not mass sensing devices.

### 1.1.2 Motion Transduction via Piezoresistive Sensing

Our work utilizes electrical displacement sensing based upon integrated piezoresistive strain sensors. The piezoresistive effect in silicon was discovered in the 1950s[17] and its application has played an important role in early silicon sensor devices[18,19] and more recently for sensitive detection of displacement within microelectromechanical devices [MEMS], both in vacuum[20] and air.[21] Piezoresistive sensors were first applied to AFM cantilevers by Tortonese *et al.* in 1993[22] and have since been adopted by a number of researchers. The sensitivity attained is comparable to that of optical sensors, yet significant advantages for size scalability and integration both in the context of reducing device dimensions to sizes where optical detection would not be possible and for arrays where optical detection is more complicated (due to the extra hardware required). Piezoresistive sensors have recently been applied to surface-stress sensor devices by Rasmussen *et al.,*[23] who have detected immobilization of ssDNA, and Wee *et al.,*[24] who

used piezoresistive surface-stress sensors to detect prostate specific antigen and C-reactive proteins (specific markers for prostate cancer and cardiac disease, respectively). Modeling of piezoresistive surface-stress sensors has been performed by Rasmussen *et al.*,[25,26] Kassegne *et al.*,[27] and Yang *et al.*[28]

## *1.2 Nanoscale Mechanical Devices: BioNEMS*

Previous techniques have all involved force sensors with active surface areas that are quite large compared to the molecular scale. This is the case since surface-stress sensors rely on interactions between a layer of molecules on the device surface; hence a significant fraction of the surface area must be coated with molecules to enable detection. It is unclear how surface-stress sensors will scale, if at all, to the few-to-single molecule regime. These are among the issues that motivate our investigation of alternative sensing techniques with BioNEMS. We are interested in both passive and active sensors for which the binding of an analyte molecule of interest leads to a direct change in the vibrational behavior of a cantilever. As mentioned, in the case of a single cantilever device this may originate from several mechanisms.[2] Increased damping will arise if an analyte with surface area comparable to the device dimensions binds to the device. A change in the device compliance (the inverse of force constant) arises for the case where the analyte is allowed to bind in such a fashion as to bridge a gap between the suspended device and a rigid support structure. In both cases, the signal arises from a change in the dynamical, fluid-coupled response function of the device as a direct consequence of the binding of the analytes under study. Clearly, with sufficient sensitivity the approach scales to the realm where single analytes may be resolvable. In what follows we

demonstrate this possibility; more than a decade of aforementioned work in force spectroscopy confirms this.

In this section we outline the translation of conceptual device design into realistic biosensing protocols. Possible BioNEMS sensors can be differentiated into two main classes that we describe in turn below: single cantilever and multiple-cantilever devices. Single cantilever devices can be actuated in a number of ways including: piezoelectric actuation – *e.g.,* via a piezoelectric actuation element patterned locally upon the cantilever; fluidic actuation – *e.g.,* via pulsatory fluidic drive delivered through the microfluidic environment in which BioNEMS devices are housed; magnetic actuation – *e.g.,* via inclusion of nanomagnets upon the cantilever tip and use of external or on-chip drive coils; or by "passive actuation" – *i.e.*, *stochastic sensing*, which employs Brownian fluctuations as the "drive" force.[2] Independent of the method of actuation employed, device response in fluid is governed by the response function discussed in Chapter 2.

Biosensing with NEMS is based upon effecting a change in the dynamical properties of the device upon capture of a target analyte. To realize this, the device must be biofunctionalized in a manner such that the immobilization event induces a change in device response – either through change in the device compliance, a change in its damping, or by the imposition of new correlations or actuation forces as a result of target immobilization. We now consider concrete realizations for each of these types of devices.

### 1.2.1 BioNEMS Detection Based on a Change in Device Compliance.

The binding of an analyte will lead to a change in the cantilever's effective spring constant if its immobilization forms a structural bridge between the motional element and some other body. This is most effective if the other body is a rigid structure; Fig. 1.2.A shows such a device in which a cantilever becomes tethered to a rigid dock upon target capture. In this example, the fine gold lines at the cantilever tip and along the dock in the vicinity of the tip are functionalized with a receptor that is specific to the analyte of interest. This illustrates the general protocol involving the binding of an analyte between two functionalized regions to form a biomolecular bridge, which increases the effective device spring constant.

### 1.2.2 BioNEMS Detection Based on a Change in Device Damping.

Fluid coupling depends upon the cross-sectional surface presented by the device, normal to the direction of its motion. To effect a measurable change in this coupling, the cross section presented must be increased by some fraction of the total effective surface area; the absolute fractional change required depends upon the measurement resolution. These considerations make it clear that the effective surface area of an analyte to be detected must be sufficient as to lead to an appreciable change in the fluid loading of the device. If this is the case, then the binding of an analyte can lead to a direct change in the device response through an increase in damping. This, in turn, leads to a change in the response function of the device which can also lead to a change in the requisite driving force (the latter would be the case for both fluidic drive and drive based on Brownian fluctuations). This "damping assay" is conceptually depicted in Fig. 1.2.B (b).

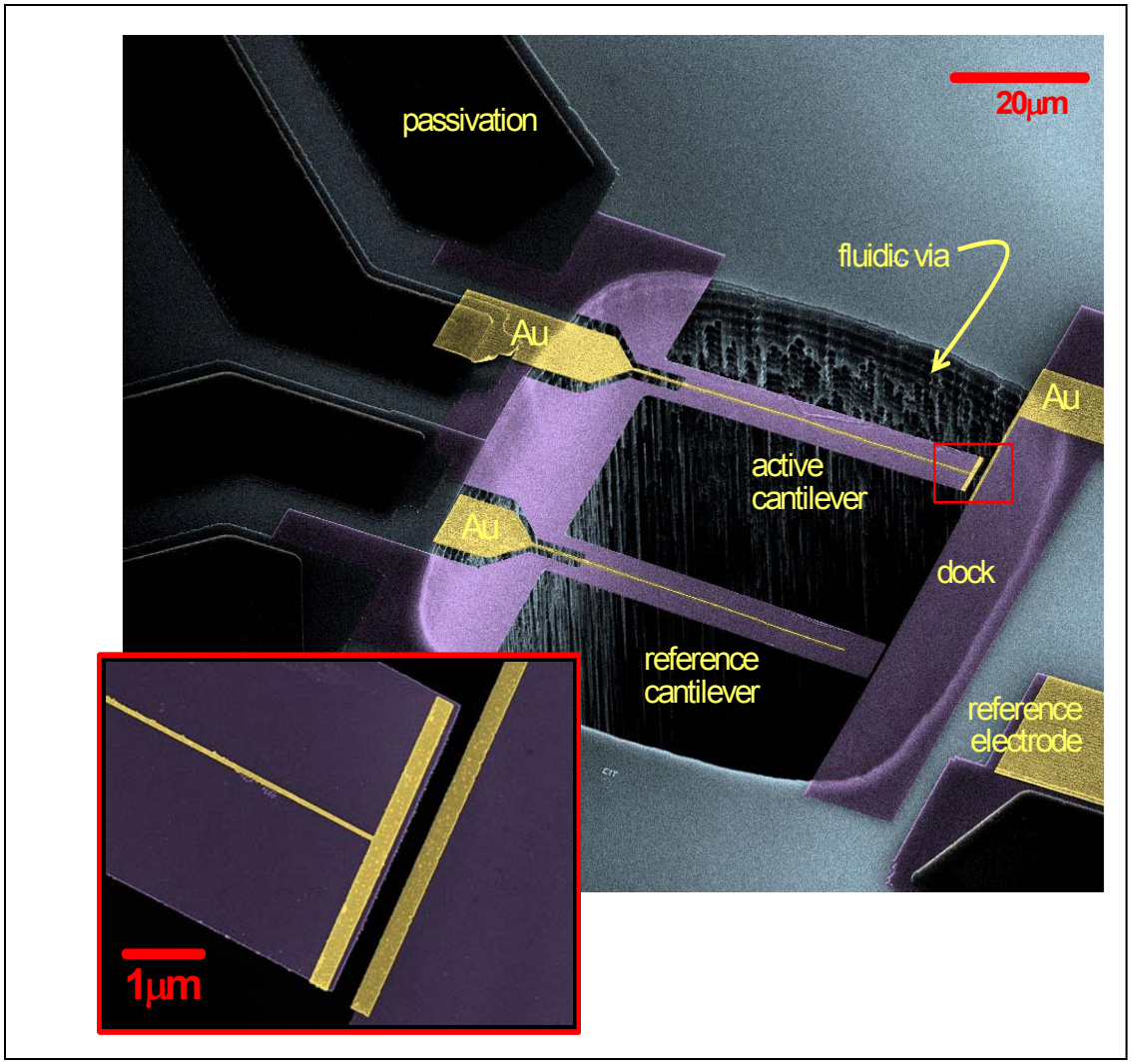


**Fig. 1.2.A BioNEMS device employing single-analyte detection via change in device compliance.**

In these devices analytes bind across the gap between the active cantilever and the dock, and their immobilization is reflected as a measurable change in the overall device compliance. This particular family of devices is configured for detection of bacterial pathogens; the fine Au lines at the active device tip and on the dock are biofunctionalized with antibody-terminated alkanethiol SAMs.[29] Electrical connections to these lines permit electrically-activated biofunctionalization protocols *in situ*. Upon specific binding, the target pathogens subtend the submicron gap between these biofunctionalized regions (see magnified view in the inset). Both the gap width and the two biofunctionalized regions are specifically tailored to capture an individual biological target of interest.

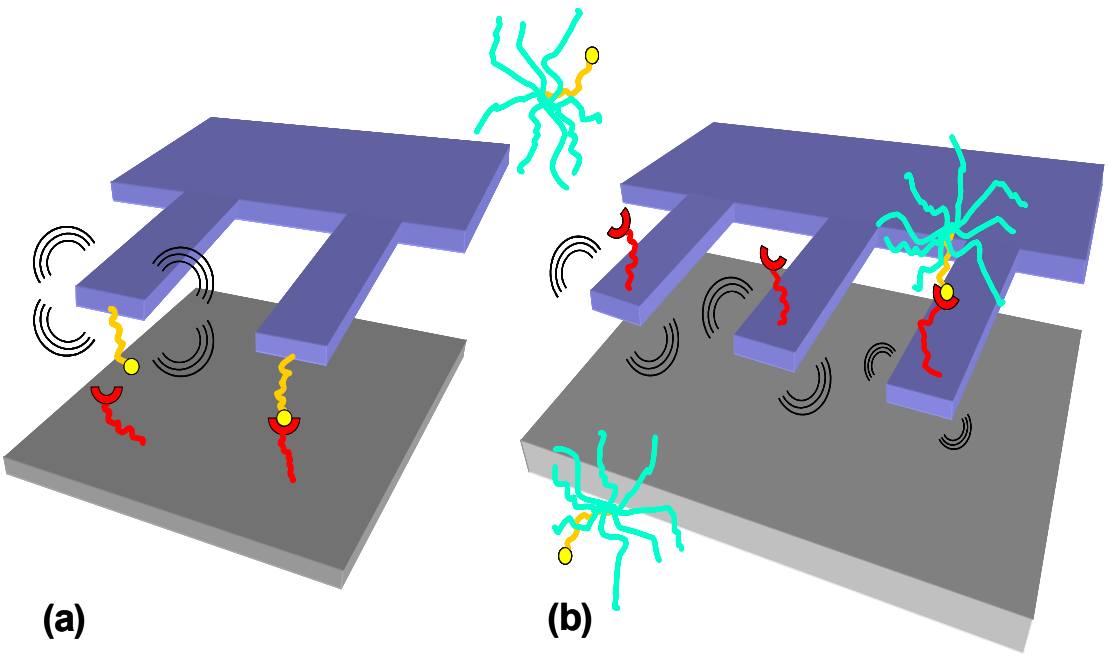


**Fig. 1.2.B Schematic of analyte detection based on single-cantilever devices.** These images detect two single-molecule sensing modalities that remain effective for heavily-fluid damped nanomechanical sensors, even when the associated molecular mass-loading is undetectable.[2] Hence, these are not mass sensing protocols. **(a) Detection based upon a change in device compliance.** The presence of a single biomolecular bond changes the force constant of the device sufficiently to alter its vibrational properties in fluid, as described in the text. **(b) Detection based upon a change in device damping.** The immobilization of a target analyte causes increased damping which is detectable by the resulting change in the device response function. The impact of an individual analyte binding event can be amplified by attaching a "label", *e.g.,* a star dendrimer, which causes enhanced fluid coupling (compared to that which is induced by immobilization of an unlabelled analyte.)

### 1.2.3 Coupled, Multiple-Cantilever Devices

More sensitive detection schemes can be based upon the use of two or more coupled cantilevers. These multiple cantilever devices fall into two general classes schematically depicted in 1.2.3, namely stochastic sensors and actively-driven sensors. Stochastic sensors make use of Brownian fluctuations of the fluid for their "actuation." As discussed previously, adjacent cantilevers are coupled by local fluidic correlations. If placed sufficiently far apart, these background correlations can be very small, and the immobilization of a biomolecular target between the two devices, as depicted in Fig. 1.2.C (a), can induce new, measurable correlations between their motion in the Brownian drive "field."

Actively-driven "force transmission" devices involve, at minimum, two cantilevers, one of which is actuated while the second serves as a sensor. This is shown schematically in Fig. 1.2.C (b). Ideally, for such a detection scheme there would be no background coupling between the actuator and sensor in the absence of analyte binding. Again, in reality there is a background coupling imposed by the fluidic coupling of the devices discussed previously. This imposes a minimum threshold for the strength of the analyte-induced coupling.[30] With a three-cantilever design (using two actuators, driven with a specific phase difference, and one follower) it is possible to place the sensor in a "node" of the fluidic coupling from the two actuators so that a null baseline can be achieved.[2]

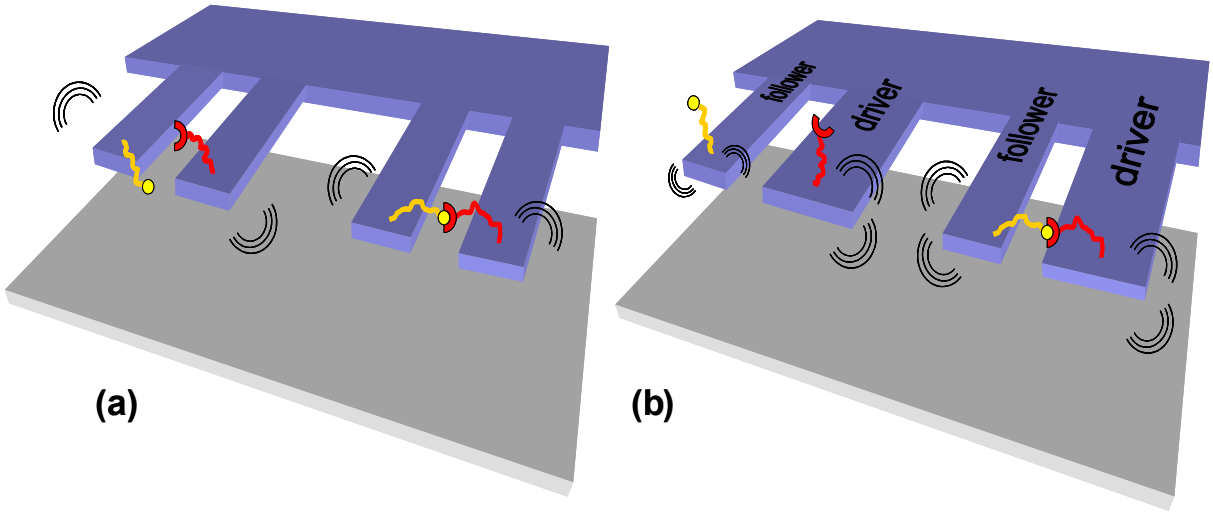


**Fig. 1.2.C Schematic of two-cantilever, analyte-coupled devices.**

In these devices coupling between the adjacent cantilevers is induced by specific interactions between immobilized biomolecules.[2] **(a) Passive stochastic correlation sensing**. In this modality the biomolecular linkage induces additional motional correlations between two cantilevers – correlations that exceed the "parasitic" background present due to mutual fluidic coupling *(see text)*. **(b) Active driver/follower lock-in force sensing.** This two-cantilever sensing protocol involves an actuator cantilever that is actively-driven (the "driver"), which imparts forces of specific frequency and phase to a second detector sensor (the "follower"). The resulting "lock-in" force detection provides increased resolution of the binding of an analyte linking two cantilevers. Both of these concepts can be translated into realistic two-cantilever biosensor protocols in multiple ways. For example, a pre-programmed linkage (such as pictured above) can be designed to become destabilized upon the arrival of a target analyte that displaces an initial ligand to bind with the immobilized receptor with higher affinity. Alternatively, a high specificity, two-cantilever sandwich assay may be formed by functionalizing the adjacent cantilever pair with two different immobilized antibodies, which then permit specific binding to two different epitopes upon the same individual target antigen.

### 1.2.4 Practical Considerations.

Embedding the BioNEMS device in a microfluidic assembly is essential in order to complete the goals of simplification and miniaturization for which the integrated sensors were chosen. Single-molecule biosensing protocols, in some sense, become practically useful only within microfluidic assembly where total fluidic volumes is minimized, recirculation protocols can be realized to create enhanced binding probabilities, and the environment to which the device is exposed can be actively controlled. The silicon devices discussed here are readily compatible with most of the common microfluidic designs, including surface-micromachined[31] and polymer-[32,33] based protocols.

### 1.2.5 Specificity and the Stochastic Nature of Single-Analyte Binding Events

The biomolecular specificity of the devices discussed herein is governed entirely by their biofunctionalization; this is the biosensors true "front end." Hence, surface biochemistry of the analyte-receptor interaction is critical – high affinity capture probes will ensure a highly selective response with good rejection of non-specific background interactions. The design of high affinity capture probes is clearly absolutely essential to future progress and real applications in all areas of biosensing, and this includes BioNEMS. However, discussion of this important topic is outside the scope of the present review.

The stochastic nature of single molecular events certainly makes for interesting science, but it also opens very significant new challenges for biosensing. This is true both in terms of device design and interpretation of data that is acquired.[34] For biosensing, it is

usually "go/no-go" sensing, rather than the ensemble-averaging of events, that is the goal. Hence, protocols must be formulated that deal directly with such considerations, for example, as the fact that the residence time and binding constant for individual events – that is successive events involving the same biochemical species – may vary.[35] One possible avenue to minimize this intrinsic "uncertainty," *i.e.,* provide biosensing protocols with high confidence levels even for single-shot measurements, is to make use of extremely high-affinity capture probes. This, again, puts the onus upon obtaining or developing optimal biofunctionalization; with extremely high affinity capture probes, false positives will be minimal and residence times will be sufficiently long as to permit temporal rejection of the ubiquitous background of non-specific binding. A second approach, which we have involved in our work, involves electrically-actuated analyte release.[29] This utilizes the fact that, although *capture* is a stochastic process, *release after capture* can be programmed deterministically, and the resultant response used to provide good rejection of false positives.[2]

## *1.3 Overview of Thesis*

This thesis will begin with an overview of piezoresistive detection (chapter 2). Motivated to achieve higher sensitivity and to fabricate devices closer to the size scale of the cells, spores, and molecules we are interested in, we began by reducing the dimensions of the device. Calculations of the sensitivity of our device and a complete motivation for the reduction of dimensions are presented in section 2.5.

A discussion of methods of fabrication and constraints is presented in Chapter 3. Here we describe a membrane-based, top-down fabrication method used here to fabricate

micro- and nano- cantilevers, but applicable to a much broader variety of geometries. We further describe the fabrication of microfluidics compatible with these devices and finally the assembly to form a microfluidic embedded piezoresistive BioNEMS device. The second part of this chapter discusses constraints on fabrication, including simulations of depletion layer effects as the thickness of the doped layer is decreased, temperature limitations due to diffusion, and a comparison of crystalline and polysilicon.

Characterization of the device is discussed in Chapter 4. This includes direct measurements of the gauge factor, 1/f noise, and noise floor in fluid. The latter includes a comparison of the noise floor for devices assembled in microfluidics with Petri dish devices.

In Chapter 5 measurements of the sensitivity of our devices in vacuum are presented. This is done through measurements of thermomechanical noise demonstrating a force sensitivity of 235 aN/√Hz at room temperature and 17 aN/√Hz at 10K. An enhancement of the p+ piezoresistive gauge factor with decreasing temperature is observed over this temperature range. From these results, the ultimate low-temperature sensitivities attainable from NEMS employing piezoresistive displacement transduction are extrapolated.

Chapter 6 discusses methods of actuation, presenting measured response in vacuum and air. Results are presented for actuation via heating, magnetic actuation, and piezoelectric actuation.

Measurements in a liquid ambient are presented in chapter 7. In section 7.2 the functionality of BioNEMS devices as a flow meter within microfluidics is presented for both silicon and metallic piezoresistive cantilevers. This was used to test the response of the devices in fluid and as a method of actuation for the bio-detection data of section 7.3. With further refinement it might be used as an application of its own for monitoring flow rates within microfluidic-based devices. Section 7.3 presents data showing BioNEMS devices as a biosensor (in this case detecting biotin labeled beads). It was mentioned in section 1.1 that most MEMS-based biosensor devices fall under the application referred to as "surface stress sensor devices." Unfortunately, inherent to the design of "surface stress sensor devices" is the property that they rely on coverage of a significant fraction of a monolayer to induce a detectable surface stress and hence a detectable response. While the minimum fractional coverage required may be improved through engineering improvements allowing for increased sensitivity and thereby achieving faster response and the ability to detect molecules at lower concentrations, the induced surface stress of the device is inherently related to the interaction between many ligands on the device surface. Therefore, in our quest to achieve single molecule detection it is insufficient to pursue decreasing the device dimensions, we must also pursue alternative detection methods. Two such detection methods were introduced in sections 1.2.1 and 1.2.2; namely, we are interested in devices for which the binding of ligand(s) to the device surface produces a change in either the device compliance or the damping experienced by the device. The data presented in section 7.3 uses a combination of these two detection mechanisms for the detection of biotin-labelled polystyrene beads. In particular, the polystyrene beads bridge a gap between the cantilever device and an adjacent beam. The

cantilever is driven via pulsatory fluidic drive, as discussed in section 7.2. The bridging of the gap has three effects: it 1) decreases the spring constant, 2) increases the fluidic drive and 3) increases the damping. Unfortunately, the 0.2μm polystyrene beads are not large enough to individually bridge the gap (the size of which ranged from 300nm to 5μm). The experiments of section 7.3 were therefore designed to detect aggregates of beads. In section 7.4 we discuss possible directions for future experiments to achieve single ligand detection of cells, spores, and other large ligands via this binding scheme. (The limitation on ligand size is primarily imposed by the requirement that the ligand bridge the gap. Engineering improvements will allow the gap size to be decreased from the 300nm gaps we can fabricate today [primarily limited by cantilevers bending out of plane]).

In chapter 8 we discussed the sensitivity of both silicon and metallic piezoresistive devices to Brownian fluctuations. This is of interest for three reasons: 1) for the scientific application of our devices to the study of Brownian noise itself, 2) for understanding the ultimate noise floor of our devices, and 3) for passive sensing applications in which the change in Brownian fluctuations upon ligand binding is used to sense the binding of a ligand. Finally a discussion of future experiments is presented in chapter 9.

## *1.4 References*

[1] M.L. Roukes, Technical Digest of the 2000 Solid-State Sensor and Actuator Workshop, Hilton Head, NC, (Cleveland: Transducer Research Foundation, 2000); downloadable at http://arxiv.org/pdf/cond-mat/0008187

[2] M.L. Roukes, S.E. Fraser, J.E. Solomon, and M.C. Cross, *"Active NEMS arrays for biochemical analyses"*, United States Patent Application 20020166962, Filed August 9, 2001, referencing U.S. application Ser. No. 60/224,109, Filed Aug. 9, 2000.

[3] J.H.Hoh, J.P. Cleveland, C.B. Prater, J.-P. Revel, and P.K. Hansma, J. Am. Chem. Soc. **114** 4917-4918 (1992).

[4] G.U. Lee, D.A. Kidwell, and R.J. Colton, Langmuir, **10** 354-357 (1994).

[5] E.L. Florin, V.T. Moy, and H.E. Gaub, Science, **264** 415-417 (1994).

[6] U. Dammer, O. Popescu, P. Wagner, D. Anselmetti, H.-J. Güntherodt, and G.N. Misevic, Science, **267** 1173-1175 (1995).

[7] E. Evans, K. Ritchie, and R. Merkel, Biophys. J. **68** 2580-2587 (1995).

[8] M. Radmacher, M. Fritz, H.G. Hansma, and P.K. Hansma, Science **265** 1577-1579 (1994).

[9] M. Rief, M. Gautel, F. Oesterhelt, J.M. Fernandez, and H.E. Gaub, Science **276** (1997) 1109-1112.

[10] G.U. Lee, L.A. Chirsley, and R.J. Colton, Science **266** 771-773 (1994).

[11] H-J. Butt, Journal of Colloid and Interface Science **180**, 251-259 (1995).

[12] R. Raiteri, G. Nelles, H-J. Butt, W. Knoll, and P. Skládal, Sensor and Actuator B-Chem. **61**, 213-217 (1999).

[13] R. Raiteri, M. Grattarola, H-J. Butt, and P. Skládal, Sensor and Actuator B- Chem. **79**, 115-126 (2001).

[14] G. Wu, R.H. Datar, K.M. Hansen, T. Thundat, R.J. Cote, and A. Majumdar, Nature Biotechnology, **19,** 856-860 (2001).

[15] J. Fritz, M.K. Baller, H.P. Lang, H. Rothuizen, P. Vettiger, E. Meyer, H.J. Güntherodt, Ch. Gerber, and J.K. Gimzewski, Science, **288**, 316-318 (2000).

[16] G. Wu, J. Halfeng, K. Hansen, T. Thundat, R. Datar, R. Cote, M.F. Hagan, A.K. Chakraborty, and A. Majumdar, PNAS, **98** 1560-1564 (2001).

[17] C.S. Smith, Phys Rev **94** 42-49 (1954).

[18] O.N. Tufte, P.W. Chapman, and D. Long, J. Appl. Phys. **33**, 3322 (1962).

[19] A.C.M. Gieles, IEEE Int Sol St, 108-109 (1969).

[20] J.A. Harley and T.W. Kenny, Appl. Phys. Lett. **75**, 289-291 (1999).

[21] M. Tortonese, R.C. Barrett, C.F. Quate, Appl. Phys. Lett. **62**, 834-836 (1993).

[22] M. Tortonese, H. Yamada, R.C. Barrett, R.C., and C.F. Quate, Atomic force microscopy using a piezoresistive cantilever. TRANSDUCERS '91. 1991 International Conference on Solid-State Sensors and Actuators. Digest of Technical Papers, 448-451 (1991).

[23] P.A. Rasmussen, J. Thaysen, O. Hansen, S.C. Eriksen, and A. Boisen, Ultramicroscopy **97**, 371-376 (2003).

[24] K.W. Wee, G.Y. Kang, J. Park, J.Y. Kang, D.S. Yoon, J.H. Park, and T.S. Kim, Biosensors and Bioelectronics **20**, 1932-1938 (2005).

[25] P.A.Rasmussen, O. Hansen, and A. Boisen, Appl. Phys. Lett. **86**, 203502 (2005).

[26] P.A. Rasmussen, A.V. Grigorov, and A. Boisen, J. Micromech. Microeng. **15**, 1088-1091 (2005).

[27] S. Kassegne, J.M. Madou, R. Whitten, J. Zoval, E. Mather, K. Sarkar, H. Dalibor, H., and S. Maity, Design Issues in SOI-based high-sensitivity piezoresistive cantilever devices Proc. SPIE Conf on Smart Structures and Materials (San Diego, CA 17-21 March) (2002).

[28] M. Yang, X. Zhang, K. Vafai, and C.S. Ozkan, J. Micromech. Microeng., **13**, 864-872 (2003).

[29] C.A. Canaria, J.O. Smith, C.J. Yu, S.E. Fraser, and R. Lansford, Tetrahedron Letters **46,** 4813 (2005); C.A. Canaria, *et al.*, to be published, 2005.

[30] D.E. Segall and R. Phillips, to be published, 2005.

[31] D.J. Harrison, K. Fluri, K. Seiler, Z.H. Fan, C.S. Effenhauser, and A. Manz, Science **261**, 895-897 (1993).

[32] H.-P. Chou, C. Spence, A. Scherer, and S. Quake, PNAS, **96**, 11-13 (1999).

[33] M.A. Unger, H.-P. Chou, T. Thorsen, A. Scherer, A. and S. Quake, Science, **288**, 113-116 (2000).

[34] J.E. Solomon and M. Paul, "The Kinetics of Analyte Capture on Nanoscale Sensors", submitted to Biophysical Journal (2005).

[35] E. Evans, Annu. Rev. Biophys. Biomol. Struct. **30**, 105-128 (2001).

[36] A.-R.A. Khaled, K. Vafai, M. Yang, X. Zhang, and C.S. Ozkan, Sensors and Actuators B, **94**, 103-115 (2003).

# 2 Theoretical Foundation of Piezoresistive NEMS Detection and Realizable Force Sensitivity

## 2.1 Overview

For nanometer-scale cantilevers, the most important dynamical regime is that of very low Reynolds number flow. Below we evaluate the realizable sensitivity of fluid-coupled systems that take into account noise of practical readouts; our results are based upon initial experiments, analytic calculations, and numerical modeling. Thermal noise is typically characterized by its power spectral density, defined as the Fourier transform of the autocorrelation function for the process of interest (in this case the stochastic thermal noise). The total noise is given by the square root of the integral of the PSD over the experimental frequency bandwidth. Limits to force sensitivity imposed by thermal fluctuations appears better than 10fN/√Hz for small but realizable device dimensions via advanced nanofabrication techniques. *Transducer-coupled* force sensitivity (referred to the input, *i.e.,* force domain) – which includes all additional noise processes generated downstream from the mechanical probe by the displacement transducer and its essential electrical readout scheme – is still well below the 0.1 pN/√Hz realm and permits bandwidths greater than 1MHz. This opens a new range of possibilities for biological force measurements on extremely short time scales.

## 2.2 Fluid-Coupled Nanomechanical Devices: Analysis

### 2.2.1 Introduction

Fluid dynamics are quite different at small size scales, compared to what is familiar from our macroscale intuition. Much of biology, however, involves fluidic interactions on the

micro- and nano- scale.[1] The equations governing the motion of an incompressible fluid are the well-known Navier-Stokes equations (shown below in nondimensional form):

$$\Re_f \frac{\partial u}{\partial t} + \Re_u \vec{u} \cdot \vec{\nabla} \vec{u} = -\vec{\nabla} p + \nabla^2 \vec{u} \quad \text{and} \tag{1}$$

$$\vec{\nabla} \cdot \vec{u} = 0. \tag{2}$$

In these equations $\vec{u}$ represents the fluid velocity and p the pressure. The frequency- and velocity-based Reynolds numbers are $\Re_f$ and $\Re_u$, respectively. The velocity-based Reynolds number $\Re_u = uL/\nu = uw/2\nu$ expresses the ratio between inertial convective forces and viscous forces. $\nu$ is the kinematic viscosity (defined as $\eta/\rho$, where $\eta$ is the dynamic or shear viscosity and $\rho$ the density). $L$ is the characteristic length scale which has been chosen as the half-width of the device, $w/2$. It is clear that for MEMS and NEMS devices both the characteristic velocity and length scales become quite small, resulting in what is commonly referred to as the low Reynolds number regime. A precise definition of what is here meant by "low" is not clear; for perspective note that the typical Reynolds number for the flow field over a microorganism is on the order $10^{-5}$, for insect flight it is on the order of 10, and for flow in a pipe to become turbulent it is on the order of $10^3$. As the Reynolds number becomes smaller, viscous effects dominate inertial effects, and in the limit of zero Reynolds number flow (Stokes Flow) one can envisage a massless object in an infinitely viscous fluid. For nanoscale devices under consideration it is anticipated that $\Re_u << 1$ and, as a result, the nonlinear convective inertial term $\vec{u} \cdot \vec{\nabla} \vec{u}$ is negligible and the equations become linear, greatly simplifying the analysis.

The frequency-based parameter $\Re_f = \mathsf{L}^2 / \nu\ \mathsf{T} = w^2 f / 4\nu$ expresses the ratio between inertial acceleration forces and viscous forces where the inverse oscillation frequency, $1/f$, has been used for the characteristic time scale. This form of the Reynolds number becomes important when the oscillations are imposed externally. This is the case when micron and nanometer scale cantilevers immersed in fluid exhibit stochastic dynamics due to their constant buffeting by fluid particles, *i.e.* by their Brownian motion. However, for the nanoscale cantilevers under consideration here the Reynolds number is $\Re_\omega \sim 1$. This estimate can be calculated using approximate values for the cantilever geometry, for example w~1μm, $f$~1MHz, and using water as the working fluid with $\nu$=1x10$^{-6}$ m$^2$/s. As a result, the first inertial term in Eq. 1 must be included making the resulting analysis more difficult. In the analysis below we model the stochastic dynamics of a long and slender cantilever (as is common in atomic force microscopy) by coupling the classic equations of beam elasticity with the two dimensional flow field around an oscillating circular cylinder.[2,3] For a more rigorous numerical approach to the modeling of BioNEMS devices in fluid, the reader is referred to the work of M.R. Paul and M.C Cross.[4,5] Hereafter we shall simply refer to the frequency-based Reynolds number as $\Re$.

### 2.2.2 Analytical Calculations for Experimentally Relevant Conditions

Devices displaying an elastic response are generally characterized according to their force constant, $K$, where the force constant obeys Hooke's law, $F = -Kx$. In the case of a distributed body such as a cantilever, such analysis continues to apply, but care must be taken with respect to what is meant by $x$ and $F$. Throughout this thesis $x$ will be taken to refer to the displacement of the cantilever tip. Forces can be applied either in the form of point loading at the distal end of the cantilever or uniform loading throught the cantilever.

Examples of point loading would be magnetic exctitation of a cantilever on which only the tip is magnetic or a change in device properties due to the binding of a ligand to a device on which the distal end has been selectively functionalized to control the binding region (such as those devices depicted in Fig. 1.2.A and Fig. 1.2.B). Examples of uniform loading would be Brownian fluctuations/fluidic damping or non-specific binding of analytes over the entire device surface. The spring constants for the two types of forces are related through the expression $K_{\substack{\text{uniform}\\\text{loading}}} = K_{\substack{\text{point}\\\text{loading}}} / \alpha$. The parameter, $\alpha$, is derived in section 2.3.2. To simplify the discussion, instead of referring to two different force constants, we will use a single compliance, $K$, which we define to be the compliance for point loading. Where we are interested in uniform loading, such as for fluidic damping, we will use an effective force, $F_{\text{eff}} = \alpha F_{\substack{\text{uniform}\\\text{loading}}}$. For a cantilever of width, thickness, and length ($w, t, l$), respectively, vibrations in the fundamental mode involve a force constant[6] $K \cong 0.25 E w (t/l)^3$, where $E$ is the Young's modulus. The cantilevers mass can also be composed of two components; namely the mass composing the structural integrity of the device, which is uniformly distributed, and an additional component arising from any additional mass placed at the device tip, such as metal pads for specific functionalization or magnetic actuation. For consistency with our analysis (based on deflection of the cantilever tip and force loading applied to the cantilever tip), we define an effective mass in vacuum, $M_{eff,\,vac} = \alpha M_o + M_{tip}$, where $M_o$ is the mass uniformly distributed across the cantilever, and $M_{tip}$ is the mass concentrated at the device tip. $\alpha$ is the same parameter as that relating the spring constant for uniform and point

loading. Based on the expression for the effective mass in vacuum, we refer to $\alpha$ as the effective mass ratio. In vacuum $\alpha$=0.243[6].

The motion of a cantilever in a fluid vibrating in its fundamental mode can be described by the equation of a simple damped harmonic oscillator:

$$F(t) = M_{eff}\frac{\partial^2 x}{\partial t^2} + \gamma_{eff}\frac{\partial x}{\partial t} + Kx. \qquad 3$$

In vacuum, $M_{eff}$ is given by the above expression, and the frequency for oscillations of the cantilever in the fundamental mode is $f_{eff} = \sqrt{K/M_{eff}}/2\pi \rightarrow f_0 \cong 0.507\sqrt{E/\rho_c}\ (t/l^2)/\pi$. Here, $\rho_c$ is the cantilever's mass density. An oscillating device in a fluidic medium will have a characteristic boundary layer of fluid (dependent on the device geometry, frequency of oscillations, and fluid properties) which effectively oscillates with the device. This is referred to as fuid loading and adds an additional contribution to the effective mass beyond that already described for a device in vacuum. The effective mass of the device including fluidic loading is discussed in section 2.2.3 as is the effective damping coefficient, $\gamma_{eff}$. As described below, in all cases of interest here the cantilever's coupling to the fluid completely dominates its internal materials-dependent loss processes.

Noise is often characterized by its power spectral density, S, defined as the Fourier transform of the autocorrelation function of the parameter of interest. For example $S_x$, the displacement spectral density, is given by

$S_x = \int_{-\infty}^{\infty} \left( \lim_{\tau' \to \infty} \frac{1}{2\tau'} \int_{-\tau'}^{\tau'} x(t+\tau)x(\tau)d\tau \right) e^{i2\pi ft} dt$, where $x$(t) represents the displacement fluctuations. The sensitivity is then given by $\sqrt{S}$. Finally, the total r.m.s. noise is given by the integral of the sensitivity over the measurement bandwidth. Although we are concerned here with quite small, *i.e.* nanoscale, systems, the mechanical structures themselves are still quite large compared with the size of solvent molecules. The thermal motion of a fluid-loaded nanocantilever may thus be modeled in terms of stochastic forces, which are Markovian (because the time scale of molecular collisions are short compared with frequencies of macroscopic motion) and Gaussian (because many molecular collisions combine to force macroscopic motion). Hence, the fluctuation-dissipation theorem may be used to analyze this motion. The force spectral density is given by the Nyquist formula, $S_F = 4k_B T\gamma_{eff}$.[7] This is the fundamental limiting force sensitivity of a sensor in fluid. Hence, the force sensitivity can be optimized by minimizing this force noise while at the same time optimizing the sensing protocol to allow a force sensitivity very close to this fundamental limit to be achieved. One finds that a uniform reduction of *all* device dimensions accomplishes both goals. The damping of the cantilever arising from the fluid loading is most dependent upon its dimensions transverse to the motion, *i.e.* its width and length, and the reduction of these dimensions therefore leads to a direct reduction of the force spectral density from fluctuations. Reduction in device thickness, by contrast, leads to improvements in the device responsivity, which allows signals at forces comparable to the Brownian noise floor to be readily "transduced" to experimentally measurable voltage signals at levels above the noise floor set by transducer noise processes and readout preamplifier noise

limitations. It will be shown that such a scaling downward of dimensions has the profound additional benefit of leading to a marked reduction in response time. This decrease arises primarily from the reduction in cantilever mass loading with the decreased dimensions.

A very rough estimate of the drag constant is possible by considering the drag on a sphere in low Reynolds number flow far from any surface. In this case, $\gamma_{eff} = 6\pi\eta a$, where $\eta=\rho\nu$ is the shear viscosity of the solution and *a* is the radius of the sphere. For *a* = 1μm, in water, the Nyquist formula yields $S_F^{1/2} \sim 17\ \mathrm{fN/Hz^{1/2}}$.

### 2.2.3 BioNEMS Displacement Response Function

The motion of the free end of a cantilever in fluid at frequency $f$ is described by

$$S_x(f) = S_F(f)\left|H(f)\right|^2 = S_F(f)\frac{1}{[(K-4\pi^2 M_{eff} f^2)^2 + 4\pi^2\gamma_{eff}^2 f^2]}. \qquad 4$$

This equation represents the average squared magnitude of the Fourier transform of equation 3. $S_x$ is the power spectrum density of the tip displacement (*i.e.* the Fourier transform of the autocorrelation function for the cantilever's tip displacement).[7] The constant $\gamma_{eff}$ is the effective damping coefficient. This provides a complete description of the cantilever's displacement response both to the externally applied forces and, through the fluctuation-dissipation theorem, to the stochastic forces imparted from the fluid. As shown below, in all cases of interest here the cantilever's coupling to the fluid completely dominates its internal materials-dependent loss processes.

Sader has presented a very useful analysis of the coupling of the fluid to long thin cantilevers in the context of the atomic force microscope.[2] Numerical evidence suggests that loading of a rectangular cantilever is well approximated by the loading of a circular cylinder of diameter equal to the width of the beam.[8] The fluid loading of an infinite cylinder, first calculated by Stokes, is well known[9] and can be written as an equivalent mass per unit length:

$$L(f) = \frac{\pi \rho_L w^2}{4} \Gamma(\Re). \qquad 5$$

The prefactor is simply the volume displaced by the cylinder, while the function $\Gamma$ which depends solely upon Reynolds number must be calculated from the motion of the fluid. In this approximation, the fluidic forces at each frequency and on each section of the cantilever are proportional to the displacement at that point. For this case it can be shown that the structure of the cantilever modes is unchanged – only their frequency and damping is modified. The Stokes calculation for a cylinder yields

$$\Gamma(\Re) = 1 + \frac{4iK_1\left(-i\sqrt{i\Re}\right)}{\sqrt{i\Re}K_0\left(-i\sqrt{i\Re}\right)}, \qquad 6$$

where $K_o$ and $K_1$ are modified Bessel functions. There are two important consequences of this relation; first, $2\pi f \,\mathrm{Im}\{\Gamma\}$ gives an effective, frequency-dependent, viscous force per unit length, $\Re\,\mathrm{Im}\left\{\Gamma(\Re)\right\}\pi\eta u$, where $u$ is the velocity. The prefactor, $\Re\,\mathrm{Im}\left\{\Gamma(\Re)\right\}$, is of order 4 at $\Re$=1 and is only a slowly varying function of $\Re$. The similarity with the expression for the Stokes force $6\pi\eta a u$ acting upon a sphere of radius $a$ is apparent. However, unlike the case for the sphere, the dissipative drag coefficient for a cylinder does not asymptotically approach a constant value at low Reynolds numbers —

instead the prefactor decreases asymptotically as $8/\ln\Re$ at very small $\Re$. For the fundamental mode of a rectangular cantilever, the fluidic damping term can be written as

$$\gamma_{eff} \cong \alpha \ell \left[ 2\pi f \, \mathrm{Im}\{ L \} \right]. \qquad 7$$

This is weakly frequency dependent, since the factor $2\pi f \, \mathrm{Im}\{\boldsymbol{\Gamma}\}$ is not constant. The parameter $\alpha$ relates the mean square displacement along the beam to the displacement at its end. For the fundamental mode of a simple rectangular cantilever, $\alpha = 0.243$[6]; for a cantilever that acts as a hinge (see Fig. 2.2.A), $\alpha = 0.333$. Realistic cantilever geometries will be discussed in more detail in section 2.3, where the actual expressions used for $\alpha$ and K will be mentioned.

The second consequence of fluidic loading is an increase in the effective mass per unit length given by $\mathrm{Re}\{\boldsymbol{\Gamma}\}$. This term becomes quite large at small $\Re$. For the fundamental mode of a cantilever,

$$M_{eff} \cong \alpha \left( \rho_C V_c + \ell \, \mathrm{Re}\{ L \} \right). \qquad 8$$

Here, $V_c$ is the cantilever volume. Note that the fluid loading is determined by $w^2$ and not $wt$; hence thin beams experience relatively large fluid loading. The value of $\mathrm{Re}\{\boldsymbol{\Gamma}\}$ is unity for large $\Re$, is around 4 at $\Re = 1$, and continues to increase as $\Re$ decreases. Hence, for a silicon cantilever in water at a value of $w/t = 2$, the mass loading factor (defined as the ratio of fluid loading to inertial mass) is approximately 3 at $\Re = 1$ and increases for proportionately thinner beams and lower Reynolds numbers.

If we assume that the fluid mass dominates, the quality factor $Q$ of the oscillator can be estimated simply from the fluid properties as

$$Q \sim \frac{\omega M_{eff}}{\gamma_{eff}} \sim \frac{\mathrm{Re}\{\mathbf{\Gamma}(\Re)\}}{\mathrm{Im}\{\mathbf{\Gamma}(\Re)\}}. \qquad 9$$

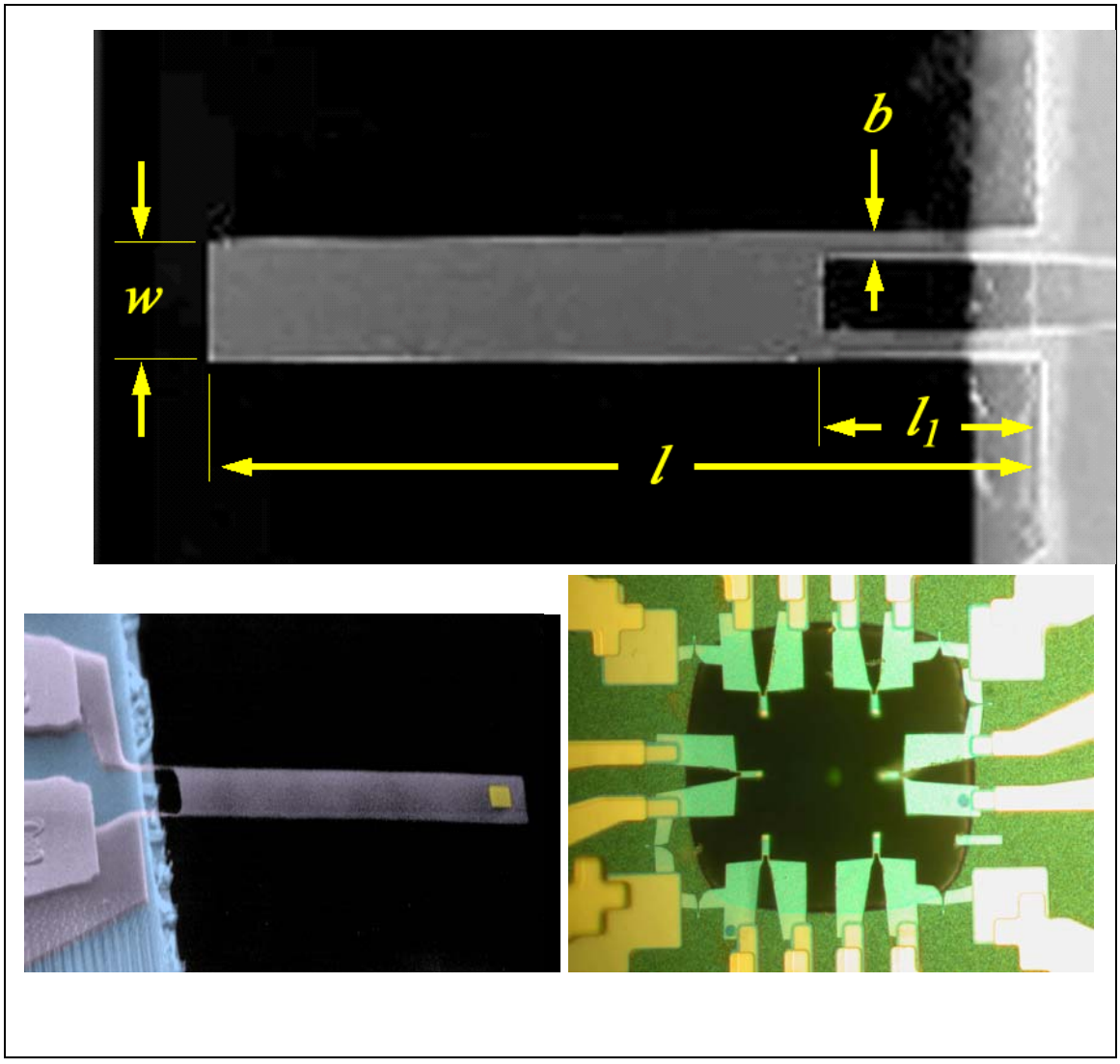


**Fig. 2.2.A Prototype silicon nanocantilevers.**

The cantilevers extend over a fluidic "vias" (dark regions) formed by deep-etching the wafer through to its backside. The topmost electron micrograph shows the following geometrical parameters for this particular prototypical two-leg device: $\ell$=15μm, $w$=2.5μm, $b$=0.58μm, and $\ell_1$=4μm. The cantilever thickness is $t$=130nm, of which the top 30nm forms the conducting layer (with a boron doping density of $4\times10^{19}/cm^3$). From this top layer the transducer and its leads are patterned. The two electrical terminals are visible on the right. For this cantilever, the current path is along the <110> direction for which $\pi_L \sim 4\times10^{-10}$ $Pa^{-1}$. [11,12] The two lower colorized images show other nanocantilevers above their respective fluidic vias (dark regions). The small gold pad visible at the cantilever tip is used for thiol-based biofunctionalization protocols.

This expression is rather independent of frequency, varying only over the range $0.2<Q<0.9$ as $\Re$ changes from $10^{-3}$ to 1. As expected, this is many orders of magnitude smaller value than the $Q$'s obtained from semiconductor resonators in vacuum.[1,10] Note that since $M_{eff}$ and $\gamma_{eff}$ are frequency-dependent, this notion of $Q$ is only approximate.

The displacement response function is given by the Fourier transform of equation 3:

$$H(f) = \frac{\tilde{x}}{\tilde{F}} = \frac{1}{K - M_{eff}(f) + i2\pi f \gamma_{eff}(f)} \quad . \qquad 10$$

(The average squared magnitude of $H(f)$ was given in equation 4). We shall use this in the analysis below to relate effective sources of displacement noise back to the force domain (in electrical engineering parlance, "refer them to the input") to enable evaluation of the practical force sensitivity attainable. The resultant motion of the cantilever tip from an applied force, F, is consequently dependent on the spring constant, K, which depends on the elastic properties of the material and device geometry and the frequency-dependent effective mass and damping which characterize the response of the beam in fluid. (This is analogous to the response function for a resonant device in vacuum, except that in the case of the latter the effective mass and damping are frequency-independent.) In Fig. 2.2.B we plot theoretical calculations of a normalized response function, $K\,H(f)$, for three different cantilever geometries. At high frequencies (greater than 10% of the vacuum resonance frequency) the roll-off in device response due to fluid-induced effective stiffening (from fluid loading) is evident. At low frequencies (less than 1% of the vacuum resonant frequency) the effect of fluid on the cantilever response is

slight. It is in the intermediate region that a sharp resonance would be observed for a device in vacuum. In fluid there is a peak in responsivity (at least for cantilevers 1 and 2), but it is a very broad peak, greatly suppressed compared to the responance in vacuum. The experiments of Viani *et al.*[13] involving silicon nitride microcantilevers in water confirm this; a peak intensity response of order of twice the low frequency response is found.

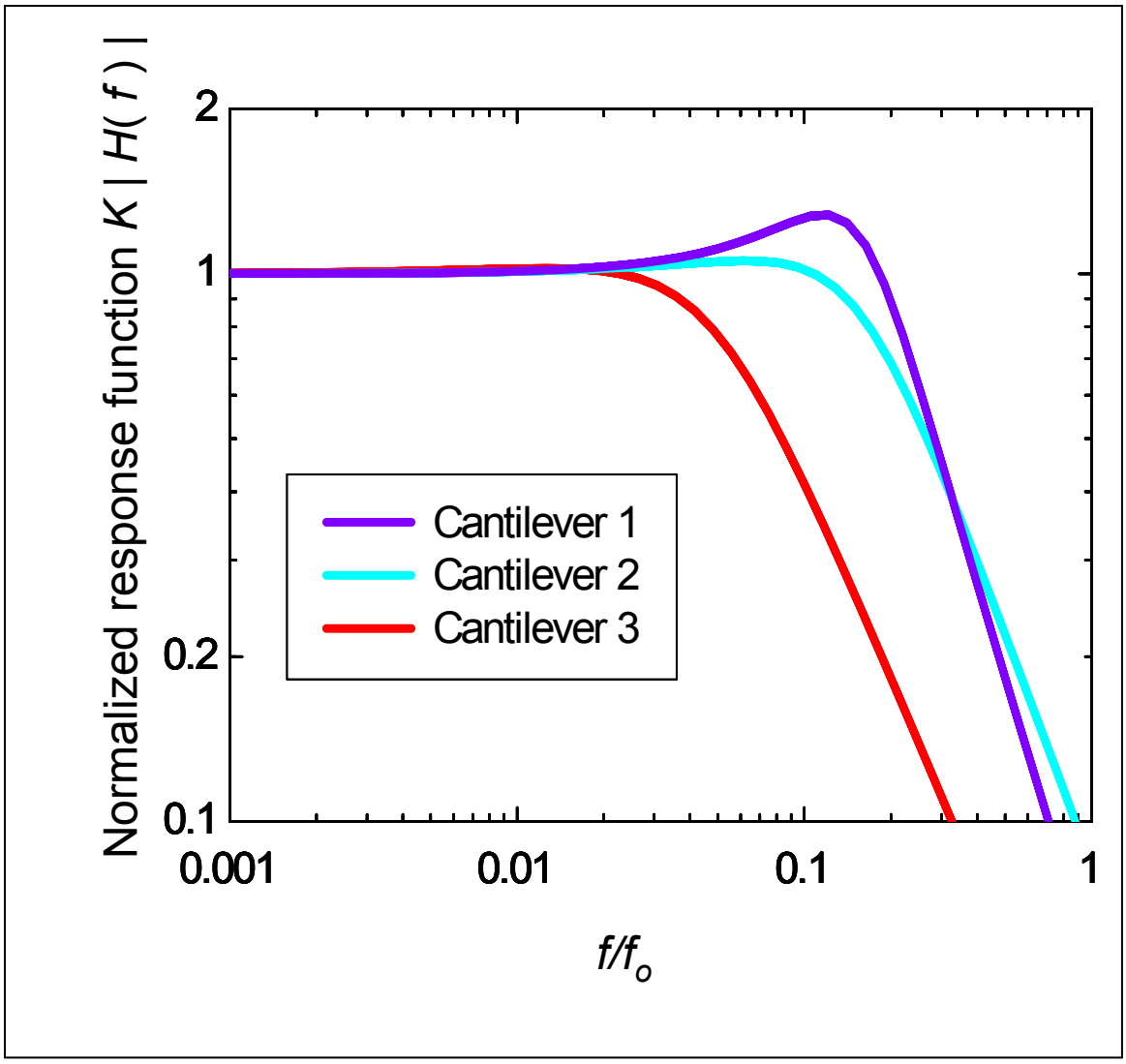


**Fig. 2.2.B Amplitude response functions for three prototypical fluid-loaded nanocantilevers.**

The spring constant, $K$, is used here to plot a dimensionless, "normalized", modulus of the response function (*c.f.* equation 10). The curves correspond to three examples whose properties are delineated in Table I. The Reynolds number for fluidic motion ranges from 5.0, to 0.19, to 0.07, respectively, and the response is seen to evolve from nearly critically damped to strongly overdamped.

**Table 2.2.A Physical parameters for three prototype Si nanocantilevers.**

| # | $t$ (nm) | $w$ (μm) | $\ell$ (μm) | $\ell_{leg}$ (μm) | $w_{leg}$ (nm) | $f$ (MHz) | $K$ (mN/m) | $\Re$ |
|---|---|---|---|---|---|---|---|---|
| 1 | 130 | 2.5 | 15 | 4.0 | 600 | 0.51 | 34 | 0.8 |
| 2 | 130 | 0.3 | 10 | 2.0 | 100 | 1.3 | 20 | 0.03 |
| 3 | 30 | 0.1 | 3 | 0.6 | 33 | 3.4 | 2.2 | 0.01 |

Parameters tabulated are thickness, $t$; width, $w$; length, $\ell$; constriction (leg) width, $w_{leg}$, and length, $\ell_{leg}$; frequency in vacuum, $f$; force constant, $K$; and Reynolds number at the resonant frequency in vacuum, $\Re$. (For a description of the dimensions referred to here see figure Fig. 2.5.A.)

## 2.3 Transducer Performance: Calculation of Parameters for Piezoresistive Transduction in p-type NEMS

We turn now to consider a concrete implementation of fluid-based mechanical force detection. Perhaps one of the most important engineering challenges is that of the readout system, which provides continuous interrogation of cantilever displacement. The devices under study will be referred to as "cantilevers," but in fact they are somewhat more complex than simple "diving board" cantilever geometry. Prototypical devices are shown in Fig. 2.2.A. By removing a region to create two "legs" near the anchor point at the end of the device, a higher degree of compliance is attained (along with a slight reduction in cantilever mass). Because these "two-legged" geometries are rather non-standard, we derive approximate expressions for the effective force constant, $K$ (for point loading at the end of the cantilever), the effective mass ratio in vacuum, $\alpha$ (relating the mean square displacement along the beam to the displacement at its end), and the piezoresistive transduction coefficient, $\partial R_d / \partial x$ (for determing the change in device resistance expected for a known displacement of the cantilever tip). Combining these parameters allows us to make calculations of the expected resistance change for a given force and to make comparisons with the noise floor.

### 2.3.1 Calculation of the Spring Constant and comparison with simulations

The effective spring constant for a prototypical device depends both on the device dimensions and on the form of support at the base, generally defined as either "clamped" ($d\xi/dy=0$ at the base) or "supported" (no constraint on $d\xi/dy$ at the base). The devices studied here are not rigidly clamped since the ledge from which they extend will have some compliance; nevertheless the ledge is designed to be much less compliant than the

cantilever, and they may therefore be approximately treated as clamped devices (this is supported by numerical simulations). The cantilever studied is not a simple cantilever (for which calculations may be found in the literature[14]) but one with legs such as that shown in Fig. 2.2.A.

The spring constant of the device may be estimated by first considering a small beam segment, as shown in Fig. 2.3.A, which subtends an angle $\delta\theta$ at the center of curvature. Let $R$ be the radius of curvature of the neutral surface (unstressed plane). Consider an infinitesimal element at height $\xi$ above the neutral plane. Then the stretched length is $(R+\xi)\delta\theta$, and the unstretched length is $R\delta\theta$. Therefore, the strain is given by $\xi/R$ and, consequently, the stress is $E\xi/R$ or, more precisely, $E\xi\ d^2\xi/dy^2$, where E is the Young's modulus for the material. Now consider the torques exerted at a position y along the length of the beam. The external torque from the force applied at the tip is given by $\Delta F(\ell - y)$ while the internal torque is given by $\int E\xi^2 \frac{d^2\xi}{dy^2} dA$. For the beams of interest $t << \ell$. Under this approximation, $d^2\xi/dy^2$ may be pulled through the integral to yield

$$EI_{xx}\frac{d^2x}{dy^2} = \Delta F(\ell - y) \qquad 11$$

where we now use the parameter $x(y)$ to refer to the vertical displacement of the beam at position y and

$$I_{xx} = \begin{cases} \frac{w_{leg}t^3}{6} & x<\ell_{leg} \\ \frac{wt^3}{12} & x>\ell_{leg} \end{cases} \qquad 12$$

is the moment of inertia for constricted and unconstricted portions of the cantilever (treated as a rigid body). The product $EI_{xx}$ is often referred to as the flexural rigidity, B. Therefore,

$$x=\begin{cases}\dfrac{\Delta F}{EI'_{xx}}\left(\dfrac{\ell y^2}{2}-\dfrac{y^3}{6}\right) & y<\ell_{leg},\ I'_{xx}=\dfrac{w_{leg}t^3}{6}\\ \dfrac{\Delta F}{EI_{xx}}\left(\dfrac{\ell y^2}{2}-\dfrac{y^3}{6}\right)+ay+b & y>\ell_{leg},\ I_{xx}=\dfrac{wt^3}{12}\end{cases}. \qquad (13)$$

Matching boundary conditions gives

$$\begin{aligned}a&=\frac{6\Delta F}{Et^3}\left(\ell\ell_{leg}-\frac{\ell_{leg}^2}{2}\right)\left(\frac{1}{w_{leg}}-\frac{2}{w}\right)\\ b&=\frac{\Delta F}{Et^3}\left(2\ell_{leg}^3-3\ell\ell_{leg}^2\right)\left(\frac{1}{w_{leg}}-\frac{2}{w}\right).\end{aligned} \qquad (14)$$

From this we obtain the spring constant

$$K=\frac{\Delta F}{y_{tip}}=\frac{Et^3}{\dfrac{4\ell^3}{w}+\left(2l_{leg}^3-6\ell\ell_{leg}^2+6\ell^2\ell_{leg}\right)\left(\dfrac{1}{w_{leg}}-\dfrac{2}{w}\right)}. \qquad (15)$$

For thin devices, the dependence of the Young's modulus on thickness must be accounted for in the above formula.[15] Equation 15 was very useful for quick estimations; finite element simulations were performed to test its accuracy. A device of dimensions $\ell$=40$\mu$m, $w$=10$\mu$m, $\ell_{leg}$=5$\mu$m, $w_{leg}$=2$\mu$m, $t$=110nm was used for this simulation (these dimensions correspond to one of the devices on which measurements will be presented later in this thesis) for which equation 15 gives a spring constant of 3.65mN/m. (A Young's modulus of 105GPa was interpolated from the data of Li et al who studied the Young's modulus in thin silicon resonators[15]). From finite element simulations a spring constant of 3.57 mN/m was attained.

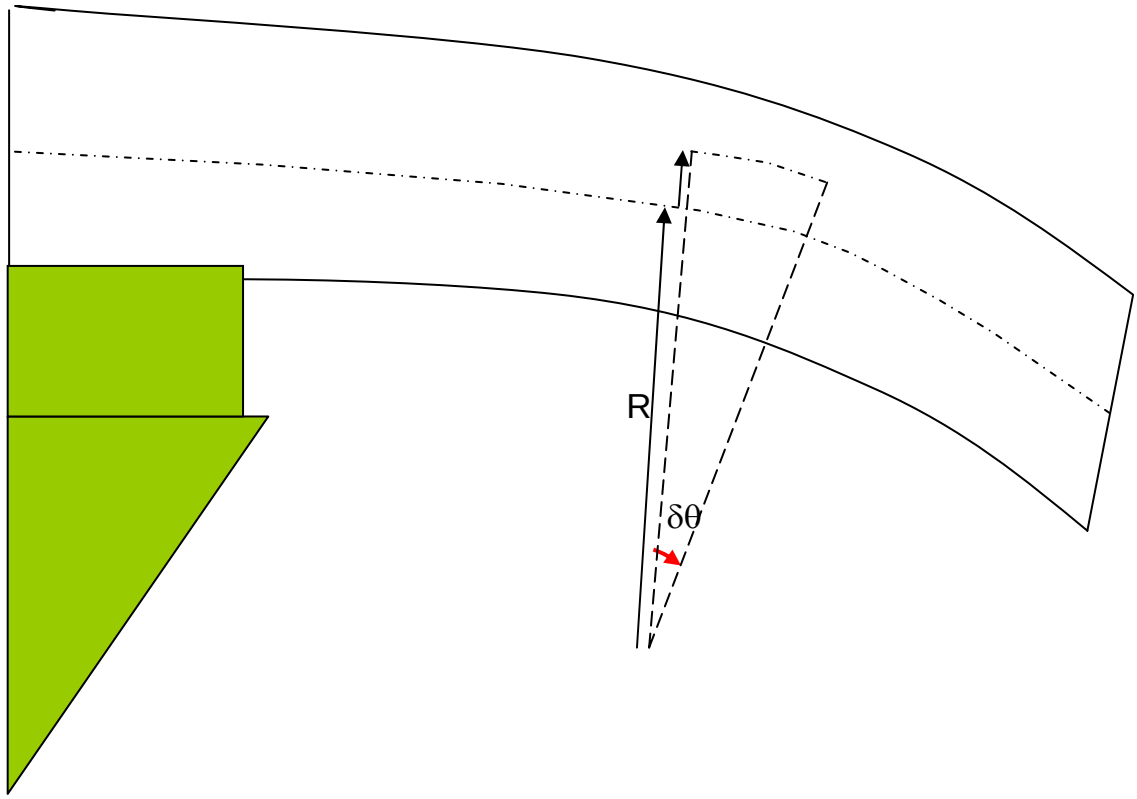


**Fig. 2.3.A Geometrical considerations for spring constant calculation**

The parameter R is defined as the radius of curvature of the neutral surface. $\xi$ is the distance above the neutral surface for the region of interest.

### 2.3.2 Calculation of the Cantilever's Effective Mass in Vacuum

A useful parameter for characterizing the cantilever's behavior is the effective mass in vacuum defined by the equation $M_{eff}=K/\omega^2$, where $f$ is the cantilever's resonance frequency and $\omega = 2\pi f$. The immediate use of this parameter will be to allow us to calculate resonance frequencies based on the cantilever dimensions without having to look back to the details of the cantilever motion. It will also allow us to account for the mass of gold and magnetic pads on the cantilever tips and will be applicable to calculations involving forces that are distributed across the cantilever rather than acting at the tip such as the Brownian fluctuations in fluid. An exact calculation of this parameter would require solving the equations of motion; here we present only an approximate solution based on energy equality at zero and maximum deflection (Rayleigh solution)[16].

Under maximum deflection the energy is stored entirely as strain and is given by $W_s = Kx_{tip}^2/2$, where $x_{\text{tip}}$ is the vertical deflection of the cantilever tip. (As a consistency check this may be derived from $W_s = \frac{E}{2}\left[ I'_{xx}\int_0^{\ell_{leg}} \frac{\partial^2 x}{\partial y^2}dy + I_{xx}\int_{\ell_{leg}}^{\ell} \frac{\partial^2 x}{\partial y^2}dy \right]$ using the expressions for $x(y)$, $I_{xx}$, $I'_{xx}$, and $K$ in the previous section). If the cantilever deflection is given by $x(y,t)=x(y)e^{i\omega t}$ with $x(y)$ defined by equation 13, then the energy at zero deflection (stored as kinetic energy) is

$$W_K = \frac{\rho t \omega^2}{2}\left[ w_{leg}\int_0^{\ell_{leg}} x^2(y)\,dy + w\int_{\ell_{leg}}^{\ell} x^2(y)\,dy \right]. \qquad 16$$

The above integral, while straight forward, has many terms. It may be simplified with the following assumptions that hold true for all cantilevers discussed here; namely that the total cantilever length is much greater than the leg length. Under this simplifying assumption the first term in equation 16 drops out entirely (as expected since the kinetic energy of the legs should not be a leading contribution), and the entire expression simplifies to

$$W_K = \frac{33}{280}\frac{\dfrac{\ell^2}{w^2}+\dfrac{35}{11}\ell_{leg}^2\left(\dfrac{1}{w_{leg}}-\dfrac{2}{w}\right)^2}{\left(\dfrac{\ell}{w}+\dfrac{3}{2}\ell_{leg}\left(1-\dfrac{\ell_{leg}}{\ell}\right)\left(\dfrac{1}{w_{leg}}-\dfrac{2}{w}\right)\right)^2}\rho t\ell w\omega^2 y_o^2. \qquad 17$$

Combining this expression with that for the strain energy we have

$$\omega^2 = \frac{140}{33}\frac{K}{t\ell w\rho}\frac{\left(\dfrac{\ell}{w}+\dfrac{3}{2}\ell_{leg}\left(1-\dfrac{\ell_{leg}}{\ell}\right)\left(\dfrac{1}{w_{leg}}-\dfrac{2}{w}\right)\right)^2}{\dfrac{\ell^2}{w^2}+\dfrac{35}{11}\ell_{leg}^2\left(\dfrac{1}{w_{leg}}-\dfrac{2}{w}\right)^2} \qquad 18$$

for an effective mass ratio of

$$\alpha = \frac{M_{eff}}{M_{total}} = \frac{33}{140}\frac{\dfrac{\ell^2}{w^2}+\dfrac{35}{11}\ell_{leg}^2\left(\dfrac{1}{w_{leg}}-\dfrac{2}{w}\right)^2}{\left(\dfrac{\ell}{w}+\dfrac{3}{2}\ell_{leg}\left(1-\dfrac{\ell_{leg}}{\ell}\right)\left(\dfrac{1}{w_{leg}}-\dfrac{2}{w}\right)\right)^2}\frac{\ell w}{\left(\ell w-\ell_{leg}w+2w_{leg}\ell_{leg}\right)}. \qquad 19$$

The accuracy of this method may be tested by looking at the limit of a conventional cantilever for which an exact solution gives $\alpha$=0.243[6]. From the above expression for $\ell_{leg}=0$, $\alpha$ =0.236. In the limit of very narrow legs where the following condition is met: $w_{leg}/w \ll \ell_{leg}/\ell \ll 1$, equation 9 reduces to $M_{eff}=M_o/3$, the expected value for a hinge.

For reference we give the value for $M_{eff}$ for three typical cantilevers. For the first, $\ell = 30\mu m$, $\ell_{leg} = 0.5\mu m$, $w$=10μm and $w_{leg}$=0.2μm, $M_{eff}$=0.15$M_o$. For $w_{leg}$=0.05μm and all other dimensions the same, $M_{eff}$=0.24$M_o$. For $w_{leg}$ =0.05μm, $\ell_{leg} = 5\mu m$ we begin to approach the hinge limit with $M_{eff}$=0.32$M_o$. Equation 19 is useful for quick estimations, but where accurate numbers are required, finite element simulation is preferred. In particular, for very narrow legs ($w_{leg}$<$w$/10), this formula has been observed to underestimate $\alpha$ by as much as 35% as compared to the results of finite element simulations. For wider legs the agreement is better.[17]

### 2.3.3 Piezoresistivity: an Overview

When a mechanical stress is applied to a conducting material it results in a change in resistivity. Any conducting material will experience a change in resistance when stretched due to geometrical changes (this is the principal under which all strain gauges work), but in semiconducting material such as silicon and germanium the piezoresistive coefficient is about a hundred times greater than that observed in metallic conductors, with the influence of geometrical stretching and compression playing a minor role. This effect was discovered in the 1950s,[18] and its application played an important role in early silicon sensor devices.[19,20] Piezoresistive sensors were first applied to AFM cantilevers by Tortonese et al. in 1991[21] and since then have been adopted by a number of researchers, achieving sensitivity comparable to that of optical sensors but with significant advantages for scalability both in the context of reducing device dimensions to sizes where optical detection would not be possible and for arrays where optical detection is more complicated (due to the extra hardware required).

A number of factors are believed to contribute to the piezoresistive effect of a material. For instance, a change in volume has a direct effect on the energy gap, leading directly to a change in the number of carriers and hence a change in the resistivity. However, this effect is not large enough to explain the observed change. For n-doped silicon the experimental observations are in agreement with theoretical predictions based on the directional mobility dependence. In brief, the first Brouillon zone in silicon is comprised of six valleys aligned with the six <100> directions. Within each valley, the k-vector projection of the constant energy surface is directionally dependent. When the material is unstressed, all six valleys are equally populated. However, the application of anisotropic stress shifts the relative energy of these valleys. Hence the population is no longer equally distributed. Within a single valley the differing k-space projections lead to an aniosotropic carrier mobility. Therefore, the population shift between valleys leads to a directionally-dependent change in resistance. For p-type silicon this explanation alone is inadequate to explain the experimental observations; the full theoretical underpinning does not lend itself as easily to a quick overview but may be found in the literature.[22] For the purposes of our study it is sufficient to note that independent of the underlying physical cause of piezoresistivity, it can be described by a tensor, the values of which depend on material and doping concentration but are readily available in the literature.[3,22]

### 2.3.4 Calculation of the Piezoresistive Tranduction Factor

The displacement transducer converts the motion of the cantilever into an electrical signal; in this case this occurs via the strain-induced change of the resistance of a conducting path patterned from a p+ doped Si epilayer on the topmost surface of the device.[23] We characterize the transducer's performance by its responsivity (with units

volts/m), $\mathcal{R}_T = I\frac{\partial R_d}{\partial x}$, where $I$ is the bias current and $\frac{\partial R_d}{\partial x}$ is the resistance change per unit displacement of the cantilever tip. $\mathcal{R}_T \delta x$ is the signal (in volts) that will be observed for a tip displacement $\delta x$. (Note that this *transducer* responsitivity is distinct from the device's compliance, which is its *mechanical* responsivity.) To calculate the parameter *G* we must take into consideration both the geometrical properties of the device and its material properties; piezoresistivity, resistivity, and stiffness (Young's modulus). Here we present a calculation of this parameter.

Piezoresistive materials are typically characterized by their piezoresistive coefficient, $\pi_\ell$, defined as the fractional change in resistivity per unit stress:

$$\pi_\ell = \frac{1}{S}\frac{\Delta\rho}{\rho}. \qquad 20$$

While deriving the spring constant we showed that the stress at position y along the length of the cantilever is given by

$$S = E\xi\frac{d^2x}{dy^2} = E\frac{\Delta F(\ell - y)\xi}{YI_{zz}} = \frac{6\pi_\ell \Delta F(\ell - y)\xi}{w_{leg}t^3}. \qquad 21$$

From this we may calculate

$$\frac{\Delta R_d}{R_d} = \frac{\frac{1}{2w_{leg}t}\int_0^{\ell_{leg}}\frac{\Delta\rho}{\rho}\,dy}{\frac{\ell_{leg}}{2w_{leg}t}} = \frac{3\beta\pi_\ell}{2w_{leg}t^2}\left(2\ell - \ell_{leg}\right)K\Delta x, \qquad 22$$

where we have used ξ=βt/2, with β accounting for the finite thickness. A value of 0.7 is used based on the results of J.A Harley and T.W. Kenny[23]. This yields the following result for the piezoresitive transduction factor:

$$\frac{\partial R_d}{\partial x} = \frac{3\beta\pi_\ell}{2w_{leg}t^2}\left(2\ell - \ell_{leg}\right)KR_d \,. \qquad 23$$

The above expression is very useful for quick estimates. To test its accuracy finite element simulations were performed. The stress throughout the cantilever was calculated numerically using the CRDRC Ace Solver.[24] From equation 20,

$$\frac{\Delta R_d}{\Delta x} = \frac{R_d\pi_\ell \oint_{V_C} S_{xx}dV}{\Delta x \ell_{leg} w_{leg} t_{doped}}, \qquad 24$$

where $S_{xx}$ is the stress in the direction of current flow and the volume integral is performed over the conduction portion of a single leg (the stress in the conducting tip region is ignored), and $t_{doped}$ is the thickness containing dopants. For a cantilever of dimensions $\ell$=40μm, w=10μm, $\ell_{leg}$=5μm, $w_{leg}$=2μm, $t$=110nm, from equation 23 we obtain $\frac{1}{\pi_\ell R_d}\frac{\partial R_d}{\partial x} = 1.19\text{x}10^{13}$ N/m$^3$ (using a spring constant calculated from equation 15). Using equation 14 and a finite element simulation to calculate the stress for a given tip displacement, $\frac{1}{\pi_\ell R_d}\frac{\partial R_d}{\partial x} = 1.18\text{x}10^{13}$ N/m$^3$, in excellent agreement with the above analytical value.

## 2.4 Force Sensitivity of Piezoresistive BioNEMS Devices: Noise Analysis

To account for the effect of degradation of force sensitivity by readout process we add three additional terms (arising from electrical noise) to the spectral density of fluid-induced displacement fluctuations, $S_x^\gamma = 4k_BT\gamma\left|H(\omega)\right|^2$. Again, to assess their role in limiting the practical force sensitivity of the transducer-coupled device, these must be

referred back to the displacement domain using the factor $1/\mathcal{R}_T^2$ where $\mathcal{R}_T^2 = I\frac{\partial R_d}{\partial x}$ is the electrical transduction factor discussed in section 2.3.4. The first term arises from the thermal voltage noise of the piezoresistive transducer, $S_V^J = 4k_B T R_d$, while the second arises from the readout amplifier's voltage and current noise, $S_V^A = S_V + S_I R_d^2$, where $S_V$ and $S_I$ are the spectral density of the amplifier's voltage and current noise, respectively. If the response extends down to low frequencies, we must also consider a third term, the flicker noise (often termed "1/*f*" noise) in the transducer, $S_V^{1/f}$. The sum of these fluctuations yields what we term the total *coupled* displacement noise, which is the actual displacement sensitivity of the entire system:

$$S_x^{(tot)} = S_x^{\gamma} + \frac{1}{\mathcal{R}_T^2}\left\{S_V^J + S_V^A + S_V^{1/f}\right\}. \qquad 25$$

From this we can determine the coupled force sensitivity of the electromechanical system,

$$S_F^{(tot)} = S_x^{(tot)} / \left|H(\omega)\right|^2 = 4k_B T\gamma_{eff} + \frac{1}{\left|H(\omega)\right|^2 \mathcal{R}_T^2}\left\{S_V^J + S_V^A + S_V^{1/f}\right\}. \qquad 26$$

## 2.5 BioNEMS: Practical Considerations Determining Realizable Sensitivity.

### 2.5.1 Maximal Transducer Current Bias

We now investigate the constraints upon the level of current bias that can be applied. The force sensitivity attainable clearly hinges on the maximum current level that is tolerable, given that the responsivity is proportional to bias current, $\mathcal{R}_T = I_b\frac{\partial R_d}{\partial x}$. However, this applied bias current leads to self-heating of the device. Several

considerations are important in determining the optimal (maximum) current level: first, the highest tolerable temperature rise within the device must be considered both at its biofunctionalized tip (to avoid damage to the SAM) and at the position of peak temperature rise within the device (to avoid device failure). Additionally, if the electrical elements of the device are unpassivated, it may prove important to limit the transducer voltage drop to below 0.5V to prevent undesired electrochemical processes. Here we consider the self-heating of the device due to electrical power dissipation. The geometry of the prototype devices causes dissipation to occur predominantly within the constriction regions , treated as a beam of width, $w_{leg}$, length, $\ell_{leg}$, and cross sectional area A (*c.f.* Fig. 2.2.A) with a one dimensional heat sink at the supporting end. For $x > \ell_{leg}$, a rough estimate of the heat loss to the surrounding fluid may be obtained through the relationship $\kappa_{\mathrm{Si}}\, A\, \frac{d^2T}{dx^2} = \kappa_{H_2O}\, P \nabla_{\mathrm{n}} T$, where $P$ is the perimeter around cross-sectional area $A$ of the beam. Estimating $\nabla_n T \sim T/w$, $\frac{d^2T}{dx^2} \sim \frac{2(w+t)\kappa_{H_2O}}{\kappa_{\mathrm{Si}} t w^2}$, where $\kappa_{Si}$=1.48x10$^2$ W/ m K [25] is the thermal conductivity of silicon and $\kappa_{\mathrm{H_2O}}$=0.607 W/ m K [26] is the thermal conductivity of water. In the dissipative region $x < \ell_{leg}$ we have $2\kappa_{\mathrm{Si}} t w_{leg} \frac{d^2T}{dx^2} \sim -\frac{I_b^2 R_d}{\ell_{leg}} + 4(w_{leg}+t)\frac{T}{w_{leg}}\kappa_{H_2O}$. As boundary conditions we have that the temperature is continuous at $\ell_{leg}$, as is the heat flux, and the temperature must monotonically decrease for $x > \ell_{leg}$. For a bias current of 30μA, this calculation yields a temperature rise at the cantilever tip of 0.01K. The maximal temperature rise of 0.1K

occurs within the constricted region, approximately 2.3μm from the support. For this bias current, our prototype device yields a responsivity $\mathcal{R} = I_b \frac{\partial R_{dev}}{\partial x} \sim 20\mu V/nm$.

With knowledge of these parameters we now estimate the coupled force sensitivity of the prototype system. For cantilever 1, assuming that a 1K rise at the tip is tolerable, the transducer-induced displacement noise is found to be $\sqrt{S_V^J}/\mathcal{R}_T = 5\times10^{-13}$ m/√Hz. This number represents the square root of the power spectral density for displacement fluctuations of the cantilever tip due to thermal mechanical ("thermomechanical") motion. For a typical low noise readout amplifier with voltage and current noise levels (referred to input) of ~4nV/√Hz and ~5 fA/√Hz, respectively*, these same parameters yield an amplifier term $\sqrt{S_V^A}/\mathcal{R}_T = 2\times10^{-13}$m/√Hz, this number represents the square root of the power spectral density for displacement fluctuations that would yield a noise equivalent to the square root of the power spectral density for the combined Johnson and preamplifier noise.

Fig. 2.5.A shows the coupled force sensitivity per unit bandwidth for this device, as given by Eq. 26, this includes the combined noise from fluidic, transducer, and readout amplifier sources referred to input (*i.e.* the force domain) using the above parameters.

---

* This is a typical value for JFET input low noise amplifiers, for frequencies beyond the 1/f noise knee.

For comparison, separate traces representing only the fluidic noise are displayed; these are calculated from the Nyquist formula with equation 7 for the damping term in water.

Fig. 2.5.A shows that even the largest device (cantilever 1) yields a remarkably low *coupled* force sensitivity, $\left[S_F^{(tot)}\right]^{1/2} \leq 30$ fN/√Hz for frequencies below 100 kHz, at a bias voltage of 0.5V. This means dynamical measurements on the ~10μs scale are possible for absolute forces on the level of <8 pN without averaging. This is comparable to the average force of a single hydrogen bond (~10 pN) [27-29], whereas typical antibody-antigen binding forces are in the 50-300 pN range[30,31]. Two higher bias voltages are also shown in Fig. 2.5.A. The heating at the cantilever tip remains modest at these voltages. For a bias voltage of 4.3 V across the device, the expected temperature rise at the tip is only 0.9K, and a coupled force sensitivity $\left[S_F^{(tot)}\right]^{1/2} \leq$ 33 fN/√Hz for frequencies below 500 *K*Hz can be attained. This is only 20% above the thermomechanically determined thermal noise floor and means that dynamical measurements on the ~2 μs scale are possible for absolute forces on the level of <22 pN without averaging.

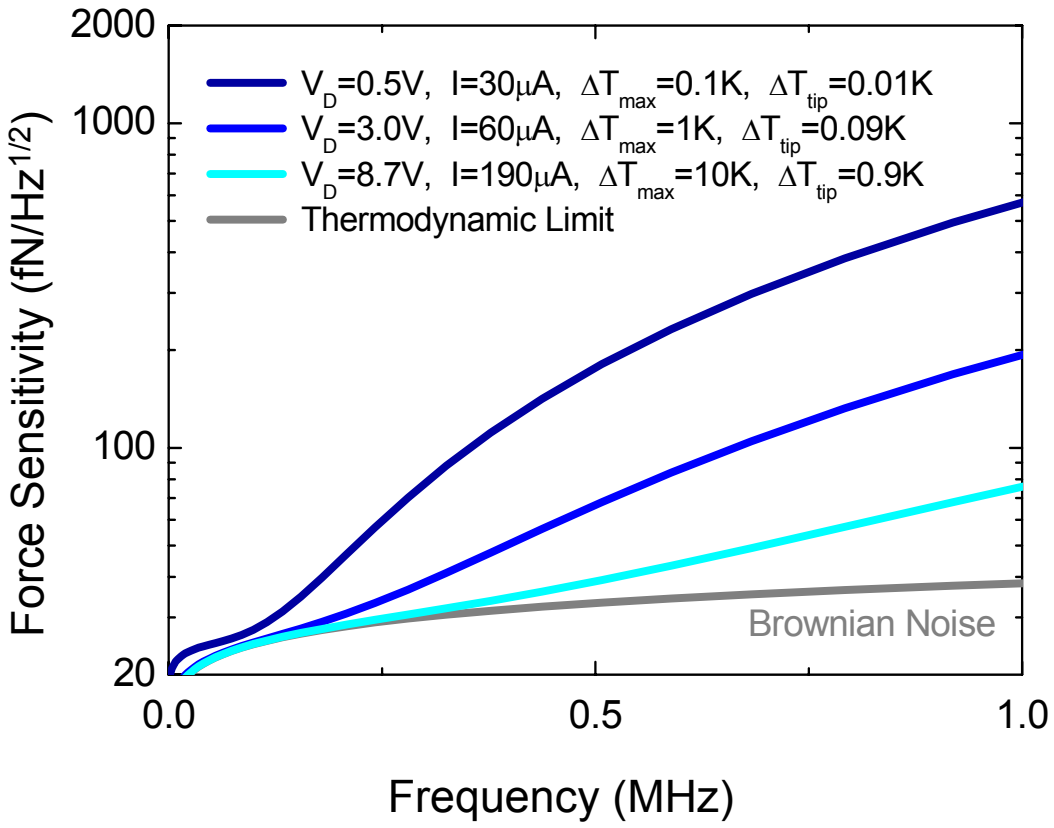


**Fig. 2.5.A Total, coupled force spectral density for cantilever 1.**

The analytic model, based upon fluid coupling for an infinite cylinder, is used for analysis of the device that has parameters shown in Table 2.2.A. As described in the text, the force noise includes noise contributions from the electrical domain, referred back to the input (force domain) – specifically, electrical fluctuations arising from Johnson noise in the piezoresistive transducer and noise from the subsequent read-out amplifier. The fluidic fluctuation limit is displayed for reference; at higher bias currents this is more closely approached.

In Fig. 2.5.A the transducer noise is clearly dominant. At fixed voltage, V, the Johnson noise contribution to the force sensitivity is given by

$$\sqrt{S_F^J} = \frac{4t^2\sqrt{2w_{leg}\ell_{leg}\rho_{epi}k_BT}}{3\beta\pi_\ell V\left(2\ell-\ell_{leg}\right)\sqrt{t_{epi}}\left(K\left|H\left(\omega\right)\right|\right)}, \qquad 27$$

where the spring constant $K$ and displacement response function $H(\omega)$ have been lumped together to give a dimensionless value which is generally close to 1 at frequencies below the roll-off frequency (Fig. 2.2.B). It is clear from Eq. 27 that to minimize the Johnson noise it is desirable to maximize $\beta$, $\pi_\ell$ and V. Since $\pi_\ell$ decreases with increasing doping (boron concentration),[11,32] in the Johnson noise-limited regime it is desirable to work at low doping concentrations. (Below $1\text{x}10^{17}$ $\text{cm}^{-3}$ $\pi_\ell$ is essentially independent of doping concentration.) While modest improvements can be made in these areas, there is more potential in improved device design through the reduction of device dimensions, particularly $w_{\text{leg}}$, $t$, and $\ell_{leg}$. It is actually also beneficial to increase the total device length $\ell$, although this increased sensitivity comes at the expense of bandwidth. However, by far the greatest improvement is achieved through a reduction in the device thickness.

With these considerations in mind we evaluate two additional devices; *cantilever 2,* which has comparable thickness but reduced dimensions, and *cantilever 3,* in which all dimensions have been reduced by a factor of 3 from the second device. We stress that all of these dimensions, as tabulated in Table 2.2.A, are *practical*; they are readily achievable by top-down nanofabrication processes in our laboratory. For the second

device, cantilever 2, we assume its 130nm thickness comprises epilayers with the same composition as cantilever 1; this yields $R_d$ = 70kΩ and $\frac{\partial R_d}{\partial x}$ = 4.5x10$^9$ Ω/m (with current path oriented along the <111> direction). For this second prototypical device we again begin by assuming that a maximum voltage drop across the device of 0.5V is tolerable (the associated temperature rise in the constricted regions is ~0.2K and only 0.5mK at the device tip). The resulting force sensitivity is shown in Fig. 2.5.B0. The value attained, <20 fN/√Hz for frequencies below 0.5 MHz, means dynamical measurements on the ~2μs scale are possible without averaging for forces at the ~10 pN level, again comparable to the average force of a single hydrogen bond. With a higher bias voltage of 3.8V across the device (for which the expected heating of the cantilever tip is 0.03K), a force sensitivity of <14.8 fN/√Hz is now maintained out to a frequency of 1 MHz, a value only 5% above the Brownian-fluctuation-limited thermodynamic noise floor. With this sensitivity, dynamical measurements of ~13 pN forces are possible on the 1 μs scale without averaging. Finally, we consider a smaller device, cantilever 3, where the device thickness is reduced to 30 nm. For this device, with dimensions tabulated in Table 2.2.A, we obtain $R_d$ = 270 kΩ, and $\frac{\partial R_d}{\partial x}$ = 9.9x10$^9$ Ω/m. We again first assume that a maximum voltage drop across the device of 0.5V is tolerable. The resulting force sensitivity is shown in Fig. 2.5.C0. This smaller device provides very impressive force sensitivity: $\left[S_F^{(tot)}\right]^{1/2} \leq$ 6 fN/√Hz for frequencies below 0.5 MHz. This permits dynamical measurements on the 2 μs scale with force resolution at the 4 pN level without averaging. For a larger bias voltage of 4.1V across the device, the bandwidth can be increased to 2

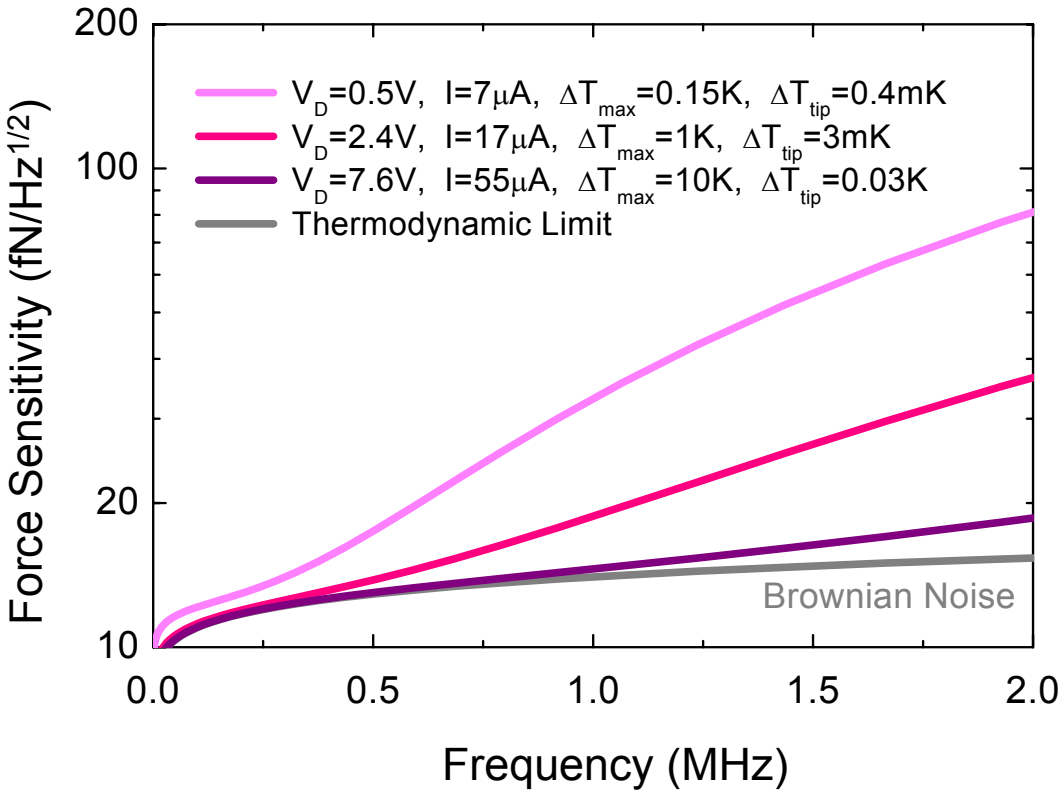


**Fig. 2.5.B Total, coupled force spectral density for cantilever 2.**

The qualitative behavior obtained is similar to that of cantilever 1, but enhanced sensitivity is obtained for the smaller device. The lowest values attained, <20 fN/√Hz for frequencies below 0.5 MHz (for a bias voltage of 0.5V across the device), enables single-shot dynamical measurements on the ~2 μs scale (without averaging) for forces at the ~15 pN level.

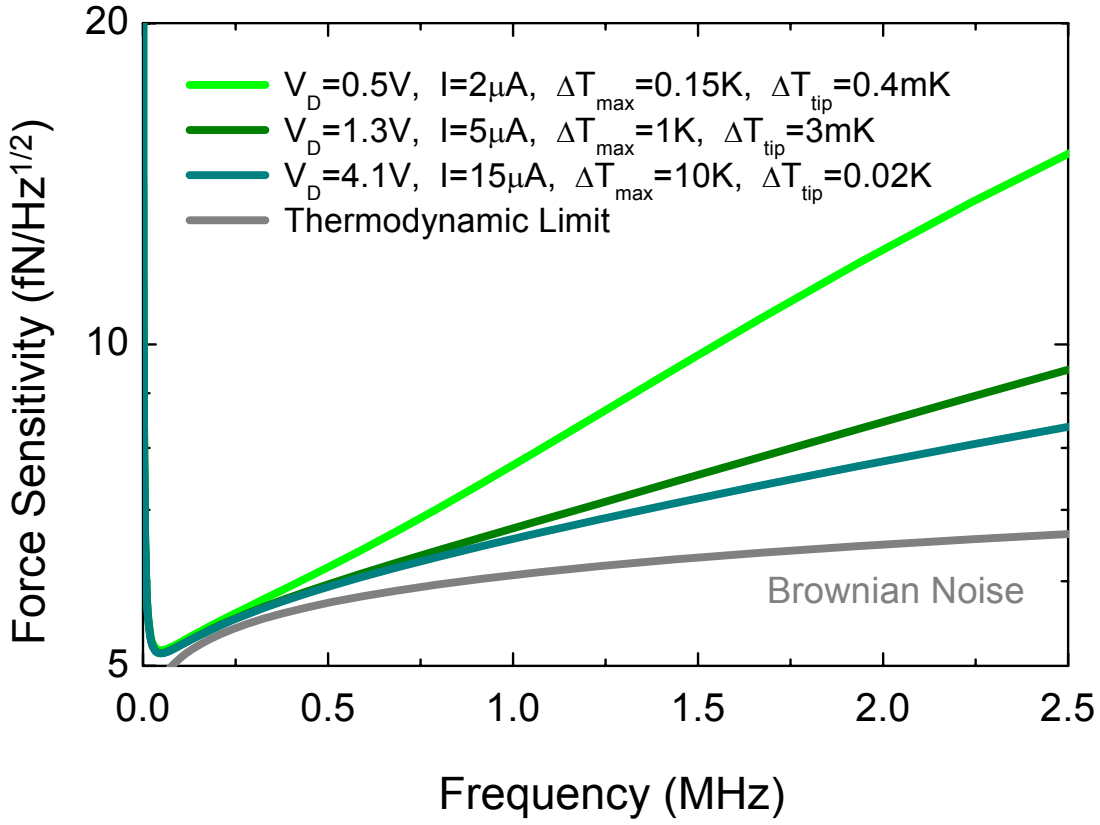


**Fig. 2.5.C Total coupled force spectral density for cantilever 3.**

The noise performance obtained is again qualitatively similar to that of the two larger devices considered, but substantially higher sensitivity is obtained for this, the smallest device analyzed. Note that at frequencies <1 MHz, the transducer is quite capable of matching the thermodynamic limit imposed by Brownian fluctuations, and the coupled sensitivity remains within about 20% of the fluidic noise floor at a bias voltage of 0.5V. Below 0.25 MHz, the spectral density is only of order 5 fN/√Hz (for reasonable bias voltages). The low frequency noise rise in these spectra includes the expected contributions from low frequency resistance fluctuations arising within the piezoresistors (see text), which is more clearly displayed in Fig. 2.5.D.

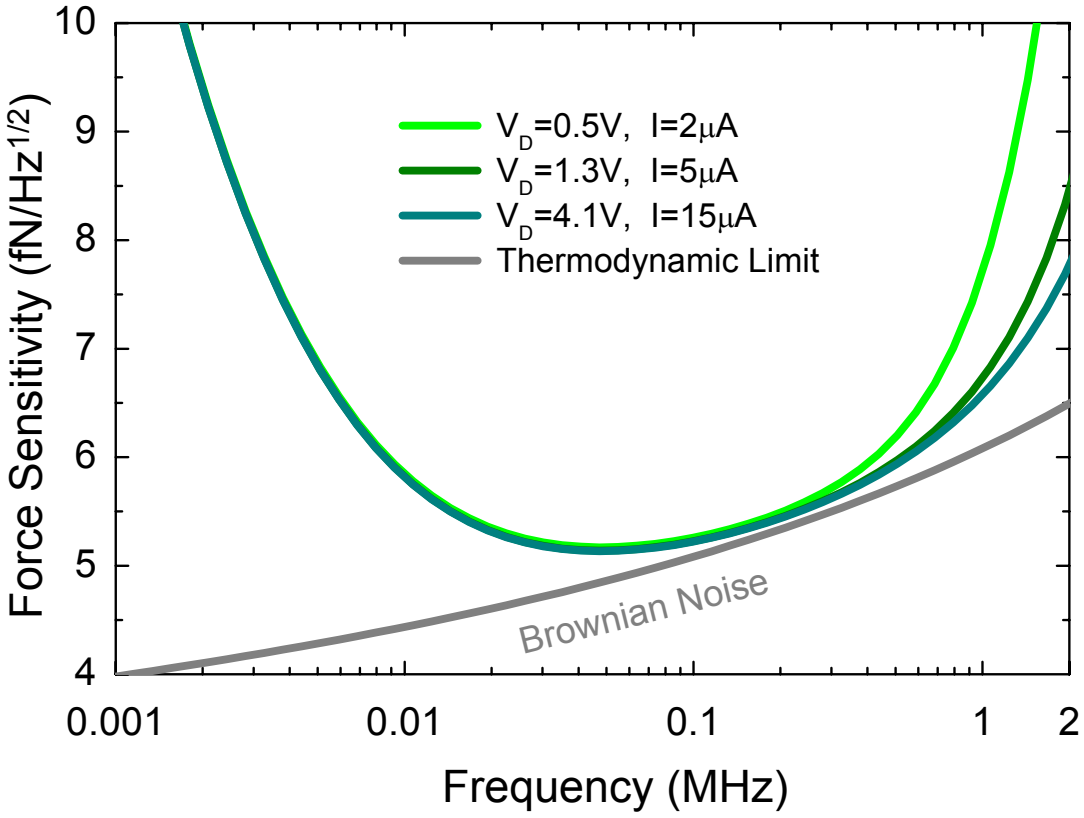


**Fig. 2.5.D Total, low frequency, transducer-coupled force spectral density for cantilever 3.**

The increase in the low frequency spectral densities arises from flicker noise processes in the displacement transducers (see text). This unavoidable voltage noise contribution from the semiconducting piezoresistors of cantilever 3 (*c.f.* Table 2.2.A) is referred back to the input (force domain) and contributes to the overall noise spectra for the transducer-coupled devices. As can be seen, despite this contribution, above a few kHz the low frequency noise is not significant for these cantilever dimensions.

MHz while maintaining a coupled force sensitivity $\left[S_F^{(tot)}\right]^{1/2} \leq 8$ fN/√Hz, allowing dynamical measurements on the 500 ns time scale for absolute forces at the 10 pN level. Again, resulting temperature rises for these higher biases are negligible on biochemical scales.

### 2.5.2 Low Frequency Transducer Noise

An important consideration is the low-frequency "flicker" noise that arises within the transducer under conditions of current bias from its intrinsic resistance fluctuations, $S_V^{1/f} = I^2 S_R^{1/f}$. An empirical model first proposed by Hooge[33] and applicable where the number of carriers is small, relates the spectral density of the transducer's resistance fluctuations to the number of carriers involved in conduction, $S_R^{1/f} = 2\pi\varsigma R_{dev}^2 / N\omega$. Here, $\varsigma$ is a sample-specific materials parameter, and *N* is the number of carriers within the sample. This formula assumes uniform conduction; based upon the work of Harley and Kenny[32] this is a reasonable approximation if N is taken to represent the combined number of carriers in the two legs, and from their work we expect $\varsigma \sim 10^{-5}$ for our devices. (This assumes a 3 hour anneal at 700°C.) Based on numerical calculations of the depletion length, the number of carriers in the doped region is estimated to be $1.2 \times 10^4$ for cantilever 3.[†] In the plots of Figure 6 we have included the low frequency flicker

---

[†] In addition to concerns over the depletion length, one might be concerned as to whether a total thickness of 30nm (comprised of 7nm doped and 23nm intrinsic silicon) is feasible due to migration of carriers into the intrinsic region. Numerical calculations, presented in section 3.3, show that for this dopant concentration, 2.3nm into the intrinsic region, the concentration of holes has dropped by about an order of magnitude, and by 7.3nm it has dropped by 2 orders of magnitude.

noise for this device at the current bias levels used in Figure 5. Note that above about 10 kHz the total noise floor for the coupled device is dominated by either Brownian fluidic fluctuations, or the combined Johnson noise of the transducer and its readout amplifier.

## 2.6 Conclusions

The achievable *coupled sensitivity* presented herein, as low as ~8 *f*N/√Hz, limited predominantly by the fluidic fluctuations, opens exciting new potential for single molecule sensing with wide bandwidths ~MHz and at correspondingly fast time scales. Additionally, the high level of dimensional control available through the nanofabrication technique offers immense potential for patterning arrays of such cantilevers within very small volumes. Large scale integration of BioNEMS offers the possibility of sensing many different types of molecules simultaneously in the fashion of existing "bioarray" technology, or of using sensor redundancy to enhance detection of a particular analyte in the extremely dilute limit. Moreover, these arrays may be used for a robust implementation of cross-correlation techniques to achieve even greater absolute sensitivity, as first demonstrated by Meiners and Quake using a pair of optical traps.[34]

We have shown that BioNEMS offer the potential of vast improvements in force sensitivity and temporal response compared to current biological force assays. Additionally, they offer significant potential for integration into large-scale arrays. We anticipate that these attributes will provide important new avenues in biotechnology.

## 2.7 References


[1] E.M. Purcell, Am. J. Phys. 45, 3-11 (1977).

[2] J.E. Sader, J. Appl. Phys. **84**, 64-76 (1998).

[3] J.W.M. Chon, P. Mulvaney, and J. Sader, J Appl. Phys. 87, 3978-3988 (2000).

[4] M.R. Paul and M.C. Cross, Phys. Rev. Lett., **92**, 235501 (2004).

[5] J.L. Arlett, M. Paul, J. Solomon, M.C. Cross, S.E. Fraser, and M.L. Roukes, "BioNEMS: Nanomechanical Systems for Single-Molecule Biophysics" in *"Controlled Nanoscale Motion in Biological and Artificial Systems"* (Nobel Symposium 131, June 2005), H. Linke et al., Eds. (Springer Verlag, Heidelburg, *to be published*).

[6] D. Sarid, Scanning Force Microscopy with Applications to Electric, Magnetic, and Atomic Forces (New York), pp. 9-13 (1991).

[7] F. Gittes and C.F. Schmidt, Eur Biophys J, **27**, 75-81 (1998).

[8] E.O. Tuck, J. Eng. Math. **3**, 29-44 (1969).

[9] L. Rosenhead, *Laminar Boundary Layers,* Oxford University Press (Oxford, Great Britain), pp. 390-393 (1963).

[10] K.Y. Yasumura, T.D. Stowe, E.M. Chow, T. Pfafman, T.W. Kenny, B.C. Stipe, and D. Rugar, J MEMS **9,** 117-125 (2000).

[11] O.N. Tufte and E.L. Stelzer, J Appl. Phys. **34**, 313-318 (1963).

[12] W.P. Mason and R.N. Thurston, J. Acoust. Soc. Am. **29**, 1096-1101 (1957).

[13] M.B. Viani, T.E. Schaffer, A. Chand, M. Rief, H.E. Gaub, and P.K. Hansma, J Appl. Phys. **86**, 2258-2262 (1999).

[14] A.E. Love, A Treatise on the Mathematical Theory of Elasticity, Dover Publications (New York), pp. 370-373 (1944).

[15] L. Xinxin, T. Ono, Y. Wang, and M. Esashi, Appl. Phys. Lett. **83**, 3081-3083 (2003).

[16] D. Sarid, Scanning Force Microscopy with Applications to Electric, Magnetic, and Atomic Forces (New York), pp. 7-9 (1991).

[17] James Maloney, graduate student, Caltech, private communication.

[18] C.S. Smith, Phys Rev **94**, 42-49 (1954).

[19] O.N. Tufte, D. Long, and P.W. Chapman, J. Appl. Phys. **33**, 3322-3327 (1962).

[20] A.C.M. Gieles, Digest, IEEE ISSCC, Philidelphia, 108-109 (1969).

[21] M. Tortonese, H. Yamada, R.C. Barrett, and C.F. Quate, Atomic force microscopy using a piezoresistive cantilever. TRANSDUCERS '91. 1991 International Conference on Solid-State Sensors and Actuators. Digest of Technical Papers, 448-451 (1991).

[22] B. Kloeck, "Piezoresistive Sensors," Mechanical Sensors, chap 5, VCH, Weinheim, Germany, 1994.

[23] J.A. Harley and Kenny, T.W. Appl. Phys. Lett. 75, 289-291 (1999).

[24] CFD-ACE, Computational Fluid Dynamics Research Corporation, Huntsville, AL.

[25] C.Y. Ho, R.W. Powell, and P.E. Liley,. J. Phys Chem Ref Data **1**, 279-421 (1972).

[26] J.V.Sengers and J.T.R. Watson, J. Phys Chem Ref Data **15**, 1291-1314 (1986).

[27] J.H. Hoh, J.P. Clevland, C.B. Prater, J.-P. Revel, and P.K. Hansma, J. Am. Chem. Soc **114**, 4917-4918 (1992).

[28] M. Grandbois, M. Beyer, M. Rief, H. Clausen-Schaumann, and H.E. Gaub, Science **283**, 1727-1730 (1999).

[29] E. Evans and K. Ritchie, Biophys. J. 76, 2439-2447 (1999).

[30] U. Dammer, M. Hegner, D. Anselmetti, P. Wagner, M. Dreier, W. Huber, and H.-J. Güntherodt, Biophys. J. **70**, 2437-2441 (1996).

[31] P. Hinterdorfer, W. Baumgartner, H.J. Gruber, K. Schilcher, and H. Schindler, Proc. Natl. Acad. Sci. USA. **93**, 3477-3481 (1996).

[32] J.A. Harley and Kenny, J MEMS **9**, 226-235 (2000).

[33] F.N. Hooge, Phys Lett. A **A29**, 139-140. (1969).

[34] J.-C. Meiners and S.R. Quake, Phys Rev Lett. **82**, 2211-2214 (1999).

.

# 3 Methods of Fabrication and Considerations

## 3.1 Fabrication Details

### 3.1.1 Fabrication Overview

A schematic of a prototypical device is shown in Fig. 3.1.A. At the heart of the device is the piezoresistive cantilever shown in the inset of Fig. 3.1.A (b). This structure is a two layer device; the lower layer is lightly doped (ideally intrinsic) to keep conduction through this layer to a minimum. The device resistance is determined by the upper, heavily doped, epitaxially grown layer. Microfluidic channels (top and bottom) are fabricated separately from the device, and then the three components are bonded together to form a sandwich structure. Two vias have been etched through the silicon wafer to complete the flow channel.

While the devices themselves are very small (submicron width and 2 μm-25 μm in length), the density of devices is currently limited by engineering considerations for making simple contacts to the outside world. We currently use a pogo pin assembly with 32 contacts on a 1.1 cm *x* 1.1 cm die (the pads for connection to the off-chip electronics covering roughly half of the chip). This density could easily be increased with engineering refinements. The density of the microfluidic channels is also a consideration for miniaturization constraints. Again, it is not the channels themselves, which are small (typically ~50μm), but the "plumbing" connections to the outside world required both to insert fluid into and out of the channels and to control the valves which take up the most real estate. We currently have 40 microfluidic connections on the above die.

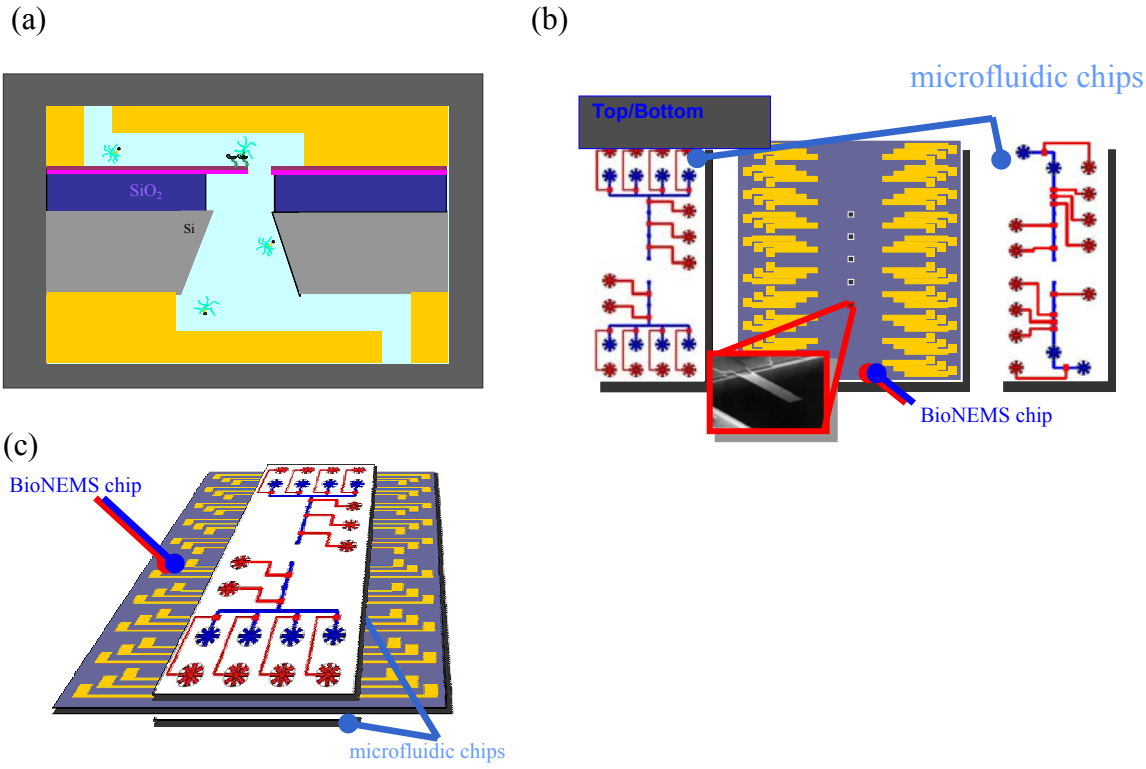


**Fig. 3.1.A Device assembly**

a) Schematic of device showing flow channel through the device, b) chip assembly, c) schematic of assembled microfluidic/BioNEMS chip, and d) chip assembled with microfluidics.

Fabrication begins with a silicon on insulator [SOI] wafer which will form the central layer of the sandwich structure. Silicon on insulator wafers are a commercial 3 layer product comprised of: a lower silicon layer (referred to as the handle wafer for bonded SOI), a central oxide layer (referred to as the "buried oxide"), and a top silicon layer (referred to as the transducer layer). There are two options for the purchase of these wafers; SIMOX material or "bonded" wafers. To create SIMOX wafers the manufacturer begins with a bulk silicon wafer, implants oxygen to form the oxide layer, and then anneals to restore the crystal quality of the top silicon transducer layer through which the implantation was done. To create bonded wafers one would hope to avoid the implantation process and ensuing residual damage through the use of bonded wafers; unfortunately the bonding process currently in industrial use has its own implantation process, albeit serving a different purpose. Soitec is one of the primary suppliers of silicon on insulator [SOI] with a thin (<340nm) transducer layer. Their fabrication begins with two silicon wafers. Thermal oxidation is performed on both wafers. Once bonded, the combined thickness of the oxide layer from each of the two wafers forms the buried oxide. However, in order to fabricate the desired thin transducer layer, the crystalline structure of the silicon wafer must first be weakened at the desired depth. This is done by the implantation of hydrogen through what will be the device and buried oxide layers. The wafers are then bonded together, and the top wafer is split along the pre-weakened plane. This means that once again the transducer layer has suffered an implantation process which will affect the crystal quality. Nevertheless, the residual damage from the hydrogen ions is expected to be much less than that for the thermal oxidation process.[1] The downside of the wafer bonding process is that the bonded wafers generally suffer

from a bowing affect which limits the minimum thickness that can be achieved, particularly for 4" wafers on which the bowed region is more noticeable. The data discussed below comes from a number of lots of silicon-on-insulator wafers. The first consisted of 4" bonded SOI from Soitec. Due to the aforementioned bowing difficulties Soitec ceased production of 4" thin (<200nm) bonded wafers, and the next two runs of material were SiMox ordered from Ibis Technology. More recently, we have returned to bonded material, but ordered 8" wafers and arranged for them to be cut down to two 4" wafers. The important parameters for each of these wafers are summarized in table Table 3.1.A. The wafers ordered from Ibis were subsequently thinned to 80nm by Protron Microtechnic, a German company. This was done through oxidation and a hydrofluoric acid wet etch. Many of the wafers used for metallic piezoresistive detection were thinned to 30nm using this technique (performed by Tronic's Microsystems, S.A.). Gold piezoresistive layers were preferred for the very thin devices due to difficulties with growing high quality epitaxial layers on the 30nm silicon. (Two layers of different conductivities are necessary for piezoresistive detection so that the region of the device under compressive stress and region under extension do not combine to give a null response.) For the silicon piezoresistive devices a 30nm heavily boron-doped ($4x10^{19}$ $/cm^3$), conducting silicon layer was grown epitaxially by Lawrence Semiconductor Research Laboratory, Inc.[2] after the transducer layer had been thinned.

**Table 3.1.A Properties of SOI material**

| Batch | Supplier | Transducer layer thickness | Oxide thickness | Transducer layer Resistivity |
|---|---|---|---|---|
| 1 | Soitec | 100nm | | |
| 2 | Ibis | 200nm thinned to 80nm | | 10-20Ωcm |
| 3 | Ibis | 225nm±4nm thinned to 80nm | 384nm±7nm | 10-40Ωcm |
| 4 | Soitec | 70nm [±3σ min: 62.5nm, max: 77.5nm] | 400nm [±3σ min: 392.5nm, max: 407.5nm] | 8.5-11.5 Ωcm |
| 5 | Soitec | 73.5nm [±6σ: ±9nm] | 400nm [±6σ : ±3nm] | 14-18.9 Ωcm |

The initial wafers were 500 μm thick. The channel through this wafer which in our current implementation is 75μmx75μm in cross section represents a large fraction of the total fluidic volume (the remaining microfluidics is only 50μmx10μm in cross Section). We thinned the wafers to 300μm to reduce this volume. This had an additional advantage of reducing the aspect ratio for the DRIE from 1:6.7 to 1:4. Following thinning, the silicon was polished to improve the adhesion of the microfluidics.

A through-wafer etch plays a central role in the cantilever fabrication process. Here we describe the motivation for using membrane-based device processing for this project. To begin, a suspended membrane it facilitiates the cantilever fabrication. (the full membrane-based fabrication procedure is described later in this chapter). A commonly employed alternative to membrane based fabrication for NEMS and MEMS devices is to use surface based micromachining. In the latter procedure the oxide under the device is removed from the top, undercutting the device and leaving a suspended structure. The silicon which was underneath the buried oxide (from the ~300μm thick handle wafer) remains. There are several advantages to the membrane technique. Many of the long, compliant cantilevers designed to achieve high force sensitivity for applications such as detection of Brownian fluctuations would not be possible if the underlying silicon substrate was not removed, as stiction would cause adhesion to the underlying substrate. Even for short, stiff cantilevers, the absence of an underlying silicon layer greatly increases their robustness to being immersed in fluid and dried. Indeed, membrane-based fabrication eliminates the need for critical point drying, except for the most compliant devices. It is also possible to pattern smaller structures on

suspended membranes thanks to reduced scattering during electron beam lithography. Finally, the channel through the membrane also serves as part of the fluidic architecture. For surface nanomachine devices, given the low Reynold's number flows involved in the application of these devices, the fluid "pool" at the cantilever can make it very difficult to ensure that the liquid in that region is adequately exchanged whenever a new fluid is introduced.

There are two standard techniques for through wafer backside etch in silicon. For our early prototypes we used a KOH wet etch. This does not require any expensive equipment and can be done in house. Unfortunately there are several drawbacks. This process involves a six hour etch in concentrated KOH at 80°C. These are not ideal conditions for survival of typical maksing layers employed in the fabrication process, and indeed the only mask we have found to tolerate this etch is silicon nitride grown by LPCVD. However, there were a number of drawbacks to the use of LPCVD-grown silicon nitride as a mask. In order to remove the nitride it is necessary that it be grown with an enhancement of silicon, reducing the stress. However, if the ratio of silicon to nitride is too great, it does not hold up well as a mask. Unfortunately, the material we receive has been highly variable. One of the batches of material we received failed to survive the KOH etch, while on other occasions the nitride was extremely difficult to remove and the silicon was damaged in the process (bearing in mind the thin epitaxially grown doped layer of 30nm). The time for removing the same thickness of nitride ranged from 11min to over half an hour, where in the latter case there were obvious color variations in the silicon showing that it had been etched in some places while pockets of

nitride remained. This led to devices curling due to the stress of the nitride at the end of processing if we were unfortunate enough to have it on our active devices. Another disadvantage of using LPCVD nitride is the high temperatures involved in the deposition. This deposition is typically done at 810°C or greater, at which temperature diffusion of the boron becomes a concern. (See section 3.2.) Alternative masks were investigated, including nitride deposited by PECVD (this can be done at a much lower temperature: ~400°C), several metals including gold (with several different adhesion layers) and palladium; and silicon dioxide. None of these were successful as a mask for such a long etch. The damage to the silicon epitaxial layer during nitride mask removal is believed to be responsible for an observed degredation in piezoresistive gauge factor (by a factor of ~20). Later material fabricated by DRIE attained the expected gauge factor for silicon. Finally, whereas DRIE results in vertical side walls, the KOH etch terminates on planes at ~55°, hence it is possible to achieve the same size membrane with a much smaller volume using the DRIE etch.

Therefore, while our early devices were made using KOH etches, all subsequent etches were done by Deep Reactive Ion Etching [DRIE]. Three suppliers were used for the DRIE processing (on different samples): the Jet Propulsion Laboratory [JPL], PHSMEMS, SA, and Tronics, SA. The Bosch DRIE process is comprised of two alternating processes, namely the deposition of a passivating layer (typically $C_4F_8$) and exposure to an etching plasma. Care was required to ensure no passivation remained at the bottom of the trench (which would interfere with oxide removal, Fig. 3.1.B). This

was an issue for early material but was overcome in latter runs, leading to a great improvement in yield.

Once it was determined that we would engage a foundry to carry out the DRIE etch we began to investigate having the frontside photolithography performed there as well. This had several advantages. It was mentioned earlier that, in spite of the small size of individual devices, the individual die must have a minimum size on the order of

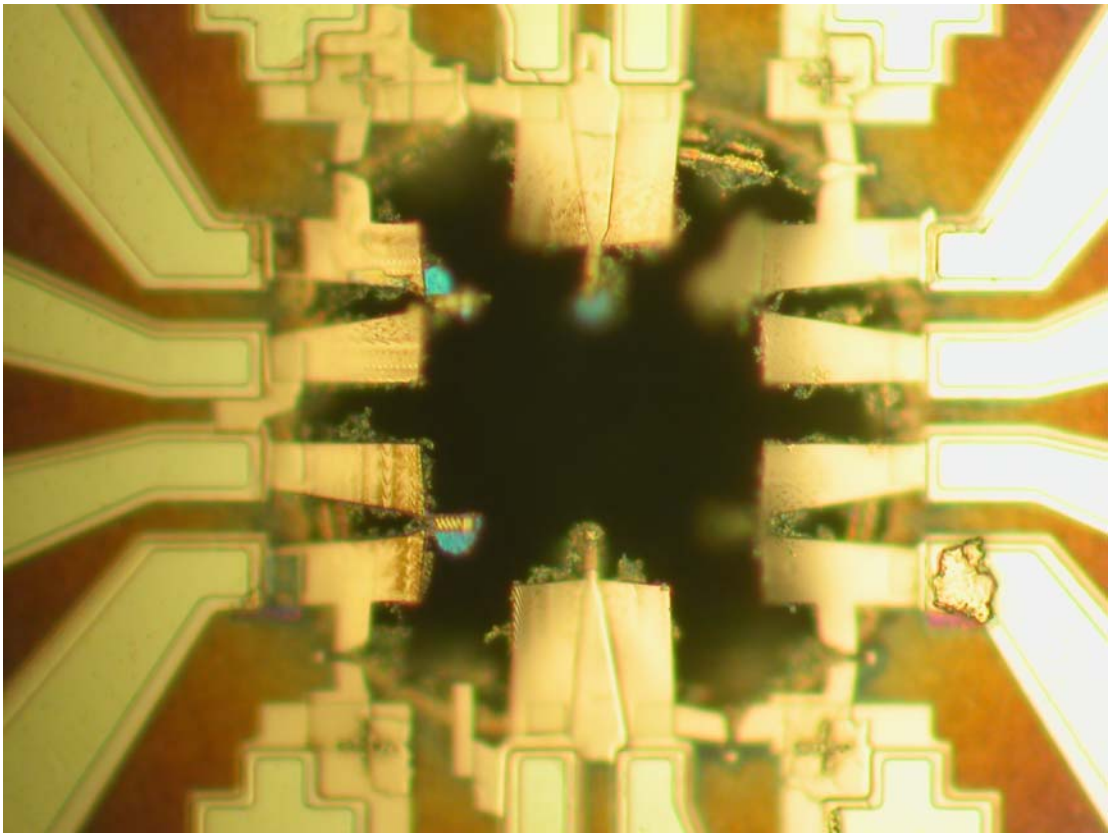

**Fig. 3.1.B Sample device showing residue remaining after DRIE**

In some of the early DRIE runs, residue from the DRIE process remaining on the lower side of the membrane was a major issue. This was overcome by the use of a post-DRIE KOH etch by PHSMEMS. For later runs performed by Tronics, the KOH etch was not necessary due to better control on the DRIE etch.

$1cm^2$ in order to merge them with the microfluidics. Due to the size of feedthroughs on our equipment and the active area for our photomasker, this limited us to processing at most nine die at a time, which quickly became tedious. (Ideally we would like to process a full wafer of electrodes and then focus on individual die for the final steps of cantilever definition). Having the electrodes patterned and passivated by a foundry allowed us to focus on what we do best; namely the processing of submicron features.

For the original prototypes that were fabricated in-house, liftoff techniques were used for the electrode patterning. Aluminum was used for the ohmic contact to the doped silicon. Immediately before placing the sample in the thermal evaporator, it was dipped in a bath of 0.5%HF for sixty seconds to remove the native oxide. 80 nm of aluminum was evaporated at a rate of 0.8 nm /sec. The sample was then annhealed for 1 hour and 40 minutes at 430 $^{o}$C. Gold was then used to mask these pads for protection in the fluid. A number of devices fabricated by this procedure are shown in Fig. 3.1.C.

### 3.1.2 Complete Fabrication Procedure for Early Foundry Runs (PHSMEMS, SA)

Following receipt of the starting wafers, an oxide mask was deposited on the back side by PECVD; this would serve as an etch mask for the deep reactive ion etch (DRIE) later in the fabrication process flow. The temperature during this deposition process did not exceed 300°C to ensure stability of the dopant profiles. The next step in the processing performed by PHSMEMS was the deposition and patterning of gold electrodes on the front side of the wafer. This began with the deposition of 30nm of chrome followed by 60nm of gold on the top side of the wafer. A standard precleaning etch was not used to

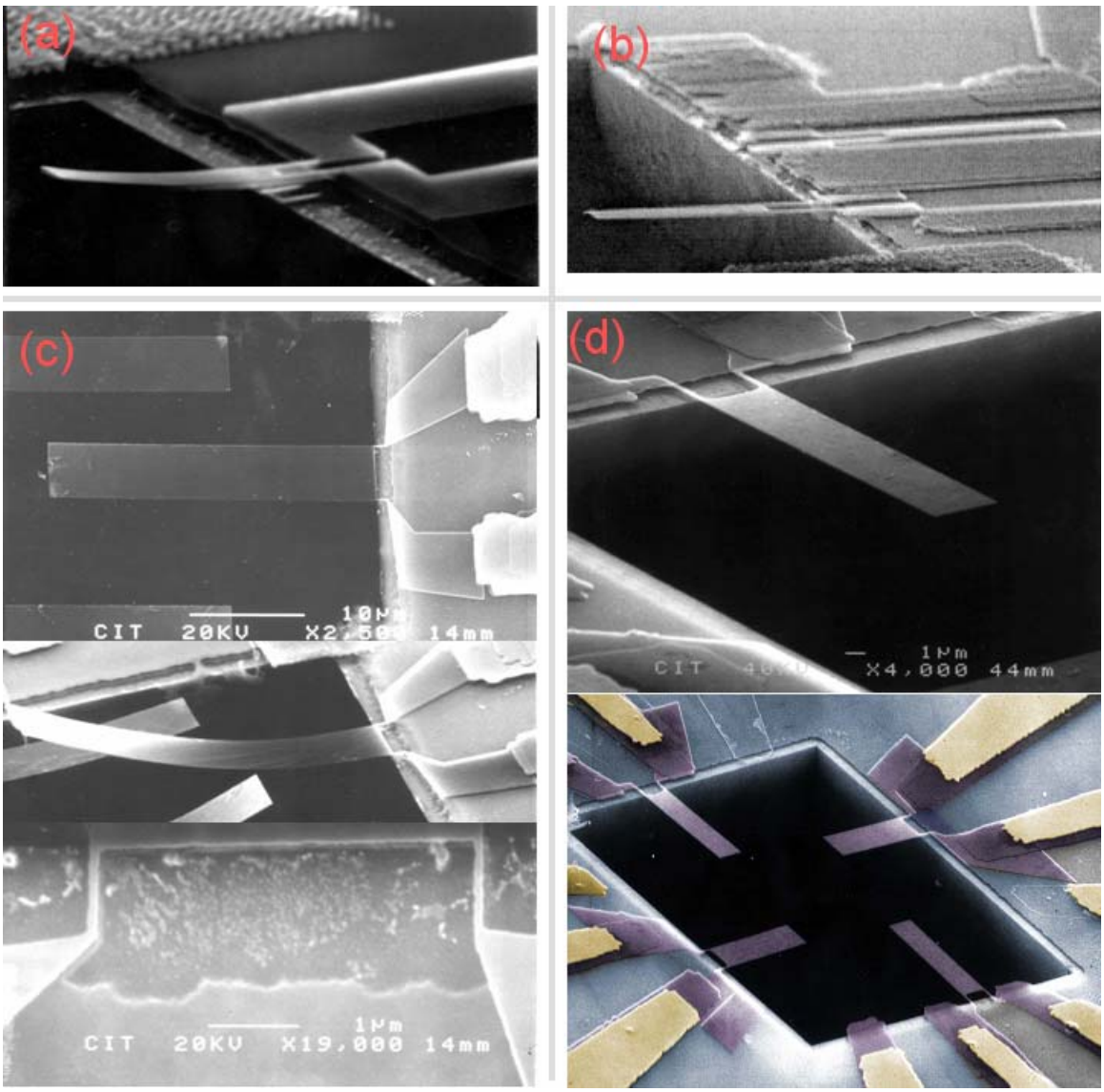


**Fig. 3.1.C Prototype devices fabricated at caltech**

These devices fabricated at Caltech using the process described in section 3.1.1. The thickness of all devices is 130nm. The remaining device dimensions are (a) $\ell$=15 µm, $w$=2.5 µm, $\ell_{leg}$=4 µm, $w_{leg}$=0.6 µm; (b) $\ell$=15 µm, $w$=2.5 µm, $\ell_{leg}$=4 µm, $w_{leg}$=0.25 µm; (c) $\ell$=35 µm, $w$=5 µm, $\ell_{leg}$=1 µm, $w_{leg}$=0.1 µm; and (d) $\ell$=25 µm, $w$=5 µm, $\ell_{leg}$=2 µm, $w_{leg}$=0.225 µm.

avoid the risk of damage to the thin epi layer. The electrodes were then defined by photolithography and patterned using a wet etch for both the gold and the chrome. 500nm of silicon dioxide was then deposited by plasma enhanced chemical vapor deposition (PECVD). Again, the temperature during the deposition process did not exceed 300°C. The passivation was patterned photolithographically and etched via a wet etch in buffered oxide etchant (BOE). Next, 30nm of chromium was deposited over the passivation, patterned via photolithography, and defined by a wet etch. The chrome served two purposes. The first was to provide a step over the thick passivation layer to allow for smooth coverage over the thick electrodes during the patterning of the cantilever devices (for which a thin PMMA resist is used). The chrome also served to protect the passivation during the same cantilever patterning. Wet etching was used during all processing to avoid damaging the now exposed silicon epi layer.

This completed the front side electrode patterning and passivation. The back side was then cleaned and the back oxide patterned (by masking and dry etching). A DRIE was performed up to the buried oxide, which was then removed with a wet etch. Finally, the wafer was diced and placed on blue tape for shipment to Caltech. This process flow is summarized in Table 3.1.A. A typical wafer is shown in Fig. 3.1.D.

### 3.1.3 Improved Fabrication Procedure for Foundry Runs (Tronics, SA)

The foundry processing was later transferred to Tronics, SA, and a number of improvements were made to the fabrication procedure. The final process flow is summarized in Table 3.1.A. Improved control during DRIE eliminated the need for the post-DRIE KOH process. Based on evidence of damage to the silicon during the

**Table 3.1.A Early BioNEMS Process Flow for Foundry Runs (PHSMEMS, SA)**

| PROCESS STEP DESCRIPTION | Units | Specs | Tolerance | Comments |
|---|---|---|---|---|
| **Wafer SOI preparation** | | | | |
| Cutting wafers to desired size and rounding of edges | mm | 100 | | Due to difficulty purchasing wafers of the desired specs in 4", 8" wafers are sized down |
| Wafer Back-grinding to + polishing | μm | 300 | | |
| **Process specifications** | | | | |
| PECVD oxide deposition on back side | μm | 3 | | This oxide serves as a mask during DRIE; T<300°C. |
| Electrode Cr and Au | nm | 30 (Cr) 60 (Au) | | No dry (plasma) cleaning etch before deposition. Wet etching to pattern. Minimum feature size: 7.5μm, minimum space between features: 9μm. Must provide ohmic contact to silicon with resistance between adjacent bond pads <200Ω. |
| $SiO_2$ deposition passivation by PECVD | nm | 500 | | T <300 °C |
| Wet etching of the passivation | | | | Minimum feature size : 11.5μm, minimum space between features : 5μm. Overlap with gold electrodes: 2μm. |
| Deposition of chromium | nm | 30 | | Wet etching to pattern. Minimum feature size: 13.5μm, minimum space between features: 3μm. |
| Patterning of alignment marks on back side of wafer - Front to back alignment | +/-μm | 3 | | Aligned to top side alignment marks. |
| Patterning and RIE etching of oxide on back side of wafer | | | | Timing requires tight control since over etch/ undercut leads to deformation of the shape of the trenches exaggerated during DRIE. Can be implemented through the use of a post RIE etch BOE rinse to ensure no residue without overetching. |
| DRIE etching squares trenches | μm | 75 | +/- 5 μm | Measured as the dimension of the top side membrane after the KOH etch). 300 μm deep through the back-side, uniformity across the wafer should be +/- 5 μm. |
| Resist protection spinning on the front side | | | | The membranes can not withstand vacuum suction;therefore this requires either using UV tape on the back side to avoid direct suction under the membranes or a special holder that would not place suction under the membranes. |
| KOH etch | | | | During development by PHSMEMS residual residue from |

| | | | | |
|---|---|---|---|---|
| | | | | the DRIE process was a problem; not allowing the DRIE to go to completion and finishing the final couple of microns with a KOH etch solved this problem. The top side must be protected in a mechanical holder during this step. |
| HCL rinse | | | | To remove residue left by the KOH etch). The top side must be protected in a mechanical holder during this step. |
| Removal of buried oxide at the bottom of the trenches | | | | The resist serves as a protection of the top side. This is a two sided protection, both from etching by the BOE and from breakage of the membrane, which is only 100nm by the end of the etch. (Supplemental protection with a mechanical holder has also been considered.) |
| Dicing | | | | Membranes are easily broken by flying particles during the dicing process and must therefore be protected. Care must be taken in applying the protection so that this process doesn't itself break the membranes. |
| Chip size x | mm | 11 | +/- 50 μm | |
| Chip size y | mm | 11 | +/- 50 μm | |
| Delivery of diced chips on blue tape | | | | |

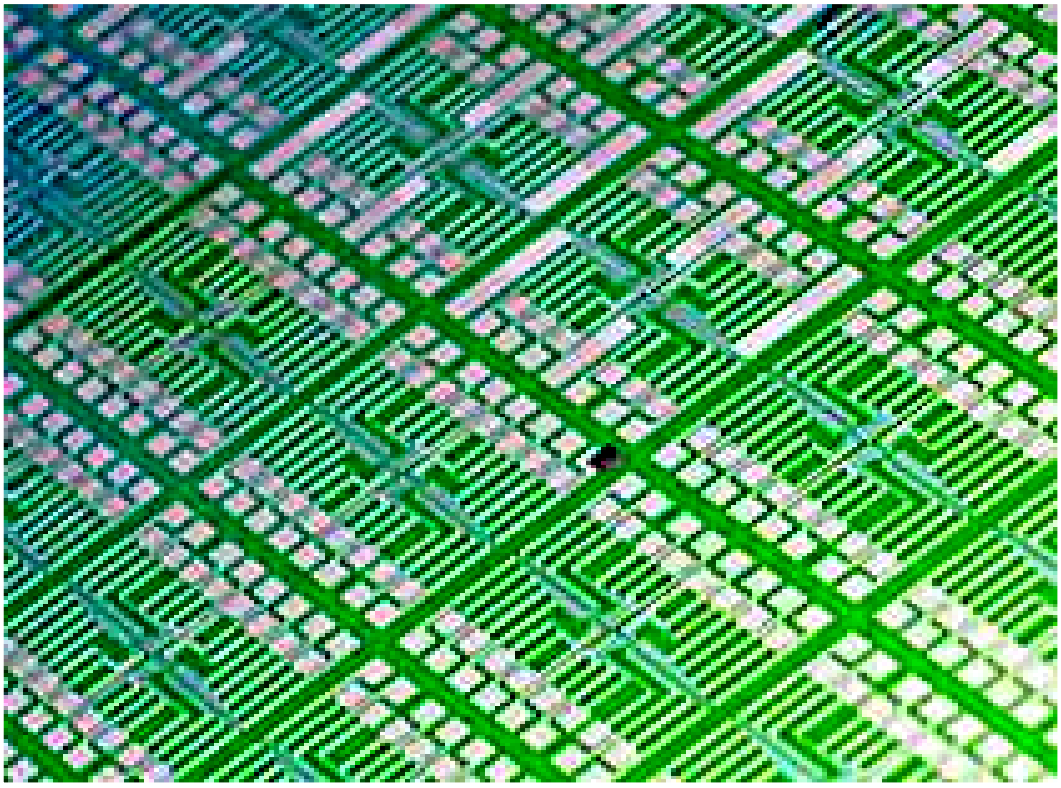

**Fig. 3.1.D Typical wafer after processing by PHSMEMS.**
Processing of the gold contact electrodes and DRIE etching of the through wafer vias was performed on 4” SOI wafers by the foundry.

deposition and patterning of the oxide passivation layer (intend to cover the gold electrodes), these steps were eliminated. The passivation was not found to be necessary for the experiments presented in this thesis. For applications in which it is necessary, it is recommended that post-processing passivation of the electrodes be performed using SU-8. The combination of eliminating this passivation and replacing nitric acid cleaning steps with acetone decreased the per square resistance of the material from ~2.7kΩ to ~1.1kΩ (the latter being equal to the preprocessing value measured directly after epitaxial growth). The reduction in the spread of devices resistances was even more noticeable; prior to these changes, it was not unusual to have two devices of identical dimensions on the same die where one had a resistance of 50kΩ and another a resistance of 500kΩ.

Since the processing adjustments, the standard deviation of resistance for devices of the same dimensions is ~9%. The electrodes deposited and patterned by Tronics for the silicon piezoresistive devices are comprised of a 5nm chrome adhesive layer followed by 60nm of gold. The contact resistance for this material is consistently less than 25Ω. This is negligible compared to the device resistance, which is typically greater than 10 *k*Ω. For the gold piezoresistive devices (for which typical resistance values are 200-800 Ω), the lead resistance was a concern. The thickness of the gold electrodes was therefore increased. For this material the electrodes were comprised of two layers of which the lower layer was 30nm tungsten and the upper layer was 400nm of gold. The tungsten layer served both as an adhesion layer and as an interface at the electrode tip. To accomplish the latter, the tungsten layer was patterned to extrude from under the gold at the tip of the electrodes (see Fig. 3.1.E). The gold patterned on the device to serve as the

**Table 3.1.A Final BioNEMS foundry process flow**

| | | | | |
|---|---|---|---|---|
| Cutting wafers to desired size of 4'' and rounding of edges | mm | 100 | | Caltech can not purchase wafers of the desired specs in 100mm, so 200mm wafers are resized to 2 100mm wafers. |
| Wafer back-grinding to 300 µm + polishing | µm | 300 | +/- 20 µm | Tronic's will take charge of finding a supplier to grind and polish the 4'' wafers |
| **Process specifications** | | | | |
| Electrode Cr and Au | nm | 5 (Cr)<br>60 (Au) | | No dry (plasma) cleaning etch before deposition. Wet etching to pattern. Minimum feature size: 7.5µm, minimum space between features: 16µm. Must provide ohmic contact to silicon with resistance between adjacent bond pads < 200 Ω. |
| Patterning of membranes on back side of wafer | | | | |
| DRIE etching squares trenches (membranes) | µm | 75 | +/- 5 µm | Timing requires tight control since over etch/ undercut leads to deformation of the shape of the trenches exaggerated during DRIE. |
| Resist removal | | | | Etching of the back side resist. |
| Dicing | | | | Membranes must be protected (at least for initial prototypes that do not include the glass slide). Care must be taken in applying the protection so that this process doesn't itself break the membranes. Once the glass slide is included, dicing should be a two step process and the glass is to be diced with a wider saw than the silicon. |
| Chip size x | mm | 11 | +/- 50 µm | |
| Chip size y | mm | 11 | +/- 50 µm | |
| Delivery of diced chips | | | | |

Top view

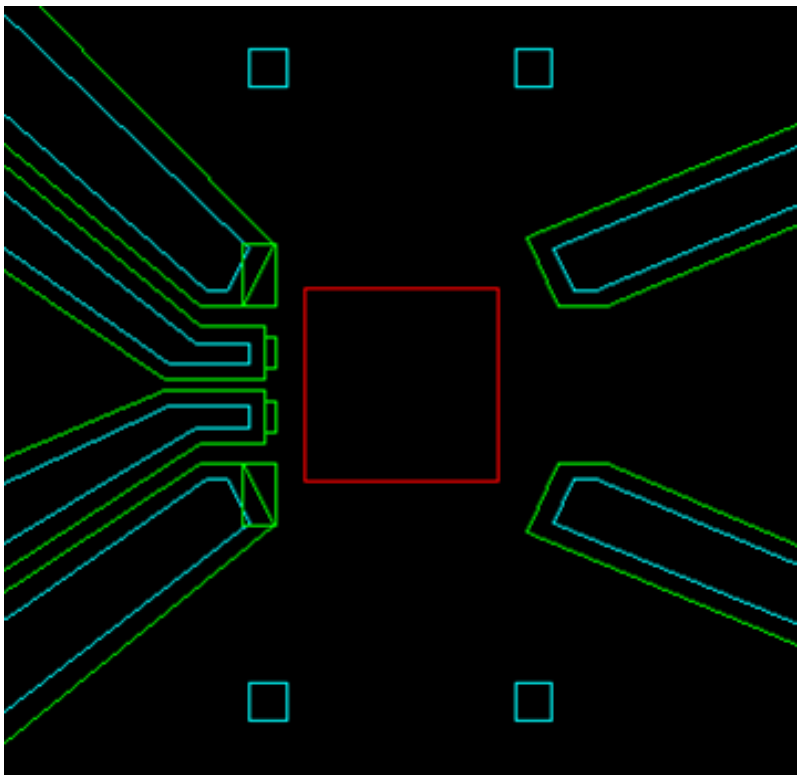

Side view


Green pattern: 30nm Tungsten (Deposited first)
Blue pattern: 400nm Gold (Deposited second)
Red pattern: silicon membrane

**Fig. 3.1.E Electrode patterning for gold piezoresistive devices**

The 30nm thick tungsten extruding from the electrode tip provides electrical continuity for patterning the device.

piezoresistive stress sensor is very thin (~20 nm) compared to the thick gold electrodes (400 nm). In the absence of the tungsten interface region there would be a high risk of mechanical breaks in the gold coverage at the interface region. This could be avoided by patterning the device first. However, since device patterning is performed on a die by die bases at Caltech, whereas the electrode patterning is performed on a wafer scale by the foundry, it is logistically preferable to pattern the electrodes first). The tungsten interface allows good electrically continuity to be attained.

### 3.1.4 Nanofabrication Processes Performed at Caltech

The fabrication process begins with the removal of the oxide layer from the bottom of the trenches. This process is non trivial since the aspect ratio of the trenches makes wetting difficult. It is possible to accomplish this as a wet etch using the following procedure; Ethanol (95% purity) was used to wet the sample. Cyclic heating (to 65°C) and cooling of the solution was used to drive the air out of the via and into the ethanol. The samples are immersed in a de-ionized water bath to displace the ethanol and then placed in undiluted BOE for 8 minutes to remove the buried oxide layer. It was determined that better control could be achieved using a hydrofluoric acid (HF) vapor etch. This is accomplished by placing the device in HF solution at a concentration of 17% for 6 minutes (the front side of the device was protected with photoresist). Without the use of the above heating/cooling technique, the air remaining in the trenches prevents the liquid etching solution from entering the vias. However, the HF vapor is able to enter the vias and etch the buried oxide via the following reaction pathway:

$$SiO_2 + 2H_2O \rightarrow Si(OH)_4$$

$$Si(OH)_4 + 4HF \rightarrow SiF_4 + 4H_2O.$$

The cantilever device is patterned by electron beam lithography and suspended by a vertical plasma etch in an electron cyclotron resonance (ECR) etch chamber. This etch is performed using the gases: argon, nitrogen trifluoride, and chlorine at flow rates 10 sccm, 5 sccm, and 13.5 sccm, respectively, and a total pressure of 30mTorr. A power of 300 Watts is used with a DC bias of -250V. Under these conditions 120nm silicon is etched in 35 sec. This recipe works well if 30nm aluminum is used as an etch mask. The aluminum mask is removed in a 1% potassium hydroxide solution. (This sample is immersed for 75 sec.) Finally, the completed device is allowed to air dry. However, certain devices, specficially those intended for the detection of Brownian fluctuations, were more fragile. Even with the use of critical point drying, the yield is very low with this procedure. For these devices, a polymethyl methacrylate (PMMA) mask is instead used to avoid the final wet etch. A mask thickness of 350nm is used for a silicon thickness of 110nm and a 30nm mask for a silicon thickness of 30nm. The PMMA mask will not withstand the ECR etch, so the μRIE is used instead. For the μRIE etch carbon tetrafluoride is used at a flow rate of 18sccm and a pressure of 100mTorr. A power of 140 Watts is used. Under these conditions 120nm silicon is etched in 105 sec. This pmma mask is etched in an oxygen plasma at a flow rate of 10sccm and a pressure of 90mTorr. A power of 140 Watts is used, and the etch time is 45 sec. (The fragility of these devices raises concerns about the applicability of these devices since they are intended for use in fluids. Fortunately, wetting these devices within the microfluidics can be achieved with moderate care. However, these devices are not robust enough to routinely survive drying.) Typical devices fabricated by this procedure are shown in Fig. 3.1.F.

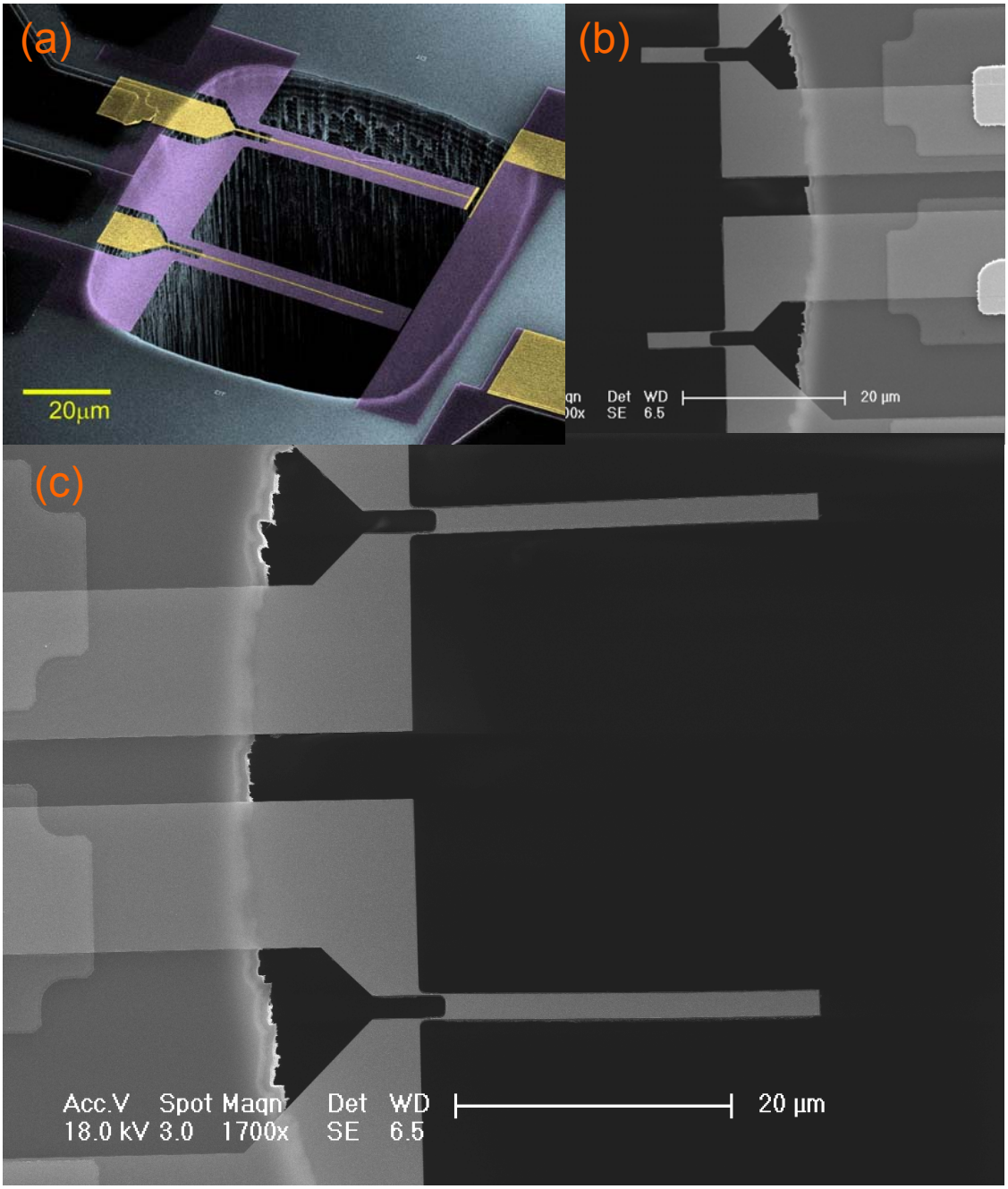


**Fig. 3.1.F Typical devices fabricated by the procedure outlined in section 3.1.5**
(a) A silicon piezoresistive device; t=130nm, $\ell$=55µm, $w$=7µm, $w_{leg}$=2µm, $\ell_{leg}$=5µm. (b) A gold (on silicon) piezoresistive device; $t_{si}$=30nm, $t_{Cr}$=3.5nm, $t_{Au}$=26.5nm, $\ell$=10µm, $w$=2µm, $w_{leg\ (Si)}$=200nm, $w_{leg\ (Au)}$=80nm $\ell_{leg}$=1.5µm . (c) Same as (b) except $\ell$=30µm.

### 3.1.5 Fabrication of the Microfluidics

The microfluidics are comprised of three parts: the bottom layer fabricated from PDMS which includes the inlet and outlet connections and all valves controlling the flow; the middle layer comprised of the DRIE channels fabricated through the silicon wafer during the device fabrication and through which the fluid flows; and the top layer fabricated from glass and SU-8 serving as a connective cannel between the inlet and outlet DRIE vias. The backside microfluidics are fabricated using two layers of PDMS (one flow layer and one control layer) as is standard in the microfluidic literature.[3,4] Channels are typically approximately 10 μm thick and 70 μm wide. The bonding of the PDMS to silicon is done through an 18 hour bake at 80°C. Both the PDMS and the silicon chip are pre-coated with ethanol to serve as a catalyst for this bonding process.

## *3.2 Temperature Constraints During Fabrication Due to Diffusion in Silicon*

Thermal diffusion is governed by the equation

$$D = \beta e^{-K/T}, \qquad 1$$

where D is the diffusion rate. For boron dopants in silicon, $K=3.57\text{x}10^4 K^{-1}$ and $\beta=0.0382$ $cm^2/s$. In half an hour this gives a diffusion of 0.11nm at 600°C, 0.89 nm at 700°C, and 8.4nm at 835°C. During processing the temperature does not rise above 450°C, and the time at such temperatures does not exceed half an hour, so we can rest assured that thermal diffusion is small compared to the 30nm thickness of the doped region.

## *3.3 Scaling of Piezoresistive Sensors*

In section 2.4 we showed the benefits of decreasing the cantilever thickness. Here we discuss ultimate limitations on the cantilever thickness and in the process show that the

dimensions used for cantilever 3 in Table 2.2.A are not unrealistic. The piezoresistors are designed to have a thin heavily doped silicon layer on top of nominally intrinsic silicon; as the devices are scaled to smaller dimensions, the effect of the depletion layer in the thin silicon layer becomes increasingly significant. Here we attempt to estimate quantitatively the size of this depletion layer.

### 3.3.1 Summary of the Calculation of the Doping Profile in Doped Silicon with Two Different Doping Levels

The carrier distribution was computed by iterating between two procedures until convergence was attained. The first calculated the bending of the valence band according to the equation

$$\frac{d^2 E_v}{dx^2} = \frac{e\rho(x)}{\varepsilon}, \qquad 2$$

where $E_v(x)$ is the valence band energy level, x is a one dimensional parametrization of the position in the sample with x=0 representing the top heavily doped surface and x=t representing the lower undoped surface, e is the carge of an electron, ε is the dielectric constant for silicon, and ρ(x) is the charge density given by $\rho(x) = p(x) - n(x) - N_A^-(x)$ where $p(x) = 1.04\text{x}10^{25} e^{-\beta(E_F - \varepsilon_V)} / \text{m}^3$ is the density of holes, $n(x) = 2.8\text{x}10^{25} e^{-\beta(E_C - E_F)} / \text{m}^3$ is the density of free electrons, and $N_A^-(x) = \#dopants / \left(0.5 e^{-\beta(E_A - (E_F - \varepsilon_V))}\right)$ is the density of charged donor atoms. Equation 2 was solved subject to the boundary condition:

$$\left.\frac{dE_v}{dx}\right|_{x=0} = \frac{e\sigma}{\varepsilon}, \qquad 3$$

where σ is the surface charge density. The density of surface states for equation 3 were estimated based on published values for interface state density at a silicon-silicon dioxide interface.[6]

The second procedure adjusted the Fermi level until charge neutrality was attained. This assures that at the lower surface the boundary condition

$$\left.\frac{dE_v}{dx}\right|_{x=t} = \frac{e\sigma}{\varepsilon} \qquad 4$$

is satisfied.

### 3.3.2 Summary of Conclusions

Fig. 3.3.A shows the calculated carrier distribution for a sample of 130nm thickness in which the dopant layer is 30nm thick and the dopant concentration is $4x10^{25}$ $m^{-3}$. The carrier distribution for a sample of 30nm thickness for which the thickness of the doped layer is 7nm is shown in Fig. 3.3.B. In both cases the carriers are well confined to the doped layer.

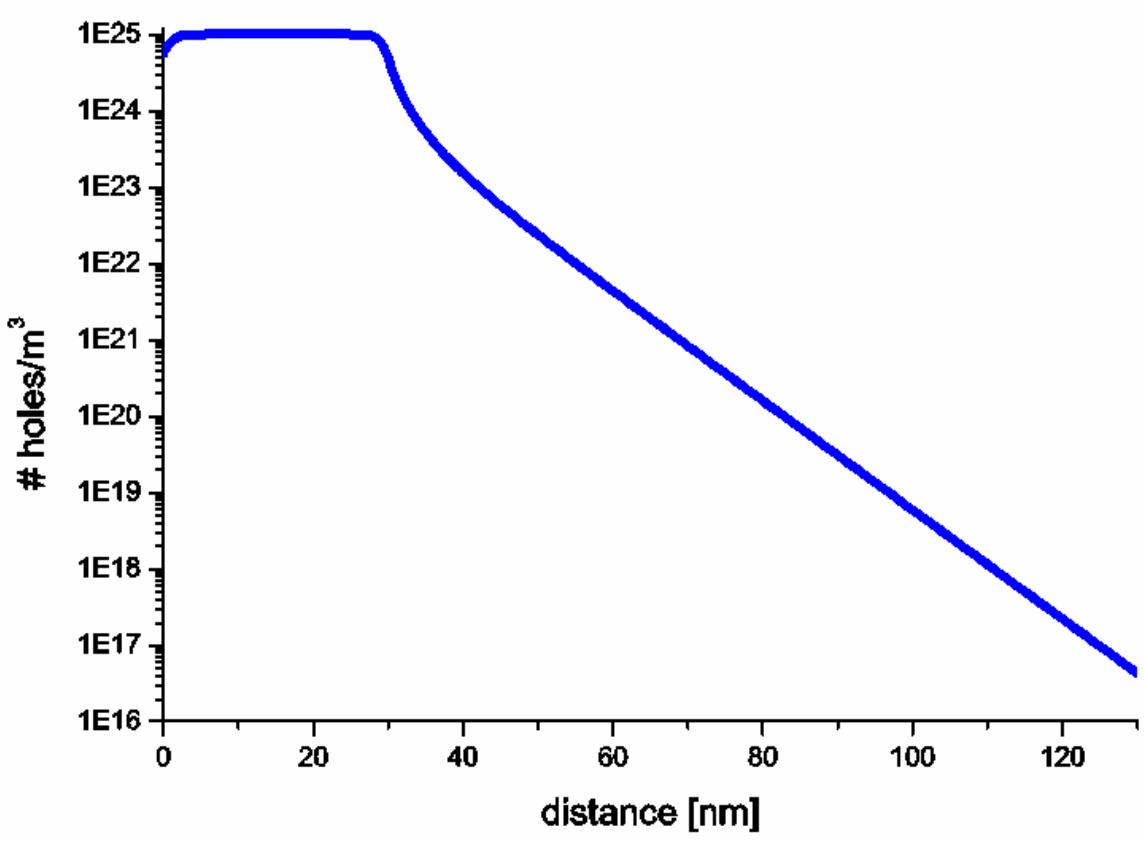


**Fig. 3.3.A Carrier distribution for a sample of 130 nm thickness**

The distribution of carriers is shown. For these calculations the dopant layer is 30nm thick, and the dopant concentration is $4x10^{25}$ $m^{-3}$. This corresponds to the material used throughout this thesis.

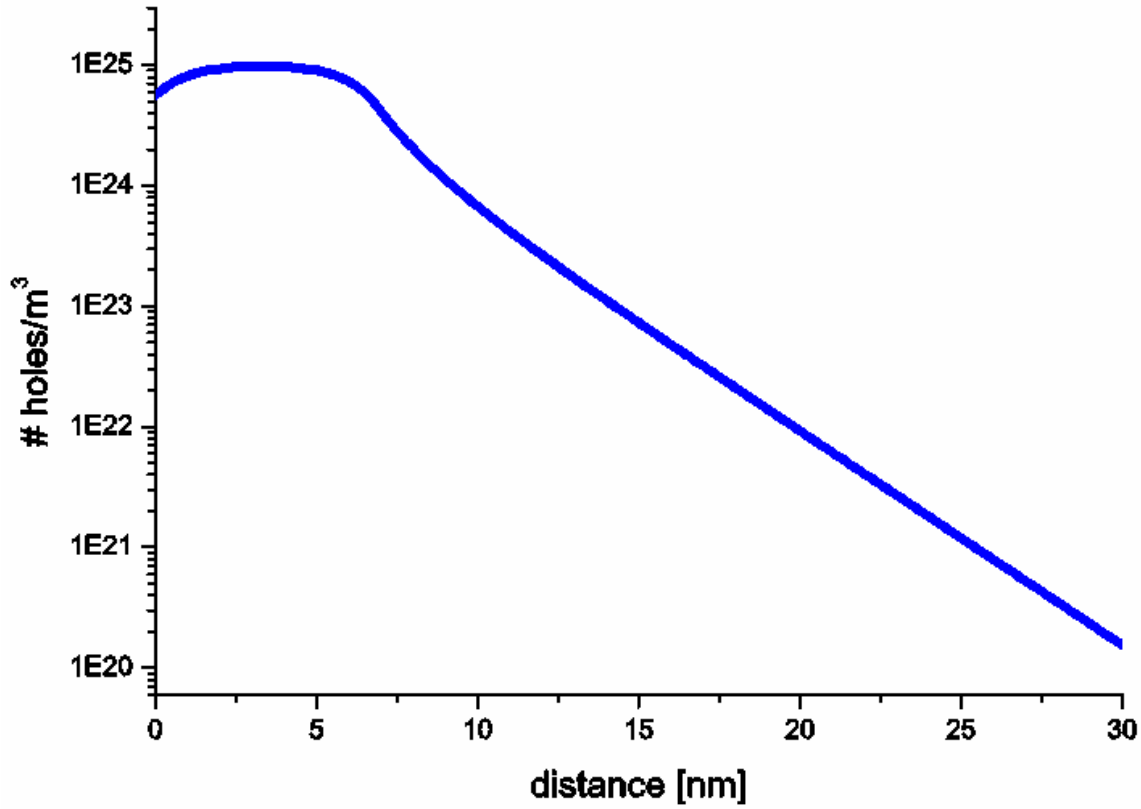


**Fig. 3.3.B Carrier distribution for a sample of 30 nm thickness**

For these calculations the dopant layer is 7nm thick, and the dopant concentration is $4x10^{25}$ $m^{-3}$. This corresponds to cantilever "3" in Table 2.2.A.

## 3.4 Use of Crystalline Silicon vs Polysilicon

The piezoresistive properties of polysilicon have been widely reported in the literature.[5] We chose to focus on crystalline silicon because the piezoresistive coefficient is approximately one order of magnitude higher[5] and the resistivity of crystalline silicon is approximately a factor of six larger at the doping concentration of interest.[5] The later is crucial for Brownian noise measurements where the background noise is limited by Johnson noise. Combining these two effects, the alternative use of polysilicon would reduce the signal to noise ratio by one and one half orders of magnitude. The only forseable benefit of using polysilicon would be the ability to deposit it directly on silicon dioxide which might be of interest if, for the alternative of epitaxially doped silicon grown on lightly doped silicon, conduction was not well confined to the doped layer either because of poor carrier confinement (addressed in the previous section and shown not to be a problem for the thicknesses of current interest) or because the relative conductivities of the two layers were too similar. For the material we use the resistivity of this lower layer which is 20 Ω cm giving a resistance per square of 2.5 *M*Ω. Compared to the 2.5 *k*Ω per square for the heavily doped epitaxially grown piezoresistive layer, conduction through the lightly doped layer is not significant.

## 3.5 References

[1] This process developed by SoiTec is described in detail at http://www.soitec.com/techno/t_2.htm and in literature they have available.

[2] Lawrence Semiconductor Research Laboratory, Inc., 2300 W. Huntington Dr., Tempe, AZ 85282

[3] Chou, H.-P., Spence, C., Scherer, A. and Quake, S., PNAS, **96**, pp. 11-13, 1999.

[4] Unger, M.A., Chou, H.-P., Thorsen, T., Scherer, A. and Quake, S., Science, pp. 113-116, 2000.

[5] Obermeier, E. and Kopysynski, P. Sensors and Actuators A, **30**, pp. 149-155, 1992.

[6] White, M. H. and J.R. Cricchi, IEEE Transactions on Electron Devices, **19**, p. 1280, 1972.

# 4 Device Characterization

## 4.1 Measurement of the Gauge Factor

An expression that relates the expected resistance change for a given displacement of the cantilever tip was calculated in the previous section. An atomic force microscope (AFM) tip, positioned at the distal end of the cantilever, was used to perform a calibrated deflection of the cantilever. This enabled a direct measurement of the displacement transduction responsivity, $\partial R_d / \partial x$. These measurements were used to assess damage to the material during processing. In particular it will be shown that the transduction factor was improved from a value that was initially a factor of 20 smaller than the expected value to one consistent with it. This improvement was achieved by taking special precautions during processing. Independent measurements of the gauge factor from the resonant thermomechanically-driven displacement fluctuations in vacuum were also performed; the results obtained were consistent and provided increased precision. The latter results, from thermomechanical noise measurements, will be presented in chapter 5.

We begin with the most recent results on devices prepared after improvements to reduce damage to the piezoresistive layer during processing. An SEM image of the device used for these experiments is shown in Fig. 4.1.A. Fabrication begins with a bonded SOI wafer. The transducer layer is composed of intrinsic silicon, 100nm in thickness. The buried oxide layer is 750nm thick. A 30nm silicon layer at a boron doping level of $4 \times 10^{19}$ /cm$^3$ is epitaxially grown on the top surface. Subsequently, 60 nm thick gold electrodes are deposited to form contact to the silicon epitaxial layer (with a 5 nm chromium adhesion layer). Following this, 75 μm *x* 75 μm trenches are etched via

DRIE through the wafer from the backside (stopping at the oxide layer) to form membranes from which the devices will be patterned. The wafers are previously thinned to 300 μm to reduce the aspect ratio for the DRIE process. The wafers are then diced into 11 mm *x* 11 mm die. The oxide layer is removed from the bottom of the trenches with BOE. The cantilever devices are then patterned by electron beam lithography and suspended by a vertical plasma etch ($NF_3$, $Cl_2$, Ar) in an electron cyclotron resonance (ECR) etch chamber. A 40nm aluminum mask is used to protect the devices during the etch.. The aluminum mask is then removed using potassium hydroxide at a concentration of 10%. Finally, the completed device is allowed to air dry.

The device dimensions are $\ell$=55 μm, $w$=7 μm, $w_{leg}$=2 μm, and $\ell_{leg}$=5 μm. For this cantilever, the current path is along the <110> direction for which $\pi_\ell \sim 4\text{x}10^{-10}$ $\text{Pa}^{-1}$.[1,2] The device resistance is measured to be 19.3 kΩ. The material has a resistance of 1 kΩ/square before processing and 1.7 kΩ/square after processing (measured on a comparable four terminal cantilever device), implying a combined contact and electrode resistance of 11 kΩ for our device.

The device is somewhat more complex than a simple cantilever; its spring constant can be estimated using the formula

$$K = \frac{Et^3}{\frac{4\ell^3}{w} + \left(2l_{leg}^3 - 6\ell\ell_{leg}^2 + 6\ell^2\ell_{leg}\right)\left(\frac{1}{w_{leg}} - \frac{2}{w}\right)}, \qquad 1$$

(see section 2.3.1) where for a three legged device, $w_{leg}=w_{wide\ leg}+w_{narrow\ leg}/2$. A Young's modulus E=110 GPa was interpolated from the data of Li et al who studied the Young's

modulus in thin silicon resonators.[4] From this formula a spring constant of 2.34 mN/m is estimated. The device has also been modeled using CFDRC[5] (a finite element numerical simulation package), yielding a spring constant of 2.46 mN/m. The gold patterned on the device (Fig. 4.1.A) is included in this simulation.

The piezoresistive response of the device is characterized using an AFM to displace the cantilever tip by a known amount. This measurement has been performed a number of times on each cantilever (with withdrawal of the AFM tip between measurements) and on a number of cantilevers fabricated to identical specifications. The expected piezoresistive transduction factor, discussed in section 2.3.4, is

$$\frac{\partial R_d}{\partial x} = \frac{3\beta\pi_\ell}{2w_{leg}t^2}\left(2\ell - \ell_{leg}\right)KR_d, \qquad 2$$

where $R_d$ is the resistance of the stressed portion of the device (the cantilever legs) and $\beta$ is a parameter first introduced by Harley and Kenny to account for the finite thickness of the piezoresistive layer. For their devices they deduced $\beta \sim 0.7$; we also use this value for our devices, which are geometrically similar.[6] $R_d$ was estimated from the device geometry and the measured resistance per square for the material. For the latter, the pre-processing value was used since modest damage to the thin silicon sensor layer is not expected to increase the piezoresistive response. A comparison between the measured results shown in Fig. 4.1.B and what is expected from equation 2 gives a measure of the dimensionless gauge factor $G = E\pi_\ell$, where E is the Young's modulus and $\pi_\ell$ is the longitudingal piezoresistive coefficient. For our cantilevers we obtain a value ranging from 45-75 for the devices measured. The expected value is 44. [1,2] The large uncertainty in the measured value arises from several factors. The first is that the AFM cantilever is

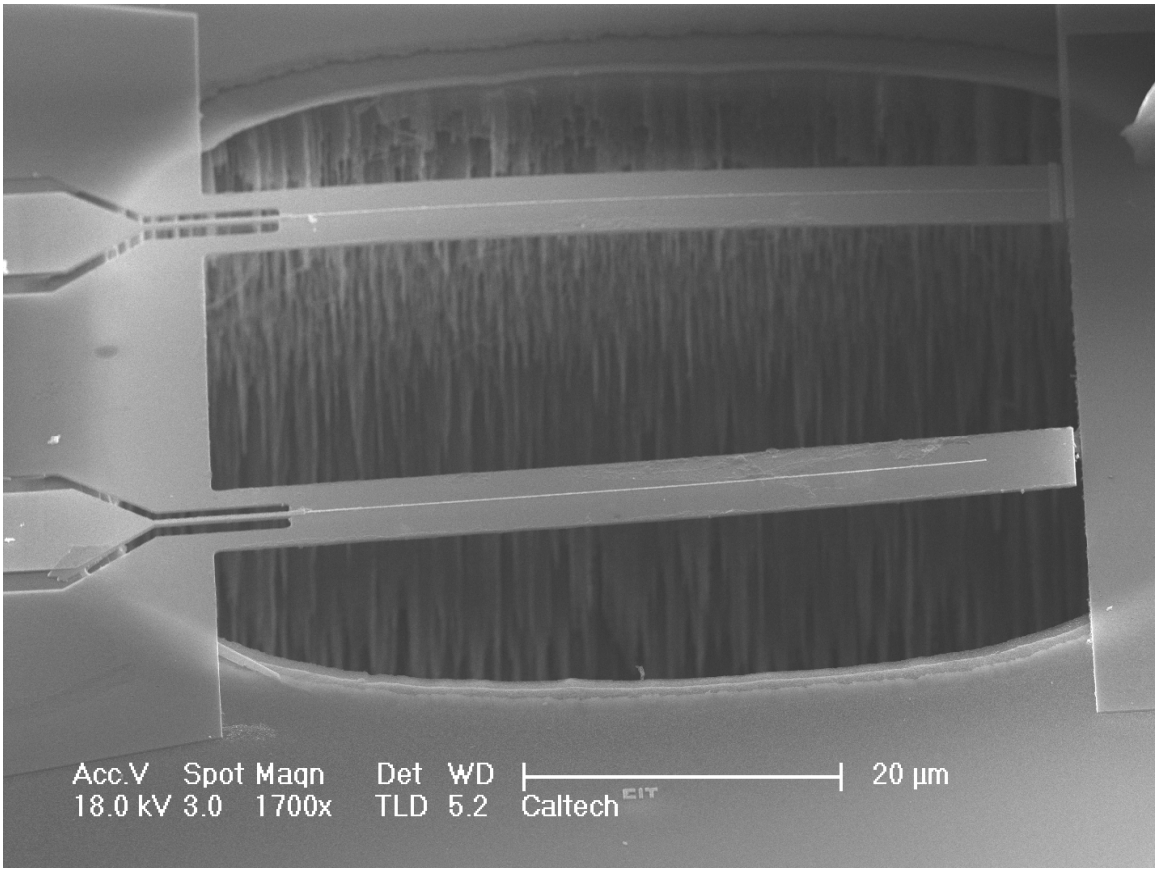


**Fig. 4.1.A SEM image of device used for probing the gauge factor**

The device dimensions are $\ell$ = 55 µm, $w$ = 7 µm, $w_{leg}$ = 2 µm, and $\ell_{leg}$ = 5 µm. The cantilever thickness is $t$ = 130 $n$m, of which the top 30nm forms the conducting layer (with a boron doping density of $4\text{x}10^{19}/\text{cm}^3$). From this top layer the transducer and its leads are patterned. For this cantilever, the current path is along the <110> direction for which $\pi_\ell \sim 4\text{x}10^{-10}$ $\text{Pa}^{-1}$. [1,2] The current path is along the two outer silicon legs. The central gold line down the center of the device is for biosensing applications.[3]

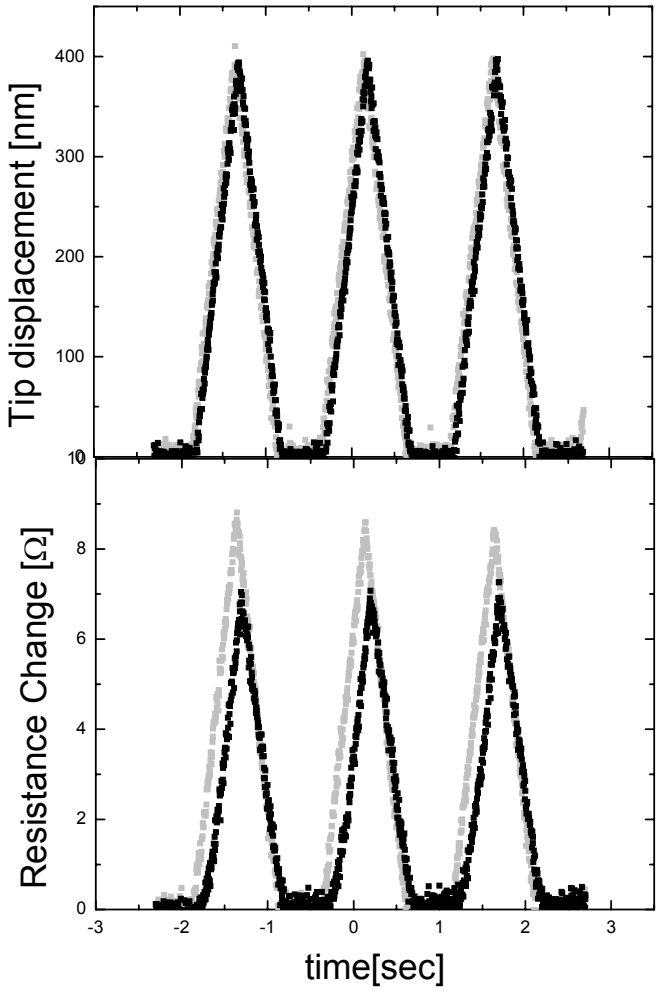


**Fig. 4.1.B Characterization of device displacement-resistance change transduction**

An AFM tip was used to displace the cantilever tip by a controlled amount. The separate traces correspond to repeat measurements on the same device; the afm tip was withdrawn from the sample between measurements to test reproducibility.

much larger than the device, making it difficult to position the AFM tip directly at the cantilever tip. The AFM cantilever has a much greater spring constant than the device (10 N/m versus 2 mN/m). This simplifies the analysis since there is no significant deflection of the cantilever tip but leads to the second difficulty – it becomes difficult to find a neutral starting position for the cantilever deflection experiment. The device cantilever will remain in contact with the AFM cantilever, into its nonlinear response regime as the AFM cantilever is withdrawn. Both of these sources of error tend to yield a larger measured gauge factor, in the former case because the actual tip displacement is greater than that used in the calculation and in the latter because the stiffness (spring constant) of a device is increased under strain. In these experiments the position of the AFM cantilever was fairly well established (to within a few microns of the device cantilever tip) by performing multiple measurements along the device until the AFM cantilever lost contact with the device. To minimize the error from prestraining the device, multiple measurements were performed with varying ramp size and starting displacement. Nevertheless, this source of error is believed to be the primary source of both the spread in measured values and the increase in the mean value from the expected value.

In early runs, only moderate care was taken to protect the thin silicon epitaxial layer during processing. Here we present data from two batches of material, the first fabricated on a DRIE-etched membrane received from PHSMEMS, S.A., and the second on a KOH-etched membrane fabricated at Caltech. In the former case, an observed increase in resistance of ~25% arose in conjunction with the deposition and patterning of

an oxide passivation layer placed over the electrodes to isolate them from the solution during measurements. These steps apparently damaged the doped conducting layer. The processing steps for passivation were subsequently eliminated once they were identified as a significant source of the problems. In the case of the KOH patterned material, protecting the front side during the 6 hour KOH etch proved difficult to achieve. A low stress silicon nitride layer served as a protective mask; unfortunately its removal required a sulfuric acid at a temperature of 160°C. Visible discoloration of the silicon following this step was a clear indication of damage.

The first of these two devices of dimensions $\ell$ = 40 μm, $w$ = 10 μm, $\ell_{leg}$= 5 μm, $w_{leg}$ = 2 μm, and $t$ = 110 nm was fabricated from material delivered by PHSMEMS (W502). The doped layer for this material was 30 nm thick with a boron doping level of $4x10^{19}$ $cm^{-3}$ (measured by SIMS analysis on a test wafer), epitaxially grown by Lawrence Semiconductor. In section 2.3.1, the spring constant for a device of these dimensions was calculated both analytically and numerically to be 3.6 mN/m. A device resistance of 86 kΩ was measured. A resistance change of 50.3Ω was observed for a tip displacement of 2.047 μm using the AFM [Fig. 4.1.C]. From equation 23 in section 2.3.4 we deduce a piezoresistive coefficient of $2.4x10^{-11}$ $m^2/N$ from these measurements. In the calculations we assume a Young's modulus of 105 GPa (a value interpolated from the data of Li *et al.,* who studied the Young's modulus in thin silicon resonators).[4] For the purpose of comparing piezoresistive properties between different materials, the dimensionless gauge factor defined as $\frac{\Delta\rho}{\rho\varepsilon} = E\pi_\ell$ is useful. For the above results the value is 2.1, significantly smaller than the expected value of 44. [1,2]

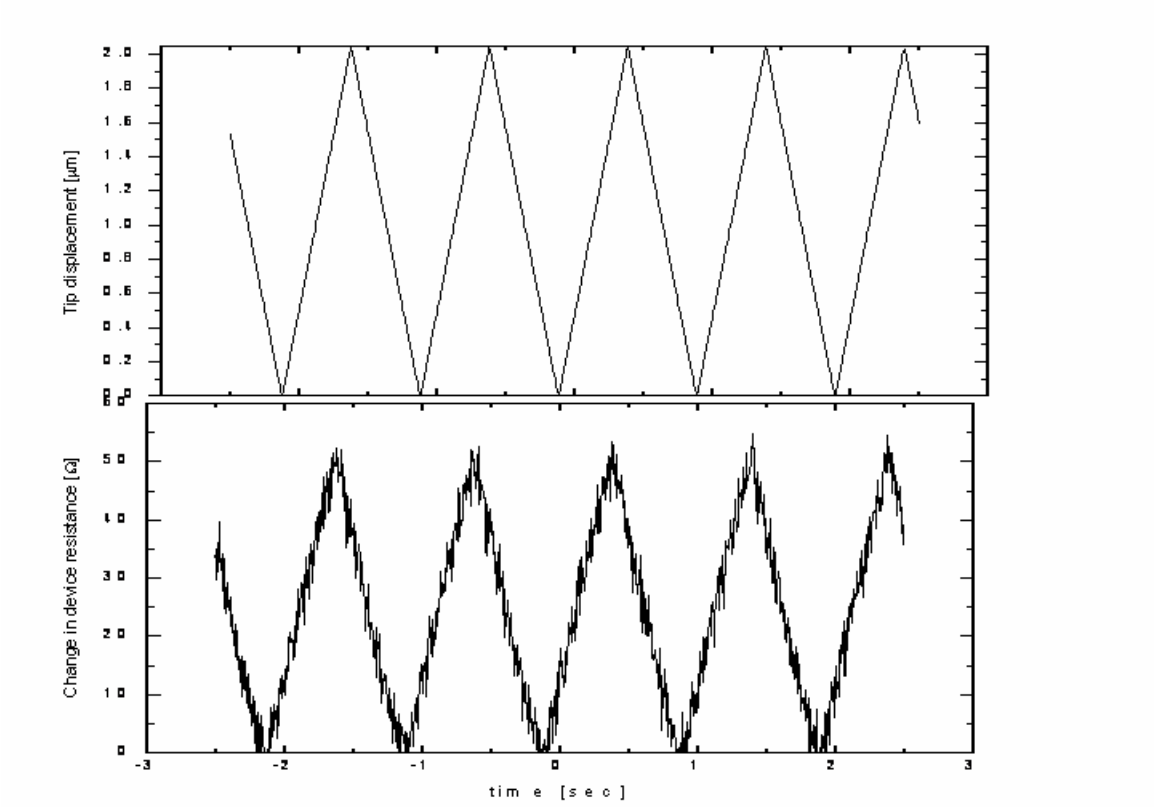


**Fig. 4.1.C Measurement of the gauge factor – DRIE etched membrane**

Change in device resistance for direct probing of the cantilever motion using an AFM. A positive tip displacement corresponds to pushing the tip downwards. These measurements were performed on a cantilever fabricated from a DRIE etched membrane purchased from PHSMEMS. The cantilever dimensions are provided in the text. A positive tip displacement corresponds to a downward motion of the cantilever tip from the neutral position.

The second device of dimensions $\ell$ =15 μm, $w$ = 2 μm, $\ell_{leg}$ = 4 μm, $w_{leg}$ = 0.5 μm, and $t$ = 125 nm was fabricated on a membrane defined by a KOH etch. From equation 15 (section 2.3.1), the spring constant for a device of these dimensions is 27 mN/m. The measured resistance of this device was 15.6 kΩ. For this device the resistance change per unit displacement under the AFM was observed to be $3x10^{7}$Ω/m [Fig. 4.1.D]. A Young's modulus of 110 *G*Pa was assumed for this device,[4] yielding a piezoresistive coefficient of $2.7x10^{-11}$ $m^2$/N. Here, the dimensionless gauge factor deduced is 3.0. The low gauge factor attained for both of these early batches of material motivated changes to the process flow, after which we were able to obtain values consistent with expectations as mentioned earlier.

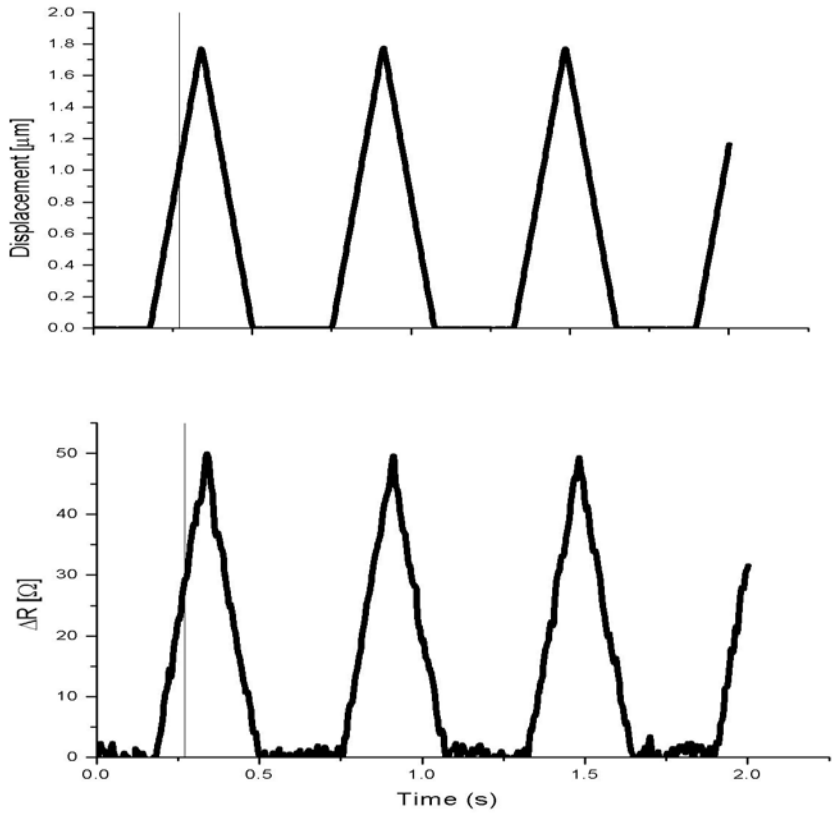


**Fig. 4.1.D Measurement of the gauge factor – KOH etched membrane**

Cantilever resistance as a function of displacement, studied using an atomic force microscope tip to move the cantilever a known amount (center trace). The measurements shown here are for the device fabricated from a KOH etched membrane (the dimensions are provided in the text). This yields a direct measurement of $\frac{\partial R_{dev}}{\partial x} = 3\text{x}10^7$ Ω/m. A positive displacement corresponds to a downward motion of the cantilever tip from the neutral position.

## 4.2 Characterization of the Experimental Setup

Measurements were performed with the device mounted in a sample holder with miniature pogo pins used to obtain electrical contact to the device (Fig. 4.2.A). The high impedance (typically ~20 kΩ for the devices discussed in this thesis) of silicon piezoresistive sensors necessitates that particular care be put into the readout circuit. In particular, to minimize pick-up and capactive shunting of the signal it is necessary that the preamplifier be placed as close as possible to the device under consideration. In a practical large scale implementation of these techniques this would presumably be done by a technique such as flip-chip bonding of an integrated amplifier chip. In theory, since these devices are made from silicon it would be possible to integrate the amplifier on-chip. However, in practice, considering the number of fabrication steps involved and incompatibilities in processing between the amplifier and the NEMS structure, it would seem preferable to fabricate them separately at least until necessity precipitates the development of fabrication techniques to integrate the two. In the absence of such capabilities a custom preamp was assembled which is placed a few inches from the sample. This custom preamplifier was used for many of the silicon piezoresistive devices and is characterized below. The lower impedance of the gold piezoresistive devices (typically ~600 Ω for the devices discussed in this thesis) permitted the use of a commercial preamplifier. For these devices a Stanford SR552 preamplifier was used. The SR552 preamplifier has a bipolar junction transistor input and a noise floor of 1.4 nV/$\sqrt{\text{Hz}}$.

### 4.2.1 Characterization of the readout amplifier

The need for a high impendence input, coupled with the desire to be able to operate over the range from a few kHz to a couple of MHz ( a regime over which MOSFET's have high 1/*f* noise) led to the choice of a JFET op-amp for the amplifier front end. To minimize the effects of pick-up (through common mode rejection), differential amplification was used. To optimize both the level of common mode rejection and drifts with temperature, a dual JFET chip was used for this differential amplifier. The AD8620 was chosen because it is one of the lowest noise, widest bandwidth dual JFETs on the market.

Parts for the remainder of the amplifier where chosen so that the noise would remain limited by the front end and the bandwidth would not be compromised. The schematic for the amplifier is shown in Fig. 4.2.B. Fig. 4.2.C shows the gain curve for this amplifer. For measurements on the devices of interest here a bandwidth of 1 MHz is sufficient. For measurements requiring a higher bandwidth, a flat bandwidth out to 3 MHz could be achieved through a reduction of gain. The noise spectrum for the preamplifier is shown in Fig. 4.2.D.

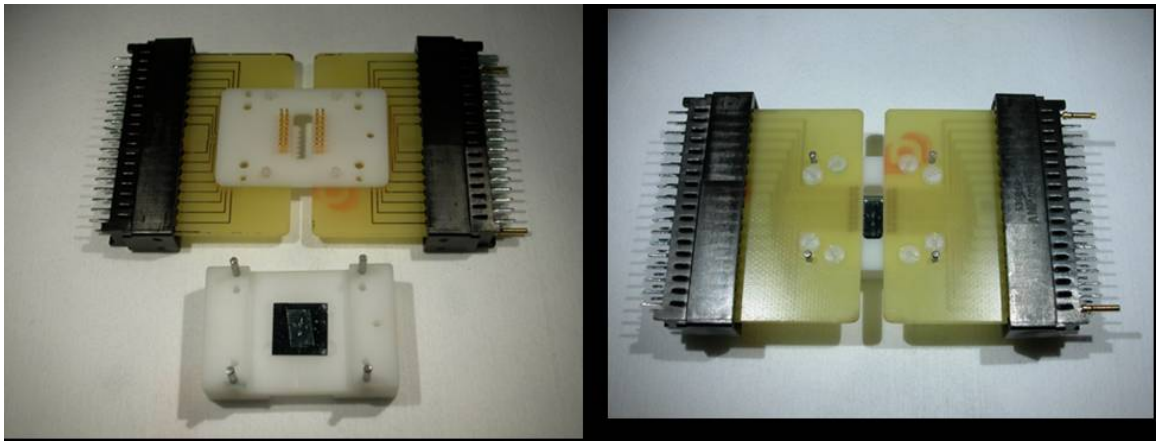

**Fig. 4.2.A Sample holder assembly**

A pogo pin assembly was used to allow easy connection to the device electrodes.

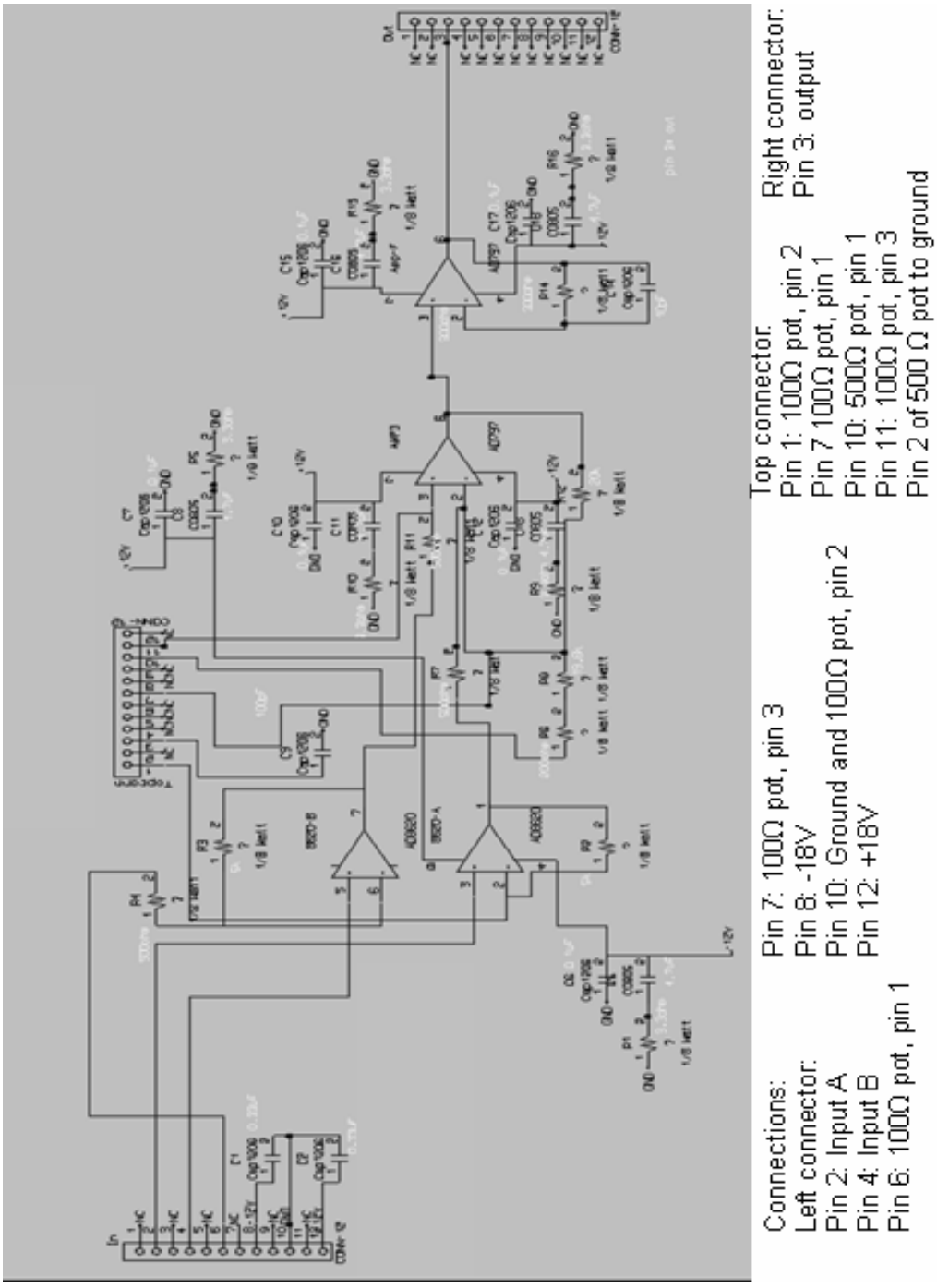


**Fig. 4.2.B Schematic for custom preamplifier.**

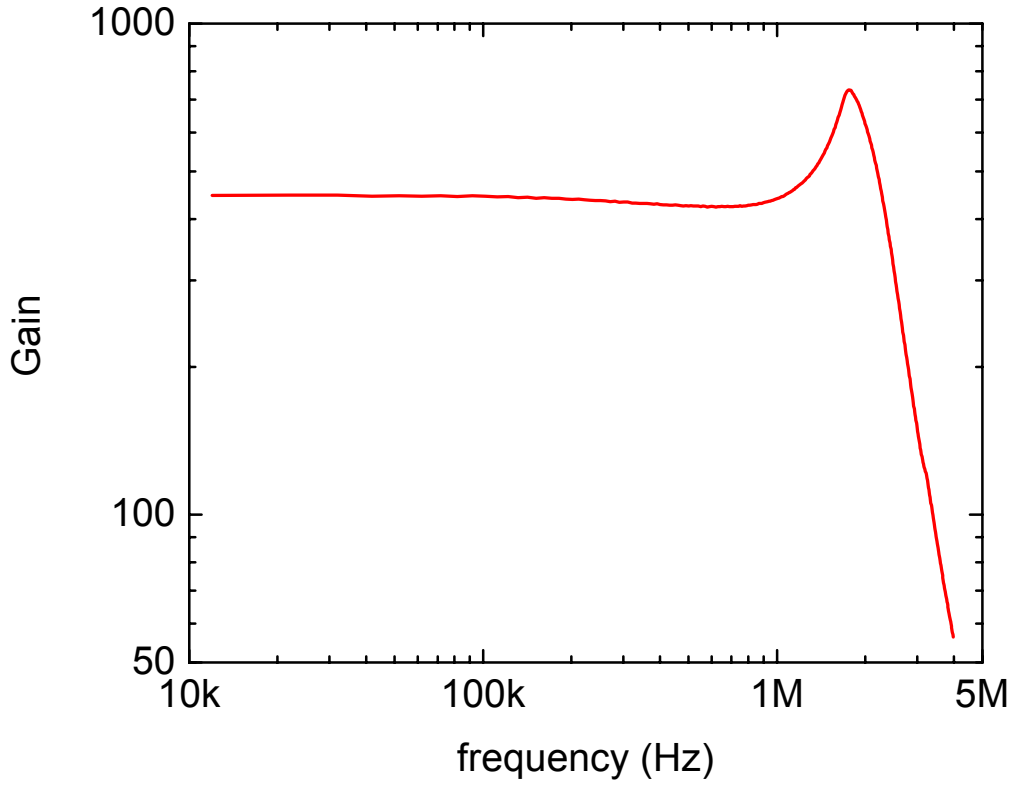


**Fig. 4.2.C Gain curve for the custom preamplifier**

The gain curve for the custom preamplifier is relatively flat over the region of interest (<1MHz) with a gain of ~470.

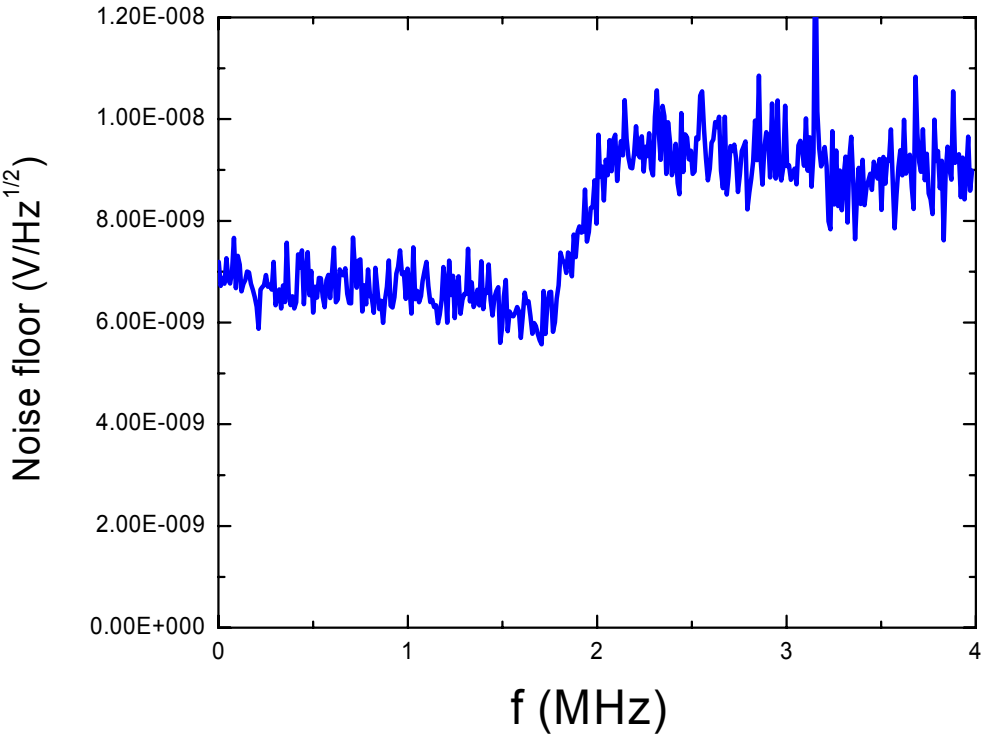


**Fig. 4.2.D Preamplifier noise floor**

The preamplifier noise floor was measured and found to be ~7 nV/Hz$^{1/2}$ (referred to input) for frequencies <1 MHz.

## 4.3 Measurement of 1/f Noise

### 4.3.1 Measurement of 1/f Noise in Air

The measured noise spectrum for a typical device is shown in Fig. 4.3.A (a). This device has dimensions $\ell = 23\mu m$, $w$ = 2 μm, $t$ = 100 nm, $\ell_{leg} = 5\mu m$, and $w_{leg}$ = 2 μm. The resistance of this device is 47.5 kΩ. Above the 1/f knee the noise approaches the expected Johnson noise-limited noise floor of 30.9 nV/√Hz (for the device plus the other resistors in the Wheatstone bridge) also shown. The expected 1/*f* noise was discussed in section 2.5.2, and from the formulae in that section we have

$$\ln S_R = \ln\left(\varsigma \frac{R_T^2}{N}\right) - \ln f \,, \qquad 3$$

where N is the number of electronic carriers and $\varsigma$ is a sample specific materials parameter. To compare our measured data with this formula, in Fig. 4.3.A (b) we plot the resistance spectral density obtained from Fig. 4.3.A (a) after subtraction of the Johnson noise (in quadrature). As expected, the data collapses onto a signle curve with slope -1 (*c.f.* equation 3). Using equation 3 and a best fit to the data in Fig. 4.3.A (b) with slope -1, we can estimate the number of carriers involved in the conduction, allowing a quantitative comparison with the Hooge formula. To do this we use $\varsigma$=1x10$^{-5}$ based on the work of Harley and Kenny, who studied devices fabricated from similar material.[7] This yields an estimate of 1.8x10$^6$ carriers involved in the conduction. A direct estimation of the effective number of carriers involved in conduction based on the device geometry and depletion length calculations of section 3.3 gives an estimate for the effective number of carriers in the legs of 6x10$^6$. Note that $\varsigma$ is sensitive to processing

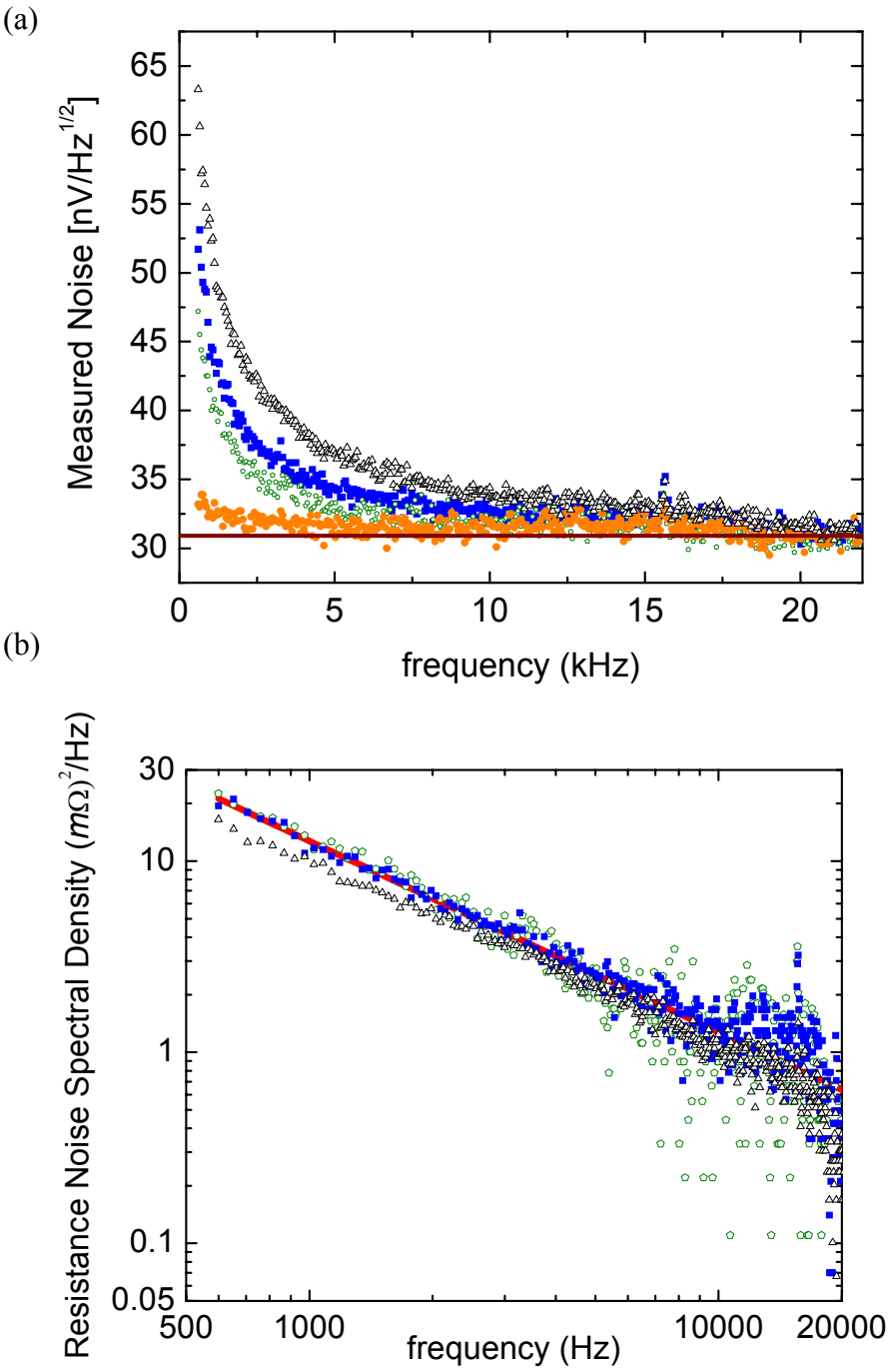


**Fig. 4.3.A Measurement and characterization of 1/f noise**

(a) Measured noise spectrum. The solid dark red curve gives the expected Johnson noise. (b) The curves collapse onto a single curve with slope -1 when viewed as a resistance fluctuation above the Johnson noise. The red curve is a linear fit to the data with 9.4 $\mu$A across the device with slope fixed at -1. For both figures, the current applied across the device for the data sets shown is: hollow black triangles: 13.6 $\mu$A; solid blue squares: 9.4 $\mu$A; hollow olive octagons: 7.5 $\mu$A; and solid orange circles: 0 $\mu$A .

Conditions,[7] and we therefore do not expect agreement to be better than an order of magnitude.

### 4.3.2 Measurement of Noise Floor in Fluid

The noise floor of a device in liquid was measured under two conditions. In the first, the device was mounted in the holder of Fig. 4.2.A which was placed in a Petri dish. Both the silicon die and pogo pins were immersed in fluid. For the second measurement the device was mounted in a microfluidic assembly so that the cantilever was immersed while the pogo pins and on-chip electrodes remained dry. The measured noise floor is shown in Fig. 4.3.B (a) for the full submersal and (b) for the microfluidic assembly. In the later case the measured noise was reproducible and comparable to that measured in air. For the fully submerged chip additional noise was observed. It is believed that the microfluidics provide vibrational isolation.

**Fig. 4.3.B Measured noise floor in fluid.**

(a)

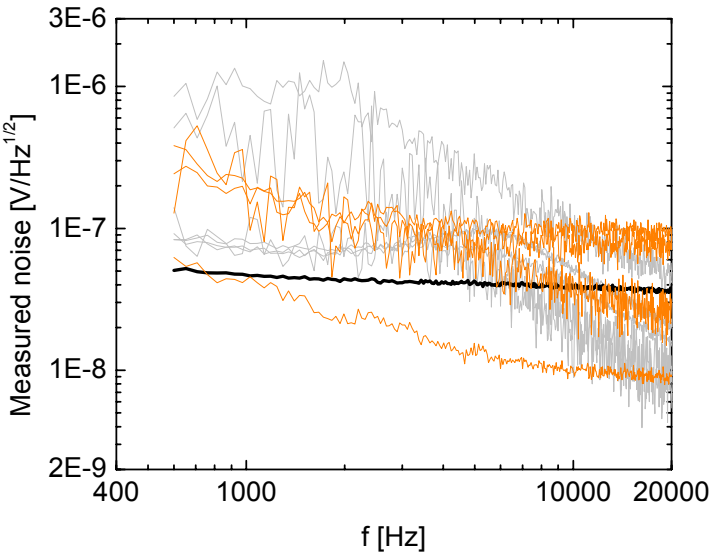


(b)

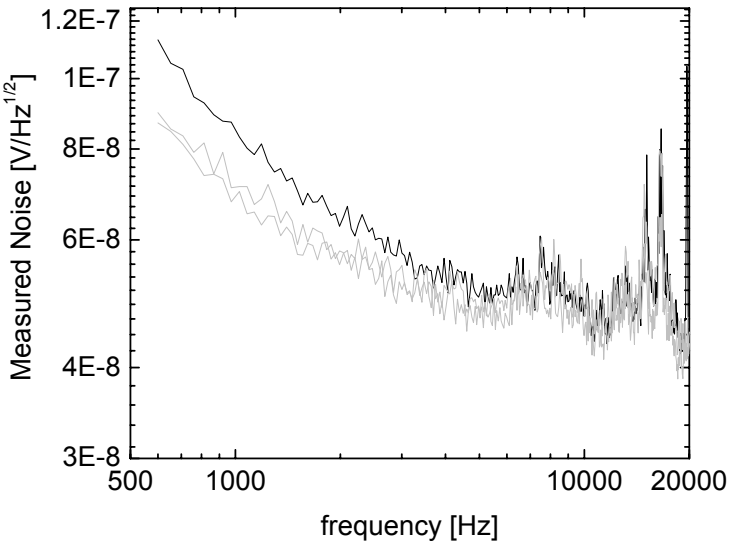


Comparison of noise floor for device submerged in Petri dish (a) and microfluidics (b). Methonal (gray) and Pentane (orange) were used in the Petri dish. The device in microfluidics was in water (gray). In both cases the data in air is shown in black.

## 4.4 References

[1] O.N. Tufte and E.L. Stelzer, J Appl. Phys. **34**, 313-318 (1963).

[2] W.P. Mason and R.N. Thurston, J. Acoust. Soc. Am. **29**, 1096-1101 (1957).

[3] J.L. Arlett, M. Paul, J. Solomon, M.C. Cross, S.E. Fraser, and M.L. Roukes, in *"Controlled Nanoscale Motion in Biological and Artificial Systems"* (Nobel Symposium 131, June 2005), H. Linke et al., Eds. (Springer Verlag, Heidelburg, *to be published*).

[4] X. Li, T. Ono, Y. Wang, and M. Esashi, Appl. Phys. Lett. **83**, 3081-3083 (2003).

[5] CFD-ACE, Computational Fluid Dynamics Research Corporation, Huntsville, AL.

[6] J.A. Harley and T.W. Kenny, Appl. Phys. Lett. **75**, 289 (1999).

[7] J.A. Harley and Kenny, J MEMS **9**, 226-235 (2000).

# 5 Self-sensing Nanocantilever Force Sensors Yielding Attonewton-scale Resolution

Thin, piezoresistive silicon cantilevers are shown to provide unprecedented sensitivity for force detection in an integrated, self-sensing, readily-scalable configuration. The devices realized herein are patterned from single-crystal Si epilayer membranes utilizing bulk micro- and nano- machining processes. We demonstrate an electrically-transduced force sensitivity of 235 aN/√Hz at room temperature and 17 aN/√Hz at 10K. Enhancement of the p+ piezoresistive gauge factor is observed at cryogenic temperatures. The results are employed to elucidate the ultimate, low-temperature sensitivity attainable from self-sensing nanoelectromechanical systems (NEMS) utilizing displacement transduction based upon semiconducting piezoresistors.

## 5.1 Introduction

Silicon microscale and, more recently, nanoscale cantilevers enable important applications such as atomic force microscopy (AFM) and biological force spectroscopy. Most efforts in these areas employ cantilever probes with *external* displacement transduction via off-chip sensing systems. These systems are typically optically-based, involving simple optical beam deflection or more sensitive interferometry. Self-sensing cantilevers, which possess integrated displacement transducers, offer important advantages that are not attainable with external optical methods. Perhaps most prominent are: 1) scalability to extremely small cantilever dimensions (far below an optical wavelength) and, thereby, to very high frequencies; 2) measurement without optical perturbation of susceptible samples; 3) suitability for large-array technologies and

portable sensing; and 4) ease of applicability to multiple-cantilever sensors that permit correlated or stochastic detection.[3] Furthermore, use of on-chip electronic readout is especially advantageous for detection in liquid environments of low or arbitrarily varying optical transparency, as well as for operation at cryogenic temperatures where maintenance of precise optical component alignment becomes problematic.

Emerging forefront applications such as magnetic resonance force microscopy (MRFM) of single spins[2] and BioNEMS (biofunctionalized NEMS) for single-molecule biosensing[3] require compliant mechanical nanosensors with force sensitivity at the thermodynamic limit. A milestone along the path towards ultralow noise, self-sensing devices is the work of Harley and Kennyb who demonstrated piezoresistive microcantilevers achieving a force noise spectral density of 8.6 fN//√Hz in air at a frequency of ~1 kHz with extremely compliant 30 μN/m devices.[23] More recently, Bargatin *et al*. report measurements of piezoresistive nanocantilevers operating at very high frequencies, up to ~71 MHz, attaining a force sensitivity of 350 aN/√Hz in vacuum at room temperature.[4] In this work we demonstrate self-sensing cantilevers with greatly improved sensitivity, and, for the first time, we explore the ultimate limits to the performance of such devices that can be expected at low temperatures where thermal noise is small. In addition to studying the temperature dependence and force sensitivity of such devices, we characterize the piezoresistive gauge factor, *G*, for silicon from cryogenic to room temperature. Previous studies of *G* have focused upon just a few temperatures[5] or solely explored the range above 50 K.[6]

Our small cantilevers employ high sensitivity piezoresistive strain sensing based upon an integrated semiconducting epilayer. This embodiment of electrical displacement transduction opens a wide parameter space permitting ultrasmall scale, very low stiffness, and very high-frequency devices – a regime not approachable via conventional optical detection. This transduction method is also well suited for scaled-down versions of complex detection schemes such as that of Chui *et al.,* which enables independent resolution of both vertical and lateral forces.[7]

Below we present a detailed method of fabrication for membrane-derived piezoresistive cantilevers based upon bulk micro- and nano-machining processes and provide an experimental and theoretical evaluation of their performance. A scanning electron microscope [SEM] image of a typical device is shown in Fig. 5.2.A (a); the cantilevers are situated at the top of a deep-etched "fluidic via" through the substrate, a configuration devised for embedding the devices within microfluidic systems for biosensing applications.[1] In this chapter we describe characterization of such cantilevers *in vacuo*, carried out from room to cryogenic temperatures, to demonstrate the utility of the devices for ultrasensitive force detection.

## *5.2 Fabrication*

Fabrication begins with a bonded silicon on insulator [SOI] wafer comprised of a 100 nm thick structural layer of undoped silicon, beneath which is a 750 nm sacrificial layer of silicon dioxide ($SiO_2$). On top of this a 30 nm thick doped Si transducer layer is epitaxially grown, which has a boron doping level of $4\times10^{19}/cm^3$. Above this, 60 nm

**Fig. 5.2.A Piezoresistive nanocantilever force sensor.**

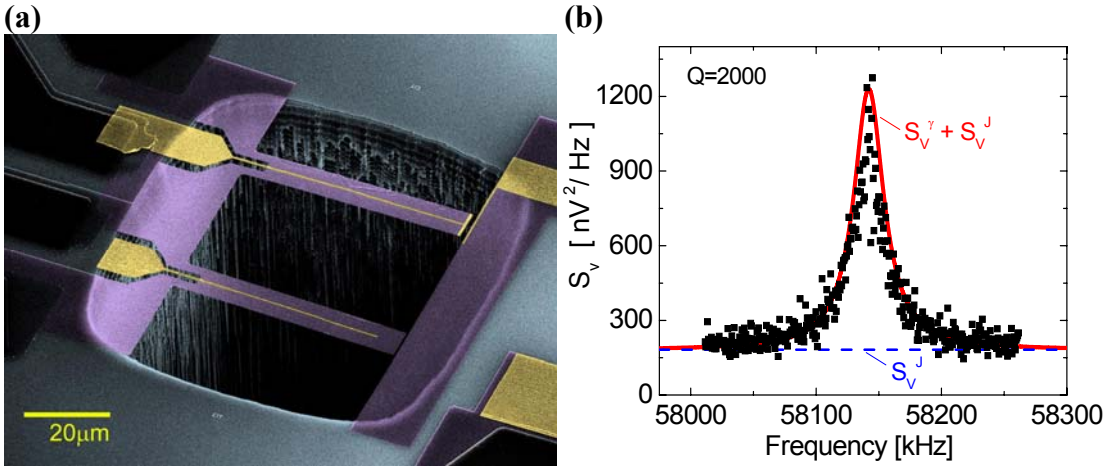


(a) SEM image of the cantilever device with thickness 130nm, of which the topmost 30nm comprises the p+ transducer layer. The current path flows along the two outer silicon "legs"; the central Au-coated Si "line" running longitudinally along the center of the device enables biosensing applications.3 (b) Voltage noise spectral density obtained at room temperature with a 0.3V bias, measured at the device output terminals. The two principal components evident originate from electrical-domain (Johnson) noise from the transducer itself, $S_V^J$, and piezoresistively-transduced thermomechanical fluctuations, $S_V^\gamma$.

thick gold electrodes are patterned (each with a 5 nm chromium underlayer to promote adhesion); these form Ohmic electrical contacts to the doped silicon epilayer. A membrane, from which the devices are subsequently patterned, is created by a backside deep reactive ion etch [DRIE] to form a deep trench through the substrate (75$\mu$m *x* 75$\mu$m cross section). This etch is carefully terminated at the oxide layer and ultimately yields the aforementioned fluidic via (Fig. 5.2.A(a)). The wafers are then diced into individual 11mm x 11mm dies. Prior to the nanofabrication steps the oxide layer is removed from the back side of the trenches using a buffered oxide etch. The cantilevers are then defined by electron beam lithography, employing lift-off to pattern a 30*n*m aluminum mask that protects the active areas during the subsequent vertical electron cyclotron resonance (ECR) plasma etch process using the gasses $NF_3$, $Cl_2$, and Ar that defines the devices. The aluminum mask is subsequently removed using a 10% potassium hydroxide solution.

## *5.3 Device Characterization*

These devices have a geometry that is somewhat more complex than a simple cantilever; they are attached to the supports by two small "legs" which serve to concentrate both strain and current flow within the same region to enhance sensitivity (Fig. 5.2.A (a)).[3] The completed devices employed in the present study have dimensions $\ell$=55μm, $w$=7μm, $w_{leg}$=2μm, and $\ell_{leg}$=5μm. Much smaller devices have been patterned; this methodology has proven well-suited to fabrication at the sub-100nm scale. Assuming end-loading and fundamental mode response, the force constant for these devices can be approximately represented as

$$K_0 = \frac{Et^3}{\frac{4\ell^3}{w} + \left(2l_{leg}^3 - 6\ell\ell_{leg}^2 + 6\ell^2\ell_{leg}\right)\left(\frac{1}{w_{leg}} - \frac{2}{w}\right)} \tag{28}$$

(see section 2.3.1). Assuming a Young's modulus of $E$ =110 GPa,[15] we deduce from Eq. 28 a value $K_0$=2.34 mN/m for the devices of this study. This value is closely confirmed by finite-element numerical simulations[9] which yield $K_0$=2.46 mN/m. The effect of the gold electrode patterned along the center of the device has been included in these simulations. These devices are oriented so that current flow within the legs occurs along the <110> direction for which the piezoresistive coefficient, $\pi_\ell$, is ~4x10$^{-10}$ Pa$^{-1}$ .[11,12] As grown, the p+ transducer layer has a measured resistivity of 1kΩ/square; an increase of ~25% was noted after processing. The total 2-terminal resistance of the device was 19.3 kΩ. This resistance comprises three contributions: 6.3 kΩ from the strain sensing leg region, 5.5 kΩ/leg for the resistance from the contact pad to the cantilever legs (measured on a 4-terminal device of comparable geometry), and 2 kΩ from the spreading resistance at the neck of the cantilever legs and the contribution from the end region of the cantilever.

## *5.4 Noise Performance and Responsivity*

We now analyze the noise performance of these devices that, ideally, should be limited by the thermomechanical (mechanical-domain) noise of the force sensor itself. We characterize the device noise via $S_F(f)$, the force spectral density with units (force)$^2$/Hz, which is defined as the fourier transform of the autocorrelation function of the fluctuating (time-dependent) effective force at the cantilever tip. The "force sensitivity" is then given by $\sqrt{S_F(f)}$ (units force/(Hz)$^{1/2}$). The total r.m.s. force noise is the integral of this

force sensitivity over the measurement bandwidth. The force spectral density arising from thermomechanical fluctuations, which is white over the physically relevant regime, is given by $S_F^{\gamma} = 4k_BT\gamma = 4k_BTK_0/(2\pi Qf_0)$. Here $\gamma$, $f_0$, and $Q = 2\pi M_0 f_0/\gamma$ are the damping coefficient (with units kg/s), fundamental mechanical resonance frequency, and quality factor, respectively, for the vibrational mode under consideration. $M_0 = K_0/(2\pi f_o)^2$ defines the modal mass. At room temperature the measured fundamental resonance frequency and quality factor are 58.1 kHz and 2000, respectively (Fig. 5.2.A (b)); hence the associated force spectral density expected from thermomechanical fluctuations is 235 aN/√Hz. The cantilever's dynamical response function, $H(\omega)$, transforms this force noise into displacement fluctuations:

$$S_x^{\gamma}(\omega) = S_F^{\gamma}\left|H(\omega)\right|^2 = S_F^{\gamma}\frac{1}{M_0^2\left[(\omega^2-\omega_0^2)^2+(\omega\,\omega_0/Q)^2\right]}. \qquad (29)$$

Here $S_x^{\gamma}(\omega)$ is the spectral density of thermal displacement fluctuations, and *x* represents the coordinate of cantilever motion measured at its distal end.

Other "extrinsic" noise sources affect the device performance. In the absence of force stimuli, thermodynamic displacement fluctuations are transduced by the biased piezoresistors into an equivalent voltage noise at the device output terminals. In the ideal case, the transduced contribution from $S_X^{\gamma}(\omega)$ should dominate the intrinsic, electrical-domain noise of the piezoresistors (arising from Nyquist and flicker-noise mechanisms). More formally, the voltage noise spectral density arising from electrically-transduced thermomechanical fluctuations is $S_V^{\gamma}(\omega) = S_x^{\gamma}(\omega)\,\mathcal{R}_T^2$. Here $\mathcal{R}_T = I_b\left(\partial R_d/\partial x\right)$

represents the voltage responsivity (with units V/m) characterizing the performance of the piezoresistive transducers biased with a dc current, $I_b$. The quantity $\partial R_d/\partial x$ represents the differential sensitivity of device resistance to displacement; it can be deduced empirically by fitting the electrically-transduced thermomechanical resonance peak to a Lorentzian response (Fig. 5.2.A(b)), after subtracting the predominantly white background electrical noise near resonance (which we measure experimentally). For the present device this procedure yields $\partial R_d/\partial x \sim 0.017\ \Omega/\mathrm{nm}$. Theoretically we expect this differential responsivity to be given by the expression

$$\partial R_d / \partial x = \frac{3\beta\pi_\ell}{2w_{leg}t^2}\left(2\ell - \ell_{leg}\right)K_0 R_d, \qquad (3)$$

where $R_{dev}$ is the resistance of the "sensing region" of the device. (For our two-leg devices, finite element simulations show that the narrow legs are the regions that both dominate the two-terminal resistance and develop the highest strain upon cantilever deflection.) We estimate $R_d$ from the device geometry using the measured resistance per square for the material. $\beta$ is a parameter introduced by Harley and Kenny to account for the fraction of the full strain distribution sampled by the finite-thickness piezoresistive layer; in their work $\beta \sim 0.7$. We also employ this value of $\beta$ for our devices, which are geometrically similar.[23] Using Eq. (3) and the measured $\partial R_d / \partial x$ from Fig. 5.2.A (b), we can deduce the device gauge factor as $G = \pi_\ell E = 47$. This agrees quite closely with the expected value of 44.[11,12] Similar results were obtained upon performing a direct measurement of the gauge factor using an AFM, which provided a calibrated displacement (discussed in section 4.1).

### 5.4.1 Theoretical Model for Bias-Current-Induced Self Heating of Piezoresistive Devices

To evaluate the temperature-dependent force sensitivity of the device requires evaluation of the actual device temperature, which can be affected by bias-current-induced heating. As demonstrated below, this begins to play a significant role only at our lowest temperatures and is otherwise negligible. In this regime the electronic carriers (holes) and phonons within a device under bias are not in thermal equilibrium. For the temperature range over which experimental results are presented here ($T_o \geq 6\text{K}$, where $T_o$ is the ambient temperature), thermal conduction via hole diffusion is negligible (as confirmed later in this paper). For the purpose of these calculations we therefore assume that all heat is dissipated via the phonon conduction pathway. The temperature dependence of the mechanical properties of the device are determined by the phonon temperature ($T_{ph}$). We assess this quantitatively by assuming that uniform Joule heating within the cantilever legs along their length generates a one-dimensional phonon temperature profile, satisfying the expression $2t\,w_{leg}\,\kappa_{Si}\left(d^2T_{ph}/dy^2\right) = -\dot{Q}/\ell_{leg}$. Here $y = \left[0,\ \ell_{leg}\right]$ represents the position along a cantilever leg measured from its anchoring support. We assume the thermal boundary condition at $y$=0 is established by the (regulated) substrate temperature, whereas at $y = \ell_{leg}$, the distal end of the cantilever legs, it is established by the condition that the temperature gradient vanishes in these vacuum-based measurements. Heat loss via black-body radiation is negligible. At low temperatures the thermal conductivity of silicon, $\kappa_{Si}$, is estimated assuming simple diffusive thermal transport $\kappa_{Si} \sim c_{\text{v}}\,\overline{\text{v}}_{\text{s}}\,\overline{\ell}/3 = \alpha_{ph}T_{ph}^3$, where $c_{\text{v}}$ is the specific heat per

unit volume given by the Debye formula, $c_v(T) = [12\pi^4 k_B \rho/(5m_{si})]\left(T_{ph}/T_D\right)^3$, $m_{si}$ is the atomic mass of silicon, and $T_D$ = 645K is the Debye temperature for silicon. The average speed of sound for silicon is given by $\bar{v}_s = \left\langle \sum_{i=1}^{3} 1/v_i^2 \right\rangle \Big/ \left\langle \sum_{i=1}^{3} 1/v_i^3 \right\rangle \sim 5634$ m/s (at 73K), where the summation is over propagation modes and the average is over propagation direction.[12] Here $\bar{\ell}$ is the effective phonon mean free path. Based upon previous low temperature thermal transport studies of nanoscale beams with geometry similar to the piezoresistive legs employed here,[13] we assume a boundary scattering limited value $\bar{\ell} \sim 1.12\sqrt{A}$. Here $A$ is the cross sectional area of the beam.[14] With these formulae we deduce the average temperature within the leg region in steady-state (under current bias) for all data taken below 40K. Above 40K the Debye formula ceases to be valid for determining thermal conductivity — however, for the full range of biases employed in this work we have verified that bias heating is negligible in this regime. From the thermal diffusion equation we obtain a steady-state temperature profile

$$T_{ph}(y) = \left(\dot{Q}\ell_{leg}/2tw_{leg}\alpha_p - \beta^2\left(y^2/\ell_{leg}^2 - 2y/\ell_{leg} + 1\right)\right)^{1/2}/\beta^{1/2} \qquad (4)$$

along the length of the piezoresistors, where $\beta = \left(\left(T_o^4 + 2\ell_{leg}\dot{Q}/tw_{leg}\alpha_p\right)^{1/2} - T_o^2\right)/2$ and $T_o$ is the ambient temperature. We employ its longitudinally averaged value $\left\langle T_{ph}\right\rangle = \int_0^{\ell_{leg}}\left[T_{ph}(y)/\ell_{leg}\right]dy$ as an approximate measure of the effective device temperature in steady-state.

### 5.4.2 Experimental Configuration for Temperature Control

The cryostat-mounted sample stage was engineered such that a 100Ω resistor, used for controlling the ambient temperature, passed through the center of a copper block on

which the sample was mounted. Apiezon N grease was used to ensure thermal contact of the heating resistor and copper block. A silicon diode thermometer was mounted on the opposite side of the copper block at a comparable distance from the heating resistor as the micro-cantilever device. The measured temperature from this diode was used as the ambient temperature, $T_o$. The diode thermometer and heating element were controlled using a Lakeshore 340 temperature controller.

### 5.4.3 Experimental Validation of Heating Model

To assess the validity of the effective phonon temperature of the piezoresistive sensors calculated above, we perform two control experiments summarized in Table 5.4.A In the first, we fix the bias power and evaluate the resulting temperature rise in the sensors (piezoresistors) for various ambient (substrate) temperatures, $T_o$. This procedure involves an initial calibration of the resonant frequency versus substrate temperature, measured using very small bias power (3.4μW) so that temperature disequilibrium is minimal. Significant local heating is then induced by increasing the bias current so that much more power, 22μW, is dissipated within the piezoresistors while the substrate is simultaneously regulated at several specific temperatures, $T_o$. The resulting local temperature rise at the sensors is evaluated by converting the observed resonant frequency shift to sensor temperature (Fig. 5.4.A (a)) via the initial calibration.[‡] This is then compared with the value derived from the heating calculations. In a second experiment we regulate the substrate temperature at 11.5K and apply four different

[‡] This procedure is valid since it is the temperature dependence of Young's modulus within the heated leg region that predominantly gives rise to the resonant frequency shift.

(relatively large) values of the bias power, as tabulated. A similar procedure is then employed to deduce local sensor temperature. In both cases the agreement between the local temperature rise measured from resonance frequency shifts and that estimated from the aforementioned calculations are within 7% for temperatures up to 15K and all applied bias powers (up to 47μW).

**Table 5.4.A Summary of control experiments performed to assess the validity of the heating correction**

| $P = 22\mu W$ | | | $T_o$=11.5K | | |
|---|---|---|---|---|---|
| $T_o$ | $\Delta T_{meas}$ | $\Delta T_{calc}$ | $P$ | $\Delta T_{meas}$ | $\Delta T_{calc}$ |
| 7.6 K | 13.3 K | 12.4 K | 3.4 $\mu$W | ------ | 4.0 K |
| 11.5 K | 10.4 K | 9.9 K | 6.9 $\mu$W | 5.9 K | 5.8 K |
| 15.0 K | 7.8 K | 8.0 K | 22 $\mu$W | 10.4 K | 9.9 K |
| 20.0 K | 4.6 K | 5.8 K | 43 $\mu$W | 12.6 K | 12.9 K |
| | | | 47 $\mu$W | 12.9 K | 13.4 K |

$T_o$ is the initial temperature (before heating), $\Delta T_{meas}$ is the temperature rise as determined by the resonance frequency shift (Fig. 2 (a)), and $\Delta T_{calc}$ is the temperature rise estimated from the thermal conduction calculations discussed in the text.

### 5.4.4 Experimental Results: Temperature Dependence of the Quality Factor, Gauge Factor and Thermomechanical Noise

With this validation of our procedure for evaluating effective temperature we can confidently deduce the temperature dependence of both the quality factor and gauge factor. These are displayed in Fig. 5.4.A (b) and (c), respectively. The quality factor is observed to increase from 1900 at room temperature to 10,000 for $T \leq 30K$. The gauge factor is evaluated over the temperature range from 11K to 300K by fitting to thermomechanical noise data (using a procedure based upon Eqs. (2) and (3)) after carefully subtracting the electrical noise contributions. Fig. 5.4.A (c) shows that the piezoresistive response increases with decreasing temperature, consistent with the few reports that exist in the literature.[5,6] The temperature-dependent thermomechanical noise sensitivity is shown in Fig. 5.4.B. A minimum value of 17 $a$N/√Hz is attained at an effective device temperature of 10.4K (see Fig. 5.4.B, inset).

**Fig. 5.4.A Temperature dependent performance of nanocantilever force sensor.**

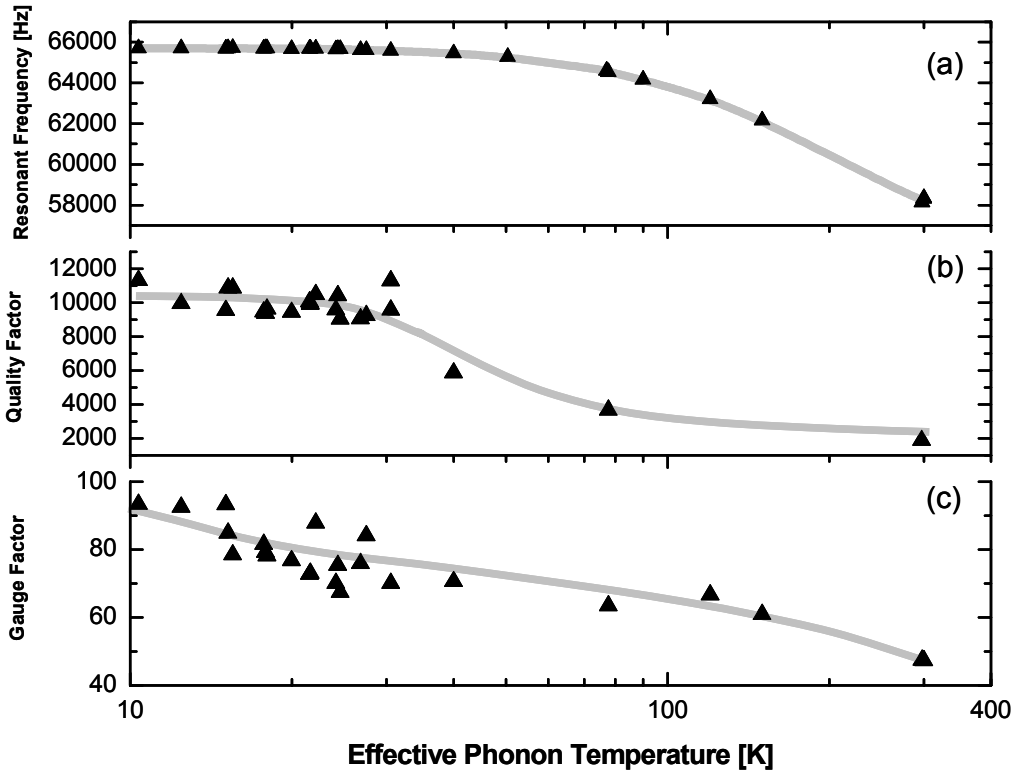


(a) Resonance frequency; (b) Quality factor; and (c) Gauge factor. The data is for the thermomechanical resonance, collected at a bias of 3.3 μW. The temperature scale has been corrected to account for heating at this bias power as discussed in the text. The solid gray lines provide a guide to the eye.

**Fig. 5.4.B Force noise spectral density for the nanocantilever force sensor.**

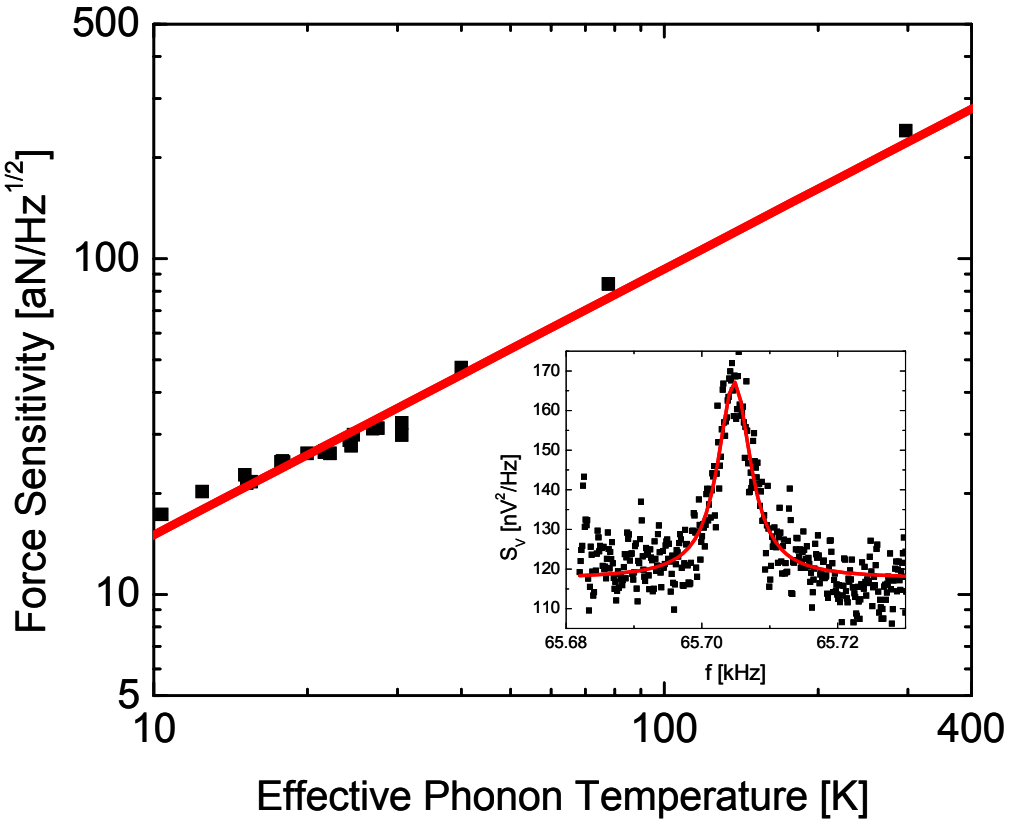


The temperature dependent magnitude of the thermomechanical force noise is shown here. Over the range shown, the data follow an approximately linear trend; a least-squares fit yields a $T^{0.8}$ dependence (solid line). **Inset:** The measured voltage noise at a device temperature of 10.4K.

## 5.5 Ultimate Limits of Semiconductor-Based Piezoresistive Sensing for NEMS

Apart from the high force sensitivity we have attained, perhaps the most compelling aspect of our present results is that they can be employed to elucidate the ultimate limits of semiconductor-based piezoresistive displacement sensing for NEMS. Specifically we can evaluate: (a) the lowest temperatures at which piezoresistive displacement transduction remains useful, (b) the optimal bias current for a given ambient temperature, and (c) the ultimate force sensitivity that is attainable with piezoresistive cantilevers at low temperatures where optimal performance is obtained. The analysis proceeds as follows. The transduction responsivity of a piezoresistive cantilever, $\mathcal{R}_T$ is proportional to the bias current applied through the device – but this bias, in turn, also determines the power dissipated within the piezoresistors, $P_{in} = I_b{}^2 R_d$. This power input, in turn, induces a temperature rise determined by the thermal conductance available from all mechanisms that serve to cool the piezoresistors. In steady state, a temperature $\left\langle T^*(T_0, I_b) \right\rangle$ is thereby established which depends upon the ambient temperature, $T_0$, and applied bias, $I_b$. We view $T_0$ as the independent variable since its value is typically dictated by the sensing application. Hence, for a given $T_0$ there exists an optimal bias current, $I_b^{(opt)}(T_0)$, that yields the optimum force sensitivity, $\sqrt{S_F^{1/2}(T_0)\big|_{opt}}$ at that temperature. However, below a characteristic temperature $T_0 < T_0^{(\min)}$, the steady-state device temperature, $\left\langle T^*(T_0, I_b) \right\rangle$, is predominantly determined by Joule heating and *not* by the ambient temperature $T_0$. In the previous analysis a single pathway for dissipation of bias induced Joule heating was considered, namely heat transfer from holes to the

phonon bath and then to the environment via phonon transport. A second potential pathway for heat dissipation is available, specifically hole diffusion along the electrical conductors. These two mechanisms for thermal conduction act in parallel, as schematically depicted in Fig. 5.5.A. For the analysis here, which extends to lower temperatures than the experimental data presented earlier, we must consider both pathways. In doing so we will explicitly justify the omission of the hole diffusion pathway in the earlier analysis of our data at higher temperatures, $T \geq 6\mathrm{K}$.

Here we evaluate the effective steady-state for the phonons and holes in the strain sensing region of the device, making it possible to evaluate the total force spectral density on resonance, referred to input (RTI). This is given by the formula

$$S_F = S_F^{\gamma} + S_F^{J} = \frac{2 k_B K_o}{\pi f_o Q} \int_0^{\ell_{leg}} \frac{T_{ph}}{\ell_{leg}} dy + \frac{4 k_B R_d}{\mathcal{T}^2} \int_0^{\ell_{leg}} \frac{T_h}{\ell_{leg}} dy, \tag{5}$$

where $S_F^{\gamma}$ is the thermomechanical noise and $S_F^{J} = S_V^{J} / \mathcal{T}^2$ is the (Johnson) electrical noise (RTI). Here $\mathcal{T} = \mathcal{R}_T \, (Q / K_o)$ is the ganged system responsivity, the product of the transducer and on-resonance mechanical responsivities, $S_V^{J} = 4 k_B T_h R_d$ is the (Johnson) voltage noise of the transducers, and $T_h$ is the effective temperature of the holes. Note the separate roles played by the phonon and hole temperatures for the mechanical and electrical degrees-of-freedom, respectively.

The calculation proceeds as follows; the temperature profile for the holes is solved for using the diffusion equation: $2 t_{doped} w_{leg} \kappa_h \left( d^2 T_h / dy^2 \right) = -\dot{Q}_h / \ell_{leg}$, where the hole thermal conductivity is given by the Widemann-Franz law

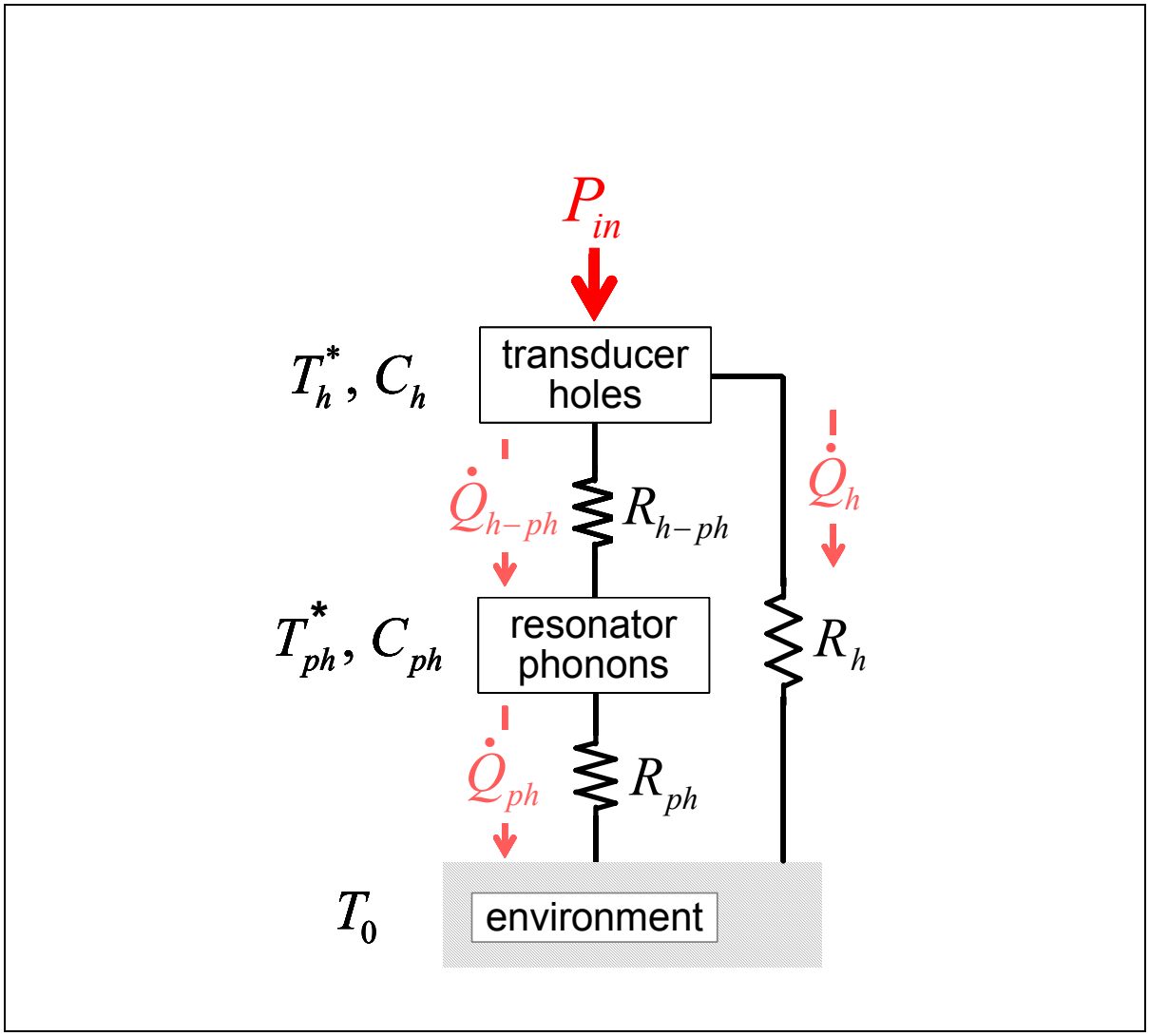


**Fig. 5.5.A Model for low low temperature thermal transport in semiconducting piezocantilevers.**

Joule heating of the transducer's hole gas arising from the applied bias, $P_{in}$, is dissipated by both phonon emission, $\dot{Q}_{h-ph}$, and hole diffusion down the electrical leads to the environment (*i.e.* substrate), $\dot{Q}_h$. The induced heating of the resonator phonons is subsequently dissipated into the environment via phonon transport, $\dot{Q}_{ph}$. The thermal resistances characterizing these processes are $R_{h-ph}$, $R_h$, and $R_{ph}$, respectively. In steady state, with the environment at temperature $T_0$, this branched heat flow raises the hole gas and resonator phonon temperatures to $T_h^*$ and $T_{ph}^*$, respectively. The heat capacities of the hole gas and resonator phonons are $C_h$ and $C_{ph}$, respectively.

$\kappa_h = \pi^2 \left(k_B / e\right)^2 \sigma T_h / 3$. The temperature dependence of the thermal conductivity makes solution of this differential equation non-trivial; hence we evaluate it numerically. In these equations $T_h$ represents the (local) effective steady state temperature of the holes, $t_{doped}$ represents the thickness of the conducting layer of the piezoresistor, $\sigma$ represents the conductivity of the piezoresistor, and $e$ is the electronic charge. The temperature profile of the phonons is determined by Eq. (4) where the heat transferred, $\dot{Q}$ ,is now $\dot{Q}_{ph}$, the heat transferred via the phonon conduction pathway.

Once the temperature profiles for holes and phonons have been evaluated, the heat transferred from holes to phonons can be calculated using the equation: $\dot{Q}_{h-ph} = \int dV \int_{T_{ph}}^{T_h} dT \; G_{h-ph}(T(y))$, where the volume integral is over the conducting region of the device and $G_{h\text{-}ph}$ is the hole-phonon thermal conductance per unit volume given by $G_{h-ph}(T) = C_h(T)\; \Gamma_{h-ph}(T) \; = g_{h-ph} T^4$, where $C_h$ is the electronic heat capacity per unit volume and $\Gamma_{h-ph}$ is the hole-phonon scattering rate.[15] We model the hole heat capacity as that of Sommerfeld free hole gas, $C_h(T) = \pi^2 \mathrm{p} k_B^2 T / \varepsilon_F = \gamma_h T$ ,where p is the hole density, $\varepsilon_F = \hbar^2 (3\pi^2 \mathrm{p})^{2/3} / 2m_h$ is the Fermi energy, and $m_h$ the (light) hole mass in the valence band. Assuming the holes and phonons are Fermi and Bose distributed, respectively, the deformation potential hole-phonon scattering rate, $\Gamma_{h-ph}$, is given by $\Gamma_{h-ph} = \dfrac{3\varsigma(3) k_B^3 D^2}{\pi \hbar^4 \overline{\mathrm{v}}_\mathrm{s}^4 \mathrm{v}_\mathrm{F} \rho} T^3 = \alpha_{h-ph} T^3$, where $D$=8.3$e$V is the deformation potential[16,17] and $\varsigma(3)$=1.202. The relative values for the heat conducted via the two thermal conduction

pathways $\dot{Q}_h$ and $\dot{Q}_{ph}$ is not known a priori. The system is solved iteratively until convergence is attained, yielding $\dot{Q}_{h-ph} = \dot{Q}_h$ (subject to the constraint $P_{in} = \dot{Q}_h + \dot{Q}_{ph}$).

The effective, electrically-transduced force noise referred to the input (RTI) calculated with this model is shown at four different ambient temperatures in Fig. 5.5.B (a) for the experimental device geometry. For very low bias currents the total force noise increases due to the smaller transducer responsivity and, consequently, the dominance of $S_F^J$ referred to input. At high bias currents, the total noise increases due to the increased device temperature. It is clear that by minimizing Eq. (5) we can determine the optimum bias power, $P_{in}$, yielding the highest sensitivity for a given ambient temperature and device geometry. The effective temperature of both the phonons and holes is shown in Fig. 5.5.B (b). It is evident that below a few degrees Kelvin, Joule heating is very significant in determining the effective device temperature. The temperature dependence of the optimum force sensitivity obtained by this procedure is shown in Fig. 5.5.B (c) for the experimental geometry. The corresponding effective temperatures for the holes and phonons are shown in Fig. 5.5.B (b). As seen, a limiting sensitivity of $S_F = 13\text{aN}/\sqrt{\text{Hz}}$ can be achieved for an ambient temperature $T_0 < 1\text{K}$.

This analysis allows us to assess the sensitivity improvements possible through optimization of geometry – for example, by reducing the width of the cantilever legs and decreasing the total device thickness. To illustrate the improvements that are easily

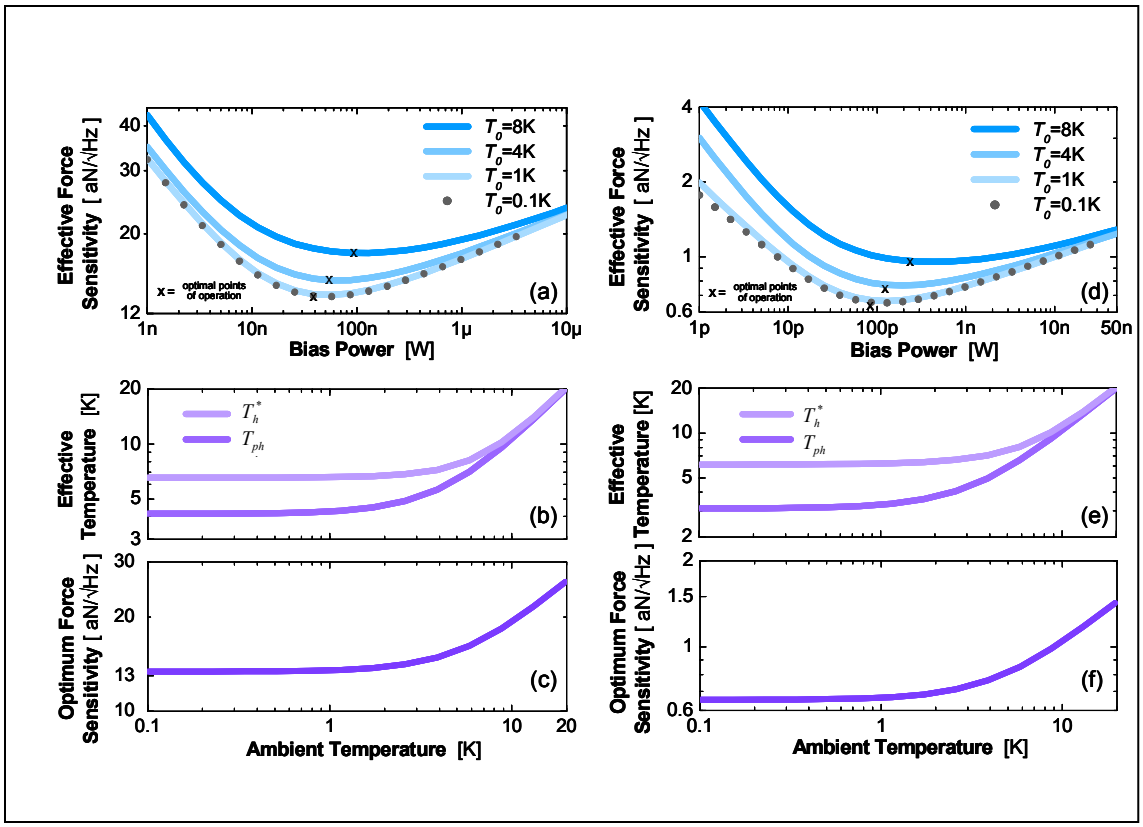


**Fig. 5.5.B Optimization of transduced force sensitivity.**

**(a,d)** Evaluation of the bias power dependence of the effective force noise, which includes both mechanical- and electrical- domain contributions (referred to input). Calculated performance is displayed for two device geometries (see text): the microdevice on which experiments were conducted in this paper (plots *a,b,c*) and a smaller, but realistic, nanodevice (plots *d,e,f*). At each ambient temperature, $T_0$, the minima define an optimal bias point, $P_{in}^{(opt)} = I_B^{(opt)} R_T^2$. At low bias power the responsivity of the transducer decreases, thereby leading to an increase in the effective force noise (referred to input). At high bias power the total force noise increases due to Joule heating. **(b, e)** At the optimal bias power the transducer hole gas and the resonator phonons attain elevated steady-state temperatures, $T_h^*$ and $T_{ph}$, which depend upon $T_0$. **(c, f)** The optimum force sensitivity attained at $P_{in}^{(opt)}(T_0)$ is shown as a function of $T_0$. Note that an improvement in force sensitivity of greater than an order of magnitude is observed for the nanoscale device.

within the scope of our present, top-down nanofabrication capabilities, we consider nanocantilever devices with $w_{leg} = 100\text{nm}$, $w$=300nm, $t$=30nm, $t_{\text{doped}}$=7nm, $\ell_{leg} = 1\mu\text{m}$ that are otherwise identical to the device of Fig. 1. For such a device one obtains an optimal sensitivity $S_F = 0.6\text{aN}/\sqrt{\text{Hz}}$ for $T_0$<1K. A quality factor of 10 000 was assumed for this device. This seems reasonable based on a survey of work that has gone on in the field.[18] The optimum sensitivity versus ambient temperature is shown in Fig. 5.5.B (f).

### 5.5.2 A Comparison of Thermal Conduction Pathways

In Fig. 5.5.A two thermal conduction pathways were shown, namely conduction via hole diffusion and conduction via phonon-mediated thermal conduction. The contributions from both pathways were assessed in the preceeding analysis. Here we look at the relative importance of these pathways in cooling the nanocantilever device (discussed in Fig. 5.5.B (d-f)). In Fig. 5.5.C (a) we show the effective phonon and hole temperatures for the device. Also shown is the relative heat flow through each of the two pathways as a function of bias powers for two ambient temperatures (0.1K and 1K). We see that at these relatively low temperatures, heat transport is dominated by the holes at low bias powers. However, a crossover to phonon-dominated heat transport occurs for a bias power of ~10pW. At this bias power the effective temperatures of the holes and phonons are ~1.7K and ~3.5K, respectively. At higher ambient temperatures the hole and phonon temperatures rise above this crossover, even for arbitrarily low bias power. In this case heat transport is entirely phonon-dominated. This is shown in Fig. 6 (b) for an ambient temperature of 4K.

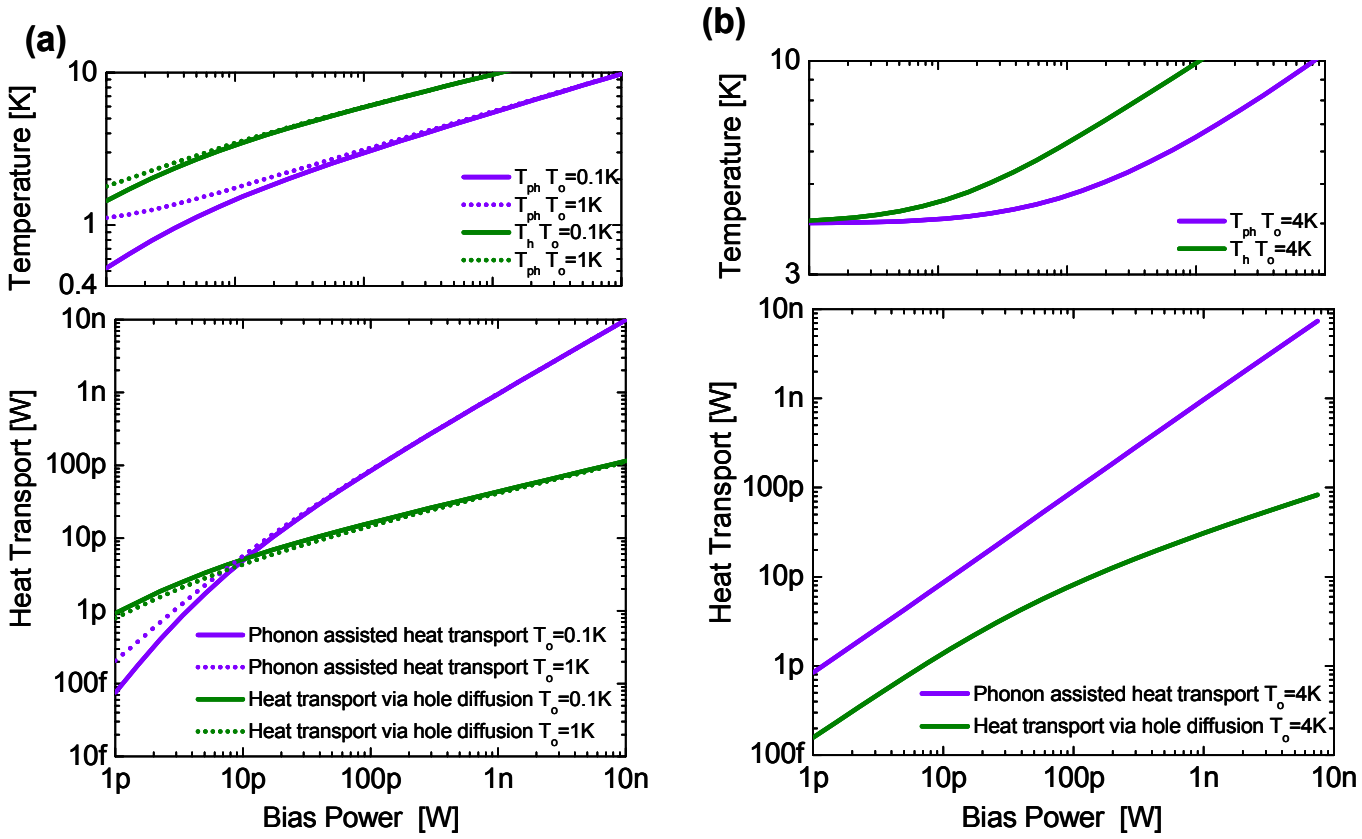


**Fig. 5.5.C Relative heat conduction via phonon- and hole-mediated pathways.** **(a)** For ambient temperatures less than 1K thermal conduction is dominated by hole diffusion at low bias powers (<10pW). A crossover to phonon-mediated thermal conduction occurs at a bias power of ~10pW (at this crossover the phonon and hole temperatures are ~1.7K and ~3.5K, respectively). For higher ambient temperatures such as the ambient temperature of 4K shown in (b), the higher ambient temperature places the device above the cross-over from hole diffusion thermal transport to phonon-mediated thermal transport even for arbitrarily low bias power.

From Fig. 5.5.B (d), the optimum bias power for the nancantilever device is seen to be approximately 100pW for the lowest ambient temperatures, putting the device in the phonon-mediated thermal transport dominated regime under optimum bias conditions. 0 shows the thermal conduction via the two pathways at the optimum bias power over a temperature range from 0.1K to 10K. As is evident, 15% of the conduction is via holes at temperatures below ~1K. At higher ambient temperatures the thermal conduction is entirely phonon-mediated.

### 5.5.3 Thermal Conduction via Hole Diffusion under Experimental Conditions

In the analysis of our experimental data we asserted that thermal conduction via holes was not significant in the temperature range studied. We revisit that assertion here. The lowest temperature of data collection was at an ambient temperature of 6.0 K , with a bias power of 1 $\mu$W. Under the assumption that the power was dissipated entirely via the phonon conduction pathway, an average phonon temperature of 10.3 K was calculated. Based on this phonon temperature and 1 μW of power transfer we obtain an effective average hole temperature of 12.8 K. The heat dissipated via hole diffusion at this effective hole temperature, estimated using the Wiedemann-Franz law, $\dot{Q}_{h-ph} \sim 2\pi^2 \left(k_B / e\right)^2 / 3R_d \left(\left\langle T_h \right\rangle^2 - \left\langle T_o \right\rangle^2\right)$, is of order 1 $n$W and therefore negligible compared to the 1 $\mu$W dissipated via phonon conduction.

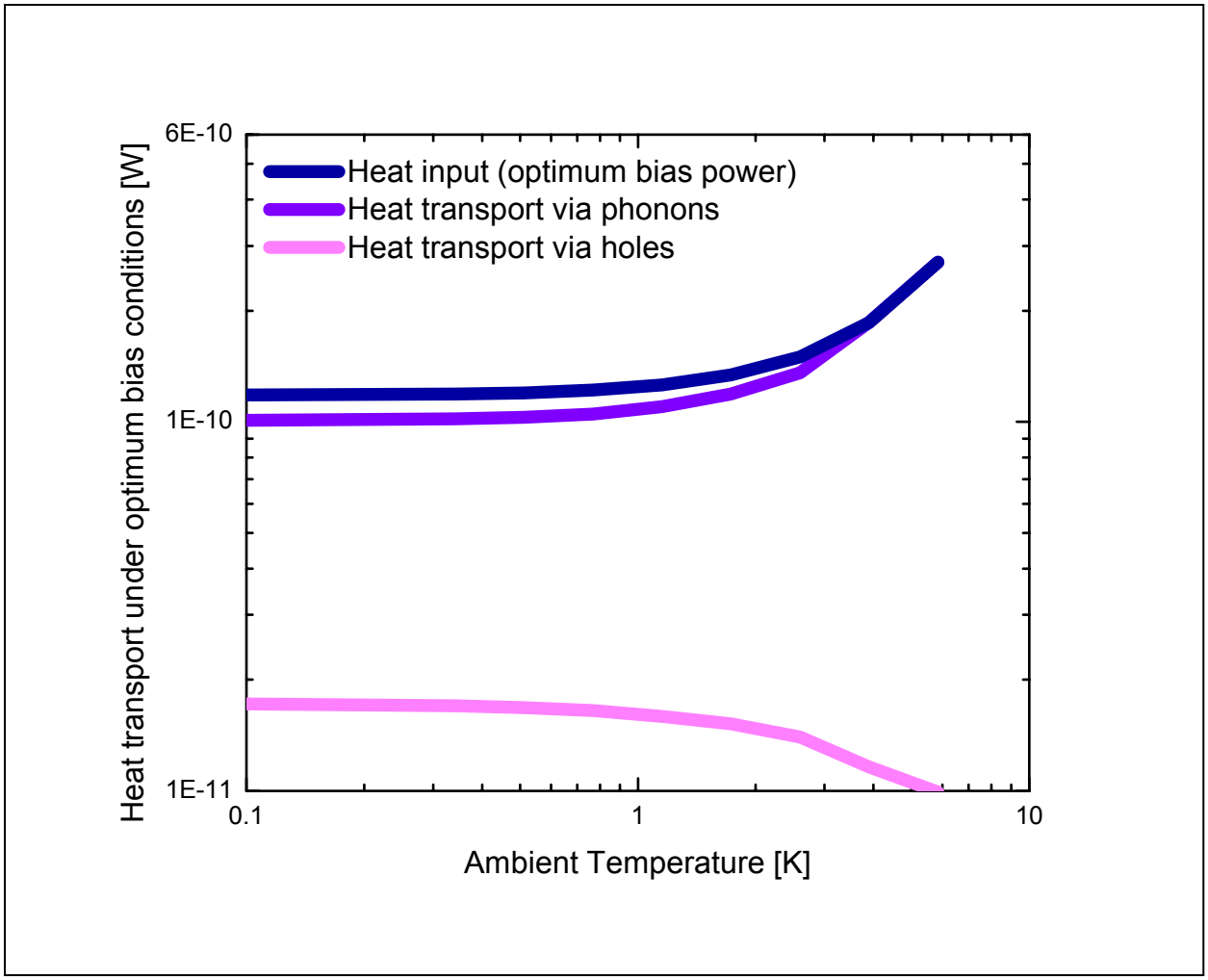


**Fig. 5.5.D Relative conduction via phonon mediated pathway and hole diffusion under optimum bias conditions**

Phonon-mediated thermal conduction dominates the heat conduction pathways under the optimum bias conditions **(see Fig. 5.5.B (d))**. The contribution from hole diffusion is 15% for ambient temperatures below approximately 1 K and decreases for higher ambient temperatures.

## 5.6 Conclusion

The results presented here elucidate the ultimate practical limits for self-sensing displacement transduction by means of semiconducting piezoresistors. We have experimentally demonstrated the attainment of a force sensitivity at the level of 17 aN/√Hz at ~10K, a record for self-sensing devices. Furthermore, our analysis establishes that sub aN/√Hz sensitivity is attainable by scaling the cantilever dimensions downward into a regime that is readily attainable by top-down methods. Our analysis also elucidates, for the first time, the existence of a temperature- and geometry-dependent optimum bias current at which the force sensitivity is maximized. This analysis shows that heating effects in micro- and nanoscale piezoresistive devices become substantial for ambient temperatures below 1 K. This would appear to preclude attainment of quantum-limited force sensitivity at temperatures $T_0 \leq \hbar\omega_0 / k_B$ where the resonant mode becomes thermally depopulated, but otherwise clearly enables a wide range of applications requiring compact integrated high frequency force sensing with unprecedented sensitivity.

## 5.7 References


[1] J.L. Arlett, M. Paul, J. Solomon, M.C. Cross, S.E. Fraser, and M.L. Roukes, in *"Controlled Nanoscale Motion in Biological and Artificial Systems"* (Nobel Symposium 131, June 2005), H. Linke et al., Eds. (Springer Verlag, Heidelburg, *to be published*).

[2] D. Rugar, R. Budakian, H.J. Mamin, and B.W. Chui, Nature **430**, 6997 (2004).

[3] J.A. Harley and T.W. Kenny, Appl. Phys. Lett. **75**, 289 (1999).

[4] I. Bargatin, E.B. Myers, J. Arlett, B. Gudlewski and M.L. Roukes, Appl. Phys. Lett. **86**, 133109 (2005).

[5] C.W. Yuan, E. Batalla, M. Zacher, A. L. de Lozanne, M.D. Kirk, and M. Tortonese, Appl. Phys. Lett. **65**, 1308 (1994).

[6] F.J. Morin, T.H. Geballe, and C. Herring, Phys. Rev. **105**, 525 (1957).

[7] B.W. Chui, T.W. Kenny, H.J. Mamin, B.D. Terris, and D. Rugar, Appl. Phys. Lett. **72**, 1388 (1998).

[8] X. Li, T. Ono, Y. Wang, and M. Esashi, Appl. Phys. Lett. **83**, 3081-3083 (2003).

[9] CFD-ACE, Computational Fluid Dynamics Research Corporation, Huntsville, AL.

[10] O.N. Tufte and E.L. Stelzer, J Appl. Phys. **34**, 313 (1963).

[11] W.P. Mason and R.N. Thurston, J. Acoust. Soc. Am. **29**, 1096 (1957).

[12] W.S. Hurst and D.R. Frankl, Phys Rev **186**, 801 (1969).

[13] W. Fon, K.C. Schwab, J.M. Worlock, and M.L. Roukes, Phys. Rev. B **66**, 045302 (2002).

[14] T. Klitsner, J.E. VanCleve, H.E. Fischer, and R.O. Pohl, Phys Rev B **38**, 7576 (1988).

[15] W.A. Little, Can. J. Phys. **37**, 334 (1959).

[16] L.J. Sham, Proc. Phys. Soc. **81**, 934 (1963).

[17] J.E. Aubrey, W. Gubler, T. Henningsen, and S.H. Koenig, Phys. Rev. **130**, 1667 (1963).

[18] K.Y. Yasumura, T.D. Stowe, E.M. Chow, T. Pfafman, T.W. Kenny, B.C. Stipe, and D. Rugar, JMEMS **9**, 117 (2000).

# 6 Measured response in Gaseous Ambients

## 6.1 Introduction

Sensors can be broadly classified into two categories, namely active sensors and passive sensors. The latter is described in chapter 5, where we studied thermomechancial motion of silicon piezoresistive micro- and nano- cantilevers in vacuum, and in chapter 8, where we investigate Brownian fluctuations using gold piezoresistive cantilevers embedded in microfluidics. In this chapter we discuss active piezoresistive sensors in gaseous ambients. (Active piezoresistive sensors in fluid will be discussed in chapter 7). Device actuation plays an important role both in the characterization of devices and in their application as practical sensors. Many methods of actuation are available, and sensors employing them range widely in their fabrication complexity, ease of use, and sensitivity. Here we discuss several methods of actuation that have proved useful in our studies. The simplest of these techniques, requiring no external hardware or extra fabrication beyond that to incorporate displacement sensing is thermal actuation. This is achieved by applying an AC current across the cantilever legs to excite the cantilever through thermally-induced strain. Off-chip piezoelectric actuation, "shaking" the entire chip, also provides a simple method of characterizing the cantilever's response and requires minimal hardware and no additional fabrication. Magnetic actuation requires extra fabrication since magnetic material must be placed at the cantilever tip and the magnetic coil must be wound and positioned in close proximity to the device. The advantage of this method over the off-chip piezoelectric actuation, in which the entire silicon chip is undergoing vibration, is that it has less coupling to the rest of the surroundings. Similar benefits could be achieved with direct on-chip piezoelectric actuation while requiring

minimal external hardware; preferable for many applications. However, due to the additional level of fabrication complexity, this method of actuation has not been pursued here.

## 6.2 Actuation by Heating

This technique is used in this work for quickly finding the resonance of cantilevers which are intended for stochastic sensing and therefore do not have an integrated drive technique. The cantilever is biased with a dc voltage ($V_{dc}$) to which an ac sinusoidal waveform is superimposed. The presence of such a voltage will lead to sinusoidal heating in the conducting layer of the device. This heating and the resulting thermal expansion of the conducting (surface layer) of the device leads to a surface strain in the device (Fig. 6.2.A (a)), measured as a resistance change of the piezoresistive sensor. To first order, the resultant surface strain (and measured resistance change) is proportional to the temperature increase. For small power levels the device temperature is in turn linearly proportional to the power which depends on the square of the applied voltage. This discussion implies that

$$\delta R_d = \beta_t \mathrm{v}^2, \qquad 1$$

where $\beta_t$ is a constant of proportionality and v is the voltage drop across the piezoresistor. The electrical configuration is depicted schematically in Fig. 6.2.A (b), where the device is placed in a bridge circuit with bias resistance, $R_b$, and a voltage, $V = V_{dc} + V_{ac}\cos(\omega t)$, is applied across the device and bias resistors. To order $\delta R_d$, the measured signal is the voltage across the device, v (= $V_A$-$V_B$ in Fig. 6.2.A (b)):

$$\mathrm{v} = V_\mathrm{A} - V_\mathrm{B} = \frac{V}{R_b + R_d} R_d = I_b R_{d_o} + \alpha_R I_b \delta R_d, \qquad 2$$

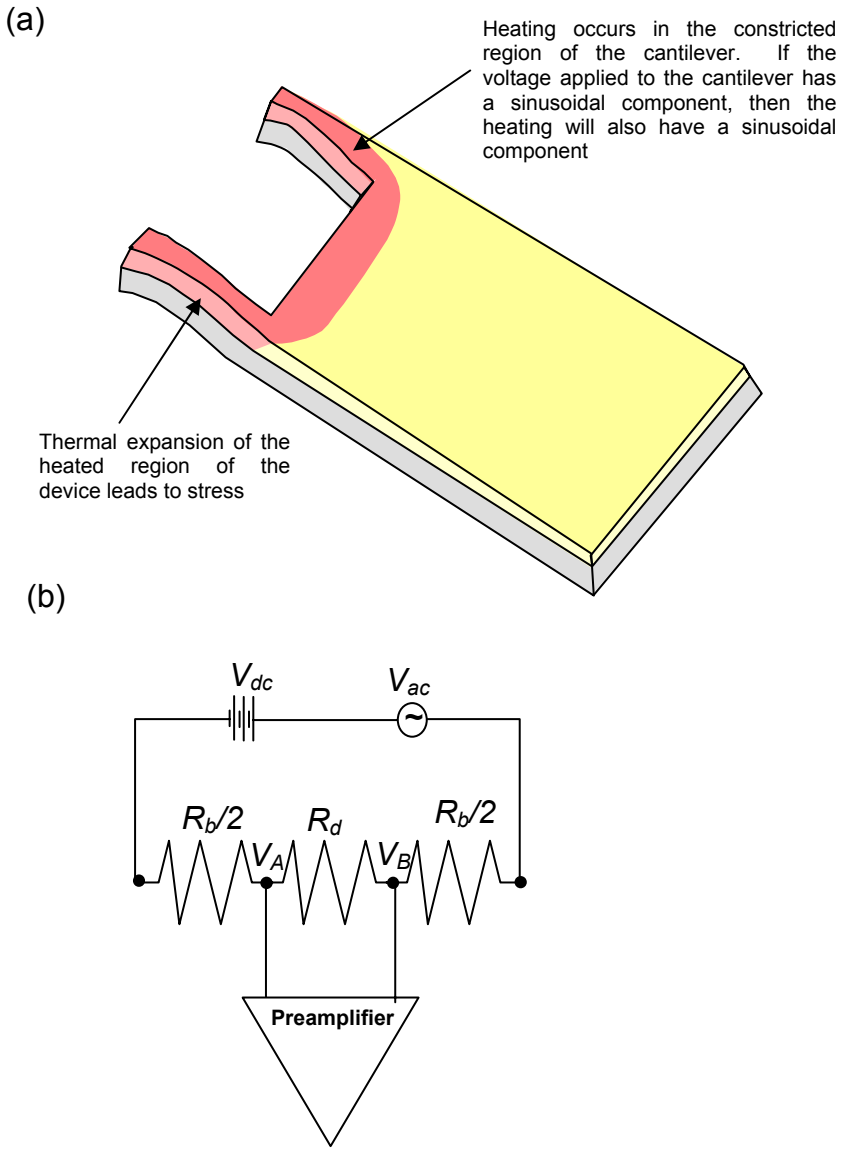


**Fig. 6.2.A Thermal excitation – schematic depiction**

(a) Heating of the conducting region of the device leads to a surface stress. If a sinusoidal current is applied to the device thent he surface stress will also have a sinusoidal component. (b) Electrical configuration for experiments employing actuation by heating. A symmetric distribution of the bias resistance is chosen so that the distal end of the cantilever is at ground. A single resistance $R_b$ can also be used and does not change the analysis. Such a configuration is preferred if a.c. coupling to the preamplifier is not an option (for low frequency measurements) since it allows nulling of the d.c. bias voltage at the preamplifier input. A grounded device tip is preferred in cases where capacitive interaction with the surroundings is to be minimized, for experiments with a voltage sensitive device tip (such as biodetection experiments), and for all experiments in fluid where capacitive coupling to the fluid is a concern.

where $R_{d_o}$ is the unstrained device resistance and the following parameters were defined to simplify the appearance of the equations: $I_b = V/(R_{d_o} + R_b)$ and $\alpha_R = R_b/(R_{d_o} + R_b)$. All terms of order $\delta R_d^2$ or greater have been dropped.

Using the expression for $\delta R_d$ from equation 1,

$$\mathrm{v} = \frac{1-\left(1-4I_b^2\alpha_R\beta_t R_{d_o}\right)^{1/2}}{2I_b\alpha_R\beta_t} \sim I_b R_{d_o} + 2I_b^3 R_{d_o}^2 \alpha_R \beta_t, \qquad 3$$

where $R_{d_o}$ is the resistance of the device for infinitesimal current flow. The first term gives a DC offset and background at frequency $\omega$. Since $I_b = V/(R_{d_o} + R_b)$ and $V = V_{dc} + \mathrm{v}_{ac}\cos(\omega t)$, the second term will give contributions at dc, $\omega$, $2\omega$, and $3\omega$. These are summarized in Table 6.2.A, where the signal's Lorentzian line shape is contained within the parameter $\beta_t$. In Fig. 6.2.B we presented data for the first harmonic of a device excited in this fashion. For this particular device the resonance was at 563 *k*Hz. This device had a resistance of 20 *k*Ω. Symmetric balance resistors of 6.2 *k*Ω were used. As expected, the signal is observed to scale as $V_{dc}^2$, shown in Fig. 6.2.B (b). From a best fit to this data we obtain $\beta_t$=0.7 Ω/V$^2$. The data presented here is for a device similar to that on which $\partial R_d/\partial x$ was measured directly using the AFM in Fig. 4.1.D. Based on that data we estimate $\partial R_d/\partial x \sim 2\mathrm{x}10^7$ Ω /m. We can now extract an actuation responsivity, $\mathcal{R}_A = \dfrac{\beta_t}{\partial R_d/\partial x} \sim 33\ n\mathrm{m}/V^2$.

| Harmonic | Signal | | |
|---|---|---|---|
| | Background | In phase component | Out of phase component |
| DC | $\frac{R_{d_o}}{R_{d_o}+R_b}V_{dc}$ | $\frac{2R_{d_o}^2R_b}{\left(R_{d_o}+R_b\right)^4}\left(V_{dc}^3+\frac{3}{2}V_{dc}V_{ac}^2\right)\beta_t$ | |
| ω | $\frac{R_{d_o}}{R_{d_o}+R_b}V_{dc}$ | $\frac{3R_{d_o}^2R_b}{2\left(R_{d_o}+R_b\right)^4}V_{ac}^3\beta_t$ | $\frac{6R_{d_o}^2R_b}{\left(R_{d_o}+R_b\right)^4}V_{dc}^2V_{ac}\beta_t$ |
| 2ω | ---------- | $\frac{3R_{d_o}^2R_b}{\left(R_{d_o}+R_b\right)^4}V_{dc}V_{ac}^2\beta_t$ | ---------- |
| 3ω | ---------- | $\frac{R_{d_o}^2R_b}{2\left(R_{d_o}+R_b\right)^4}V_{ac}^3\beta_t$ | ---------- |

**Table 6.2.A Expected harmonics excited through thermal actuation**

The harmonics excited through thermal excitation are shown here. Notice that for $V_{ac} \ll V_{dc}$ the dominant component of the signal is out of phase while the background is entirely in phase. The background can also be avoided by looking at higher order harmonics.

(a)

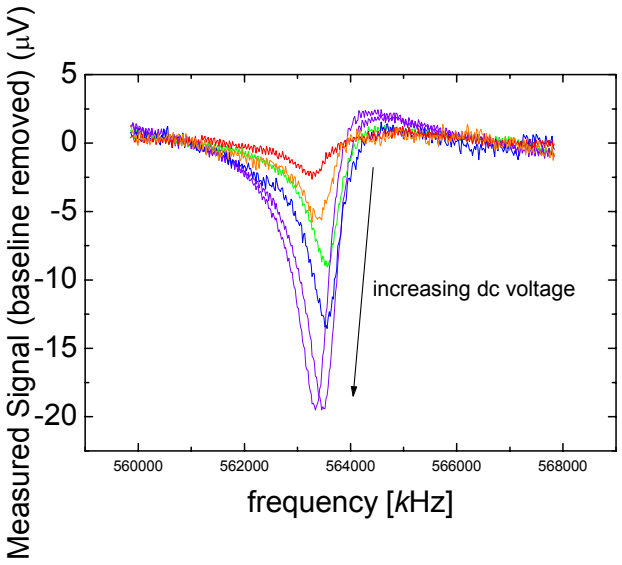


(b)

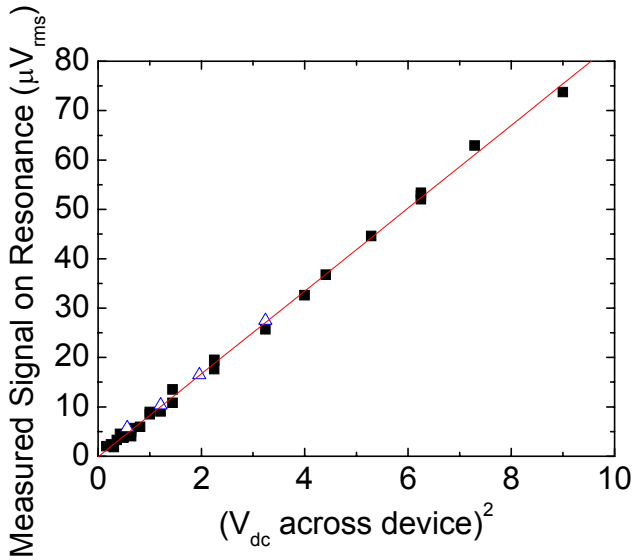


**Fig. 6.2.B Thermal actuation of a piezoresistive cantilever**

(a) Resonance detection through thermal actuation from an AC voltage applied directly across the device. DC voltages applied across the device and balance resistors: 0.5V (red), 0.8V (orange), 1.0V (green), 1.2V (blue), and 1.5V (violet). An AC root mean square voltage of 0.445V was applied in all cases. (b) Observed dependence of resonance peak height on dc voltage applied across the device (the points marked with a hollow blue triangle have the polartity of the dc bias reversed as compared to those marked with a solid black square). A best fit is shown in red from which quantitative values for the actuation responsivity are extracted (see text).

## 6.3 Magnetic Actuation

For this means of actuation, magnetic material is deposited on the cantilever tip and the cantilever is driven by an a.c. current through a small solenoid positioned directly above the current. This is depicted in Fig. 6.3.A. Permalloy is used for the magnetic tip. This was implemented both as thin pads (30nm thickness) that were deposited by e-beam evaporation and as electrodeposited columns. Both are shown in Fig. 6.3.B. The coil is fabricated by hand-winding (in a fiber optic assembly) a 25 μm diameter copper wire around a 50 μm diameter nickel-iron alloy core.[1] A picture of a typical coil is shown in Fig. 6.3.C.

### 6.3.1 Estimation of Coil – Magnetic Cantilever Tip Force

To determine the force felt by the cantilever in the presence of a magnetic coil, we must first calculate the field gradient arising from the coil. The coil is composed of a solenoid of approximately 40 turns with a core of nickel alloy 120, an alloy of 70% nickel and 30% iron. The magnetic field intensity inside the solenoid is given by

$$H = \frac{N_t I}{L}, \qquad 4$$

where $N_t$ is the number of turns, I is the current passing through the solenoid, and L is the solenoid length. For, I~0.3A and L~0.5 *m*m (the wire is 25$\mu$m thick and the turns are double wound so the coil is 20 turns in length) this yields $H$~2.4x10$^4$ A/m. This magnetic intensity is sufficient to saturate the core[2] so we have inside the core, $B_o$~1.1T. (We typically have been using I~0.02A which would give $H$~1.6x10$^3$A/m~20 Oe. If this magnetic intensity were achieved it would still be enough to saturate the core,[2]

(a) (b)

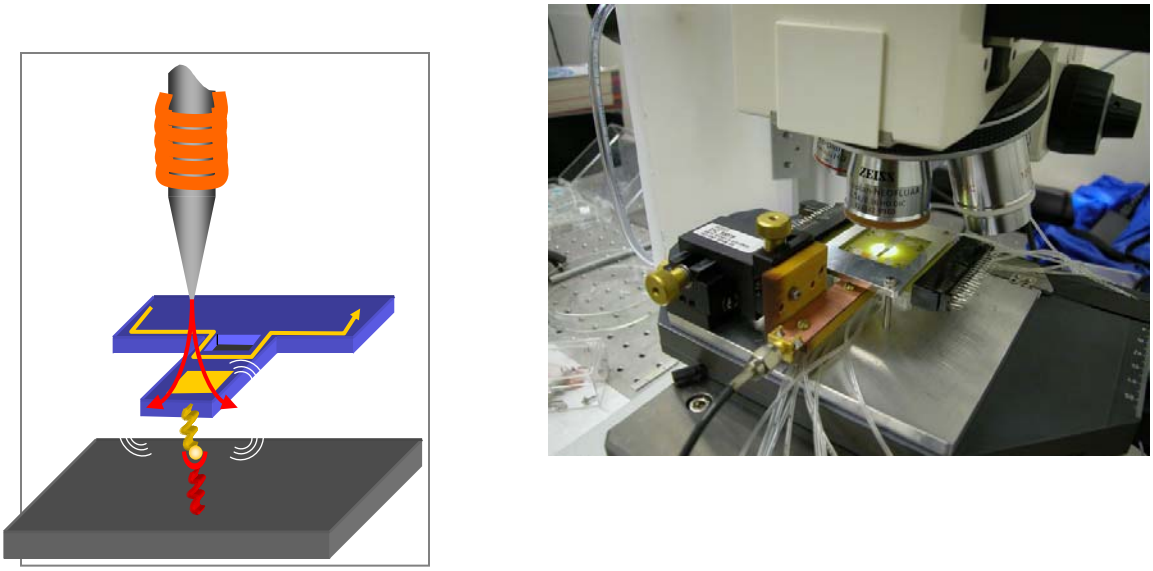

**Fig. 6.3.A Magnetic actuation**

(a) Schematic depiction of magnetic coil and cantilever with magnetic tip. (b) Actual implementation; the printed circuit board (copper) at the front of the image provides electrical contact to the coil which extends out over the device (which is located at the center of the microscopic field of view).

(a)

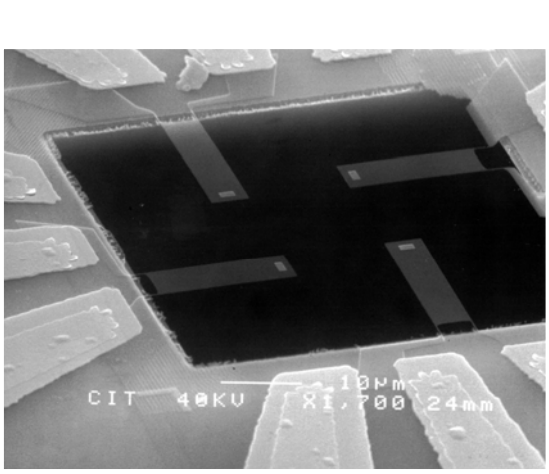


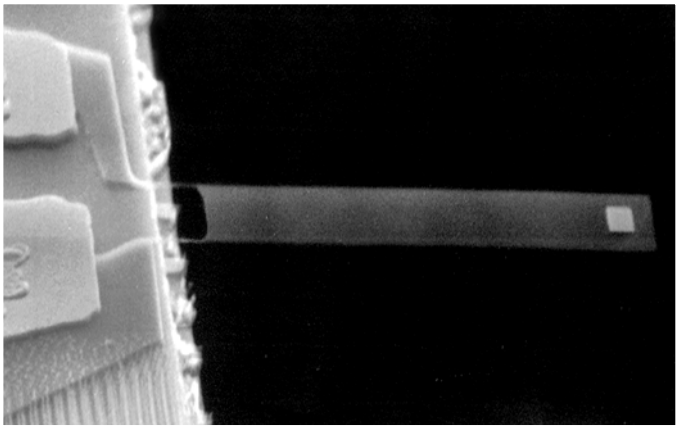

(b)

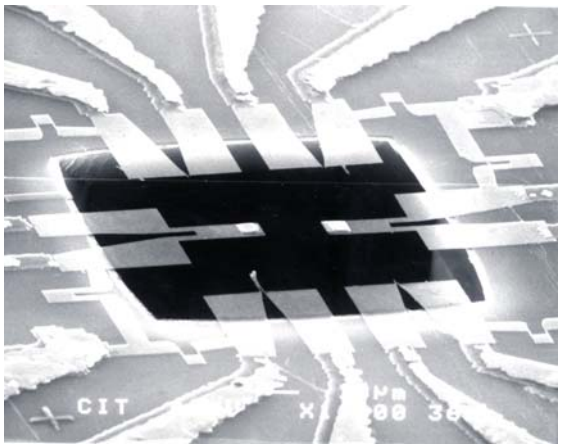


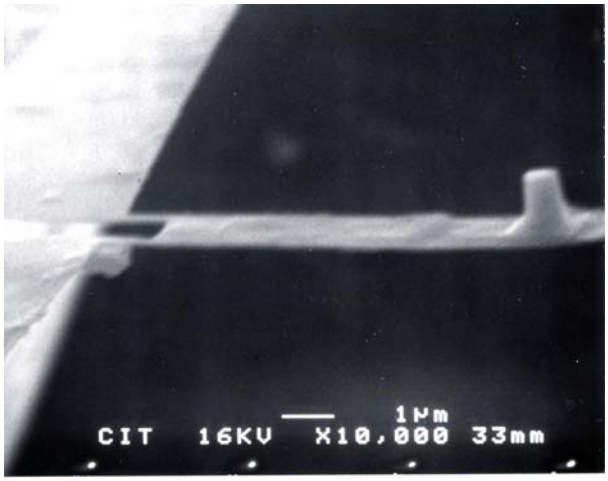


**Fig. 6.3.B Typical devices with magnetic tips**

(a) Devices with 30nm permalloy pads deposited by e-beam evaporation. (b) Devices with electrodeposited permalloy tips.


**Fig. 6.3.C Optical image of a typical magnetic tip**

The coil is composed of a solenoid of approximately 40 turns (the wire is 25µm thick and the turns are double wound so the coil is 20 turns in length) with a core of nickel alloy 120, an alloy of 70% nickel and 30% iron.

however this estimation is highly simplified, and in practice the core is not saturated at this current. The calculation presented below should therefore be considered an overestimate of the expected force.

The field and field gradient at the pad on the cantilever will be estimated in two ways. In the first (crude) approximation the tip is ignored except to approximate that the field intensity is carried to the tip through the saturated core, and it is therefore as if the solenoid were located at the tip instead of higher up on the nickel core (0). In the later improved calculation the magnetic field is calculated directly, taking into consideration the tip geometry.

### 6.3.2 First Estimate of Coil-Cantilever Magnetic Force

As an initial (crude) first estimate of the coil-cantilever magnetic force, we ignore the tip geometry and treat the solenoid is treated as if it were located at the magnetic tip; *i.e.*, to estimate the field outside the solenoid we first make the assumption that the field will be carried to the tip of the core, and we may then calculate the field as a function of the distance from the tip as if the solenoid where right at the tip (Fig. 6.3.D). At a point z along the axis of the solenoid we have[4,5]

$$B \sim \frac{B_o}{2}\left(\cos\alpha - \cos\beta\right), \tag{5}$$

where $b$ is the radius of the solenoid and subtends an angle β at the bottom of the coil and $\alpha$ at the top of the coil. The field gradient in the z direction is therefore given by

$$\frac{dB_z}{dz} \sim \frac{B_o}{2}\left(\frac{L}{\sqrt{\left(z+L\right)^2+b^2}} - \frac{1}{\sqrt{z^2+b^2}} - \frac{\left(z+L\right)^2}{\left(\left(z+L\right)^2+b^2\right)^{3/2}} + \frac{z^2}{\left(z^2+b^2\right)^{3/2}}\right). \tag{6}$$

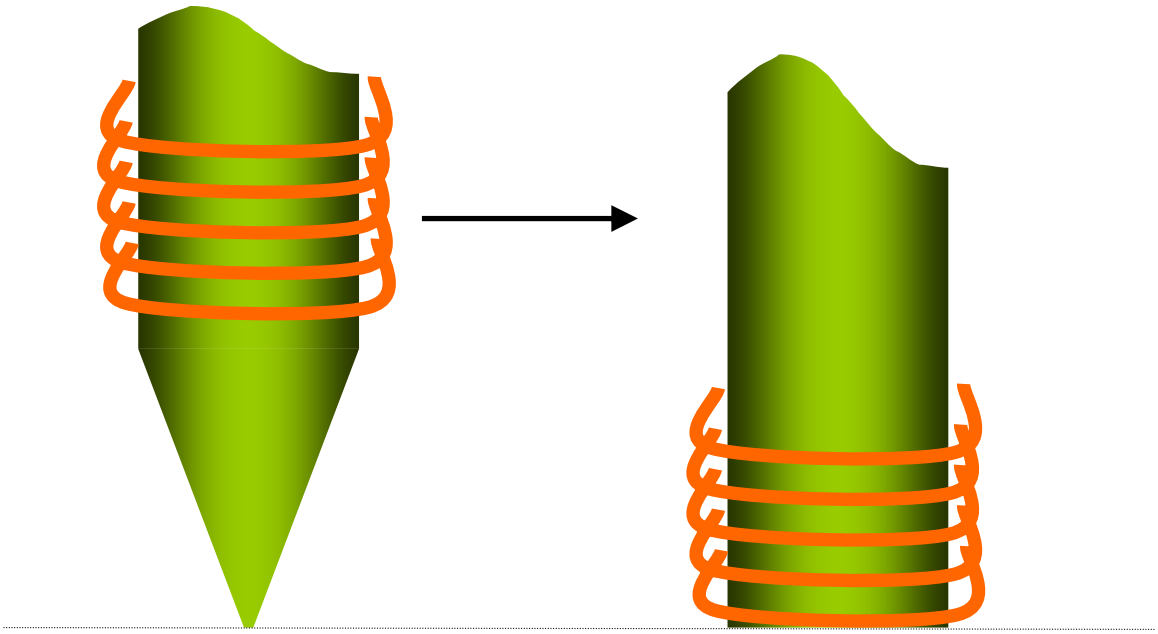

**Fig. 6.3.D Approximation for initial estimation of coil-tip force**

In the first estimate for the field gradient at the pad it is assumed that the magnetic coil/tip may be approximated by a solenoid located at the tip location.

Next we must determine the magnetic moment for the material on the tip of the cantilever. For $z$=50 μm and $b$=25 μm, the magnetic field at the cantilever tip is $B$~5.8x10$^{-2}$ T ($H$=4.6x10$^4$). For this field, for permalloy, $H$~1.6 A/m**²**. Therefore, the magnetization is given by $M=B/\mu_o-H$~4.6x10$^4$ A/m. Note that this magnetization is out of plane (if it were in plane the force would be zero). While it is difficult to produce a thin film magnet with a permanent out of plane magnetization, this problem arises from the fact that in plane magnetization is energetically favorable and thermal fluctuations are sufficient to pull the direction of magnetization back in plane. At the frequencies we are interested in (~100 kHz) this is not a cause for concern, and we will observe essentially the full magnetization. Table 6.3.A summarizes the force for pads of cross-section 1.5μm *x* 1.5 μm for three different thicknesses.

### 6.3.3 Estimation of Magnetic Force, Taking into Account the Tip Geometry

The above analysis ignored the pointed tip except to treat the solenoid as if it were located right at the pointed tip instead of further back. Here we attempt a slightly more detailed treatment of the tip. Except in the solenoid region, there are no free currents and $\nabla$xH=0. We may therefore solve the problem with a magnetic scalar potential satisfying Laplace's equation, $\nabla^2\phi_m = 0$. From the above calculation the field arising from the solenoid is adequate to saturate the core, and we may approximate that the core therefore has a uniform magnetization $\boldsymbol{M}=-B_o/\mu_o\ \hat{z}$. The magnetic potential at position ***x'***, with ***x'*** on the axis of the solenoid, is given by

$$\phi_m = \frac{1}{4\pi}\oint_S \frac{\vec{n}\cdot\vec{M}}{|\vec{x}'-\vec{x}|}d\vec{x} = \frac{M}{4\pi}\int_0^a \frac{2\pi r\sin\beta}{\sqrt{(z'+z)^2+(r)^2}}\ dz = \frac{b^2M}{2a\sqrt{a^2+b^2}}\int_0^a \frac{z}{\sqrt{(z'+z)^2+\left(\frac{zb}{a}\right)^2}}\ dz \quad ,7$$

**Table 6.3.A Initial estimate of force for several different possible pad thicknesses.**

This calculation ignores the tip except to assume that the solenoid may be treated as if it were at the location of the tip as depicted schematically in 0. A separation of 50$\mu$m is assumed for the cantilever tip to coil distance.

| Permalloy Thickness [nm] | Force [pN] |
|---|---|
| 30 | 170 |
| 400 | 2300 |
| 1500 | 8800 |

where $\vec{n}$ is the outward pointing normal vector from the surface, b is the radius of the solenoid core, a is the tip length (see Fig. 6.3.E for clarification), and β and r depend on z (the vertical distance above the magnetic tip) and are shown in Fig. 6.3.E. The side surfaces of the core outside the tip region do not contribute since $\vec{n} \cdot \vec{M}$ =0. The surface at the top of the core has been ignored (this is ~3cm from the region of interest as compared to the tip, which is ~50μm; its effect is therefore negligible). From this we have B=$\mu_o \nabla \phi_m$. Substituting b=25μm and a=80μm (see Fig. 6.3.C) and using z=50μm we obtain B~1.7x10$^{-2}$T at the pad (which gives H~1.3x10$^4$ A/m or 170 Oe). The saturation magnetization for permalloy is 8.8x10$^5$ A/m. For separations in the 50μm-300μm the magnetization goes roughly as the tip-coil separation squared. The force for several pad thicknesses and two possible tip-coil separations are shown in Table 6.3.A. For our devices we can achieve a separation of ~50μm in the absence of microfluidics. The separation when microfluidics are used is limited by the minimum glass thickness we can obtain and use for processing (130μm) and an additional 50μm of clearance to minimize the risk of damaging the coil. The force is given by $F = MV\nabla B$. Therefore, for the purpose of extrapolating to other tip-coil separations, the magnetic field gradient at the cantilever tip as a function of the vertical displacement from the magnetic coil is shown in Fig. 6.3.F. Next we consider magnetic beads. Bangs Laboritories makes beads that are 0.9μm in diameter and 63.4% magnetite. For magnetite the saturation magnetization is 4.818x10$^5$ A/m.[6] This leads to a force of 10pN per bound bead.

In practice we observe an increased signal with drive to the coil showing that the core is not in fact saturated. This must be a consequence of complications from the tip

**Fig. 6.3.E Parameters for calculation of field from magnetic tip.**

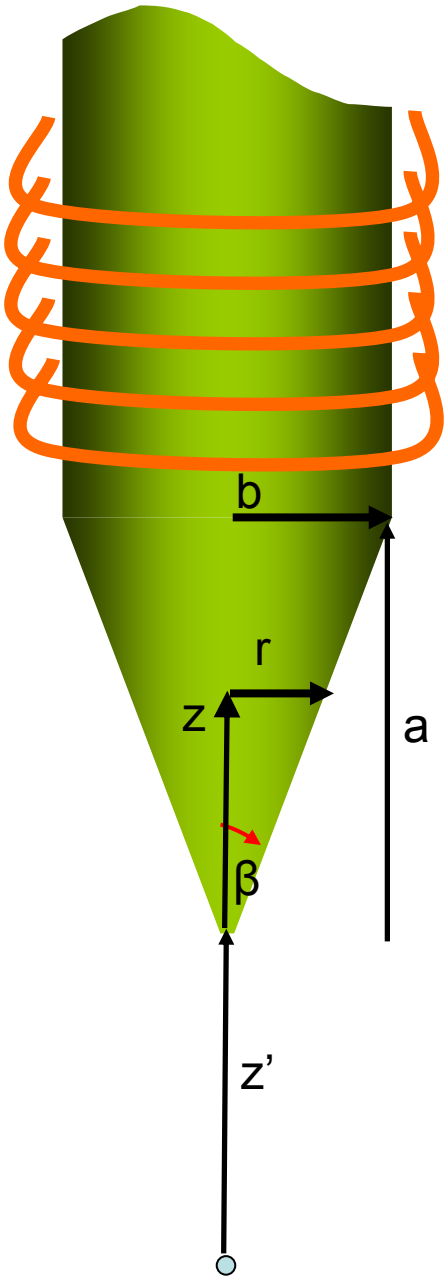


The parameters indicated on the schematic above are used for the calculation of the filed from the magnetic tip. b is the radius of the solenoid core, a is the tip length, z is the vertical distance above the magnetic tip, and β and r depend on this parameter.

**Table 6.3.A Force estimate for several different possible pad thicknesses**

This table presents the results discussed in section 6.3.3 in which the effects of the tip geometry are taken into account. For these calculations a pad of 1.5μmx1.5μm was used.

| Permalloy Thickness [nm] | Force [pN] 50μm separation | Force [pN] 180μm separation |
|---|---|---|
| 30 | 22 | 1.6 |
| 400 | 290 | 21 |
| 1500 | 840 | 61 |
| Magnetic bead diameter | | |
| 0.9 μm | 68 | 5 |

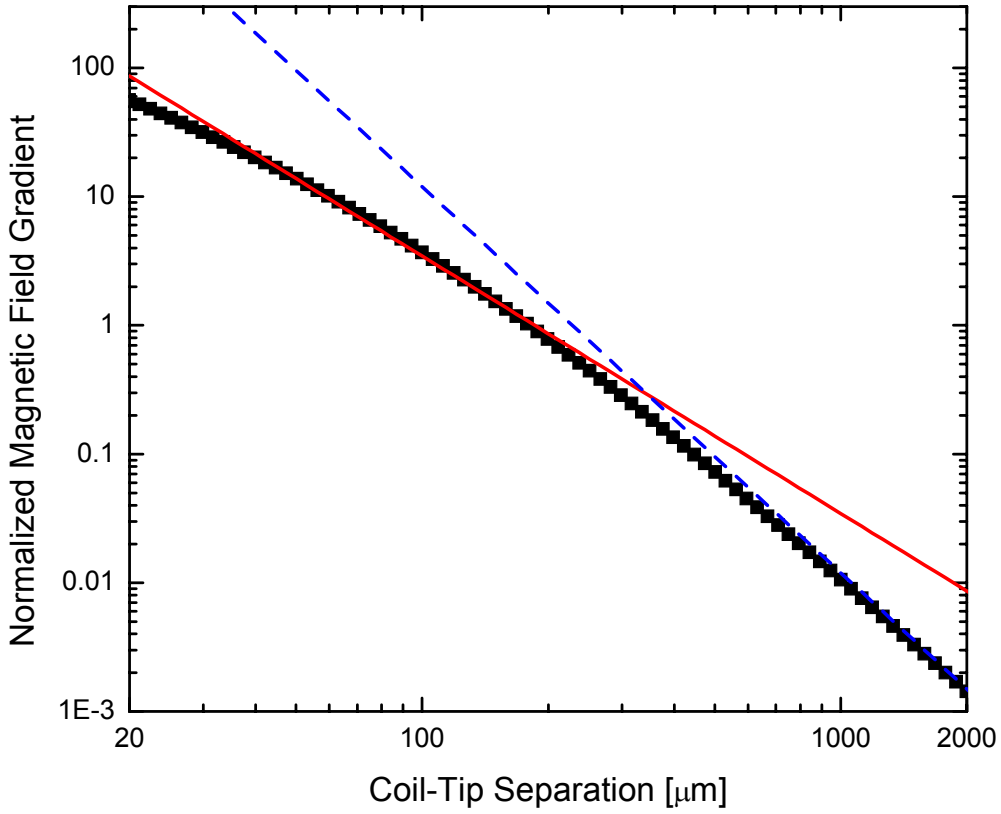


**Fig. 6.3.F Dependence of magnetic field gradient at the cantilever tip on tip-coil separation**

The dependence of magnetic field gradient at the cantilever tip on tip-coil separation (black squares). The field gradient has been normalized to its value at 180 μm. For the separations of interest the dependence is roughly the inverse of the separation squared, represented by the solid red curve as a guide to the eye. For larger separations the dependence is better represented by the inverse of the separation cubed, represented by the dashed blue curve as a guide to the eye.

Structure. While from this simplified calculation we expect the core to be saturated in the solenoid region of the core, the domain structure in the tip region could be complicated. The calculation here is therefore an overestimate of the maximum force and gives a limiting value as the current to the solenoid and number of coils is increased.

### 6.3.4 Experimental Results for Magnetic Drive in Vacuum and Ensuing Force Estimation

In this section we discuss the results for one of the larger cantilevers shown in Fig. 6.3.B(b). This cantilever is 20μm in length, 6 μm in width, has a leg length of 5 μm and a leg width of 2 μm . The permalloy tip has a 4 μm x4 μm base, is 2 μm in height, and is centered 3 μm from the cantilever tip. The device of resistance 34kΩ is placed in series with a 40kΩ resistor. Two additional adjustable resistors are placed in parallel to form a balanced Wheatstone bridge. A 2.6V battery is used to apply a potential across the bridge. $0.25V_{rms}$ is applied to the magnetic coil using the source from the HP3589A network analyzer. The estimated coil-tip vertical separation is 80μm. The custom preamp described in section 4.2.1 is used, followed by a Stanford low noise preamplifier (SR560) before entering the input of the HP3589A. The measured response at a pressure of 40mTorr is shown in Fig. 6.3.G (a). The measured quality factor for the observed resonance is 460. For this measurement the bridge circuit and custom preamplifier were inside the belljar; all other electronics (including the 2.6V battery) were outside the belljar. This data is collected by subtracting the signal when a positive and negative d.c. bias is applied across the cantilever to remove the component from direct feedthrough. We estimate this device to have a gauge factor of $5x10^{6}\Omega/m$ and an effective mass of $2.9x10^{-13}kg$. Using these numbers and the Lorentzian fit to the curve in Fig. 6.3.G (a) we

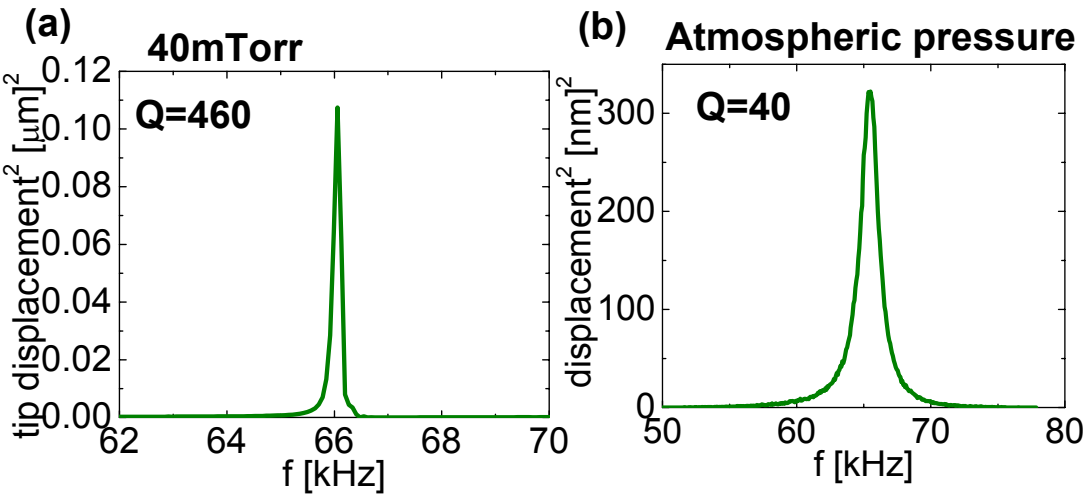


**Fig. 6.3.G Experimental data for magnetic drive at 40mT**

Measured response for one of the large cantilevers from Fig. 6.3.B (dimensions provided in the text) . (a) 40mTorr, the quality factor for this resonance is 460. (b) atmospheric pressure, the quality factor is 40.

may estimate the magnetic drive force to be 36pN. If the calculation of section 6.3.3 is performed for this geometry, a force of 3nN is obtained. The discrepancy is attributed to the assumption in the calculation that the magnetic core at the center of the coil is saturated. That we are still in the linear regime with respect to current applied to the magnetic coil (and consequently far from the saturation regime) is shown by the data in Fig. 6.3.H. This data was obtained using a different device, but the current applied across the coil spans the range used for the device in Fig. 6.3.G (a). It is interesting to compare the forces corresponding to the data of Fig. 6.3.G and Fig. 6.3.H since the volume of permalloy on the cantilever discussed in Fig. 6.3.H is a factor of 16 less than that for Fig. 6.3.G. The force corresponding to the signal measured for a voltage of $0.2V_{rms}$ applied across the coil in Fig. 6.3.H is 8pN, a factor of 4 less than that for the much thicker pads. Exact agreement is not expected due to variations in coil fabrication (number and tightness of turns and proximity of coil to the tip of the nickel-iron core) and cantilever-coil separation. For the curve with the greatest excitation in Fig. 6.3.H, namely, that with $1V_{rms}$ applied across the coil, the drive force is 50pN. The magnetic coil suffers thermal breakdown if the applied voltage is increased much beyond this.

### 6.3.5 Magnetic Driven Response in Air

The response in air for the same cantilever and configurations as discussed in section 6.3.4 is presented in Fig. 6.3.G (b). The quality factor for this resonance is 40. The results in vacuum (Fig. 6.3.G (a)) were analyzed by directly subtracting the real and imaginary components of the data obtained with a negative d.c. bias across the device from those obtained with a positive d.c. bias across the device and adding the results in quadrature. In the case of data collected in air, the signal to noise is much worse, and

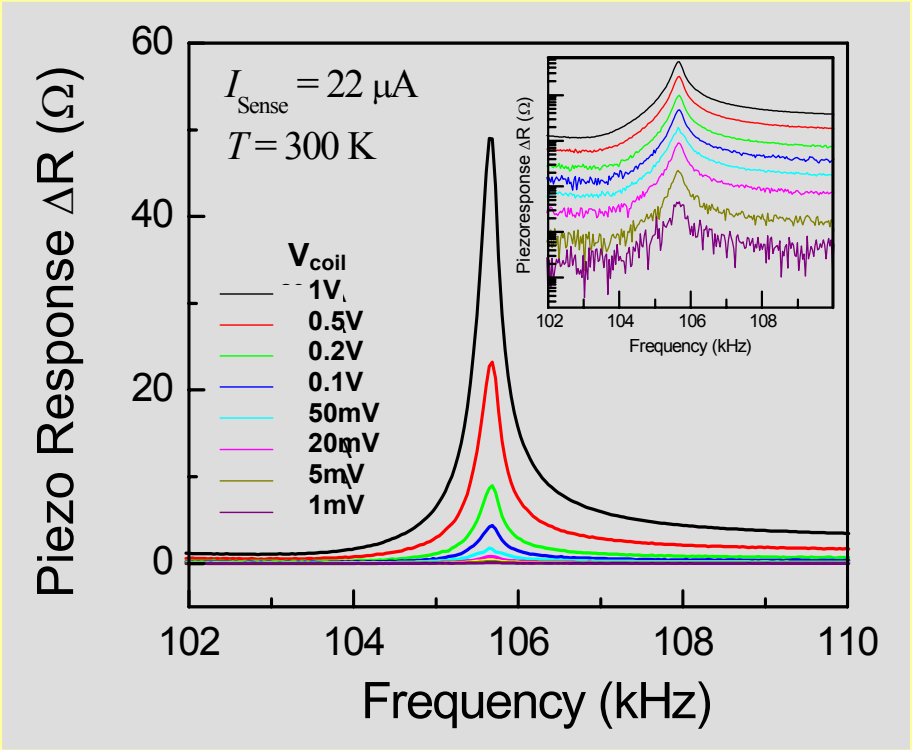


**Fig. 6.3.H Dependence of detected signal on current applied to magnetic coil**

The dependence of the observed signal on current applied to the magnetic coil is shown here. It is clear from this data that the coil is still in the linear regime. The calculations shown in section 6.3.3 (which assumed saturation) are therefore expected to overestimate the drive force. This data was collected on a cantilever with a thin permalloy pad (thickness 80nm). The cantilever length is 15.4μm, width 5μm, leg length 1.25μm, and leg width 0.3 μm. The sample resistance was 34.4kΩ. The peak deflection is 0.9μm for $I_{coil}$=20mA.

before combining the real and imaginary components it was necessary to perform a linear fit to the residual background signal and then subtract it. It is worth noting that while the offset of this linear fit was different for the real and imaginary data, the linear component of the respective residual backgrounds agreed to within the uncertainties of the fit. The source of this residual background is not fully understood but may in part be related to the fact that in the configuration used for this data, the cantilever tip was typically at ~∓0.65V relative to the coil (Fig. 6.3.I). The primary source of background signal in the measurements arises from the capacitive coil-tip coupling. The silicon epi layer of the cantilever is positively doped. When a negative voltage is applied to the cantilever tip, a large portion of the tip may be depleted of carriers due to the electrostatic cantilever/coil interaction, leading to an increase in the capacitance and a decrease in the observed fed-through signal. When the cantilever tip is positively biased relative to the tip of the magnetic coil, the carriers accumulated as close as possible to the magnetic tip, leading to a decreased capacitance and increased background feedthrough. However, due to the fixed boundary at the top of the cantilever the carriers cannot travel as far relative to their positions in the neutral (no bias applied between the cantilever/coil) state and a smaller effect is observed. This is depicted schematically in Fig. 6.3.J and reflected by the data in Fig. 6.3.K. This explanation appears consistent with the data for devices with ~30nm permalloy pads. For devices with electrodeposited pads, for which the pad thickness is of order 2$\mu$m (*c.f.* Fig. 6.3.B (b)), the proximity of the permalloy pad at the distal end of the cantilever to the magnetic coil is noticeably less than that of the doped epi layer. We therefore expect the capacitance to be dominated by the capacitive

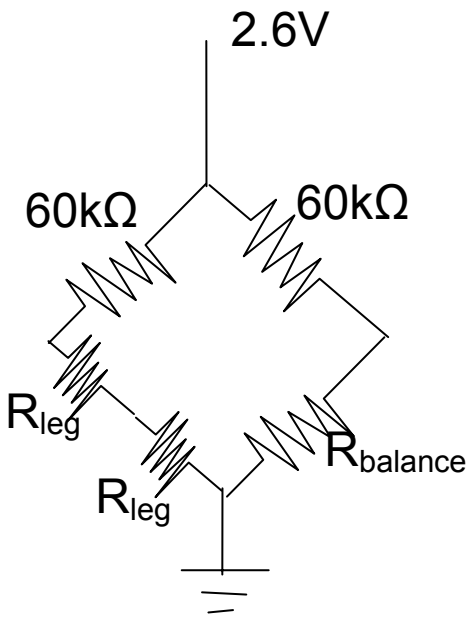


**Fig. 6.3.I Bridge used to balance the device**

The bridge configuration is shown schematically here.

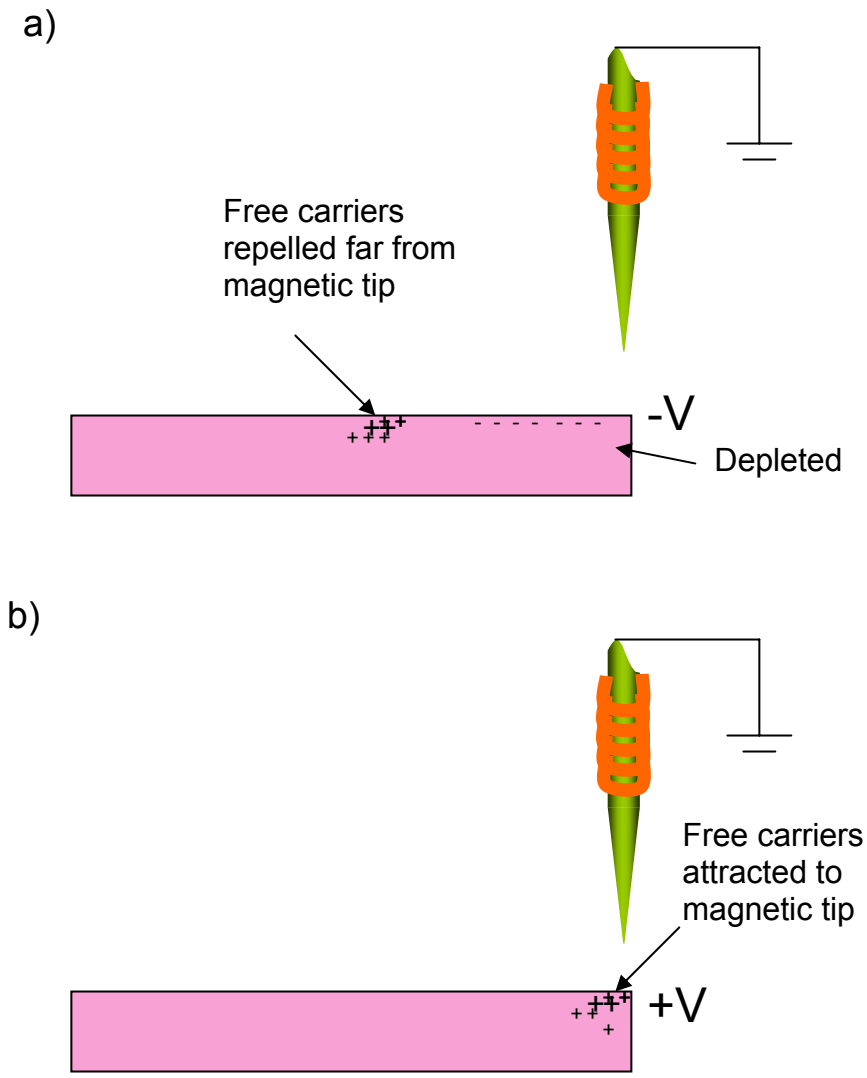


**Fig. 6.3.J Schematic depiction of Source of Residual Background**

Schematic depiction of the differing capacitance for a positive vs. negative bias applied to the cantilever tip. a) Negative bias applied to the cantilever tip. The free carriers (holes) are repelled far from the magnetic tip, increasing the capacitance. b) The free carriers are attracted to the magnetic tip, leading to a decrease in the capacitance. This effect is smaller than that for case (a) since the amount by which the free carriers may approach the magnetic tip is limited by the physical cantilever boundary.

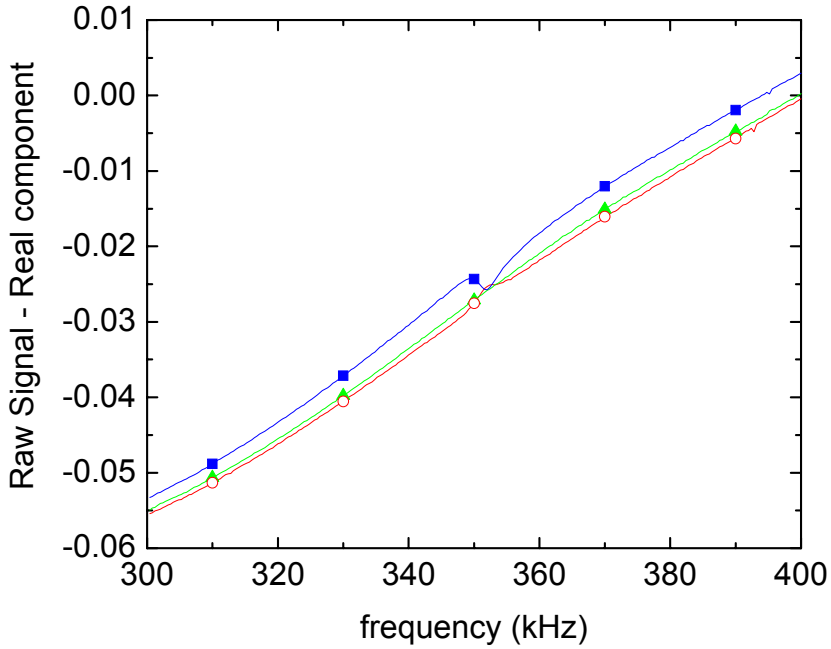


**Fig. 6.3.K Raw Data Showing Residual Background Consistent with Carrier Induced Changing Capacitance**

Raw data showing shift in background signal with applied cantilever tip – magnetic tip bias. For all curves the magnetic coil tip is grounded. Hollow red circles: positive voltage applied to cantilever tip. Solid green triangles: cantilever tip grounded. Solid blue squares: negative voltage applied to cantilever tip. This data was collected on a device with a 30nm permalloy pad.

coil-permalloy pad interaction. Indeed, the background is not observed to follow the trend discussed in this section for capacitive interaction between the entire cantilever and the magnetic coil (data shown in Fig. 6.3.L).

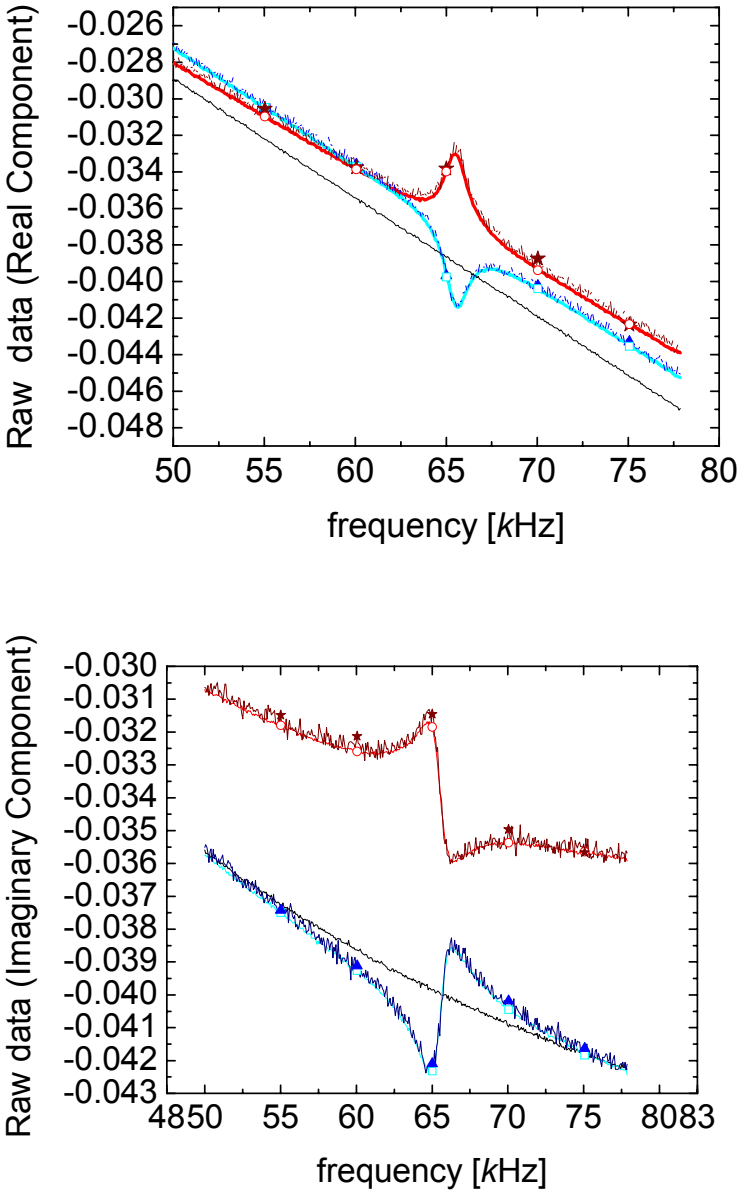


**Fig. 6.3.L Raw data for device with electrodeposited pad**

The data presented here is the raw data for the device with the electrodeposited pad (for which the data following background subtraction was shown in Fig. 6.3.G (b)). The data was collected in the following order: 1) Hollow red circles: $V_{bias}$=2.6V, average=360; 2) Hollow cyan triangles: $V_{bias}$=-2.6V, average=360; 3) Black: $V_{bias}$=0, average=220; 4) Solid wine stars: $V_{bias}$=2.6V, average=10; 5) Solid blue triangles: $V_{bias}$=-2.6V, average=10. The capacitance for these devices is dominated by the permalloy-coil interaction and therefore the background cannot be explained by analyzing the changing capacitance as discussed earlier in this section.

## *6.4 Actuation by Piezoelectric Drive*

### 6.4.1 Introduction

On-chip piezoelectric drive is conceptually the most direct actuation technique for achieving many of the goals of this project. In particular, it allows the cantilevers to be individually addressable. By contrast, for the magnetic actuation presented in the previous section, the magnetic coils are too large and the positioning too crude to address an individual device. Even if these could be improved, the "action at a distance" nature of the magnetic force would never allow as dense a packing of devices as for piezoelectric drive. Moreover, the current technique of carefully positioning a "large" magnetic coil by hand under a microscope is clearly not practical outside of a laboratory setting. Any future applications of this technology would require wafer bonding of micro-coils to the device wafer or additional fabrication steps to incorporate on-chip coils, with care taken for compatibility with the microfluidics (for either method). In this respect, the packaging of on-chip piezoelectric devices would be simpler. Unfortunately, developing a fabrication procedure for combining piezoelectric drive and piezoelectric actuation is non-trivial. As a first step we have implemented an off-chip piezoelectric drive. While this technique is impractical in fluid it allows for a quick characterization of the cantilever properties in air and vacuum.

### 6.4.2 Piezoelectric Driven Response in Vacuum

For these measurements the silicon die was placed on a piezoelectric crystal across which a sinusoidal voltage of 4V peak-to-peak was applied. The measured resonance at 30mTorr is shown in Fig. 6.4.A (a). 1.3Vdc was applied across the device for these measurements. (The bridge configuration of Fig. 6.3.I was used with 2.6V across the

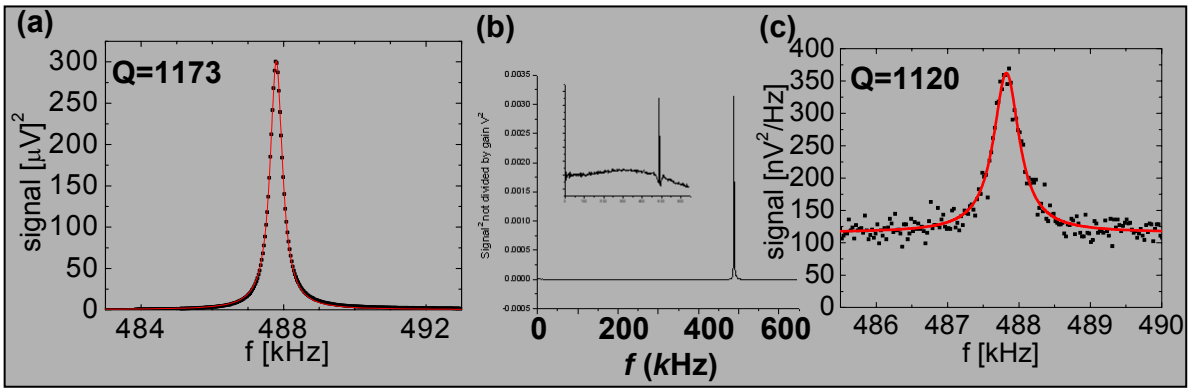


**Fig. 6.4.A Resonance Curve at 30mTorr with Piezoelectric Actuation**

(a) Piezoelectric actuation. From this fit a quality factor of 1173 is attained. (b) Same resonance as presented in (a) but shown over a 600 kHz scan. ***Inset:*** piezoelectric actuation data before any processing has been applied. Even in this "raw" form the resonance at 488 kHz is clearly visible on a 600 kHz scan. (a) and the main figure shown in (b) were collected by subtracting a background scan obtained with zero bias current applied to the cantilever. Note the reproducibility of the background. (c) Thermomechanical noise measured on the same device; the quality factor is 1120. Black: data, Red: Lorentzian fit. The cantilever dimensions are: $\ell = 8\mu m$, w=2μm, $\ell_1 = 1.6\mu m$, b=0.15μm, t=110nm.

bridge). A quality factor of 1173 was attained for this device. At resonance the peak signal was 17μV, corresponding to a resistance change of 3.7Ω. The gauge factor for this device is estimated to be $2.1 \times 10^8$ Ω/m. Using this we can calculate a peak displacement of 18nm. It was mentioned that this technique allows for quick characterization of the device resonance. In Fig. 6.4.A (b) data for the same device is shown over a much broader scan (from 0 to 600 *k*Hz). Even for the unprocessed data (shown as an inset to Fig. 6.4.A (b)), on a 600 *k*Hz scan the resonance is clearly visible at 488 *k*Hz. Moreover, the only processing applied to obtain the data shown in Fig. 6.4.A (a) and the main figure of Fig. 6.4.A (b) is the subtraction of a background scan obtained with zero bias current applied to the device. The reproducibility of the background is worth noting. The thermomechanical resonance was also measured on this device and is shown in Fig. 6.4.A (c). The measured quality factor from thermomechanical noise data is 1120.

### 6.4.3 Piezoelectric driven Response In Air

When this drive technique is used in air, the expected broad resonance of the damped response function is convolved with resonances in the sample holder assembly. This is expected due to the implementation commonly employed in the AFM community[7] in which the entire holder must vibrate, as opposed to local actuation of the device. The data are shown in Fig. 6.4.B. A rough fit to the data gives a quality factor of ~10, consistent with the value of 12 obtained for theoretical calculations based on the cantilever geometry.

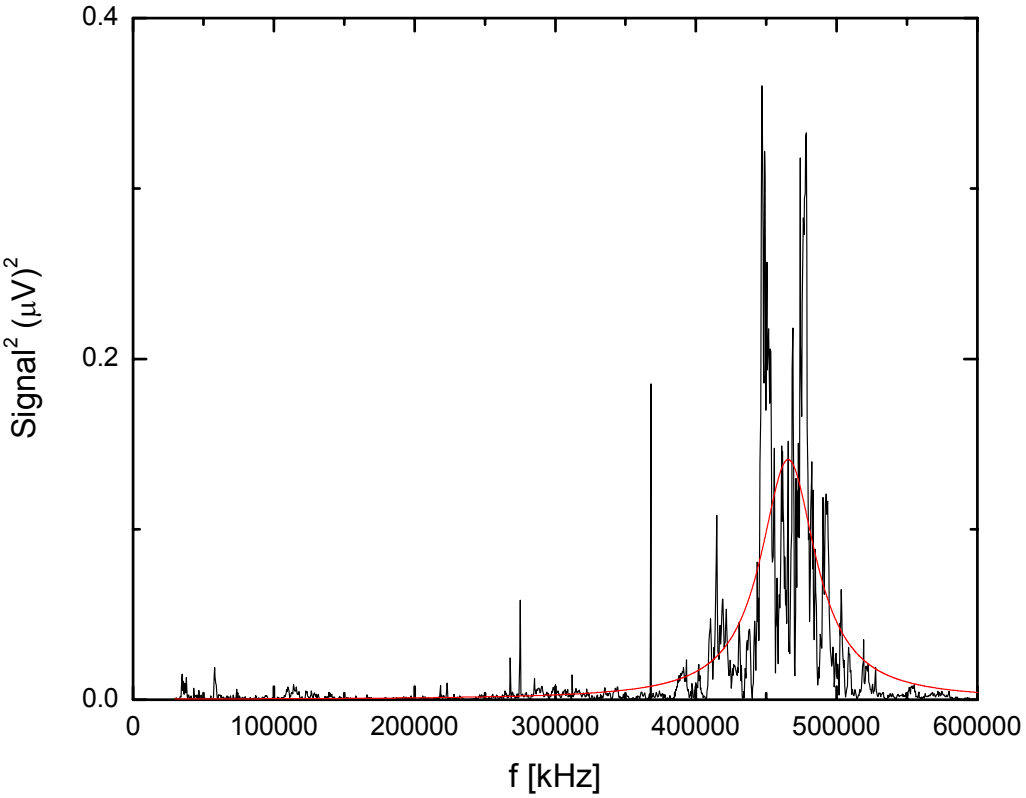


**Fig. 6.4.B Piezoelectrically driven resonance in Air**

The fine structure is consistently observed with this method of drive in air and arises from the response of the sample holder which also vibrates under this method of drive. Due to this fine structure the Lorentzian fit to the data is only presented as a guide. The quality factor for the fit shown is 10, consistent with the value of 12 obtained for theoretical calculations based on the cantilever geometry.

## 6.5 Directions for future experiments

Each of the methods of drive discussed in this chapter must be examined critically in light of the goal of using these methods of actuation for microfluidic based sensors. The first method, that of actuation by heating, is useful as a quick method for characterizing the device before immersing it in fluid. Whether it will prove useful in some form in fluid remains to be determined since the high thermal conductance of the fluidic environment permits only substantially reduced heating.

The limitations of the magnetic drive were presented in the text, namely the difficulty in achieving a sufficiently large actuation force, particularly in light of the separation imposed by the presence of the microfluidics. It is possible that these problems might be overcome, possibly through using an integrated coil that could be placed inside the microfluidics or by use of thinner glass, stronger coils and tip magnets, or some combination of the above. However, it is clear that any such solution will require extensive engineering while maintaining a number of drawbacks not shared by the on chip piezoelectric actuation discussed below. Namely:

- in its present form the magnetic drive is not localized to a particular cantilever but extends over all cantilevers in a given via,
- the drive is difficult to quantify and reproduce since it depends on the exact cantilever-coil separation, and
- it is difficult to combine magnetic drive with optical detection.

The final point is relevant since even though optical detection is not intended to be part of the final detection scheme, it is important for confirming the results of early measurements.

The (off-chip) piezoelectric drive technique used here is also not intended for measurements in fluid. (Although it might serve a purpose as an "ultrasound" to dislodge particles that become stuck and serve as a supplement to diffusion for bringing the analyte in contact with the cantilever). However, the extension of piezoelectric drive to on-chip actuation at the cantilever legs would be exciting both because the attainable drive forces are in the necessary range and because this would be a method of drive in which the cantilevers are individually addressable.

Here we perform a very crude (order of magnitude) estimate of the drive force for this form of actuation. The stress induced by a piezoelectric actuator is given by $e_p \vec{E}$, where $e_p \sim 1 C/m^2$ for typical piezoelectric materials. So for an area of 10 $\mu m^2$ and a force of 100pN (representative of typical antibody-antigen binding forces[8,9]) an electric field of 10V/m is required. Across the 100nm device thickness this corresponds to 1 μV. Clearly much higher forces could be attained while maintaining a tolerable voltage across the piezo actuator. This calculation is for a uniform force across a plate, and while the extension to a cantilever is non-trivial, this calculation suggests that the method of drive shows promise.

In order to minimize cross-talk the piezoelectric actuators should be located on separate legs from the piezoresistive sensors (Fig. 6.5.A). As mentioned in the introduction to section 6.4, the fabrication procedure for combining piezoelectric actuation and piezoresistive sensing is non-trivial (due to the number of fabrication steps involved). A new technology which would open the way to purely piezoelectric sensing and actuation is currently under development by Soitec (from whom we currently purchase SOI). Soitec is developing the techniques to fabricate new types of bonded wafers, including Gallium Nitride- On –Insulator wafers, referring to a three layer material comprised of a silicon handle layer, a buried oxide layer, and a thin Gallium nitride transducer layer. This would allow the fabrication of purely piezoelectric devices with our existing technology (the material would be fully compatible with top side electrode patterning and the DRIE plus oxide release suspension); the only new processing required would be the etching of the GaN itself, recipes for which are readily available in the literature.[10] Many of the greatest difficulties with current MEMS applications of GaN is the difficulty of selective etching and stop layers (currently accomplished using n-doped material as a stop layer for etching p-doped material).[11] This would no longer be a concern in an implementation using a bried oxide layer. Combining piezoelectric drive and sensing, allowing for the use of a single material, would greatly simplify the fabrication process.

**Fig. 6.5.A Conceptual schematic of device with piezoelectric actuation**

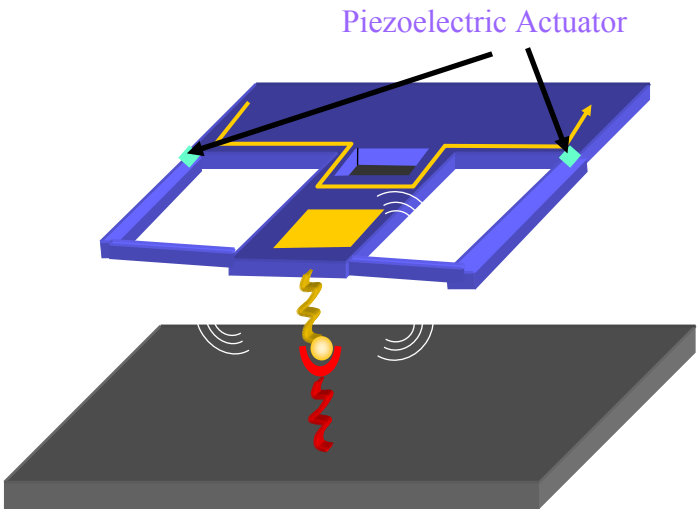


For electrical isolation the piezoelectric actuators would be located on separate legs from the piezoresistive sensors.

## 6.6 References


[1] M. Barbic, J.J. Mock, A.P. Gray, and S. Schultz, Appl. Phys. Lett., p. 1897-1899 (2001).

[2] Allegheny Ludlum Steel Corporation, Electrical Materials Handbook, Pittsburg, Pa, pVII-19 (1961).

[3] D. Jiles, Introduction to Magnetism and Magnetic Materials, Chapman and Hall, London, p. 294 (1991).

[4] I.S. Grant and W.R. Phillips, Electromagnetism, John Wiley and Sons, Chichester, p. 197 (1990).

[5] J. D. Jackson, Classical Electrodynamics, John Wiley and Sons, New York, p. 183 (1999).

[6] http://sorcerer.ucsd.edu/es160/lecture8/web6/node20.html

[7] T.E. Schäffer, J.P. Cleveland, ,F. Ohnesorge, D.A. Walters, and P.K. Hansma , J. Appl. Phys. **80**, 3622-3627 (1996).

[8] U. Dammer, M. Hegner, D. Anselmetti, P. Wagner, M. Dreier, W. Huber, and H.-J. Güntherodt, Biophys. J. **70**, 2437-2441 (1996).

[9] P. Hinterdorfer, W. Baumgartner, H.J. Gruber, K. Schilcher, and H. Schindler, Proc. Natl. Acad. Sci. USA. **93**, 3477-3481 (1996).

[10] M. Minsky, ,M. White, and E. Hu, Appl. Phys. Lett. **68**, 1531 (1996).

[11] R.P. Strittmatter, R.A. Beach, and T.C. McGill, Appl. Phys. Lett. **78**, 3226-3228 (2001).

# 7 Measurements in Liquid Ambients

## 7.1 Overview

In this chapter we discuss actively-driven fluid-based piezoresistive sensors (passive sensors for the detection of Brownian fluctuations are discussed in chapter 8). For these experiments the microfluidics are used to deliver pulsatory fluid flow, and the cantilever motion is subsequently monitored through the piezoresistive read-out. This method of actuation has been used to characterize the piezoresistive read-out in fluid and to perform preliminary cellular detection experiments.

Most of this thesis has been concerned with silicon based piezoresistive devices. Silicon and germanium have an advantage over metallic piezoresistive elements for many sensing applications due to their higher gauge factor (more than 20x greater at our doping level and as much as 60x greater for lower doping levels in silicon). Despite this higher gauge factor, metallic piezoresistive devices dominate the market of commercial strain gauges. For most applications the drawbacks to silicon devices include cost, fragility (silicon is more brittle than gold), and the greater temperature coefficient of resistance of silicon[1]. Silicon devices remain important for applications where maximum possible sensitivity can be critical, however, we will see in chapter 8 (where we investigate piezoresistive sensors for the detection of Brownian fluctuations in fluid) that even for applications which require high levels of sensitivity, for certain types of measurements the benefits of working with metallic resistors; particularly the lower resistance, absence of 1/f noise, and fabrication advantages for making thin devices, outweigh the drawbacks

of a lower gauge factor. In this section we present data for both silicon and gold piezoresistive sensors.

The fabrication of silicon-based piezoresistive sensors was discussed in Chapter 3. The gold stress sensors are fabricated by the same procedure, except before defining the cantilever by e-beam lithography a gold conducting path is patterned by e-beam lithography and deposited by liftoff along the region that will be the device legs. An SEM micrograph of a gold piezoresistive device is shown in Fig. 7.1.A.

**Fig. 7.1.A Metallic piezoresistive cantilever**

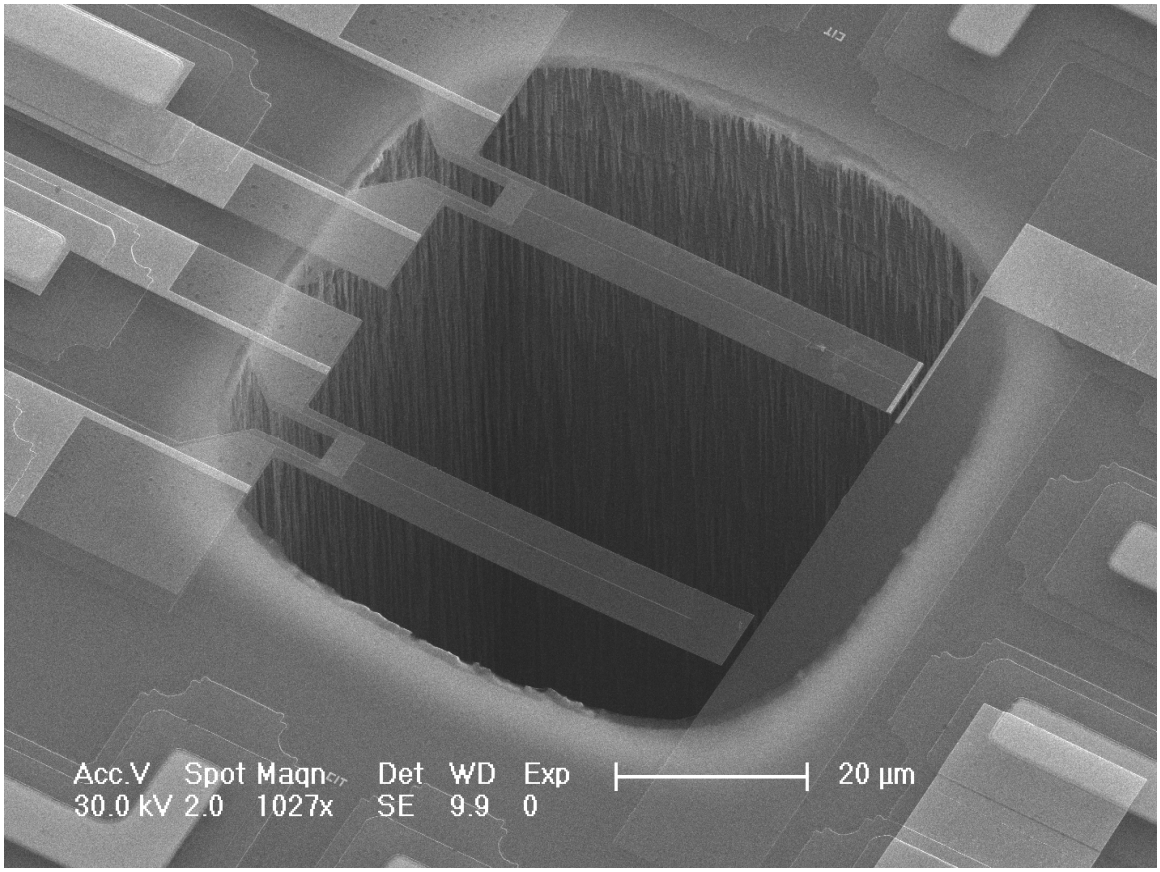


The conducting path is through the gold piezoresistive elements patterned on the device surface. The gold on the device legs is 25nm in thickness and 100nm in width. Thicker gold is patterned to the edge of the device ledge to reduce the electrode resistance.

## 7.2 Piezoresistive Cantilevers as Flow Meters

In this chapter we present experiments performed on piezoresistive micro-cantilevers embedded in microfluidics. The fabrication procedure for microfluidic embedded devices was discussed in section 3.1.5. A typical device is shown in Fig. 7.2.A. The microfluidic valves are operated using a voltage controlled pressure switch purchased from Fluidigm, Inc. This allowed an adjustable pressure (a pressure of between 21-24 PSI was used) to be applied to the control valves. The valves could be opened using a computer controlled voltage to the Fluidigm controller. In the case of fluidic drive, an oscillating voltage of square wave form was supplied to the Fludigm controller via an Agilent 33250A function generator, allowing the valve of interest (generally the output valve, although other valves also worked for this technique) to be opened and closed at known frequency.

### 7.2.1 Cantilevers with Silicon Piezoresistive Elements

We consider first a silicon piezoresistive cantilever under fluidics drive. In Fig. 7.2.B we show the measured resistance change of the device for a fluid drive at 1.1 and 1.3 Hz. The cantilever is positioned in the outflow via, *i.e.*, when the valve is opened the cantilever is deflected downward under forward flow, and when the valve is closed the cantilever deflects upward due to the back flow. The direction of resistance change is consistent with these directions of deflection. These measurements were performed on a device of length $\ell = 23\mu m$, width w=5μm, leg length $\ell_{leg} = 5\mu m$, leg width $w_{leg}$ =2μm, and thickness t=100nm. The custom preamplifier described in section 4.2.1 was used, followed by the Stanford SR560 low noise preamplifier set to gain 5 with 6dB filtering

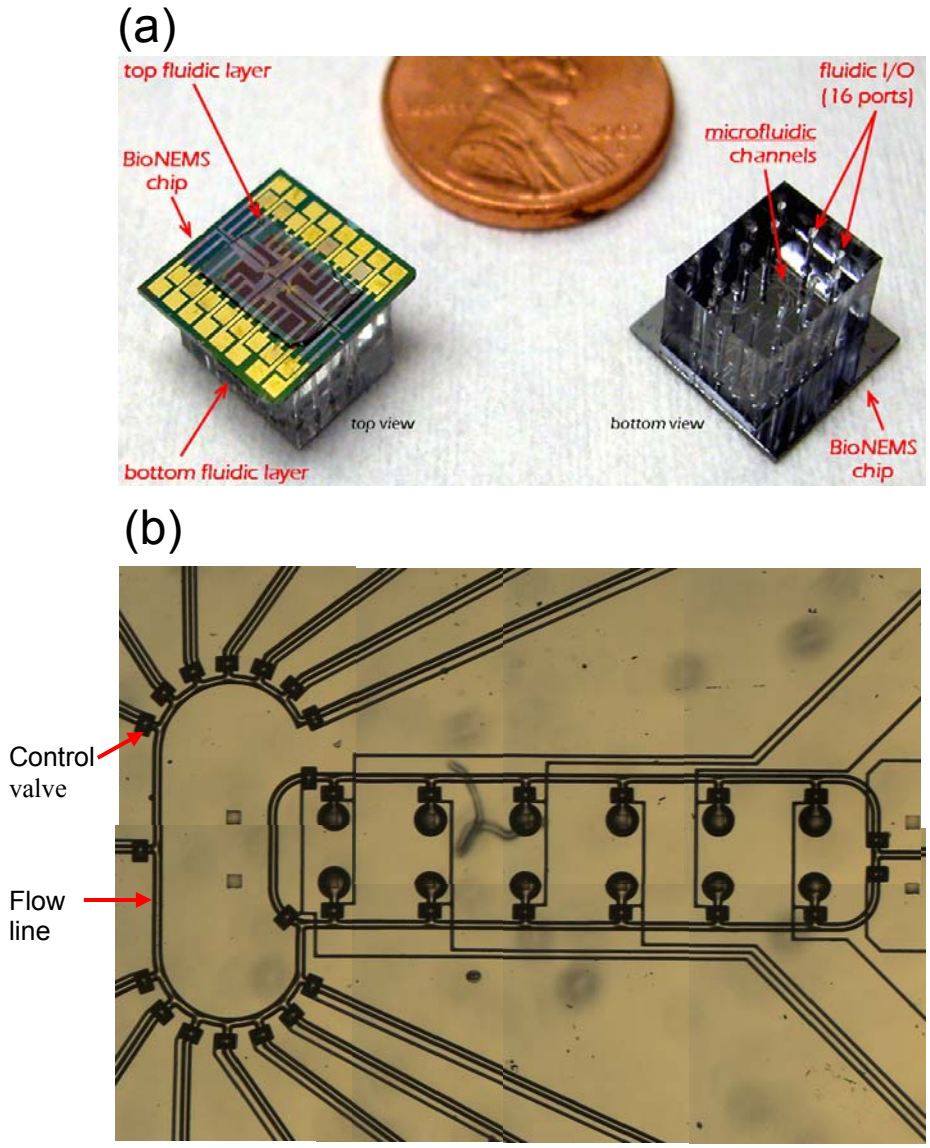


**Fig. 7.2.A Piezoresistive device embedded in microfluidics**

The microfluidic channels are comprised of three layers, a lower layer fabricated from PDMS containing all of the control valves and fluidic inlets and outlets, a DRIE etched channel through the silicon wafer, and a topside channel connectiong the DRIE etched vias fabricated from SU-8 resist patterned on a glass side. (See section 3.1.5). The entire assembled chip is shown in (a). A backside view of the control valves is shown in (b).

low pass 0.03 Hz and high pass 30Hz. The signal was then collected with the Hewlett Packard Infinium oscilloscope, AC coupled on 1MΩ input.

The piezoresistively-detected signal from fluid drive (Fig. 7.2.B) was input into a Stanford SR830 lock-in amplifier. A bridge circuit was used with a bias resistor of 81.5kΩ and 1.3V applied across both the device and bias resistor. A SR560 preamplifier was used with a gain of 1000. A time constant of 1s was used for the lock-in detection. The RMS signal from pulsatory fluidic drive was analyzed as the flow pressure was changed. The pressure of the fluid in the flow channels is directly related to the flow rate and consequently the force applied to cantilever. We begin with an estimate of the flow rates and forces which can be achieved with this means of excitation. The microfluidic channel is comprised of three paths: the PDMS flow path, flow through the silicon fluidic vias, and the topside fluidic path (through the flow channel defined by SU-8 and the glass coverslip). Of these the PDMS flow path is by far the longest and dominates the fluidic resistance. The flow channels are typically 70μm wide. They are 10μm high at the center of the channel. We model this geometry using an ellipse of equivalent cross-sectional area and use the width of the channel for the length of the major axis of the ellipse. The volumetric flow rate, $Q$, for pressure driven laminar flow through a tube of elliptical cross-section (with semi-axes a and b) is given by:

$$Q = \frac{\pi G}{4\mu}\frac{a^3 b^3}{a^2 + b^2} \qquad 1$$

where $\mu$ is the dynamic or shear viscosity and $G = \Delta p / l$ is the pressure gradient.[2] The mean flow rate is then given by $\overline{u} = Q / A$ where $A$ is the cross-sectional area of the flow.

For our flow channels $l$~7mm so $\overline{u}_{\text{PDMS}} \sim 5.6\text{mm/s/PSI}$. This gives the flow rate within the PDMS channels. However, our cantilevers are located within the silicon vias for which the cross-sectional area of 75μm x 75μm is noticeably greater. We estimate the flow rate in the vias to be $\overline{u}_{\text{via}} = \frac{A_{PDMS}}{A_{\text{via}}}\overline{u}_{\text{PDMS}}$. For our devices we obtain $\overline{u}_{\text{via}} \sim 0.55\text{mm/s/PSI}$. As a judge of the role geometry plays in this estimation, if we instead assume a circular cross-section of the same cross-sectional area, we obtain $\overline{u}_{\text{via}} \sim 2\text{ mm/s/PSI}$. Direct measurements to estimate the flow rate of beads confirms a flow rate on the order of a few mm/s.[3] Only a rough estimate was obtained directly in these experiments because the camera used on the microscope was not fast enough to accurately measure these flow rates. An alternative is to measure the flow rate in the tubing used at the inlet to the fluidics. Due to the larger cross-section the flow rate there is much slower and therefore easier to measure. Based on the above flow rates and the inner diameter of the tubing (0.01" ), at a pressure of 7PSI the fluid should flow through 1m of tubing in ~36 min. This is roughly consistent with what we observe. We obtain a rough estimate of the force exerted on the cantilever by the flow by considering the Stokes formula for the force exerted on a sphere of radius, $a$: $F=6\pi\eta a u$.[4] We approximate $a = \sqrt{A_c}/\pi$ where $A_c$ is the area of the lower surface of the cantilever. For our device this gives $F_{tip}=\alpha F$ =120pN at 7PSI. Where we used the parameter $\alpha$ introduced in sections 2.2.2 and 2.3.2.

In Fig. 7.2.C we show the pressure dependent device response. The flow rates used in Fig. 7.2.C (b) were calculated in the manner of the preceeding paragraph. The resistance of this device is 75kΩ. The force scale was calculated from the measured

resistance change using the calculated values $\partial R_d / \partial x = 1\text{x}10^8\,\Omega/\text{m}$ (section 2.3.4) and $K$=13mN/m (section 2.3.1). At 7PSI, a resistance change of 211ppm was measured. This corresponds to a force of 2.5nN. Using the calculations above we can thereby estimate a flow rate of 88mm/s at the location of the cantilever. The linearity with pressure and reproducibility is shown in Fig. 7.2.C (b). This data suggests a possible application of these devices for measuring flow rates within microfluidic channels.

This variance in the data of Fig. 7.2.C (a) provides a measure of the sensitivity for our experiments. The standard deviation in the response at 7PSI was 0.94ppm or 41pN, over a 1Hz bandwidth for a sensitivity of $41\text{pN}/\sqrt{\text{Hz}}$.

(a)

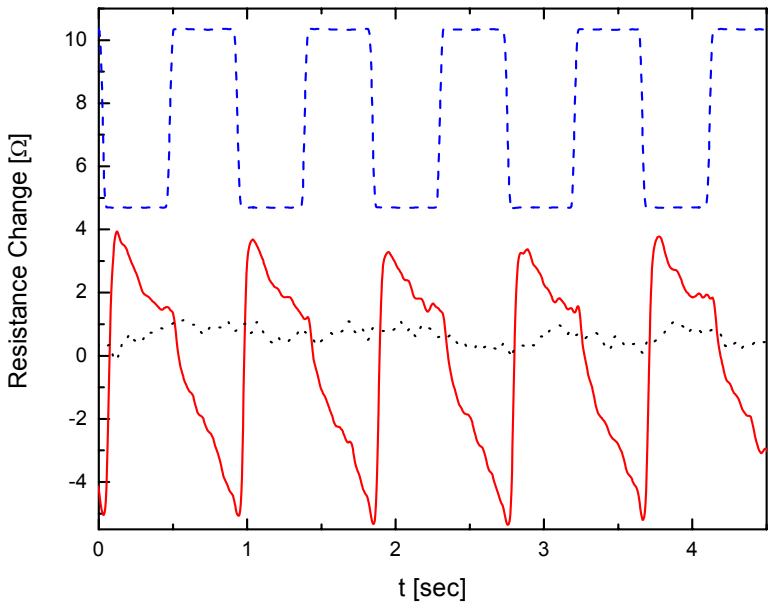


(b)

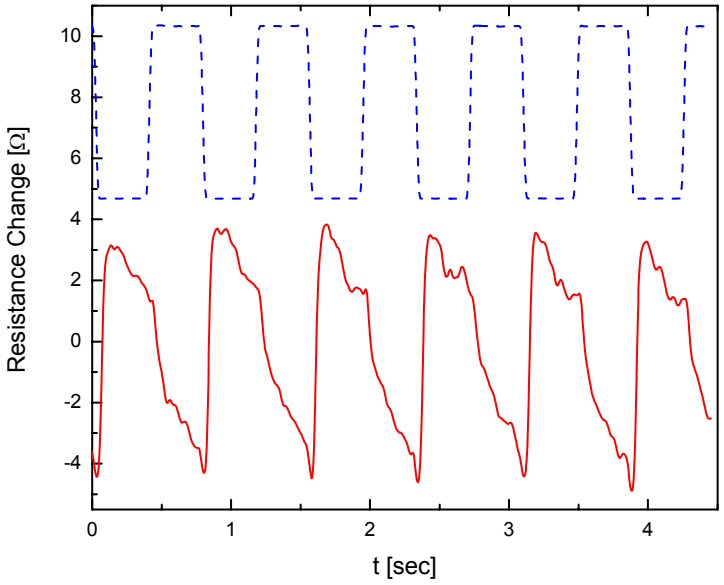


**Fig. 7.2.B Cantilever response under pulsatory fluidic drive**

Dashed blue: TTL output from control of output valve. Solid red: Output Signal from device; dotted black: noise level when function generator is disconnected from the output valve. (a) 1.1 Hz drive and (b) 1.3 Hz drive.

(a)

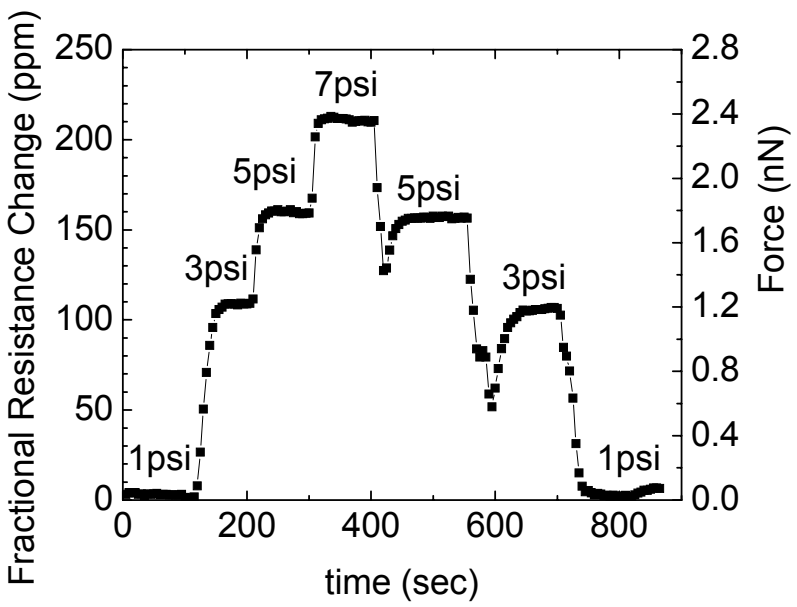


(b)

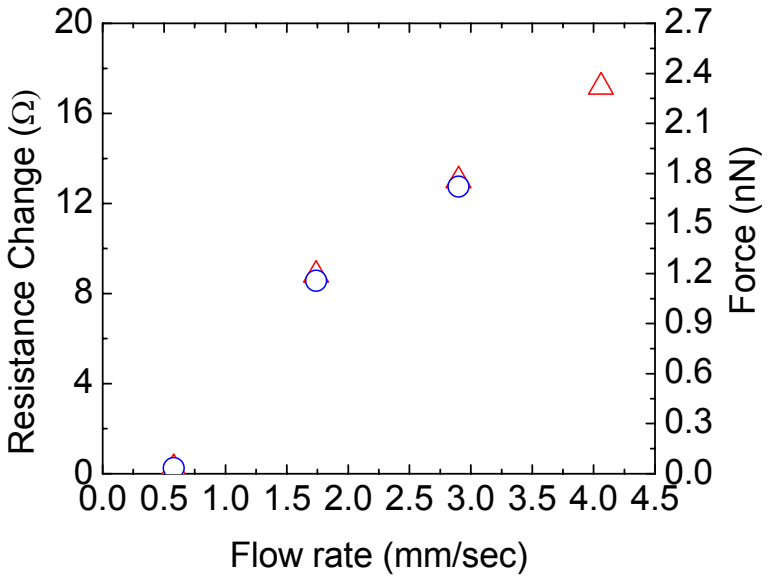


**Fig. 7.2.C Piezoresistive cantilevers as a flow meter**

(a) Raw data showing discrete steps when the flow pressure is changed. The force was calculated from the gauge factor for the material measured in section 4.1. Due to damage during processing, the gauge factor for this device was a factor of 20 less than that of comparable devices fabricated after improvements to the fabrication process. The fractional resistance change should therefore be a factor of 20 greater for the improved devices. (b) Average data at each pressure, showing reproducibility for use as a pressure gauge. Red triangles: increasing pressure. Blue circles: decreasing pressure

### 7.2.2 Metallic Piezoresistive Cantilevers

The benefits and disadvantages of metallic piezoresistive cantilevers were overviewed in section 7.1 and will be addressed in more detail in chapter 8. Here we present results using fluidic drive of metallic piezoresistive cantilevers for comparison with the fluidic drive data collected with silicon piezoresistive cantilevers in section 7.2.1. The devices discussed in this section are of length 55μm, width 7 μm, leg length 5 μm, and leg width 2 μm. The width of gold on the device legs was 100nm, and its thickness was 25nm. The silicon thickness is 100nm. The response for four devices (on a single die) are shown in Fig. 7.2.D. Variations in device response were observed, suggesting that improved control during fabrication is required to produce devices of consistent behavior. In fact, for 8 out of the 13 devices studied the response was undetectable. The response level was between 10 and 15 ppm at 8PSI for 3 of the 5 devices showing fluidic response. The response level for the fourth device (in M5 via 6) was 71ppm at 8PSI. The fifth devices displayed somewhat erratic behaviour. It was less linear with pressure than the other devices and also less reproducible. The response of this device at 8PSI varied from 6 to 12 ppm. These variations in response were observed in spite of comparable device resistance.

However, despite these variations the results are promising. As these were the first set of devices, it is expected that the device reproducibility will improve as fabrication improvements are made. Since the gauge factor for the silicon devices was well characterized by a number of means discussed in previous sections (namely: measured thermomechanical noise in vacuum, direct probing in the AFM, and

comparison with expectations), it is assumed that the calculated force of 2.5nN for a flow pressure of 7PSI is accurate. For the device whose data is presented in Fig. 7.2.D, the calculated spring constant is $9.8\text{x}10^{-4}$N/m. Based on this calculated value and the force estimated from the data using a silicon piezoresistive cantilever in Fig. 7.2.C, we estimate a tip displacement of 2.9μm at a flow rate of 8PSI for the gold cantilever of Fig. 7.2.D (which due to the differing geometry is more compliant than the silicon device discussed earlier). A measured resistance change of 0.042Ω was observed for the most sensitive device (top left in Fig. 7.2.D for which the measured resistance change was 75ppm on a device resistance of 567 Ω). This yields a piezoresistive transduction factor, $\partial R_d / \partial x = 1.5\text{x}10^4\,\Omega/\text{m}$. Using the formulae of section 2.3.4 we calculate a dimensionless gauge factor of 0.8. (The gauge factor of bulk gold is ~2).[5] That the value for the more sensitive device is roughly the expected value for a gold piezoresistor further suggests that with fabrication control we should be able to achieve a higher yield of devices with comparable behaviour to this more sensitive device. This data may also be used to obtain a direct measure of the force sensitivity for these piezoresistive devices. A value of 33pN/ $\sqrt{\text{Hz}}$ is obtained (a 1Hz bandwidth was used for this experiment).

**Fig. 7.2.D Device response to fluidic drive for gold piezoresistive cantilevers**

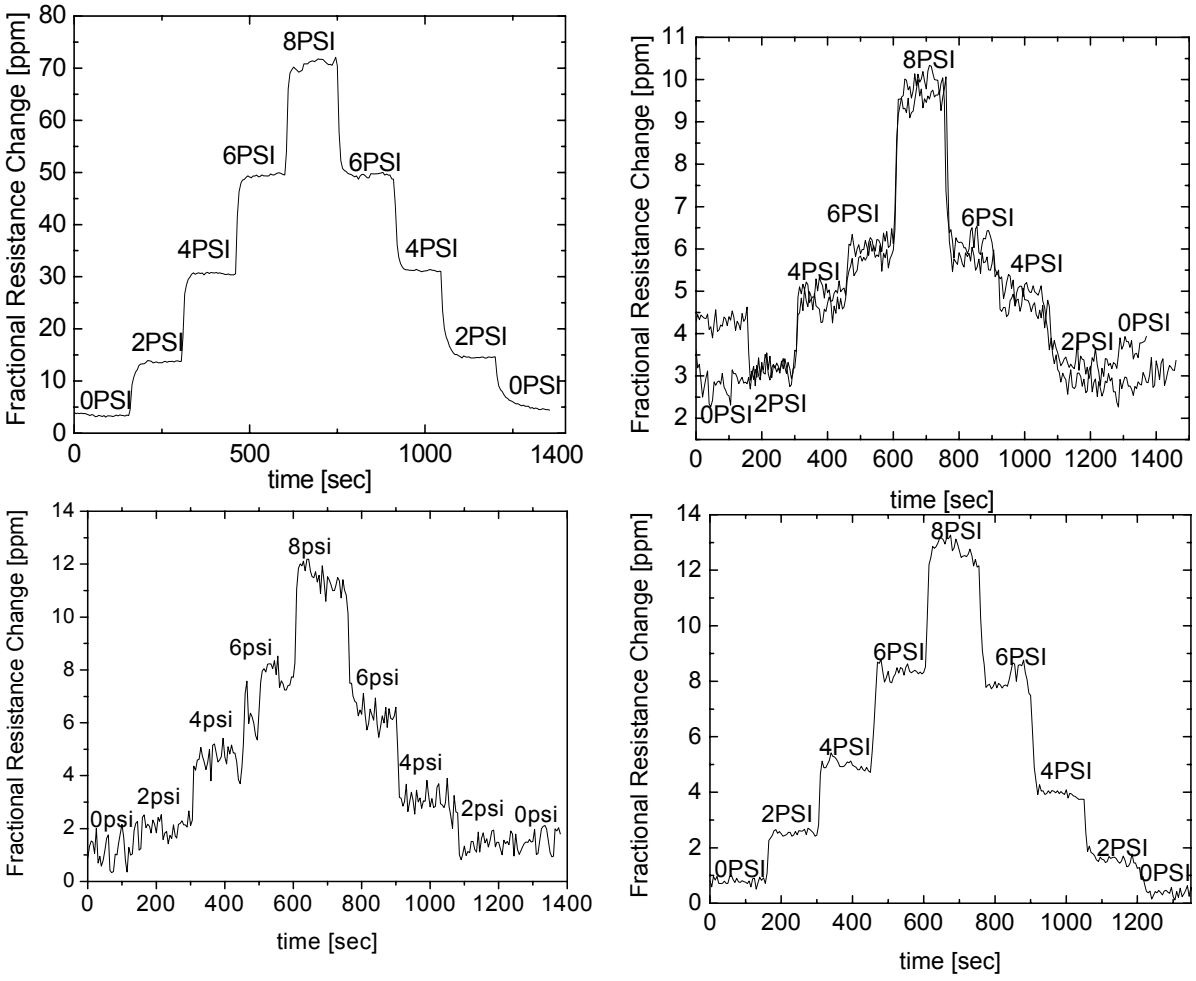


The device response is shown for 4 different devices under fluidic drive. Improved control over the fabrication is required to understand the variations in device performance.

## 7.3 BioNEMS detection of Biotin-labeled beads

The BioNEMS devices were designed as a general platform for biosensing applications. The specification lies in the choice of receptor, attached to the gold pad at the device tip through a thiol bond. A number of demonstration biosensing experiments have been performed to test the device capabilities. All of these experiments have relied on the binding of the analyte of interest across a dock such as that depicted in Fig. 1.2.A, decreasing the overall device compliance. However, for the devices employed in this work, the gap between the distal end of the cantilever and the dock was too large to allow it to be bridged with a single analyte. Moreover, the imaging was not clear enough for it to be readily apparent when an aggregate of analytes had finally bridged the gap, complicating the analysis and interpretation. Here we present the data from one such experiment and discuss improvements for future experiments that will allow for a clearer demonstration of the capabilities of these devices. In this experiment, the analyte of interest was 0.2 $\mu$m biotin-labeled polystyrene beads. The functionalization of the device for this experiment was performed within the microfluidics. To functionalize the devices a mixed SAM consisting of 20% Biotin-alkaine-thiol [BAT] and 80% Polyethylene-glycol-alkaine-thiol [PEG] (with the latter serving to place separation between the active biotin sites for the purpose of reducing steric hindrance) was introduced and allowed to incubate for 1 hour followed by a water rinse. Streptavidin (in buffered solution) was then introduced and allowed to incubate for 10 min. Streptavidin has four biotin binding sites, allowing it to bind to the biotin of the SAM and also serve as a receptor for the biotin-labeled beads. The fluid drive was then turned on and background data was collected. The response for four different devices within the same chip is shown. (The

red, blue, and green devices are located within the outflow via and the gray device is in the inflow via). Before introducing the beads the device resistance is stable. After half an hour of background data collection, 0.2μm biotin-labelled beads were introduced, whereupon large resistance flucuations are observed as the beads bind and unbind. These fluctuations decrease over time as a steady state is reached with the beads bound. It is also worth commenting that initially the magnitude of the fluid drive signal is very different for the different devices (even though they are of the same design). This is perhaps due to variations in the fluid flow. At the end of the experiment, when all the devices are bound together through the beads, the signals are much more comparable. (Note that the gray trace is for a device in a different via which can not bind to the other devices but is in a similar bound configuration in the other via).

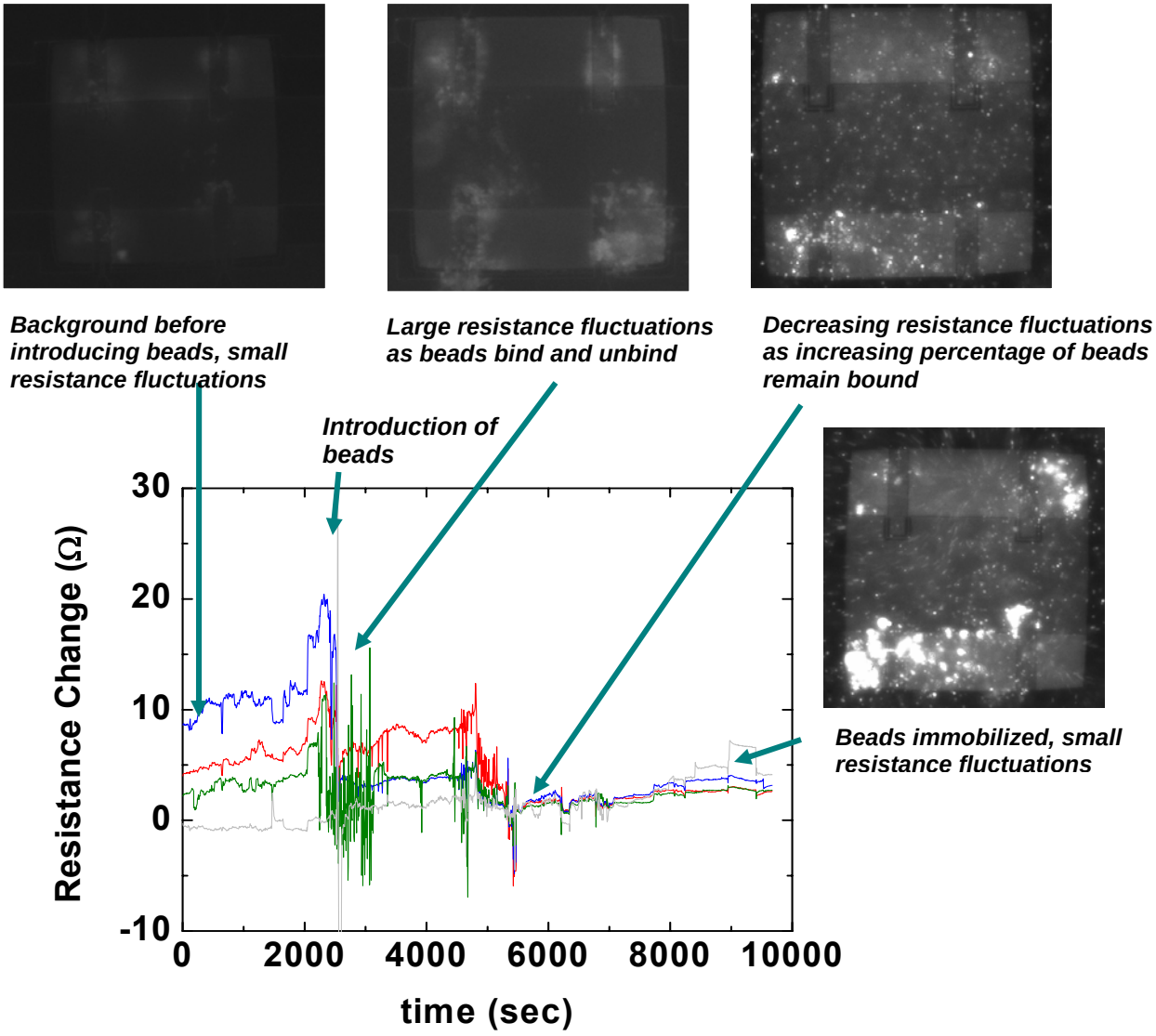


**Fig. 7.3.A Detection of 0.2µm biotin labeled beads using BioNEMS**

The response for four different devices within the same chip is shown. (The red, blue, and green devices are located within the outflow via and the gray device is in the inflow via). Before introducing the beads the device resistance is stable. As soon as the beads are introduced large resistance flucuations are observed as the beads bind and unbind. These fluctuations decrease over time as a steady state is reached with the beads bound.

## 7.4 Direction for Future Experiments

Unfortunately for the experiments of section 7.3, while the gap between the cantilever tip and dock was patterned to be on the order of 100nm, stress in the device caused the actual gap to range from 300nm-5μm, making it impossible to detect single beads. We therefore relied on aggregates of beads to cross the gap. This not only is inconsistent with our long term goals but complicates the data analysis since in order to have clumps of beads crossing the gap we needed to use high concentrations of beads. Under these conditions, it was difficult to resolve when beads were actually binding across the gap (hindered further by the fact that the bead binding was less specific than we would have liked). There are a number of improvements that could be made to this experiment. The first is to move to studying a species which is both larger (>5μm so as to be able to cross the gap) and more specific. Both of these can be accomplished by switching to the study of mammalian cells, including T cells, B cells, and epithelial cells, the latter being of particular interest for cancer research. Mammalian cells are typically a minimum of 10μm in diameter and have been extensively studied with the necessary species to achieve specific binding (and block non specific binding) commercially available. (Beads tend to be exceptionally sticky, so blocking their non-specific binding is a greater challenge).

Once the signal is well characterized with these devices it should be possible to return to smaller spores, cells, and molecules through engineering refinements to reduce the strain and, hence, the gap size. Among the most important refinements will be careful

control of the deposition conditions for the gold deposited on the cantilever to deposit it with minimal stress and geometrical changes to produce more planar structures, possibly including the transition to beams instead of cantilevers.

## 7.5 References

[1] M.L. Nagy, C. Apanius, J.W. Siekkinen, and H.V. Estrada, Sensors **18** (June, 2001).

[2] C. Pozrikidis, Introduction to Theoretical and Computational Fluid Dynamics, Oxford Univeristy Press, New York, p. 185 (1997).

[3] Blake Axelrod, Graduate student, Caltech, personal communication.

[4] C. Pozrikidis, Introduction to Theoretical and Computational Fluid Dynamics, Oxford Univeristy Press, New York, p. 266 (1997).

[5] C. Li, P.J. Hesketh, and G.J. Maclay, J. Vac. Sci. Technol. A **12**, 813 (1994).

# 8 Brownian Motion in Fluid

## 8.1 Introduction

In section 1.2 we introduced the concept of stochastic sensing wherein Brownian fluctuations serve as the "drive" force of the device and its piezoresistive response is modulated by binding of the analyte of interest. The nature of the modulation can be in the form of a change in device compliance (Fig. 1.2.A), a change in device damping (Fig. 1.2.B) or a correlation between multiple devices (Fig. 1.2.C). Stochastic sensing can enable a much lower noise floor than other methods of actuation, which inherently introduce some extra background noise through direct coupling of the "drive" force. In chapter 2 we presented the ultimate force sensitivity of such devices and their potential for single molecule experiments. It is relevant to note that to achieve the ultimate senstivitity of these devices it is essential not just to reduce the total noise floor but to optimize the device geometry such that the Brownian noise is well resolved above other contributions to the noise floor (*e.g.*, Johnson and preamplifer noise). This ensures attatinment of sufficiently high sensitivity for detecting modulations in the Brownian fluctuations. All three goals, namely the reduction of the total noise floor, the maximization of sensitivity to modulations in the Brownian fluctuations from single analyte binding, and the enhancement of Brownian noise signal relative to Johnson noise can be achieved through the reduction of device dimensions. In section 2.5 we addressed the benefits of reducing the device dimensions for the reduction of the total noise floor. We also discussed the benefits of increased bandwidth as the device dimensions are reduced. It is intuitively clear that it is beneficial to decrease the device dimensions to maximize the modulation in Brownian fluctuations from single analyte binding. As the

device geometry decreases to values closer to the dimensions of the analyte of interest, the sensitivity of the device to single analyte binding is expected to improve. This will be discussed further in chapter 10 for the case of modulation of device response from changes in the device damping.

The optimization of device geometry to enchance Brownian fluctuations relative to Johnson noise requires further thought and care. The uniform reduction of device dimensions is beneficial in this respect. This can be observed in the data of Fig. 2.5.B and Fig. 2.5.C where the devices were uniformly reduced by a factor of 3 in the latter figure. Note that at 0.1 MHz the total noise is 15% above the Brownian noise limit for the larger device and 3.5% above the Brownian noise limit for the smaller device. At 1 MHz the difference is even more noticeable, with a total noise floor relative to the Brownian noise limit of 150% *vs*. 26% for the larger and smaller devices, respectively. All of the values quoted here are for the lowest bias voltage shown in the figures, namely 0.5V across the device. That said, to truly enhance the Brownian fluctuations relative to Johnson noise, care must be taken in choosing the device geometry (relative dimensions). This is the subject of the current chapter.

Measurements of Brownian fluctuations in fluid have been performed using optical detection of cantilevers by a number of researchers.[1-5] However, to date none have used integrated sensors such as the piezoresistive devices that we discuss herein. However, the use of piezoresistive sensors presents significant challenges, in particular, additional noise contributions arise from Johnson and 1/f noise. These require that judicious care be

taken in sensor design to minimize them. Despite these obstacles, the benefits of sensor integration are a significant motivation. Integration is essential to achieving high density multiple-cantilever arrays. Morevoer, the benefits to sensitivity that may be achieved through the reduction of device dimensions were already presented. There are practical limitations on how far the device dimensions can be reduced if optical detection is to be employed due to diffraction limitations to the ability to focus the optical detection beam on the nanocantilever tip. Fortunately, it is in this limit of small devices that the detection of Brownian fluctuations becomes feasible. Here we present calculations to optimize the cantilever dimensions, including a discussion of the relative benefits of metallic- and semiconductor-based piezoresistors. Throughout this chapter signal-to-noise is used to refer to the relative value of the Brownian fluctuations to Johnson noise.

## *8.2 Optimization of Dimensions for the Detection of Brownian Fluctuations*

### 8.2.1 Expectations

In this section a detailed analysis of how the choice of cantilever dimensions affects signal-to-noise ratio and bandwidth. Before delving into the equations we first consider what is to be expected.

We first consider increasing the cantilever length with all other dimensions fixed. This increases the surface area for fluidic damping and also increases the torque that end-coupled forces and Brownian fluctuations might exert, so we would expect the magnitude of the signal to increase. Indeed, we should observe the signal to increase as $\ell^2$. Unfortunately, the device becomes both more compliant and more heavily damped as it is lengthened (with other dimensions fixed), so the increase in signal comes at the expense

of bandwidth. Increasing the cantilever width leads to two competing effects on the damping of the cantilever. First, there is a direct increase in the volume of fluid displaced by the cantilever, thus leading to an increase in the effective damping. Second, there is also an increase in the Reynold's number. Since the Reynold's number is a measure of the relative importance of inertial to viscous effects a decrease in the fluid loading leading to reduced damping is implied. It will be shown that the dependence of Brownian response on device width is very weak compared to the length dependence due to the competition between these two effects.

We next consider the dimensions of the cantilever legs. We expect to be able to maximize the signal by decreasing the width of these legs since this increases the compliance of the device. Once again we expect this to come at the expense of bandwidth. These expectations are borne out by the calculations below.

### 8.2.2 Details of the Calculations

Many of the formulae relevant to this calculation were introduced in chapter 2. We wish to optimize the signal-to-noise ratio and for this purpose we assume that the dominant noise source arises from Johnson noise, with voltage spectral density given by

$$S_V^J = 4k_B T R_d \,. \qquad 1$$

The signal from cantilever motion in the displacement domain is given by

$$\delta x = \frac{F_{\text{drive}}(f) H(f)}{K}, \qquad 2$$

where $K$ is the spring constant, $F_{\text{drive}}$ is the driving force given by $4k_B T\gamma$ for stochastic sensing, and $H(f)$ is the complex ampliftude response function of the cantilever in fluid (given by chapter 2, equation 10). This response function determines the bandwidth.

The measured change in resistance is proportional to both the displacement and the strain. At a position x along the cantilever this is given by

$$\frac{\delta R_s}{R_s} = \pi_\ell S \delta x = \pi_\ell \frac{\beta t}{2} \frac{(\ell - x)}{I_{xx}} \frac{F_{\text{drive}}(f) H(f)}{K}. \qquad 3$$

In the above expression, the parameter $\beta$ accounts for the finite thickness of the conducting layer. For an infinitesimal layer, $\beta$=1. $\beta$ decreases monotonically as the relative thickness of the conducting layer to the total cantilever thickness increases. $\pi_\ell$ is the piezoresistive coefficient, and x is the position along the cantilever. $I_{xx}=w_{\text{leg}}t^3/6$, which was introduced in section 2.3.1, is the moment of inertia for the cantilever legs for rotation about the fixed end. Integrating this expression along the cantilever length (see section 2.3.4) we have

$$\frac{\delta R_s}{R_s} = \pi_\ell \frac{3\beta}{2} \frac{(2\ell - \ell_{leg})}{w_{leg} t^2} F_{\text{drive}}(f) H(f). \qquad 4$$

Finally, we must consider the conditions under which the signal is measured. In section 2.4 we assumed that the limitation was imposed by the maximum heating the biologically active material at the tip could withstand. In practice we found that the unpassivated electrodes in our first device generations tend to react electrochemically with the solution before this limit was reached. For the purpose of these calculations we therefore assume a maximum voltage of 0.5V could be applied across the device. (With engineering improvements to future devices such as the inclusion of a passivating layer, higher voltages will be achievable). In the current configuration, the solution would be expected to equilibrate at ±0.25V relative to the two electrodes. We assume the device is measured in a balanced Wheatstone bridge (i.e., $\delta v=\delta R_d V/4$, where $V$=1V) and let $R_d$ be

the device resistance (measured purely across the cantilever and not including the electrodes leading down to the edge of the membrane) and $R_{par}$ be the parasitic resistances (arising primarily from the conduction through silicon from the tip of the gold electrodes to the edge of the cantilever). For our devices we will assume 10 squares of parasitic resistance. Then the signal to noise ratio is given by

$$\frac{\text{Signal from Brownian motion}}{\text{Johnson noise}} = \frac{3\beta\pi_{\ell}\left(2\ell - \ell_{leg}\right)\sqrt{\gamma}R_d H(f)}{8w_{leg}t^2\left(R_d + R_{par}\right)^{3/2}}, \qquad 5$$

where $R_{par}$ is the parasitic resistance (resistance not experiencing strain during device motion) comprised of both the electrode resistance and contact resistance.

From Eqn. 5 it is clear why we used the loose terms of "stiffness" and "compliance" in the intuitive analysis. The prefactor $(2\ell - \ell_{leg})/w_{leg}t^2$, although not the spring constant, behaves in the expected manner we would use for describing something as stiff or compliant. The Brownian driving force is frequency-dependent (through the damping term, $\sqrt{\gamma}$ ). The bandwidth of the response is therefore affected by both the response function and damping.

## 8.3 Doped Silicon vs Metallic Piezoresistors for the Detection of Brownian Fluctuations

For most of the thesis we have focused on doped silicon piezoresistive sensors. Compared to metallic piezoresistors, these have the benefit of a much higher gauge factor (40 vs 2). However, there are situations in which this benefit is offset by the disadvantages of working with a semiconductor over a metal, namely 1/f noise at low frequencies, higher resistance, and difficulty obtaining high quality ultra-thin material.

For the latter consideration, note that the difficulty here arises not from obtaining a single layer of high quality ultra-thin silicon but from the need for a two layer structure with layers of very different doping levels required for piezoresistive sensing. Indeed, all of these issues present serious problems for the detection of Brownian noise using silicon piezoresistors. The noise floor for a typical silicon piezoresistor designed for the detection of Brownian noise is shown in Fig. 8.3.A. Unfortunately, the expected peak in the Brownian noise at about 1 *k*Hz is dominated by 1/f noise. Adjusting the dimensions to shift the Brownian noise signal to higher frequencies compromises the signal-to-(Johnson) noise ratio. The solution to this dilemma is provided by metallic piezoresistors which largely eliminate the 1/f noise[6] within the bandwidth needed for fluidic sensing. The piezoresistive coefficient for a typical metal is 6% that of silicon. However, this is offset by the resistivity of silicon, which at the doping levels of devices used throughout this thesis is roughly 1500 times that of gold. Since we are looking at the Brownian noise relative to Johonson noise, this difference in resistance places metallic piezoresistive transduction on a roughly equal footing with doped silicon devices in spite of the difference in gauge factor. However, there is a very important distinction; transduction via metallic piezoresistive devices has a much lower 1/f knee. For metallic piezoresistive devices, however, extra care must be taken to ensure that the electrode resistance remains low compared to that of the device. This is most easily achieved by using very thin metal on the piezoresistive element (~20nm) and thick gold elsewhere (~600nm).

In Fig. 8.3.A a device was shown for which the Brownian fluctuations were a factor of ~ 2 greater than the Johnson noise out to a frequency of ~2kHz. The benefits of using metallic piezoresistive devices to eliminate the 1/f noise were already discussed .

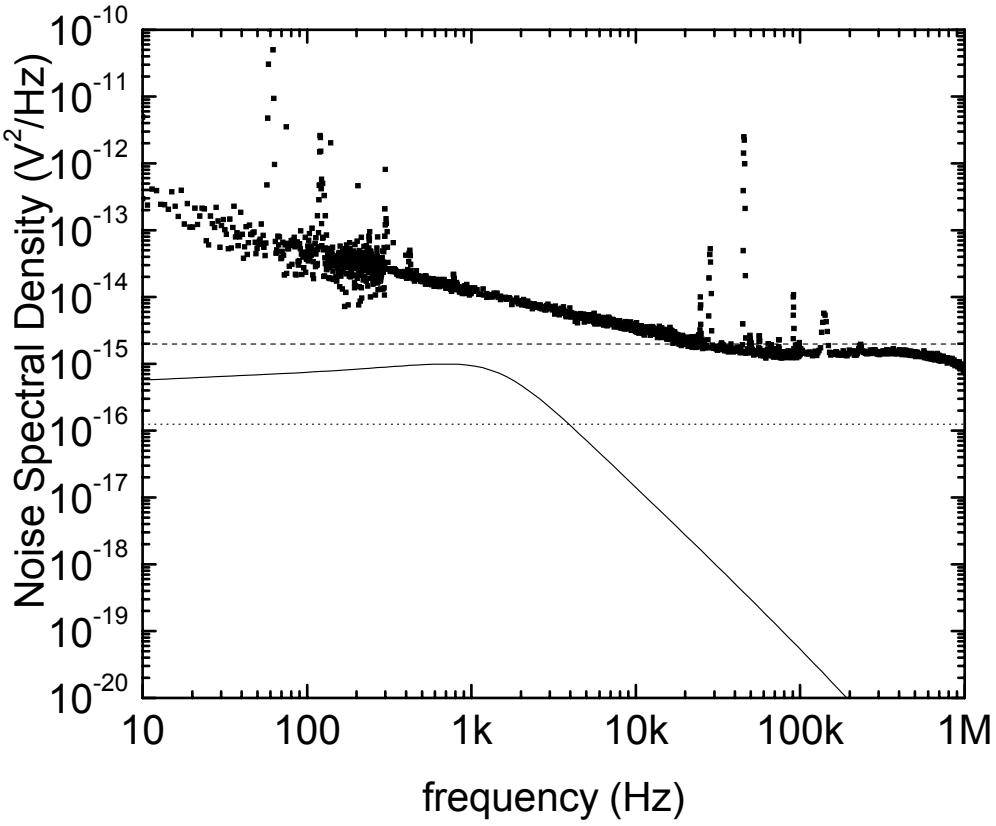


**Fig. 8.3.A 1/f noise and brownian detection for silicon piezoresistors**

Measured and calculated noise contributions are shown for a device of dimensions $\ell$=50 μm, w=2μm, t=100nm, leg length=0.5μm, and b=0.2 μm. The calculated Brownian noise (solid line) is expected to be about a factor of three larger than the expected Johnson noise (dotted line) at a frequency of 1kHz. However, at this frequency the measured signal (solid squares) was dominated by 1/f noise. The device for which data is shown here was fabricated from early material in which the silicon piezoresistive layer was damaged during processing. Due to this damage the device resistance was 119kΩ and not the 15kΩ used in the calculations. The expected Johnson noise for a 119kΩ resistor is shown as a dashed line, agreeing with the noise floor beyond the 1/f knee.

Improved signal-to-noise over a greater bandwidth can be achieved by reducing the device thickness. Here again metallic devices prove advantageous. While in section 3.3 it was discussed that it is possible for the dopants in a silicon epi layer to remain confined to ~7nm of thickness, in practice it is very difficult to avoid damaging the epi layer during further processing; even the 30nm layers proved delicate, and careful processing was required to produce good quality devices. Moreover, the epitaxial growth process produces lower quality material for the first ~7nm of growth. In theory this threshold might be improved if there were high demand for such thin material, but in practice it is unlikely we could obtain high quality 7nm epitaxial silicon layers. Metallic piezoresistive devices have two advantages: it is possible to deposit very high quality thin films if a fine grain metal such as a gold palladium alloy is chosen, and this deposition can be performed later in processing, leaving fewer opportunities for it to suffer significant damage. Finally, growing a thin silicon epi layer on top of a very thin, 20-30nm structural layer of a silicon on insulator wafer is contingent on the initial layer being of high quality. In our experience, when we have tried to thin silicon layers to ~30nm the epitaxial growth has been unreliable, probably due to the poor quality of the silicon transducer layer this close to the oxide interface. The deposition of high quality thin metallic layers by contrast is not contingent on the absence of defects in the supporting silicon material.

In section 2.5 the experimentally relevant constraint on the applied bias voltage was deemed to be a maximum voltage of 0.5V across the device due to electrochemical interaction with the solution at higher bias voltages. This applies to our current

generation of unpassivated devices. Such a bias voltage represents a much higher current density in gold nano-cantilevers than in doped silicon nano-cantilevers due to the increased conductivity. It is relevant to ask whether these current densities are achievable or whether new constraints should be imposed. For a typical metallic piezoresistive nano-cantilever with $\ell_{leg} = 1.5\mu\text{m}$, a gold thickness of 15 *n*m, and gold width in the constricted region of the device of 100 *n*m, we measure a device resistance of 600Ω. This corresponds to a current density of $5.5\text{x}10^{11}$ A/m$^2$ in the legs. This can be compared to studies of gold nanowires in air where failure is typically observed at a current density of $2\text{x}10^{12}$ A/m$^2$. Durkan and Welland studied the failure mechanisms in gold nanowires and estimate that this failure current density corresponds to a device temperature of 220 $^{o}$C.[7] Cooling by the surrounding fluid should allow our devices to withstand even higher current density. For a device of dimensions $w = 2\mu\text{m}$, $w_{leg} = 200\text{nm}$, $w_{leg_{metal}} = 200\text{nm}$, $\ell = 10\mu\text{m}$, $\ell_{leg} = 1.5\mu\text{m}$, $t_{Si} = 30\text{nm}$, $t_{metal} = 15\text{nm}$, and $R = 600\Omega$, the maximum heating in the constricted region of the devices is calculated to be 11 K for a bias of 0.5V in water. The heating at the distal end of the cantilever is calculated to be 1.4 K (details of calculations for the device heating in fluid were presented in section 2.5). These dimensions correspond to the shortest device in Fig. 8.5.A. For longer devices the heating at the distal end of the cantilever will be even less. This suggests that bias voltages of 0.5V can be achieved for these devices in fluid. Given the importance of fluidic cooling to the functioning of these devices it is important that care be taken in how these devices are ultimately electrically passivated since any additional layers to achieve electrical isolation will also decrease the cooling efficiency of the fluid.

## 8.4 Optimization of Device Dimensions for Enhancement of the Brownian Noise Spectrum Relative to Johnson Noise

In this section we vary the cantilever dimensions one at a time and look at the effects on the signal to noise ratio. Based on the preceeding discussion, particularly the reduced 1/f noise for metallic piezoresistive transduction, metallic piezoresistive elements are used for these calculations. The results are seen to conform to the expectations given in section 8.2.1.

We consider first scaling with the cantilever thickness, measured in the direction of cantilever displacement. In section 2.3.4 we saw that the transducer response function corresponding to the change in device resistance per unit force applied to the cantilever tip, G/K, was proportional to $1/t^2$. This plays the dominant role in determing the thickness dependence of the transduced Brownian noise spectrum and, indeed, in Fig. 8.4.A (a) we show that the peak Brownian noise increases roughly as $1/t^2$. Variations from an exact $1/t^2$ behaviour arise from the frequency-dependence of fluid loading of the device, influencing the mechanical responsivity. The combined Brownian and Johnson noise is shown in Fig. 8.4.A (b), with the shift in frequency of maximum-Brownian induced response shown as an inset. The dimensions used for these calculations are: cantilever length=30μm, cantilever width=2μm, leg length=5μm, leg width=0.2 μm, width of gold=50nm, and thickness of gold=20nm. The thicknesses quoted in Fig. 8.4.A are the combined silicon and gold thickness. The resistance of the gold legs for these devices is 220Ω. An additional 50Ω of electrode resistance is assumed to account for the electrical path from the cantilever to the chip's peripheries where external contact is made. A bias of 0.5 V across the device is used.

(a)

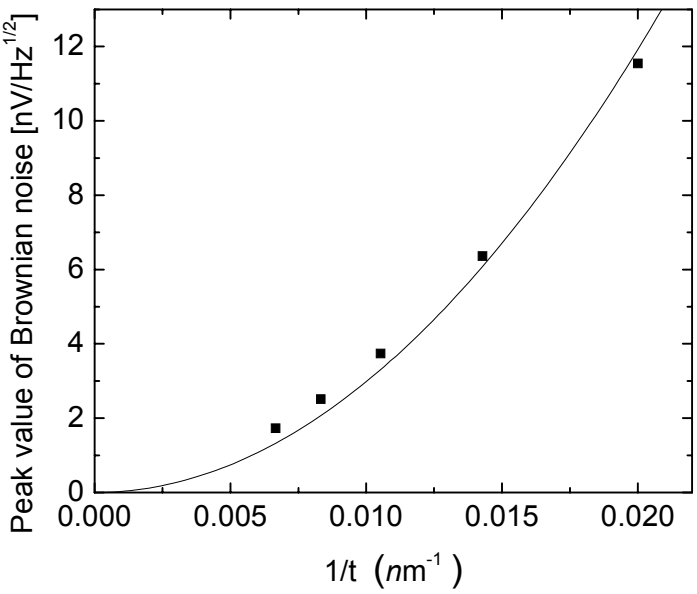


(b)

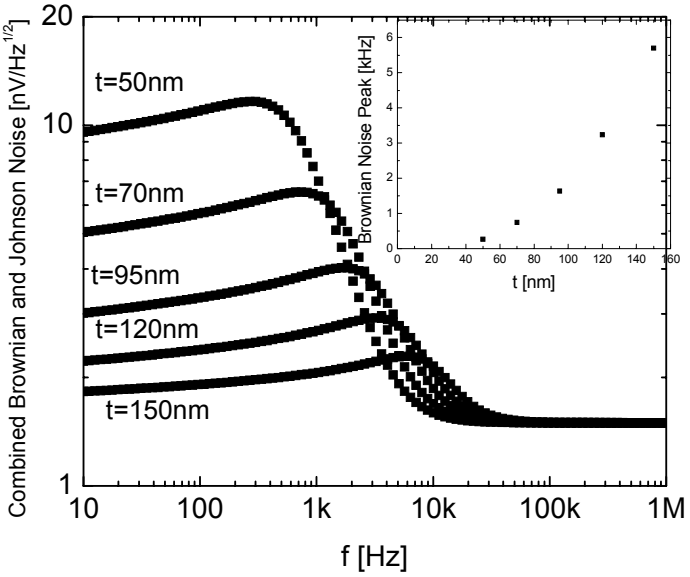


**Fig. 8.4.A Dependence of Brownian noise on cantilever thickness**

(a) The Brownian noise peak intensity is seen to increase as roughly $1/t^2$. (b) The combined Brownian and Johnson noise is shown for five thicknesses. The shift in frequency of the peak Brownian noise is shown as an inset.

We next consider scaling with the cantilever length, shown in Fig. 8.4.B. As expected, when the cantilever length is increased, the signal magnitude is observed to increase and bandwidth decreases. This is consistent with our discussion in section 8.2.1 where we predict that the signal magnitude increases with $\ell^2$ arising from the increase in both damping and lever arm for the response. This is borne out by the calculations represented in Fig. 8.4.B(b). The device dimensions used for these calculations are; cantilever width=2μm, leg width=0.2 μm, leg length=1 μm, width of gold = 50nm, thickness of gold=5nm, and thickness of silicon = 30nm. Resistance of gold legs= 180Ω, resistance of electrodes = 50Ω, bias across device = 0.5V.

Next we consider scaling with the cantilever width, measured in a direction orthogonal to that of cantilever motion. The following parameters are used for these calculations: cantilever length= 30μm , silicon thickness=30nm, leg width= 0.2μm , leg length=1μm, gold width=50nm, gold thickness=5nm, device resistance=180 Ω , electrode resistance=50 Ω, and a bias across the device of 0.5V. The results are shown in Fig. 8.4.C. Analagous to the length dependence, the signal magnitude is here observed to increase with increasing width. However, it is readily apparent that this effect is much less pronounced than for the length, that this arises from a competition between the direct increase in volume of fluid displaced and the decrease in fluid loading with increasing Reynold's number was already discussed. The choice of cantilever width for practical devices is therefore dominated by fabrication concerns. In particular, we find that wide devices are most likely to fail during the drying process after the wet etch to release the devices. The risk of failure during this step increases with the device surface area. It is therefore advantageous to design narrow devices. Fig. 8.4.C(c) shows the dependence

(a)

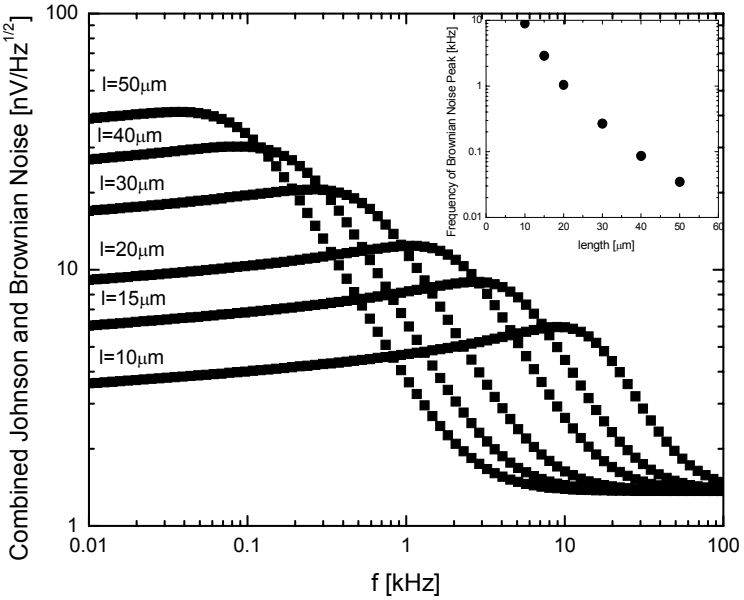


(b)

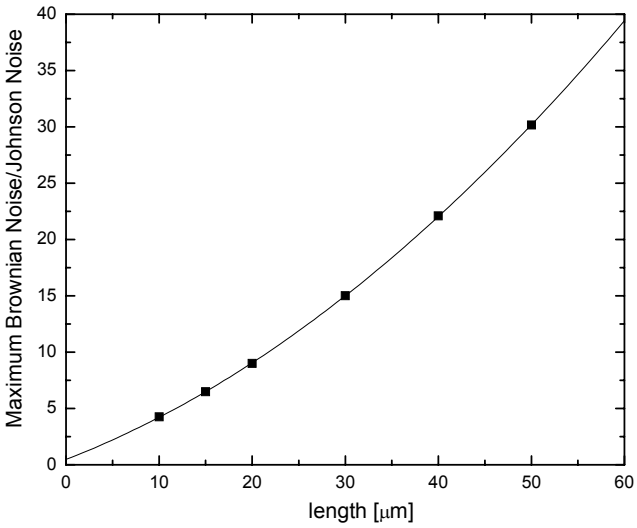


**Fig. 8.4.B Dependence of Brownian response on cantilever length**

(a) Spectrum of combined Brownian and Johnson noise. The frequency shift of the peak response is shown as an inset. (b)Length dependence of the peak Brownian response. The solid line is a fit to the length squared. The device dimensions are provided in the text.

(a)

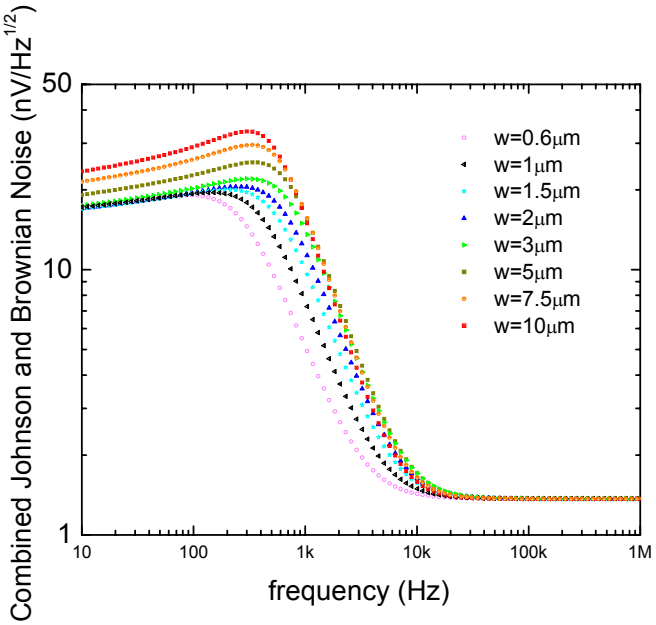


(b) (c)

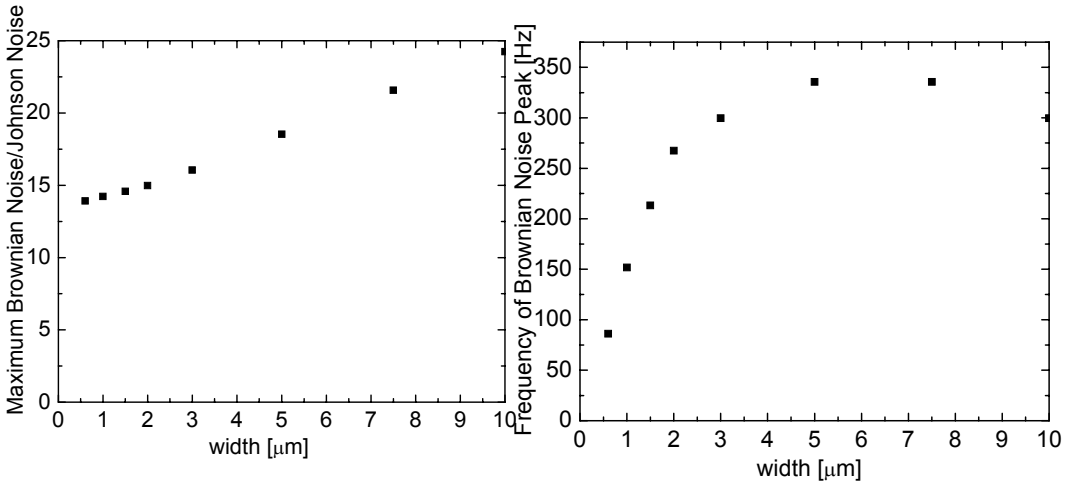


**Fig. 8.4.C Dependence of Brownian response on cantilever width**

The Brownian noise is observed to increase weakly with the cantilever width (a and b). The bandwidth dependence is also weak, except for very narrow cantilevers where the bandwidth is observed to decrease with decreasing width.

of bandwidth on the cantilever width. There are two terms contributing to observed frequency dependence of the Brownian fluctuation spectrum: the frequency-dependent fluid loading contribution to the damping term, which increases with frequency, and the frequency dependent response function, which leads to the high frequency roll-off of the signal. Both of these terms are influenced by the Reynold's number. Beginning from a very narrow cantilever, as the cantilever width is increased, the bandwidth rises due to the increased influence of damping. However, as the cantilever width continues to increase, the bandwidth plateaus and then begins to drop due to the increased roll-off from the response function. Over a large range of cantilever widths this effect is moderate. However, for very narrow cantilevers (<2μm for the cantilevers used in Fig. 8.4.C) the decrease in bandwidth with decreasing width becomes significant, and geometries motivated by the desire to increase device yield, as mentioned previously, need to be balanced against the potential loss of bandwidth.

We now turn to the dimensions of the cantilever legs. In section 2.3.4 we saw that the ganged responsivity, $\frac{1}{K}\frac{\partial R}{\partial x}$, which characterizes the change in device resistance per unit force applied to the cantilever tip, is proportional to 1/(leg width). In Fig. 8.4.D we show the Brownian noise spectrum for increasing leg width and observe this expected behaviour. The dependence of the Brownian noise spectrum on leg length is weak except for cantilevers with very long legs where the increased compliance of the device leads to a decrease in bandwidth (Fig. 8.4.E).

(a)

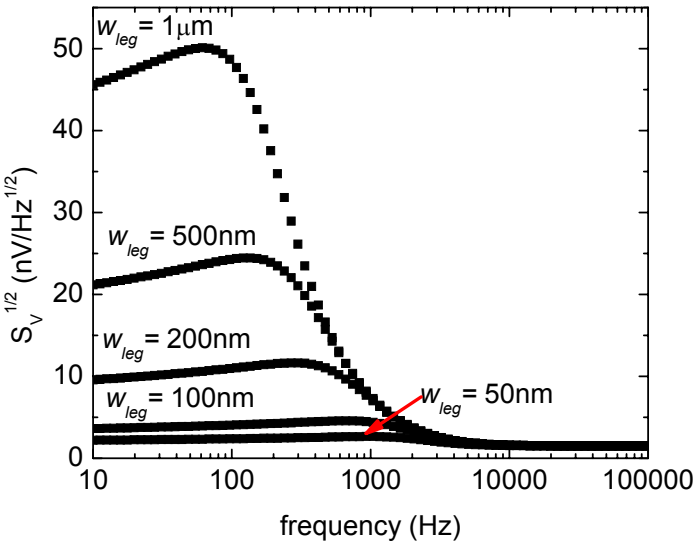


(b)

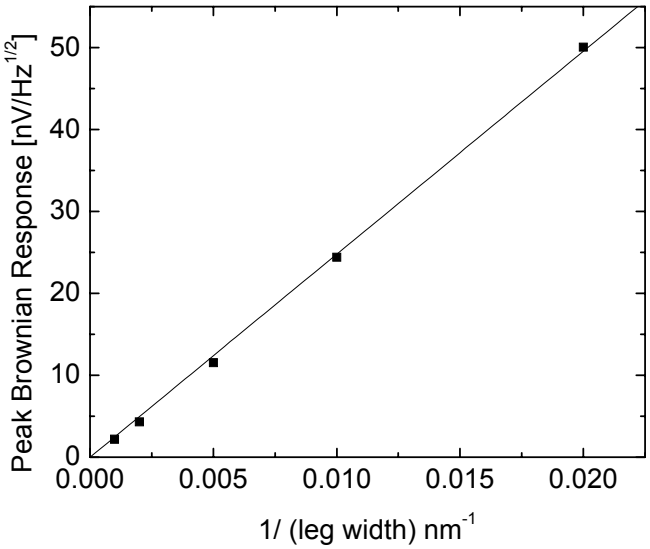


**Fig. 8.4.D Dependence of Brownian noise spectrum on width of cantilever legs**
The Brownian noise response is observed to increase as 1/(leg width).

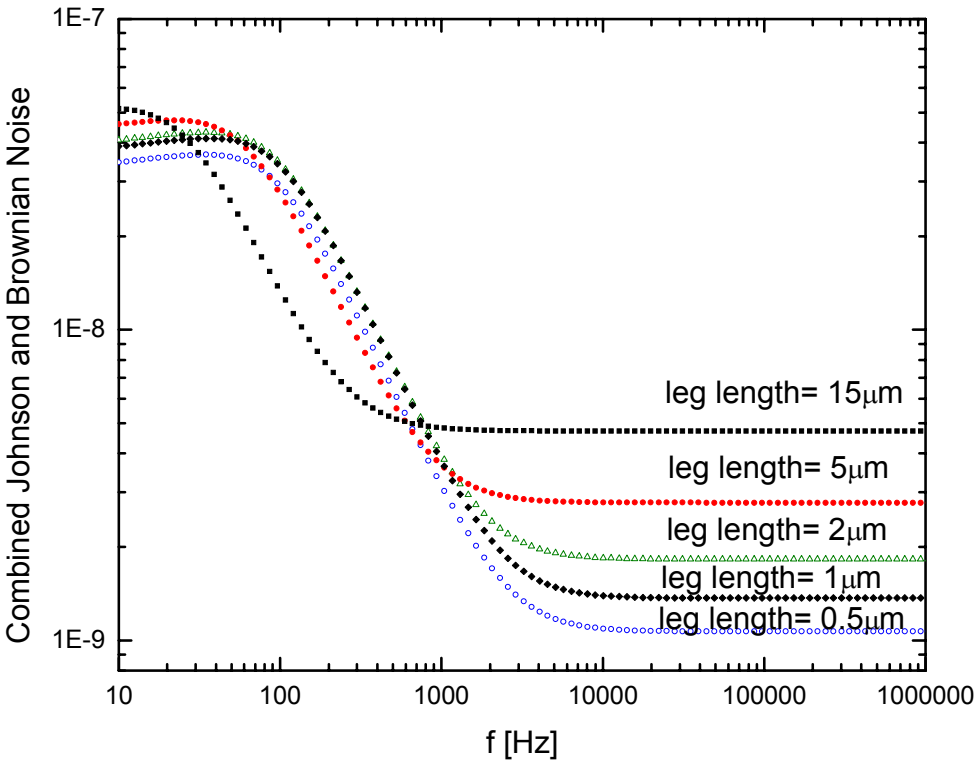


**Fig. 8.4.E Dependence of Brownian noise spectrum on length of cantilever legs**

The dependence of the Brownian noise spectrum on cantilever leg length is weak except for cantilevers with very long legs where the increased compliance of the device leads to a significant decrease in response bandwidth.

## *8.5 Experimental Protocols for the Detection of Brownian Fluctuations*

Two experimental protocols for the detection of Brownian fluctuations are discussed. The first is based on the calculations of the preceeding section, namely a study of the Brownian motion for cantilevers of different lengths. The second is a study of the Brownian motion in fluids of different viscosity.

### 8.5.1 Study of Brownian motion in Cantilevers of Differing Length

Achieving the sensitivity to detect Brownian fluctuations requires extremely compliant devices. In practice this means very thin devices with narrow legs. Our thinnest devices are fabricated with 30nm thickness. Achieving these devices reproducibly has required a number of modifications to the fabrication process flow (these were outlined in section 3.1.4). Typical devices fabricated for this experiment are shown in Fig. 8.5.A. The expected (calculated) Brownian response for these devices is shown in Fig. 8.5.B.

### 8.5.2 Viscosity Dependence of Brownian Fluctuations

One method of validating the Brownian noise measurements is to tune the viscosity (through the introduction of different fluids) and to observe the effects on the measured signal. The calculated response is shown for four different alcohols in Fig. 8.5.C. The variance shown in this theoretical plot is that of the measured noise floor data from Fig. 4.3.A. The calculated response shown includes both Johnson noise and thermomechanical noise. The data is presented for two values of parasitic resistance. The first of 14.2 squares is the value measured from typical devices we have fabricated.

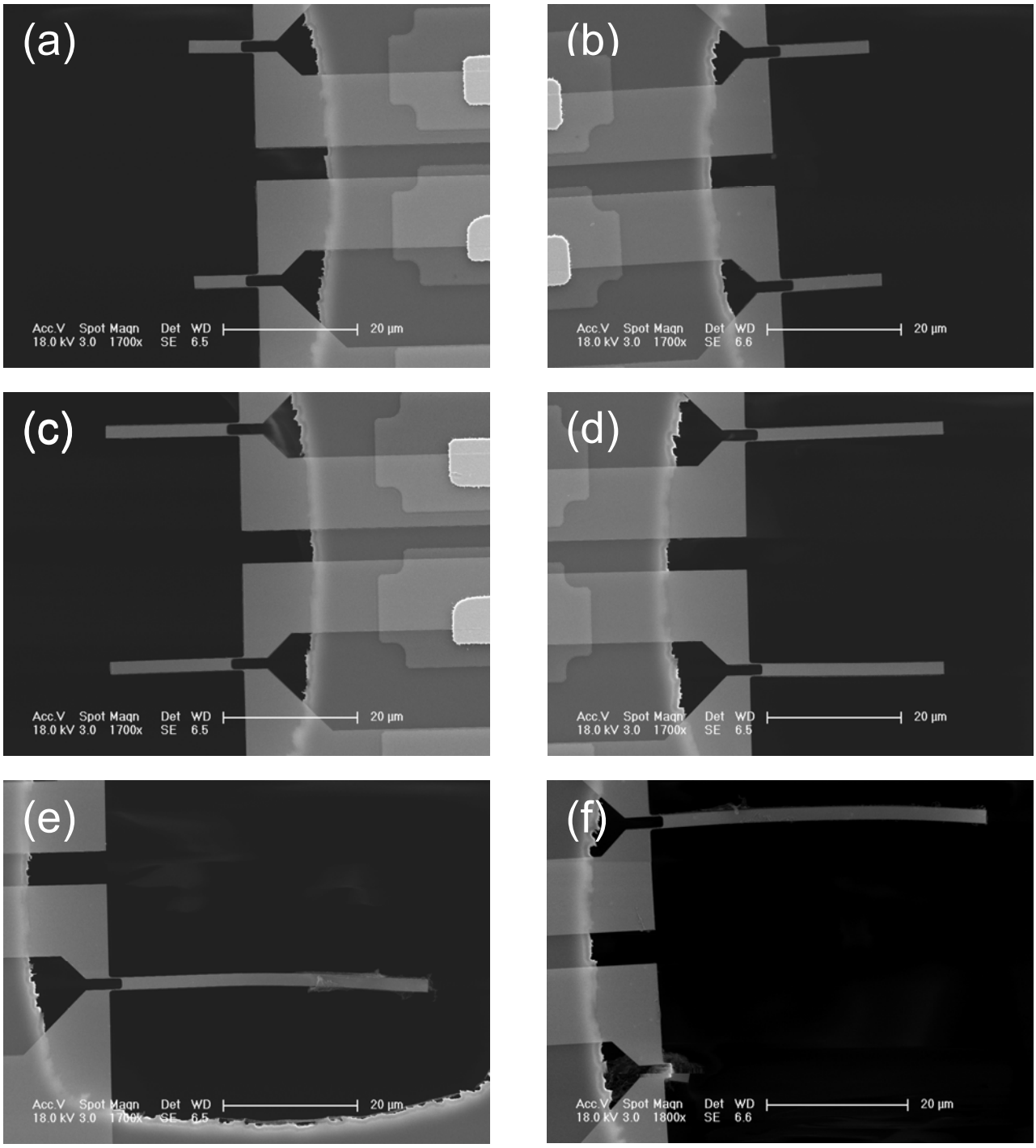


**Fig. 8.5.A Devices fabricated to enhance sensitivity to Brownian fluctuations**
All these devices have the folling common dimensions: device dimensions: $t_{Si}$=30nm, $t_{Cr}$=3.5nm, $t_{Au}$=26.5nm, w=2µm, $w_{leg\ (Si)}$ =200nm, $w_{leg\ (Au)}$ =80nm, $\ell_{leg}$ =1.5µm. We vary the cantilever lengths as follows: (a) $\ell$ =10µm, (b) $\ell$ =15µm, (c) $\ell$ =20µm, (d) $\ell$ =30µm, (e) $\ell$ =40µm, and (f) $\ell$ =50µm

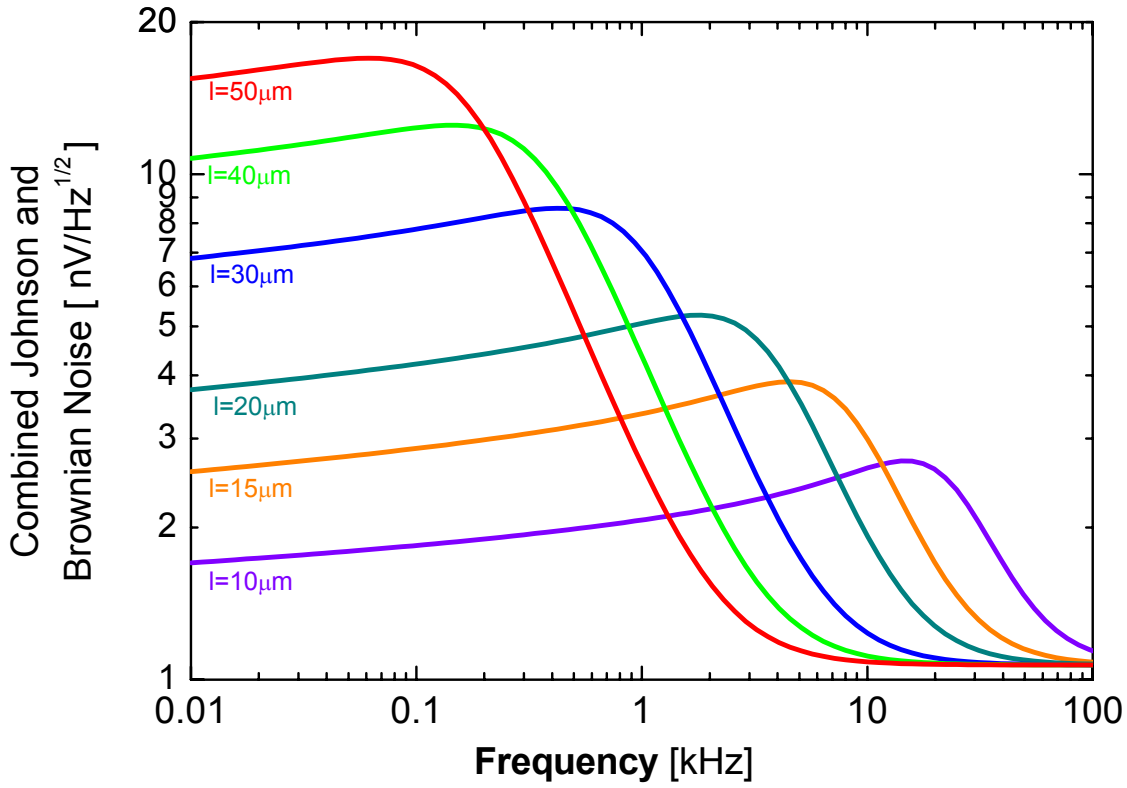


**Fig. 8.5.B Expected response from Brownian fluctions for experimentally realizable metallic piezoresistive devices**

The expected total noise spectral density is shown here for experimentally realizable (Fig. 8.5.A) metallic piezoresistive devices. The dimensions of these devices were provided in Fig. 8.5.A. Unlike the Brownian noise spectrum for the silicon piezoresistive devices which was overwhelmed by 1/f noise, this noise spectrum is expected to be experimentally realizable due to the much lower 1/f knee for metallic devices.[6]

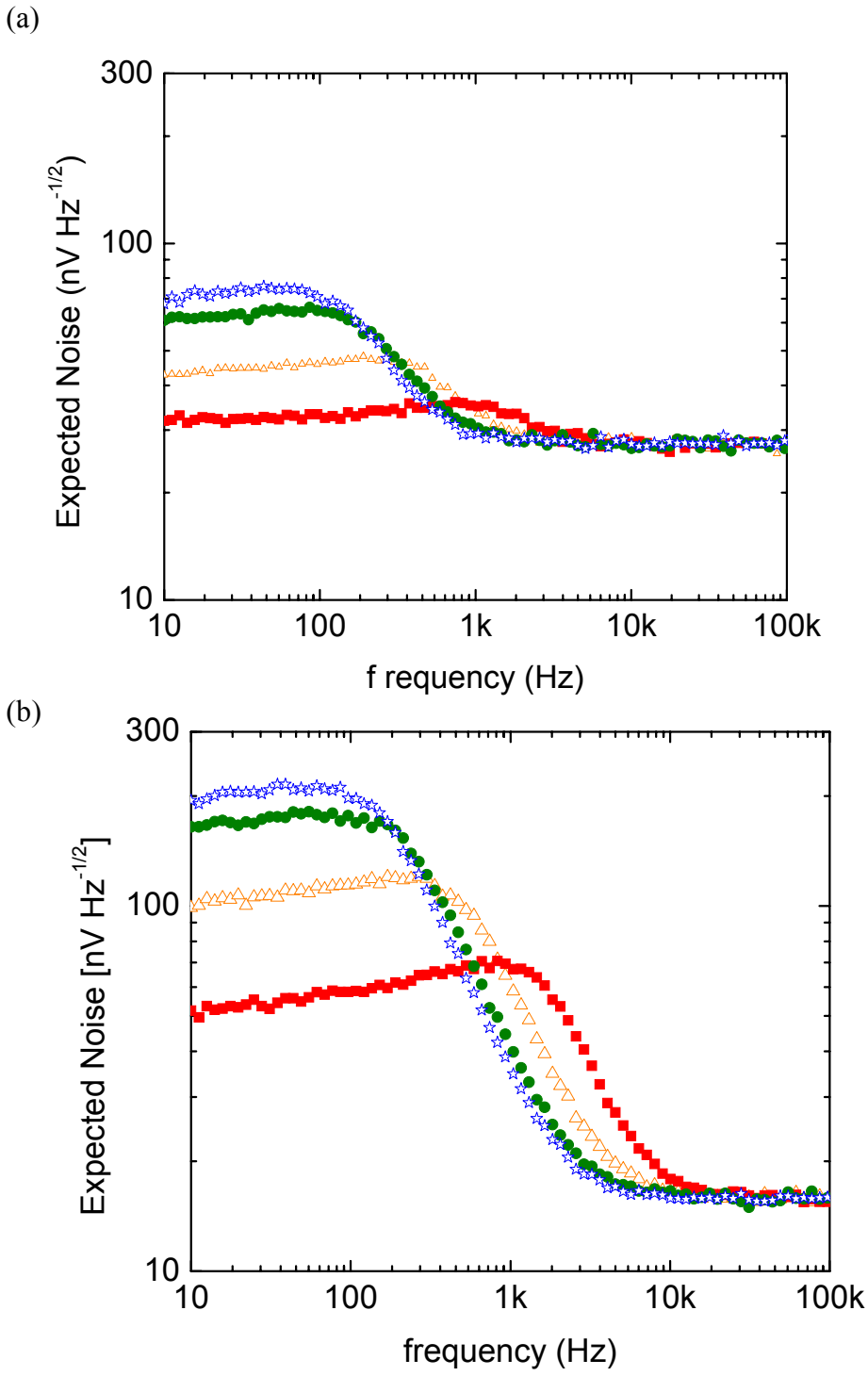


**Fig. 8.5.C Expected Brownian fluctuations in several alcohol solutions**

The expected noise from the device (comprised of Johnson and thermomechanical noise); the variance in the noise is derived from the data of Fig. 4.3.A. Solid red squares: methanol; hollow orange triangles: 1-butanol; solid olive circles: 1-octanol; hollow blue stars: 1-decanol. Device dimensions are provided in the text. (a) 14.2 squares of parasitic resistance (b) 2 squares of parasitic resistance

A resistance of 2.5 kΩ/square was assumed for the epi layer (this is the typical measured value). The second showing 2 squares should be achievable with small improvements in the fabrication. The cantilever modeled in these calculations has a silicon piezoresistive element (not the metallic piezoresistors discussed in the previous section). The device dimensions are: $\ell = 50\mu m$ , $w$=2μm, $w_{leg}$=250nm, and $t$=100nm (of which the top 30nm comprised the heavily doped piezoresistive layer). A similar calculation for a metallic piezoresistive device is shown in Fig. 8.5.D.

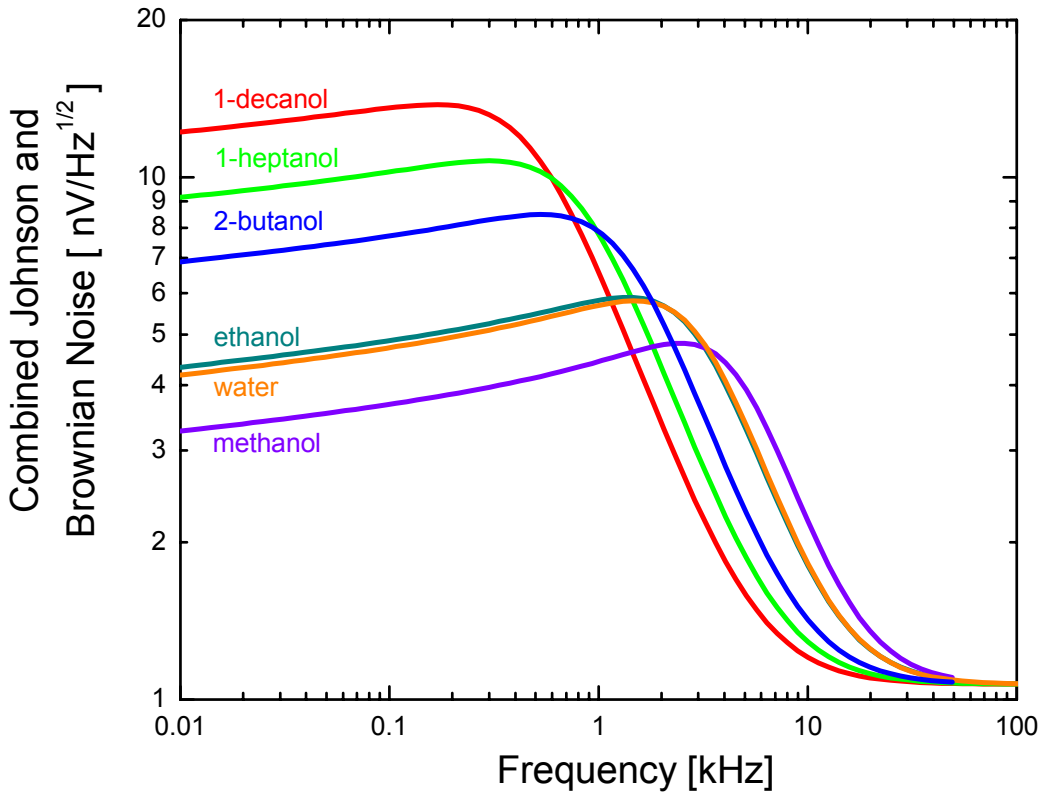


**Fig. 8.5.D Expected Brownian fluctuations for a metallic piezoresistive device in several solutions**

The expected combined Johnson and Brownian noise is shown for a gold piezoresistive device for which the dimensions are: silicon thickness: 30nm; gold thickness: 10nm; cantilever width: 2μm; leg length: 1μm; leg width: 2μm; and width of gold on legs: 50nm. The device resistance is 140Ω (including an electrode resistance of 50 Ω). A bias voltage across the device of 0.5V was used. A value of β=0.7 was used. This was the value measured by Harley and Kenny for silicon cantilevers where the conducting region was the top 30% of the device. Here metal is 25% of the total device thickness so we expect β to be comparable.

## 8.6 References


[1] D.A. Walters, J.P. Cleveland, N.H. Thomson, P.K. Hansma, M.A. Wendman, G. Gurley, and V. Elings, Review of Scientific Instruments, **67**, 3583 (1996).

[2] T.E. Schaffer, J.E. Cleveland, F. Ohnesorge, D.A. Walters, and P.K. Hansma, Journal of Applied Physics, **80**, 3622 (1996).

[3] J.W.M. Chon, P. Mulvaney, and J.E. Sader, Journal of Applied Physics, **87**, 3978 (2000).

[4] M.B. Viani, T.E. Schaffer, A. Chand, M. Rief, H.E. Gaub, and P.K. Hansma, Journal of Applied Physics, **86**, 2258 (1999).

[5] A. Mehta, S. Cherian, D. Hedden, and T. Thudat, Applied Physics Letters, **78**, 1637 (2001).

[6] H.X. Tang, ,M. Li, ,and M.L. Roukes, "Metallic thin film piezoresistive transduction in micromechanical and nanomechanical devices and its application in self-sensing SPM probes, United states patent application 20050150280, filed Dec. 14, 2004 and M. Li, H. X, Tang, and M. L. Roukes, "Very high frequency transduction of nanoelectromechanical systems using piezoresistive thin metal films", to be submitted

[7] C. Durkan and M.E. Welland, Ultramicroscopy, **82**, 125 (2000).

# 9 Conclusion

This thesis has presented an overview of piezoresistive silicon nanoscale cantilevers. We described a membrane-based, top-down fabrication method for the fabrication of micro- and nano-cantilevers and investigated the piezoresistively transduced response of these devices through both modeling and direct measurements. Three methods of actuation in vacuum and air (thermal excitation, magnetic excitation, and piezoelectric excitation) and one in fluid (pulsatory fluidic excitation) were compared. Passive actuation has been explored in vacuum from cryogenic to room temperature (thermomechanical motion) and modeled in fluid (Brownian motion). The measurements of thermomechanical motion in vacuum achieve record force-sensing performance for integrated sensors at room and cryogenic temperatures and have allowed further characterization of the device responsivity. In particular, analysis of the thermomechanical motion allows a measure of the piezoresistive gauge factor with greater precision than what we are able to measure directly using an AFM. We were able to extend this measurement of the gauge factor for doped silicon from room temperature down to cryogenic temperatures. The piezoresistive gauge factor is an important parameter for the analysis of the expected behaviour of piezoresistive doped silicon cantilevers. Previous studies have not looked at this parameter in detail in the temperature range below 50K.

Bias-induced heating is analyzed for devices in both fluid and vacuum. In the case of the former, heating analysis is used to ensure a safe operating bias to minimize the risk of damage to either the device in the constricted region where the current density is greatest or the highly temperature sensitive biofunctionunctionalized region at the

device tip. Analysis of heating in vacuum at cryogenic temperatures enabled the determination of a temperature and geometry-dependent optimum bias current at which the force sensitivity is maximized.

Both the fabrication technique described here and the underlying understanding of these devices are applicable to a large variety of geometries. We believe these will play an important generic role in future NEMS research and applications.

## 9.1 Engineering Challenges to the Development of Useful BioNEMS Sensors

In section 1.2 we introduced the concept of BioNEMS sensors. Thoroughout this thesis we hae characterized these devices and discussed expierments in which the devices were used. We consider now csome of the hurdles to achieving reproducible and conclusive biosensing. In section 7.3 we presented measurements on the detection of biotin labeled beads. The results were difficult to interpret for several reasons: firstly, the gap was too large to be spanned by individual beads, requiring aggregates of beads to achieve immobilization across the gap. Dr. Hong Tang at Caltech has recently achieved 45nm gaps on these devices.[References]

[1] This will be a significant improvement for future devices (see section 9.2.2). Nonspecific binding has also been a major issue. This has played a role in several respects: nonspecific binding to the cantilever can obscure the detection of the binding of the analyte of interest. This nonspecific binding can be reduced through silanization of the silicon cantilever. Experiments to achieve this are still in progress, the main difficulty being to ensure that the silane does not bind to the gold layer (and prevent the

functionalization necessary for specific binding). Nonspecific binding to the microfluidics can also be a problem. For low concentration experiments in can remove the analytes of interest from the medium (the surface area of the fluidics is much greater than the intended binding site). Non-specific binding to the fluidics can also lead to clogging. We have been able to greatly reduce the nonspecific binding to the PDMS microfluidics thourgh the use of biocompatible blocking agents in solution with the analytes. The blocking agents with which we have had the greatest success are: serum (rabbit serum was used), fish gelatin, and pluoronics.

A final concern, and perhaps the most significant since the path to surmounting it is less clear, is achieving specific binding. It is not enough to have a receptor present at the distal end of the cantilever and the compatible analyte in solution. The two must come into contact. We have already shown that we are in the low Reynold's number regime. At low Reynold's number, obstacles to fluidic flow (such as our cantilever) will be surrounded by a layer of fluid which is at rest relative to the cantilever and not the fluid. Analytes can only cross this boundary layer via diffusion. The mean square distance traveled by a diffusing particle of diffusion coefficient, *D,* in time, *t*, is $\sqrt{\langle x^2 \rangle} = \sqrt{2Dt}$ .[2] We estimate the diffusion coefficient from the Einstein-Stokes expression for the diffusion coefficient for a sphere of radius, *a*: $D = k_B T / 6\pi\eta a$ , where, $\eta$, is the dynamic viscosity.[3] For this expression 0.6 hours are required for a sphere 100nm in diameter to diffusion 100μm and 6 hours are required for a sphere 1μm in diameter to diffuse the same distance. For a geometry such as that depicted in Fig. 1.2.A, where the surface area for specific binding (100nm x 7μm) is very small compared to the

open cross-section of the via, introducing fluidic flow in an attempt to bring the analytes closer to the binding region is counterproductive (once they have brought close to the region) since the analytes will quickly flow through the center of the via and will not have time to diffuse to the binding site. Achieving successful functionalization therefore requires flow to bring the analytes close and then periods in which the flow is stopped to allow the analytes to diffuse to their binding sites. A better geometry would perhaps be one in which the analytes are forced to flow in closer proximity to the receptor sites.

## *9.2 Direction for Future Experiments*

Throughout this thesis, where appropriate, we have mentioned directions for futher research. We now return to the three protocols for using BioNEMS devices as dynamic biosensors introduced in section 1.2, namely BioNEMS detection based on a change in device compliance, BioNEMS detection based on a change in device damping, and correlated detection using multiple cantilevers. A change in device compliance will occur if the ligand forms a molecular bridge to another cantilever, a beam, or a sidewall (Fig. 1.2.A and Fig. 1.2.B (a)). A change in device damping will occur if the binding event leads to a significant change in the cantilever's surface area. The latter is particularly true if the geometry is optimized to increase the surface area in an appropriate direction to displace substantially more fluid through the cantilever's motion such as might occur through the binding of a cell, star dendrimer, or bead of comparable dimensions to the device. In section 9.2.1 we present theoretical calculations for the fractional change in damping that might be detected under such a scenario, henceforth referred to as a $\gamma$ to $\gamma$' type experiment. In section 9.2.2 we discuss the future of

BioNEMS detection based on changes in device compliance ("docking" experiments) and correlated multi-cantilever experiments.

### 9.2.1 Detectable damping for a γ to γ' type experiment

The measured output voltage from the device is given by $V = FH(\omega) I_b \frac{\partial R_d}{\partial x}$, where $F$ is the force applied to the cantilever, $\partial R_d / \partial x$ is the measured change in device resistance per unit displacement of the cantilever tip, $I_b$ is the current applied across the device, and $H(\omega)$ is the response function for the cantilever in fluid defined by equation 10 in section 2.2.3. The normalized modulus of the response function for a typical cantilever with dimensions $\ell = 8\mu m$, w=2μm, $\ell_1 = 1.6\mu m$, and b=0.15μm is shown in Fig. 9.2.A (a).

The dependence of the output signal on damping was assessed for five frequencies beginning with the response function peak and extending out to a frequency at which the response function has dropped to 63% of the peak value. The points chosen are shown in Fig. 9.2.A (a). Increasing the damping leads to a change in response function (provided we are not in the flat response region occurring at low frequencies), leading to a change in the measured voltage, $V = FH(\omega) I_b \frac{\partial R_d}{\partial x}$. The expected change in output voltage is shown in Fig. 9.2.A (b) for the five frequencies highlighted on the response function in Fig. 9.2.A (a). A driving force of 100pN is assumed. For a 135$k\Omega$ sample, the Johnson noise is 50$n$V/√Hz. A 10 Hz bandwidth has been assumed, giving a noise floor of 158$n$V. For the curve just beyond the resonance peak (the orange curve corresponding to $f$=168$k$Hz), an increase of damping by 4% leads to a decrease in the signal to noise ratio from 20 to 1 to 19 to 1. An increase by 25% leads to a decrease in the signal to noise

ratio from 20 to 1 to 17.5 to 1. For a higher drive force, greater sensitivity could be attained.

(a) (b)

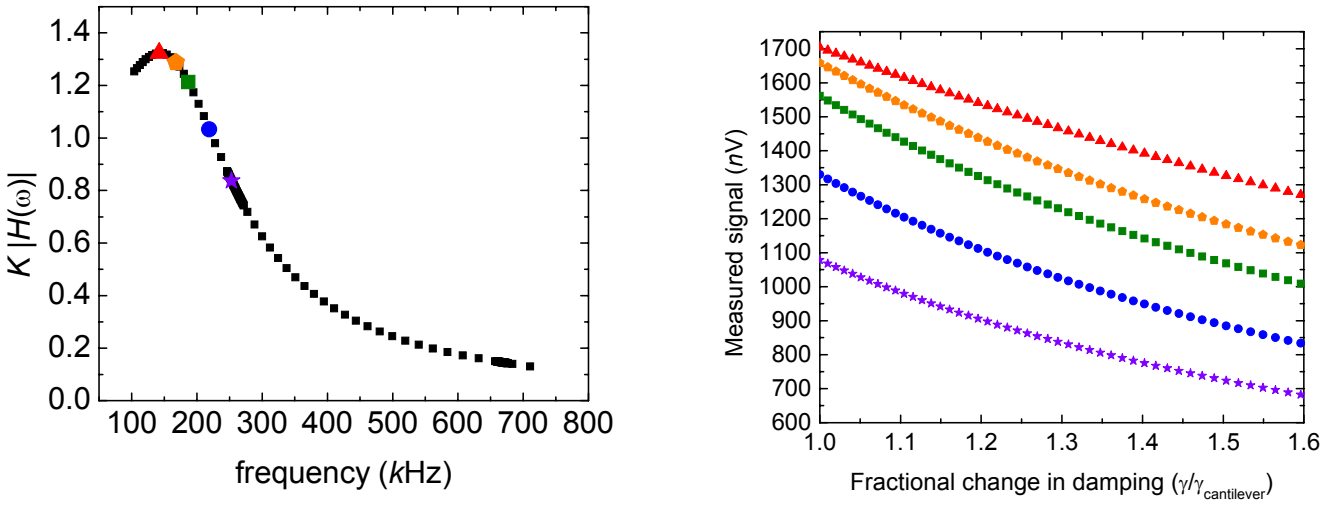


**Fig. 9.2.A Response Function for the Cantilever Used for γ to γ' Analysis**

(a) The calculated modulus of the response function is shown here for a cantilever of dimensions $\ell = 8\mu m$, w=2μm, $\ell_1 = 1.6\mu m$, and b=0.15μm. The data has been normalized by the spring constant to present a dimensionless "normalized" value. (b) The expected decrease in piezoresistive signal as the damping is increased is shown for five frequencies using a drive force of 100pN. The curves are color and symbol-coded to correspond to the frequencies highlighted on the response curve in (a). This calculation is of interest for experiments in which the binding of a large cell, spore, or bead would substantially alter the effective damping. The Johnson noise-limited noise floor for this device is estimated at 50nV. The greatest sensitivity for this device is observed for *f*=168kHz, corresponding to 97% of its peak value. For this frequency a 4% increase in damping would lead to a decrease in signal of 50nV. For a higher drive force, greater sensitivity could be attained.

### 9.2.2 Future Experiments: BioNEMS Detection Based on Changes in Device Compliance and Correlated 2-Cantilever Experiments

In section 7.3 we presented preliminary data on the use of BioNEMS devices as biosensors. In that experiment we were looking for modulation of the device response due to a change in compliance. This change was brought about by the binding of biotinylated beads across a gap separating the distal end of the cantilever from a fixed "dock." The results of that and a number of similar experiments were inconclusive and difficult to interpret. A major difficulty with this experiment was the gap size. Although it was our intention to fabricate 100 nm gaps, stress in the device caused the cantilever to curl, and the actual gap ranged from 300nm to 5μm on typical devices. Such large gas can not be bridged by single analytes. Not only has this obfuscated the analysis of experiments to date, it also presents a hurdle to one of the long term goals of this project; namely single molecule detection. H.X. Tang and B. Gudlewski have recently fabricated a device with a ~45nm gap between two end-opposing cantilevers.[References]

[1] With such narrow gaps we await a new generation of biosensing experiments based on a change in device compliance ("docking" experiments). Narrow gaps will allow briding by single analyte binding, and we anticipate the ability to perform much more conclusive biosensing experiments. Moreover, the narrow gaps between 2 cantilevers pave the way for correlated 2-cantilever detection (such as that depicted schematically in Fig. 1.2.C). The fluidic coupling between such devices is of interest in its own right. Modelling of fluidic coupling between opposing nano-cantilevers in close proximity has recently been performed by M.R. Paul and M.C. Cross.[4] The fluidic disturbance caused by an

oscillating cantilever is of order $\sqrt{\nu/\omega_{o\,fluid}}$, where $\nu$ is the kinematic viscosity and $\omega_{o\,fluid}$ is the fluid loaded resonance frequency of the device. This disturbance is long range compared to the device dimensions and can be on the order of microns for nanoscale BioNEMS devices.[5] A number of interesting results are presented by the work of M.R. Paul *et. al.* In particular they predict correlated behaviour for cantilevers at short time scales (up to ~0.3μs depending on the separation) followed by anti-correlated behaviour at longer time scales.[4] 2-cantilever BioNEMS devices will allow experimental verification of their work. Coupled multi-cantilever sensors offer perhaps the greatest potential of the three proposed biosensing protocols. For correlated sensors the coupling between the device and hence the read-out signal is created by the binding of a linking molecule. This signal must be measured in the presence of a background correlation arising from the direct fluidic coupling. Nevertheless, the experimental goal can be classified as measuring a signal in the presence of a background coupling. This should be contrasted with both of the single cantilever protocols which rely on a fractional modulation of the measured device response to achieve biosensing. Moreover, it is hoped that for correlated BioNEMS devices careful device design will allow this background to be greatly reduced. For example, this might be achieved by judicious positioning of the sensing cantilever in a node of the direct fluidic coupling, possibly generated by multiple drive cantilevers (the work of M.R. Paul *et. al.* suggests that for a given frequency band this can also be achieved by tuning the device separation[4,5]). By minimizing this coupling, a genuine biosensing "on-off" experiment may be achieved.

## 9.3 References


[1] H.X. Tang, personal communication (February 2006).

[2] P. Atkins, Physical Chemistry, fifth *ed.*, Oxford University Press, New York, p. 855 (1994).

[3] P. Atkins, Physical Chemistry, fifth *ed.*, Oxford University Press, New York, p. 850 (1994).

[4] M.R. Paul and M.C. Cross, Phys. Rev. Lett., **92**, 235501 (2004).

[5] J.L. Arlett, M. Paul, J. Solomon, M.C. Cross, S.E. Fraser, and M.L. Roukes, "BioNEMS: Nanomechanical Systems for Single-Molecule Biophysics" in *"Controlled Nanoscale Motion in Biological and Artificial Systems"* (Nobel Symposium 131, June 2005), H. Linke et al., Eds. (Springer Verlag, Heidelburg, *to be published*).